2016

A 3D Multiscale Simulation of Rough Surface Contacts at the Atomic Level

Jie Zhang
University of Wollongong

A 3D Multiscale Simulation of Rough Surface Contacts at the Atomic Level

A thesis submitted in a partial fulfilment for the degree of
Doctor of Philosophy

from

UNIVERSITY OF WOLLONGONG

by

Jie Zhang

BEng, MEng

School of Mechanical, Materials and Mechatronic Engineering
Faculty of Engineering and Information Science

2016

Declaration

I, Jie Zhang, declare that this thesis, submitted in partial fulfilment of the requirements for the award of Doctor of Philosophy, in the school of Mechanical, Materials, and Mechatronics Engineering, Faculty of Engineering and Information Sciences, University of Wollongong, is wholly my own work unless otherwise referenced or acknowledged. The document has not been submitted for qualification at any other academic institution.

Jie Zhang

August 2016

Abstract

Investigating rough surface contacts at the atomic level is instrumental to the overarching understanding of tribology across the scales. Limitations of traditional techniques, such as purely atomistic and continuum simulations, motivate the development of multiscale simulations accounting for nanoscale contact.

In this work, multiscale models are developed, and applied to investigate rough surface contacts at the atomic level with consideration of elastic deformation, elasto-plastic deformation, effects of temperature and lubricant.

The derivation and parallel implementation of a 3D multiscale model is based on an existing 2D multiscale code (DAMAS) coupling finite element method (FEM) and molecular dynamics (MD). The extended code leads to a model that features minimum degrees of freedom in comparison to other multiscale methods. It is validated by studying single asperity contacts between a rigid tip and a deformable substrate. DAMAS is applicable to elastic contacts at low temperature, with a speedup of up to 9 times, compared to purely atomistic simulations for the same domain. The model also captures important features such as discontinuous increase of contact radius and periodicity of the kinetic frictional force.

The DAMAS is used to perform 3D simulations of elastic contacts of flat-on-rough and rough-on-rough with different surface roughness. Results confirm the importance of the third dimension, and the effects of the system size. Compared to about 10 from previous 2D work, the proportionality constant κ of the linear relation between the average pressure and the rms slope, obtained in this work, is close to Perrson's prediction $\kappa = 1.6$. The slope of the relationship between contact area and load is variable for different system sizes but converges to a constant value as the system size reaches a threshold. Similar to prediction of continuum mechanics, the real contact area decreases with an increase of root-mean-square (rms) slope of the surface at the atomic level.

In light of the limitations of the model to small elastic deformation and low temperature, a hybrid simulation method (HSM) is proposed, including its coupling scheme and parallel implementation. The simulation of single asperity contact with adhesion at low temperature is performed to validate the HSM. As a new work, the HSM is extended to study rough surface contacts at finite temperature. It is found that temperature affects the changes of root-mean-square and skewness factor of the surface. Small effect of the temperature on the linear relationship between contact area and load is observed.

Study of the role of lubricant in rough surface contacts at temperature of 300K is carried out using the HSM. To the best of author's knowledge, this 3D multiscale model has not been proposed previously. Results indicate that the contact area decreases as the number of lubricant molecules is increased. The friction force is slightly sublinear to the loads for dry sliding while the relationship between the friction force and the loads for lubricated sliding shows a more pronounced non-linearity. The friction force reduces considerably when lubricant molecules provide a large portion of the supporting load. In partial lubrication, the friction force is determined by the contact area.

List of Figures

List of Tables

List of Abbreviations

AFM	**A**tomic **F**orce **M**icroscope
BCC	**B**ody **C**entred **C**ubic
BDM	**B**ridging **D**omain **M**ethod
BGT	**B**ush-**G**ibson-**T**homas
BSM	**B**ridging **S**cale **M**ethod
CADD	**C**oupled **A**tomistic/**D**iscrete **D**islocation method
CBR	**C**auchy-**B**orn **r**ule
CGMD	**C**oarse-**g**rained **M**olecular **D**ynamics method
CLS	**C**oupling of **L**ength **S**cales
CNA	**C**ommon **N**eighbor **A**nalysis
CSP	**C**entral **S**ymmetry **P**arameter
DMT	**D**erjaguin-**M**uller-**T**oporov Model
EAM	**E**mbedded **A**tom **M**ethod
FCC	**F**ace **C**entred **C**ubic
FEA	**F**inite **E**lement **A**nalysis
FEM	**F**inite **E**lement **M**ethod
FFM	**F**riction **F**orce **M**icroscope
GLE	**G**eneralized **L**angevin **E**quation
GW	**G**reenwood-**W**illiamson Model
HCP	**H**exagonal **C**losed **P**acked
HSM	**H**ybrid **S**imulation **M**ethod
IPFEM	**I**nteratomic **P**otential **F**inite **E**lement **M**odel
JKR	**J**onhson-**K**endall-**R**oberts model
LJ	**L**ennard-**J**ones potential
MAAD	**M**acroscopic **A**tomistic **A**b-initio **D**ynamics method
MC	**M**onte **C**arlo method
MD	**M**augis-**D**ugdale Model
MD	**M**olecular **D**ynamics

MEMS	**M**icro**E**lectro**M**echanical **S**ystems
MPI	**M**essage **P**assing **I**nterface
NEMS	**N**ano**E**lectro**M**echanical **S**ystems
PBC	**P**eriodic **B**oundary **C**ondition
QC	**Q**uasi-**C**ontinuum **M**ethod
RMD	**R**andom **M**idpoint **D**isplacement
RMS	**R**oot **M**ean **S**quare
STM	**S**canning **T**unneling **M**icroscope
THK	**T**ime **H**istory **K**ernel
UA	**U**nited-**A**tom model
VAC	**V**irtual **A**tom **C**luster

Acknowledgements

I would like to thank Dr. Guillaume Michal for his valuable guidance in academic research and especially in programming which will be really useful in my career. The wise words, ‘difference between capacity and capability’, ‘always simple, simple is best’, that you told me, really inspires me. I also would like to thank Dr. Hongtao Zhu for his technical support and helpful discussions. Particularly, I express my gratitude with all my heart to my main supervisor, Professor Kiet Tieu, for giving me an opportunity studying in University of Wollongong, and for fully supporting me to complete this thesis. I would say Professor Kiet Tieu is not only an academic supervisor, but also a life guide to me. Thank you very much, Professor Kiet Tieu.

I would like to thank China Scholarship Council and University of Wollongong for providing my scholarships.

My sincere thanks to my friends, Dr. Liang Zhang, Dr. Hui Wang, Mr Yuxiang Liu, Dr. Dr. Su Huang, Dr. Jun Zhang, Mr Zhenjun shan, Dr Guanyu Deng, Dr. Peitang Wei, Dr. Xin Zhao, Dr. Linping Chan, and Mr. Thi Ta. They gave me academic help to finish this work, and shared happiness and sadness of my life in the past years in Wollongong. Hope our friendship lasts. Particularly, I would like to thank my girlfriend, Miss Weiting Liao, for helping me and looking after me in the whole journey. Finally, I would like to thank my father Zhisheng Zhang, my mother Fengying Gao, my sister Hui Zhang, for their full support so that I can finish this work.

Publications

1. Peitang Wei, Cheng Lu, A.Kiet Tieu, Guanyu Deng, **Jie Zhang**, 2015, Modelling of Texture Evolution in High Pressure Torsion by Crystal Plasticity Finite Element Method, Applied Mechanics and Materials, Vols. 764-765, pp. 56-60.

2. **Jie Zhang**, Liang Zhang, A.Kiet Tieu, Guillume Michal, Hongtao Zhu, Guanyu Deng, 2016, Finite-Temperature Multiscale Simulations for 3D Nanoscale Contacts, Applied Mechanics and Materials, Vol. 846, pp. 288-293.

3. **Jie Zhang**, Guillume Michal, A.Kiet Tieu, Hongtao Zhu, Guanyu Deng, 2016, Hertz Contact at the Nanoscale with a 3D Multiscale Model, Applied Mechanics and Materials, Vol. 846, pp. 306-311.

4. Thi D. Ta, A. Kiet Tieu, Hongtao Zhu, Qiang Zhu, Prabouno B. Kosasih, **Jie Zhang**, Guanyu Deng, 2016, Tribological Behavior of Aqueous Copolymer Lubricant in Mixed Lubrication Regime ,ACS Applied Materials & Interfaces, Vol.8, pp.5641-5652

5. Liang Zhang , Cheng Lu, Kiet Tieu, Guillaume Michal, **Jie Zhang**, Guanyu Deng, 2016, Tension/compression asymmetry of grain boundaries with non-planar structure,2016, Materials Research Express, Vol.3, pp.085025

6. Liang Zhang, Cheng Lu, **Jie Zhang**, Kiet Tieu, 2016 ,A dual deformation mechanism of grain boundary at different stress stages, Materials Letters, Vol.167 , pp.278–283

7. Guanyu Deng, Qiang Zhu, Kiet Tieu, Hongtao Zhu, Mark Reid, Ahmed Saleh, Lihong Su, Thi Ta, **Jie Zhang**, Cheng Lu, Qiong Wu, Dale Sun, 2016, Evolution of microstructure, temperature and stress in a high speed steel work roll during hot rolling: experiment and modelling, Journal of Materials Processing Technology, under review.

List of Contents

Chapter 1: Introduction

1.1 Motivation

Amontons's law proposed in 1699 states that the friction force between two contacting objects is linearly proportional to the normal load, and is independent of the contact area [1]. Despite of being based on macroscopic assumptions, Amontons' law has been widely used to model friction behaviors over a range of scales. However, macroscopic friction law does not hold in general at the nanoscale. For instance, it is not applicable to the contact between atomically smooth surfaces with strong adhesion [2]. Moreover, it has been found that single asperity contacts at the nanoscale do not exactly follow macroscopic contact mechanics [3]. The breakdown of the continuum mechanics is not limited to non-lubricated contact. Down to the atomic level, lubricant fluid between two contacting bulk has different properties, and cannot be described by classical fluid mechanics [4]. Therefore, on the theoretical side, a full understanding of nanoscale contacts plays a crucial role in developing a law that governs atomic behaviors and links with macroscopic laws; on the practical side, it is necessary to investigate fundamental mechanisms of nanoscale contacts as the size of the modern devices such as MEMS/NEMS decrease to the nanometer scale [5].

With a number of sophisticated instruments, such as atomic force microscope (AFM), friction force microscope (FFM) and scanning tunneling microscope (STM), experimental techniques have been widely used to investigate contacts at the atomic level[6]. However, there are some difficulties with experimental techniques. For instance, it is difficult to directly measure the interface between tip and substrate from AFM [7]. Moreover, as mentioned by Carpick et al. [8] , contamination of the interface is inevitable, even if AFM is operated under ultrahigh vacuum conditions. It is contamination such as oxide that makes it a challenge to investigate the exact nature of the interface. Simulations can model pure materials of interest, and provide solutions to these difficulties in experimental techniques. Compared to the aforementioned

experiments, it is relatively easier for simulations to provide information about molecular systems at very small scale (nanometer) that cannot be obtained experimentally. Furthermore, simulations feature highly predictive ability, and lower cost of money compared to expensive experimental instruments particularly for nanoscale[9].

At the macro to meso scale, the use of continuum simulations such as finite element method (FEM) is natural candidates to study contact problems. Providing wear is negligible, contact conditions can be reasonable predicted through the definition of the friction coefficient. However the details of the contact mechanisms at micro and nanoscale, such as the interaction of the contact surfaces with polymeric lubricants, cannot be represented with continuum mechanics. In contrast, molecular dynamics (MD) simulations are capable of describing atomistic phenomenon. The friction coefficient is not a parameter but rather an outcome. Complex interactions between solid and fluid mechanics as well as chemistry can be studied.[10-12].

On the other hand, with reference to nanoscale asperity contact, a large number of papers on single asperity contact have been published, while the work of rough surface contacts (both unlubricated and lubricated) at this scale is limited. And the breakdown of continuum mechanics for rough surface contacts has not been considered much. This is probably due to limited computational resources. It is expensive to run a 3D atomistic model of rough surface contacts with an appropriate size (larger than 100nm) using fully MD simulations. The limitations of the continuum and MD models motivate development of a multiscale model, in which it is not necessary to describe atomistic details everywhere. Multiscale coupling techniques have been developed for more than two decades [13]. However, a large atomistic domain in the current multiscale models that works for 3D problems is needed. The rough surface contact should be represented realistically by a model with an adequate number of atoms that can produce accurate results with acceptable computational time. Furthermore, only few papers present finite temperature coupling until very recently, whereas most of

current multiscale models focus on zero Kelvin. As temperature effects on rough surface contacts could be crucial, it requires new work on finite temperature coupling.

1.2 Objectives

The objectives of this thesis consist of two parts. One part is to develop a new multiscale model with the minimum number of atoms, and investigating a finite temperature coupling scheme that works for isothermal process. The other part focuses on studying rough surface contacts at the nanoscale using advantages of the multiscale method, as a further investigation of breakdown of continuum mechanics. For the simulations of rough surface contacts, more specifically, we focus mainly on the following:

1) Effects of the system size on the relationship between contact area and load during elastic deformation, and making comparisons with continuum prediction.

2) Effects of temperature on the rough surface contacts with plastic deformation.

3) Role of lubricant in rough surface contacts, and comparing with dry contact.

1.3 Scope

This thesis consists of seven chapters. The main work of each chapter is outlined in the following.

In chapter 2, classic continuum models are reviewed with their main derivations and limitations in the first section, serving as a comparison for the results obtained in the following chapters. The theory of finite element method (FEM) and molecular dynamics (MD) techniques are briefly presented in section 2.2 and 2.3. The existing applications of the two techniques for nanoscale contacts are also summarized in section 2.2-2.3. Section 2.4 focuses on a technique of multiscale coupling between FEM and MD. The key ingredients of multiscale coupling are illustrated, following a review of classical multiscale methods. More importantly, one of the multiscale methods, called the Hybrid simulation method, is introduced. As the HSM features

simple implementation, high accuracy and low computational expense, it is well suited for the modelling of rough surface contacts.

In chapter 3, a 3D multiscale model that bridges FEM and MD is presented. Following an introduction of the theoretical framework, the governing equations of the model are formulated. Details of the validation of the model are conducted by modelling the contact between a rigid spherical tip and a deformable substrate. Results from both static and kinetic simulations are discussed, and compared with MD simulations and classic contact mechanics. Finally, the advantages and limitations of the proposed model are discussed. Chapters 4 to 6 focus on more complex simulations of contact problems.

Chapter 4 focuses on the application of the proposed model in chapter 3 to the simulation of elastic contact between rough surfaces. Simulations of the flat-on-rough and rough-on-rough contacts are performed. Details of the method used to generate the rough surface and the mesh are provided. A simple interpolation method is applied to rough meshed surfaces. The use of the multiscale technique permits a much larger system than presented in the previous MD simulations. Effects of surface roughness and material properties on contact parameters are considered. The results are benchmarked by both MD simulations and continuum theory.

In chapter 5, a hybrid simulation method (HSM) is introduced to study the influence of temperature on rough surface contact with possibility of plastic deformation. Firstly, comparisons between the HSM and the model proposed in chapter 3 are made. The implementation of the HSM is presented. In section 5.2, the validation and accuracy of the HSM are evaluated by analyzing contact parameters, plastic deformation and stress continuity from the simulations of single asperity contact with adhesion. Section 5.3 is the core of the chapter, in which a patch test is used to evaluate the performance of the HSM at different temperatures (up to 500K). Finally, the method is applied to simulations of rough surface contact at finite temperatures.

In chapter 6, lubricated contact is investigated by the HSM in the previous chapter. It was first started with the preparation of atomic surface with given roughness and lubricant molecules. After a detailed introduction of model set-up, the multiscale simulations of non-lubricated and lubricated contacts are carried out. Effects of load, surface roughness on contact area, surface pressure and friction force are discussed. Influences of lubricant on the change of contact area and friction force in lubricated contacts are investigated.

In the final chapter, the main results of this thesis are summarized and suggestions are proposed for future work.

To the best of author's knowledge, the following improvement have been contributed to the research of multiscale methods

1) A 3D multiscale model is developed and validated to study nanoscale contacts. The model features with the minimum number of atoms that only used describe atomic interactions between two bodies.

2) The HSM is extended to study nanoscale contacts at finite temperature. Compared with other complicated methods such as bridging domain method, the implementation of the HSM is simpler, and the results indicate the high performance of the HSM at finite temperature.

The following innovations have been contributed to the research of nanotribolgy:

1) The multiscale model is used to propose perform 3D simulations of the flat-on-rough contacts and the rough-on-rough contacts. Results show that the third dimension has an important effect the proportionality between average pressure and contact area. In the previous 2D simulation, proportionality is larger than 10, while it is close to Perrson's prediction 1.6 in this thesis. It is also found that the slope of the linear relation between contact area and load converges to a constant value when the system size reaches a threshold.

2) It is the first time that the multiscale method is used to perform the simulations of lubricated rough surface contact. The size of the deformable bulk is 8 times than that in the previous MD simulations. The larger size permits a generation of more asperities on the rough surface, and a reduction of statistical error of results. Results indicate the important role of lubricant in determining surface roughness, contact area and friction force.

Chapter 2: Literature review

Classical contact mechanics has been developed for more than a century since the pioneering work of Hertz's, and its theories are widely used in a variety of industrial and research areas. As experimental and simulation techniques develop, the scales of the objects for observation decrease from macroscale to nanoscale. Interestingly, some continuum theories still hold under certain conditions at the nanoscale [11]. However, in most cases, deviations emerge when using the continuum models to nanoscale contacts. This is known as the breakdown of continuum models [3]. Over the last few decades, much work has been done on the quantitative analysis of such deviations in order to determine the effects that lead to them, and demonstrate the applicable conditions of the continuum theories at the nanoscale [12, 14-16]. In these studies, the contacting parameters such as contact area, contact pressure, friction forces etc. are quantitatively compared with those in the classical theories. As the continuum models serve as the benchmarks for nanoscale contacts, we first introduce some theories of classic contact mechanics in section 2.1.

There are several modelling methods used to analyze nanoscale contacts. Among them, finite element method (FEM) and molecular dynamics (MD) simulation are the most widely used. Both FEM and MD have their own advantages, but they are not free of limitations. In this chapter, one of the aims is to demonstrate their individual limitations having influence on a study of nanoscale contacts. Detailed introductions of FEM and MD are presented in sections 2.2 and 2.3, respectively. Apart from that, their applications to nanoscale contacts are reviewed. In section 2.4, the focus is on multiscale method which can overcome the limitations of FEM and MD, and combine their advantages. Details of the major problems with the multiscale coupling, and some widely used multiscale methods are described. Finally, a summary on previous work and new contribution in this study is presented.

2.1 Classic contact mechanics:

2.1.1 Single asperity contact

Hertz contact. Heinrich Hertz investigated the contact between two elastic spheres, known as Hertz contact. Hertz's solution on elastic contact problems is based on the following assumptions [17]: (1) the surfaces are continuous and non-conforming; (2) strain is small; (3) each body can be considered as an elastic half-space and (4) there is no friction between the surfaces. The contact between two elastic spheres is equivalent to the contact between a rigid sphere of effective radius R* and an elastic plane of effective moduli E*. R* and E* are given in equations (2.1-2.2), where the symbols are Young's moduli E_1 and E_2, Poisson ratios ν_1 and ν_2, and radius R_1 and R_2.

$$\frac{1}{R^*} = \frac{1}{R_1} + \frac{1}{R_2} \tag{2.1}$$

$$\frac{1}{E^*} = \frac{1}{E_1} + \frac{1}{E_2} \tag{2.2}$$

In Hertz theory, the contact area is circular with a radius a and the contact pressure is assumed to be in an elliptical shape. If the rigid sphere is compressed into the elastic plane under the load P, according to Hertz theory, the contact radius and the indent displacement δ can be calculated by equations 2.3 and 2.4, respectively.

$$a = \sqrt[3]{\frac{3}{4}\frac{R^*}{E^*}P} \tag{2.3}$$

$$\delta = \sqrt[3]{\frac{9}{16}\frac{P^2}{R^* E^{*2}}} \tag{2.4}$$

Hertz contact is widely used in the theoretical development of continuum mechanics and also in industrial design and manufacturing, such as ball bearings. However, Hertz contact is only applicable to non-adhesive contact problems. Due to the

significant influence of adhesion on contact, many adhesion-based models have been developed, which will be presented next.

The Johnson-Kendall-Roberts model. Johnson, Kendall and Roberts [18] proposed a new model that accounts for adhesion between two elastic bodies, which is commonly known as the JKR model. They assumed that the adhesive interaction only exist in the contact area. The JKR model predicts a larger contact area compared to the predictions of Hertz contact at small loads. According to the JKR model, the contact radius is

$$a = \sqrt[3]{\frac{3}{4}\frac{R^*}{E^*}\left(P + 3\pi\Delta\gamma R^* + \sqrt{6\pi\Delta\gamma R^* P + (3\pi\Delta\gamma R^*)^2}\right)} \tag{2.5}$$

where $\Delta\gamma$ is the work of adhesion, which is defined as the work in separating the unit area of the surfaces from the state of contact to infinity. If $\Delta\gamma$ is zero, equation (2.5) equals equation (2.3) of Hertz's prediction. The JKR model also predicts a non-zero contact area at zero loading, due to the attractive forces. Therefore, there is a minimum load that is required to separate two surfaces, which is called a pull force given in equation (2.6).

$$P_{c(JKR)} = -\frac{3}{2}\pi\Delta\gamma R \tag{2.6}$$

where $P_{c(JKR)}$ stands for the pull force of JKR model. JKR model is applicable to the interactions between compliant materials, large sphere radii and large surface energy.

The Derjaguin-Muller-Toporov model. Derjaguin, Muller and Toporov (DMT) [19] present a different theory, in which the contact profile remains the same as in Hertz contact but attractive forces exist outside the contact area. According to the DMT model, the area of adhesive contact is just the Hertz's prediction with an additional term due to the adhesion. Actually, the expression of the contact area in the DMT model was firstly given in Maugis's work [20], equation (2.7).

$$a = \sqrt[3]{\frac{3}{4}\frac{R^*}{E^*}(P + 2\pi\Delta\gamma R^*)} \tag{2.7}$$

The pull force of the DMT model is

$$P_{c(DMT)} = -2\pi\Delta\gamma R^* \tag{2.8}$$

Compared to the JKR model [18], the DMT model is more accurate when dealing with the contact between stiff materials, small sphere radii and low surface energy. Besides, there is no singular stress in the DMT model, in contrast to the JKR model where the surfaces separate in the limit of contact with infinite slope.

Tabor parameter.

Both JKR and DMT model have been verified many times, making them powerful tools for studying the adhesion between elastic bodies. However, they are appropriate for two completely opposite ends of the contact behavior spectrum and it seems there is a transition area. Tabor [21] proposed a transition parameter (equation 2.9) which resolves the discrepancy between the JKR and DMT models.

$$\mu_t = \sqrt[3]{\frac{R^*\Delta\gamma}{E^{*2}z_0^3}} \tag{2.9}$$

where z_0 is the equilibrium separation of the surfaces. The DMT model corresponds to small μ_t while the JKR to large ones.

The Maugis-Dugdale model. Maugis [20] proposed anther parameter λ that governs the transition zone from JKR and DMT, see equation (2.10). In the Maugis-Dugdale model, the surface force is represented based on a potential interaction of Dugdale so that the work of adhesion is defined as a product of tensile stress σ_0 and a finite distance h_0, which is $\Delta\gamma = \sigma_0 h_0$.

$$\lambda = \sigma_0 \sqrt[3]{\frac{9R^*}{2\pi\Delta\gamma E^{*2}}} \tag{2.10}$$

The parameter λ in equation (2.10) is 16% larger than Tabor's parameter with the relation $\lambda = 1.1570\mu_t$.

2.1.2 Rough surface contact

It is widely known that the surface consists of numerous asperities with a wide range of scales and surface roughness formed by those asperities plays an important role in contact problems. In 1939, the first investigation of surface roughness was conducted by Bowden and Tabor [22]. They found that the real contact area is a small fraction of the nominal (apparent) contact area. Motivated by their work, Archard [23] studied the elastic contact between a flat plane and a sphere covered by small spherical asperities. To determine the effects of roughness, he covered small asperities with smaller ones. Archard found that the contact area is proportional to the normal load. Archard's work sheds light on elastic contact between rough surfaces, but the asperities on the real surfaces are not simple as Archard assumed. Later, three models (i.e. Greenwood-Williamson model [24], Bush-Gibson-Thomas model [25] and Perrson theory [26]) with more applicable insights into this topic were proposed. We briefly present the three models in the following.

The Greenwood-Williamson model. Greenwood and Williamson (GW) [24] studied the contact between a rigid plane and a nominally flat surface covered by a larger number of spherical asperities shown in figure 2.1. They showed that the contact area is nearly proportional to the normal load at small loads. In the GW model, those asperities had several characteristics. They all had equal radius of curvature R, but their heights z vary randomly following a Gaussian (exponential) distribution $\phi(z)$. Therefore, the probability that an asperity height between z and $z + dz$ is $\phi(z)z$. Furthermore, the GW model assumed that each asperity deforms according to Hertz

contact and not influenced by the deformation of their neighbors.

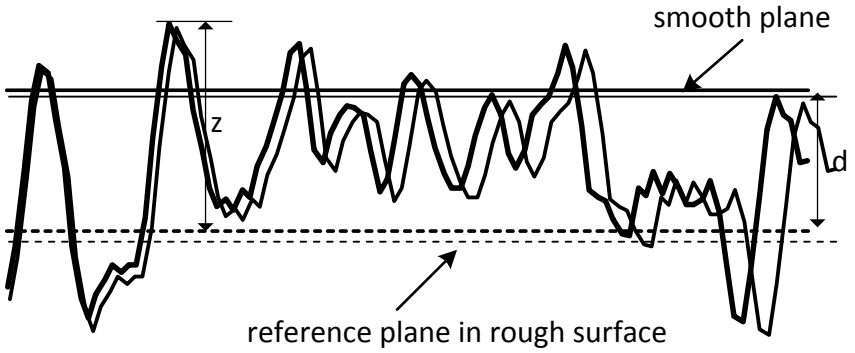

Figure 2.1: Contact of rough surfaces. The load is supported by those asperities whose heights z are higher than the separation d between two reference planes (from [24]).

In the GW model, the number of contacting asperities and contact area were statistically calculated. As shown in figure 2.1, those asperities having heights greater than the separation d, are in contact with the flat plane. Assuming that there are N asperities on the rough surface, the number of contacting asperities n is

$$n = N\int_{d}^{\infty}\phi(z)dz \tag{2.11}$$

The indent displacement $\delta = z - d$, and based on the Hertz theory, the contact area A_1 of each asperity is $A_1 = \pi R\delta$, so the real contact area is

$$A_r = \pi NR\int_{d}^{\infty}(z-d)\phi(z)dz \tag{2.12}$$

Despite the simplifications, such as no consideration of the asperity interaction, the predictions of the GW model were qualitatively consistent with the experiments. The basic formulations of the GW model has been modified and extended by many groups [27-29].

The Bush, Gibson and Thomas model. Bush, Gibson and Thomas (BGT) [25]

proposed an elastic contact model of a rough surface covered by asperities treated as elliptical paraboloids with randomly distributed curvatures and heights. Following the GW model, they also applied the Hertz contact to describe the deformation of each asperity and did not consider the effects of the asperity interactions on the contact. The main improvement the BGT model boasts is that the surface roughness occurs on several length scales, which is closer to real surfaces when compared to that used in the GW model. The BGT model predicts a strict linear relationship between the contact area A_r and the load P as seen in equation (2.13).

$$A_r = E^{*2} \int_{k_0}^{k_L} k^3 S(k) dk \; P \tag{2.13}$$

where k is the wave number and $S(k)$ is the surface roughness power spectrum. k_0 is the roll-off wavenumber while $k_L = 2\pi/L$, where L is the lateral size of the surface.

The Perrson theory. Both the GW model and the BGT model were limited to the cases where the real contact area is much smaller than the nominal contact area. Furthermore, they ignored the factor that the deformation of one asperity has effect on its neighbor asperities. However, Perrson [30] developed a more general theory for the full contact with asperity interactions.

Perrson theory starts with the magnification of the surface, which is defined as $\zeta = L/\lambda$, where L is the lateral size of the nominal contact area and λ is the shortest wavelength roughness. It shows in figure 2.2 that when a contact area is studied at low magnification ($\zeta = 1$) it appears as if complete contact occurs, but when the magnification is increased partial contacts become visible.

Perrson assumed that a complete contact satisfies a diffusion-like equation (2.14)

$$\frac{\partial P}{\partial \zeta} = \alpha' \frac{\partial^2 P}{\partial \sigma^2} \tag{2.14}$$

where $P(\sigma, \zeta)$ is the stress distribution in the contact area at the magnifications ζ.

$\sigma(\mathbf{x},\zeta)$ is the stress as a function of the spatial coordinate $\mathbf{x}$ and the magnifications ζ. The coefficient α' is the derivative of α, which is given as

$$\alpha = \frac{\pi}{4}E^{*^2}\int_{k_0}^{\zeta k_L} k^3 S(k)dk \tag{2.15}$$

where k is wave number and $S(k)$ is the surface roughness power spectrum. k_0 is the roll-off wavenumber while $k_L = 2\pi/L$, where L is the lateral size of the surface. Equation (2.14) is also valid for a partial contact. The diffusion equation can be solved with the boundary conditions $P(0,\zeta) = P(\infty,\zeta) = 0$.

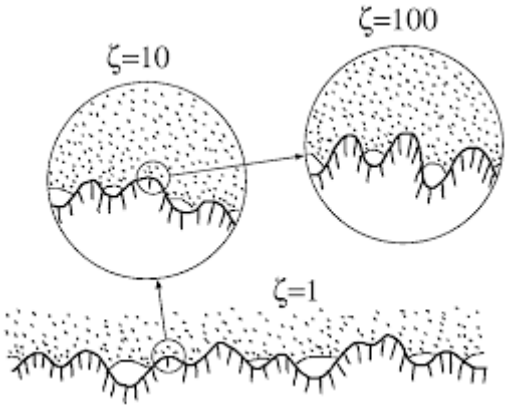

Figure 2.2: An elastic (e.g., rubber) block (dotted area) in adhesive contact with a hard rough substrate (dashed area) (from [31]). The substrate has roughness on many different length scales and the rubber makes partial contact with the substrate on all length scales.

The projected contact area at the magnification ζ is obtained as

$$A(\zeta) = A_0 \int P(\sigma,\zeta)d\sigma \tag{2.16}$$

where A_0 is the nominal area of contact. Perrson theory also indicated that the contact area is proportional to the load. For the surface heights following the Gaussian distribution, the coefficient of proportionality of Perrson theory is $2/\pi$ smaller than the prediction of the BGT theory. The mathematical derivation of the Perrson theory is complicated and the details can be found in original work [26, 30]. Manners and

Greenwood [32] critically analyzed the Perrson theory and its results. They indicated that Perrson underestimates the real area of contact for a given condition.

2.2 Finite element method

2.2.1 Introduction

Physical problems are mathematically governed by differential equations. It is difficult to obtain the analytical solutions for those differential equations in most cases. The equations are usually solved by numerical techniques with reasonable accurate solutions. Finite element method (FEM), also referred to as finite element analysis (FEA), is one of the most popular numerical techniques. The basic idea of FEM is to discretize a continuum domain into smaller and simpler parts called finite elements. The algebraic equations that approximate the governing differential equations for the whole domain are obtained by assembling the simple functions that are used to describe those finite elements. In the following paragraphs, we will briefly review the governing equations for a continuum with the Lagrangian formulation and their finite element equations.

The continuum is governed by five equations: the conservation of mass, the conservation of linear momentum, the conservation of energy, the strain-displacement equation and the constitutive equation [33]. The conservation of linear momentum equation is given below:

$$\frac{\partial P_{ji}^{K}}{\partial X_j} + \rho_0 b_i = \rho_0 \ddot{d}_i \tag{2.17}$$

where $\mathbf{P}^{K}$ is the first Piola-Kirchhoff stress tensor, $\mathbf{X}$ is the reference position vector of a material point, ρ_0 is the mass per unit of volume at initial time, $\mathbf{b}$ is the body force per unit mass and $\ddot{\mathbf{d}}$ is the second time derivative of the displacement. To solve equation (2.17), boundary and initial conditions must be given.

The boundary conditions, including the displacement boundary denoted by Γ_d and the traction boundary denoted by Γ_t, are

$$\mathbf{d} = \bar{\mathbf{d}}, \text{ on } \Gamma_d \tag{2.18a}$$

$$\mathbf{n}^0\mathbf{P}^K = \bar{\mathbf{t}}_{\mathbf{X}}^0, \text{ on } \Gamma_t \tag{2.18b}$$

where $\mathbf{n}^0$ is a unit normal to the body and $\bar{\mathbf{t}}_{\mathbf{X}}^0$ is equivalent to prescribing $\frac{\partial d}{\partial X}$ at the initial time $t = 0$. The initial conditions in terms of the displacements and velocities at time $t = 0$ are written as

$$\dot{\mathbf{d}}(\mathbf{X}, 0) = \mathbf{d}_0(\mathbf{X}) \tag{2.19a}$$

$$\mathbf{P}^K(\mathbf{X}, 0) = \mathbf{P}_0^K(\mathbf{X}) \tag{2.19b}$$

The finite element method uses the variational form equation of (2.17) with initial and boundary conditions [33]. The variational form of equation (2.17) is

$$\int \frac{\partial \delta u_i}{\partial X_j} P_{ji}^K d\Omega_0 - \int \delta u_i \, \rho_0 b_i d\Omega_0 + \int \delta u_i \, \rho_0 \ddot{d}_i d\Omega_0 - \int \delta u_i \, \rho_0 \bar{t}_i d\Gamma_0 = 0 \tag{2.20}$$

where δu_i is a test function and $\bar{t}_i$ is the prescribed traction boundary condition. All integrations are performed over the reference configuration.

The test function is approximated by using finite element interpolation in the following

$$\delta u_i(\mathbf{X}) = \delta u_{ij} N_j(\mathbf{X}) \tag{2.21}$$

where N is the shape function, which satisfies the properties of the interpolants [34].

The matrix form of finite element equation can be written as

$$\mathbf{M}_{FE}\ddot{\mathbf{d}} = \mathbf{f}_{ext} - \mathbf{f}_{int} \tag{2.22a}$$

$$\mathbf{M}_{\mathrm{FE}} = \int \rho_0 \mathbf{N}^{\mathrm{T}} \mathbf{N} \mathrm{d}\Omega_0 \tag{2.22b}$$

$$\mathbf{f}_{\mathrm{ext}} = \int \mathbf{N}^{\mathrm{T}} \rho_0 \mathbf{b}_{\mathrm{i}} \mathrm{d}\Omega_0 + \int \mathbf{N}^{\mathrm{T}} \rho_0 \bar{\mathbf{t}} \mathrm{d}\Gamma_0 \tag{2.22c}$$

$$\mathbf{f}_{\mathrm{int}} = \int \frac{\partial \mathbf{N}^{\mathrm{T}}}{\partial \mathbf{X}} \mathbf{P}^{\mathrm{K}} \rho_0 \mathrm{d}\Omega_0 \tag{2.22d}$$

where $\mathbf{M}_{\mathrm{FE}}$ is the mass matrix**.**

2.2.2 Nanoscale contact using finite element method

Although using the FEM can only obtain approximate solutions, it has been widely used in a variety of physical problems. For nanoscale contacts, there are mainly two aspects of work that has been done. Firstly, the adhesive forces between two bodies are integrated into the FEM models. This usually assumes that the atomic interactions are governed by the Lennard-Jones potential (details about the Lennard-Jones potential will be presented in the next section). As the parameters of Lennard-Jones (LJ) potential for different materials have been analytically derived [35], it can easily be applied to various materials. In FEM model, the effect of adhesive forces on two bodies is achieved by adding an extra term into the nodal equation. Du et al [36, 37] added negative pressure due to the adhesion, to each node on the surfaces. Cho and Park [38] modeled the adhesive force as a body force, called the adhesive body force, which overcame the difficulty in estimating the magnitude of the attractive force. Both Du and Cho's models are consistent with Maugis's model [20].

Secondly, the constitutive relation can be formulated in the FEM model to describe the behaviour of the crystals at the nanoscale. A constitutive law based on the interatomic potentials has been obtained implicitly. Li et al [10] proposed the interatomic potential finite element model (IPFEM) incorporated into two different criterions for predicting elastic instabilities such as dislocation and twin. IPFEM has been used to study nanoindentation of FCC single crystals [10, 39, 40]. Figure 2.3 shows the results of nanoindentation obtained from IPFEM against pure molecular dynamics (MD) simulation. One extension of IPFEM is the lattice dynamical finite-element method

(IDFEM), which is proposed for complex crystals [41].

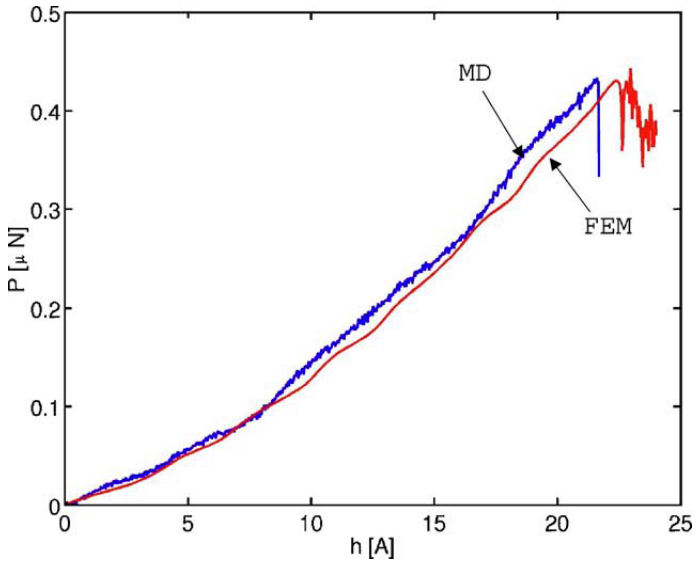

Figure 2.3: Load-displacement responses in nanoindentation (from [39]).

Another type of the constitutive relation for the FEM is obtained by fitting the results of separate molecular dynamics simulations proposed by Eid et al. [42]. They used the fitted results to model nano-aspertiy as a force-distance element. The rough surface of the finite element model was constructed by placing nano-asperities on it shown in figure 2.4. They showed that nanoscale roughness reduces the adhesion and the real contact area, compared with the FEM model without nano-asperities.

The use of the traditional FEM in the nanoscale contacts can save considerable computation time, compared to pure MD simulations. However, the results obtained from the FEM at this scale are only reliable when the deformation is very small. Increased deviation is expected when there is more deformation. Several characteristics of the standard FEM are responsible for such deviation. The constitutive model in the FEM cannot accurately describe the behavior of individual atoms within an element because it represents uniform behavior. Besides, unlike the interactions between the adjacent nodes in the FEM, the atomic interactions are non-local. Finally, under critical loading conditions, the crystals will exhibit some discontinuous phenomenon, such as dislocation, while the standard FEM cannot

capture a discontinuity within an element.

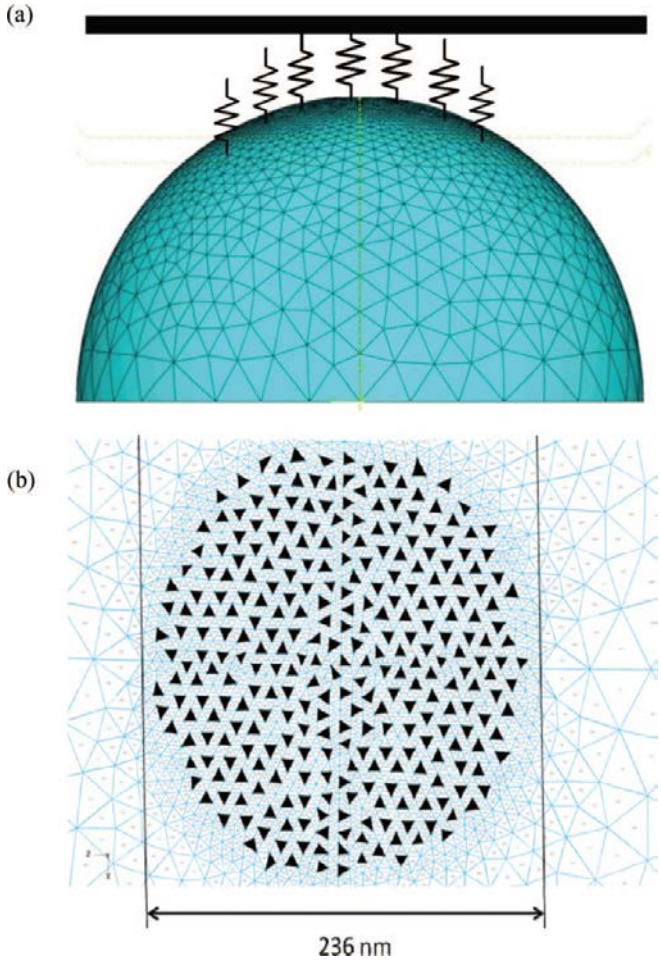

Figure 2.4: Force-distance element (shown as a spring) as nano-asperities on meshed sphere: (a) side view; (b) top view (from [42]).

2.3 Molecular dynamics

2.3.1 Introduction

Molecular dynamics (MD) simulation is a numerical technique that is used to simulate materials at the nanoscale and determine their non-equilibrium and equilibrium properties. Materials in the MD simulation are represented by individual particles, which construct a multi-body system. Each particle in such system obeys Newton's equations of motion given in equation (2.23).

$$m_{\alpha}\ddot{\mathbf{u}}_{\alpha} = \mathbf{f}_{\alpha} \tag{2.23}$$

where m_{α} is mass of the particle α. $\ddot{\mathbf{u}}_{\alpha}$ is its acceleration, which is the second derivative of its displacement $\mathbf{u}_{\alpha}$ in terms of time. $\mathbf{f}_{\alpha}$ is the inter-particle force on the particle α exerted by all other particles in the system, which can be written as

$$\mathbf{f}_{\alpha} = \sum_{\alpha,\beta\neq\alpha}^{N} \mathbf{f}_{\alpha\beta} \tag{2.24}$$

In the MD, the interactions between the particles are governed by the potential energy U. The force on the particle α is the gradient of the potential energy of the system about its position shown in equation (2.25).

$$\mathbf{f}_{\alpha} = -\nabla_{\alpha} U\left(\mathbf{x}_{\alpha}, \mathbf{x}_{\beta}, \ldots, \mathbf{x}_{N}\right) \tag{2.25}$$

where **x** is the position of the particle.

2.3.1.1 Potential function

One of the most important factors that influence the accuracy of the results obtained from the MD simulation is the potential function. Many potential functions have been derived to deal with typical problems. Some of the potential functions that are widely used in the simulations of nanoscale contacts are introduced in the following.

Lennard-Jones potential. The Lennard-Jones (LJ) potential is an empirical function which describes two-body interactions. The use of the LJ potential is wide, since it can represent the general behavior of many materials. Its expression is

$$U_{LJ}(r) = 4\varepsilon\left[\left(\frac{\sigma}{r}\right)^{12} - \left(\frac{\sigma}{r}\right)^{6}\right] \tag{2.26}$$

where ε and σ are characteristic energy and length scales, respectively. For modelling different materials, ε and σ can be changed. r is the distance between two particles. The first term of equation (2.26) represents the repulsion while the second term represents the van der Waals interactions or attraction between two

particles. Taking the gradient of the LJ potential equation gives the LJ force, which is expressed as

$$f_{LJ}(r) = \frac{48\varepsilon}{r}\left[\left(\frac{\sigma}{r}\right)^{12} - \frac{1}{2}\left(\frac{\sigma}{r}\right)^{6}\right] \tag{2.27}$$

We show the relation between the distance and the LJ force in figure 2.5. When $r = 2^{1/6}\sigma$, the LJ force equals zero. It shows in figure 2.5 that with the distance $r > 1.5\sigma$, the LJ force decreases quickly. Therefore, the LJ potential can be truncated without loss of accuracy. Moreover, the number of the interacting particles for each particle considerably reduces due to the truncation, so computational costs are saved. The truncation can be achieved by setting a cutoff radius r_c.

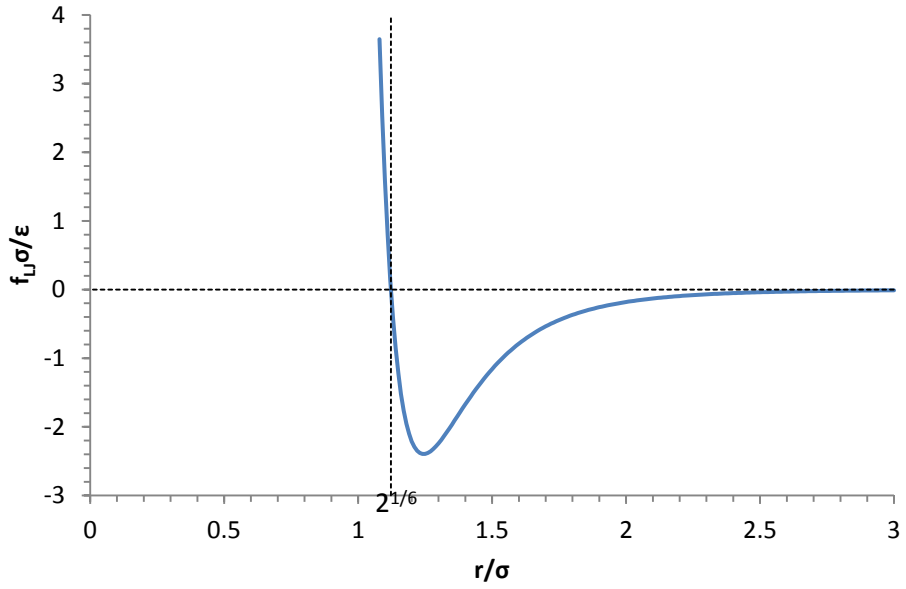

Figure 2.5: LJ force $f_{LJ}(r)$ as a function of the distance r in dimensionless unit.

The two-body empirical potentials spend much less computational expense than the multi-body potentials for the same model-setup. However, it is not easy to fit appropriate parameters for typical materials, such as metals, when using the two-body potentials.

Embedded atom method. The embedded atom method (EAM) [43] is a multi-body potential that is widely used to describe the atomic interactions in metallic systems. The expression of the EAM potential couples the pair potential term with the local electron density term given in equation (2.28).

$$U_{EAM} = \frac{1}{2}\sum_{\alpha,\beta\neq\alpha} V(r_{\alpha\beta}) + \sum_{\alpha} G(\rho_{\alpha}) \tag{2.28}$$

where V is a pair potential term, which is a function of the distance $r_{\alpha\beta}$ between two atoms. G is the embedding energy, associated with placing an atom in the electron density represented by ρ_{α}. The electron density ρ_{α} is expressed as

$$\rho_{\alpha} = \sum_{\alpha,\beta\neq\alpha} g(r_{\alpha\beta}) \tag{2.29}$$

The electron density ρ_{α} denotes the sum of the electronic density contribution $g(r_{\alpha\beta})$ from other atoms to atom α. The atomic force due to the EAM potential can be easily obtained based on equation (2.25)

2.3.1.2 Time integration

After calculation of the atomic force based on the potential function, the trajectories of the atoms in the system are obtained by solving Newton's equations of motion. Velocity Verlet integration [44] is an effective method to integrate the Newton's equations of motion, which is also used in this work. The steps of updating displacement, velocity and acceleration via the velocity verlet algorithm are given in equations (2.30), assuming that the quantities at time n are known.

$$\mathbf{u}^{n+1} = \mathbf{u}^{n} + \Delta t\dot{\mathbf{u}}^{n} + \frac{1}{2}\Delta t^{2}\ddot{\mathbf{u}}^{n} \tag{2.30a}$$

$$\dot{\mathbf{u}}^{n+\frac{1}{2}} = \dot{\mathbf{u}}^{n} + \frac{1}{2}\Delta t\ddot{\mathbf{u}}^{n} \tag{2.30b}$$

$$\ddot{\mathbf{u}}^{n+1} = \frac{\mathbf{f}(\mathbf{u}^{n+1})}{\mathbf{M}_a} \tag{2.30c}$$

$$\dot{\mathbf{u}}^{n+1} = \dot{\mathbf{u}}^{n+\frac{1}{2}} + \frac{1}{2}\Delta t\ddot{\mathbf{u}}^{n+1} \tag{2.30d}$$

where Δt is the time step. $\mathbf{u}$, $\dot{\mathbf{u}}$, $\ddot{\mathbf{u}}$ and $\mathbf{f}$ represent the displacement, velocity and acceleration, force vectors of the system, respectively. $\mathbf{M}_a$ is the diagonal atomic matrix. The energy in the above algorithm is conserved. However, in most cases, the system needs thermostat to dissipate kinetic energy. Accordingly, a modified velocity Verlet algorithm is often used. The latter is equivalent to the above algorithm and implemented with a thermostat.

$$\dot{\mathbf{u}}^{n+\frac{1}{2}} = \mathbf{u}^n + \frac{1}{2}\Delta t\ddot{\mathbf{u}}^n \tag{2.31a}$$

$$\mathbf{u}^{n+1} = \mathbf{u}^n + \Delta t\dot{\mathbf{u}}^{n+\frac{1}{2}} \tag{2.31b}$$

$$\ddot{\mathbf{u}}^{n+1} = \frac{\mathbf{f}(\mathbf{u}^{n+1})}{\mathbf{M}_a} \tag{2.31c}$$

$$\dot{\mathbf{u}}^{n+1} = \dot{\mathbf{u}}^{n+\frac{1}{2}} + \frac{1}{2}\Delta t\ddot{\mathbf{u}}^{n+1} \tag{2.31d}$$

Velocity Verlet integration prevails because of its easy implementation, low memory requirements and high stability. There are other integration methods that can solve the equations of motion, such as the Gear predictor-corrector method [45]. The Gear predictor-corrector method is a multiple-value method which makes use of several earlier time steps. Compared with the velocity Verlet method, the order of the gear predictor-corrector method is higher but requires more computational expense due to the storage five displacement derivatives at each time step.

2.3.1.3 Thermostat method

The other important aspect for MD simulations is the control of temperature. A canonical ensemble, in statistical mechanics, is the statistical ensemble that represents a thermal equilibrium with a heat bath at some fixed temperature [46]. Thermostat is a technique introduced to handle the temperature of the system or keep the temperature

constant in MD simulation, approximating a canonical ensemble, or NVT (N: number of particles, V: volume, T: temperature). In experiments, thermal energy due to any work done can flow into the surrounding environment. In MD simulations, there is no natural exit. Excessive kinetic energy is controlled by the thermostat. A variety of thermostat methods are available, and some of the widely used are presented here, such as the Langevin, Berendsen and Nosé-Hoover thermostats.

Langevin thermostat. In the Langevin dynamics [45], the particles in the system are assumed to interact with an implicit solvent consisting of frictional particles. The kinetic energy of the particles in the system reduces through the interaction with the solvent, which is mathematically expressed by the Langevin equation given by equation (2.32).

$$m_{\boldsymbol{\alpha}}\ddot{\mathbf{u}}_{\boldsymbol{\alpha}} = \mathbf{f}_{\alpha} - \frac{m_{\boldsymbol{\alpha}}}{c}\dot{\mathbf{u}} + \mathbf{f}_{\mathrm{rand}} \tag{2.32}$$

where the damping factor c determines the speed of the energy dissipation. The random force term $\mathbf{f}_{\mathrm{rand}}$ is proportional to $\sqrt{m_{\boldsymbol{\alpha}}\, k_B T_0/(c\Delta t)}$, where T_0 is the desired temperature, Δt the time step , and k_B the Boltzmann constant. The average magnitude of $-\frac{m_{\boldsymbol{\alpha}}}{c}\dot{\mathbf{u}}$ and $\mathbf{f}_{\mathrm{rand}}$ is linked by the fluctuation-dissipation theorem [47]. The Langevin thermostat is a stochastic technique, which has advantages of sampling a canonical ensemble and guaranteeing an ergodic system.

Berendsen thermostat. Berendsen et al. [48] proposed a method, in which the system is weakly coupled to an external bath with a constant temperature. In the Berendsen thermostat, the difference between the actual temperature T and the desired temperature T_0 is decreased by rescaling the particle velocities with a scaling constant α following:

$$\alpha = \sqrt{1 + \frac{\Delta t}{c}\left(\frac{T_0}{T} - 1\right)} \tag{2.33}$$

The Berendsen thermostat is one of the velocity rescaling techniques. However, unlike other velocity rescaling techniques, one advantage the Berendsen thermostat has is that it allows the temperature fluctuations.

Nosé-Hoover thermostat. The idea of the Nosé-Hoover thermostat [49] is mimicking a heated bath that couples with the system. The system temperature is maintained to a desired value by a two-way interaction with the baths. Mathematically, a frictional term is added to the Newton's equations of motion, which gives

$$m_{\boldsymbol{\alpha}}\ddot{\mathbf{u}}_{\boldsymbol{\alpha}} = \mathbf{f}_{\alpha} - \boldsymbol{\xi} m_{\boldsymbol{\alpha}}\dot{\mathbf{u}} \tag{2.34}$$

where $\boldsymbol{\xi}$ is a friction coefficient whose the derivative with respect to time is given as

$$\frac{d\xi}{dt} = \frac{1}{Q}\left(\sum_{\alpha=1}^{N} \frac{m_{\alpha}\dot{\mathbf{u}}_{\alpha}^{2}}{2} - \frac{3N-1}{2} k_B T_0\right) \tag{2.35}$$

where N is the number of the particles in the system. Q determines the coupling between the bath and the system. The magnitude of Q must be appropriately chosen: if Q is too large, the equilibrium time of the system will extend unrealistically; if Q is too small, non-physical high-frequency temperature vibrations will be introduced.

2.3.1.4 Boundary conditions

In MD simulations, the appropriate choice of boundary conditions is also important. When the effect of boundaries is not significant, free boundary condition in which the boundary atoms are not constrained can be applied. If the coordinates of the boundary atoms are fixed, which is called fixed boundary condition, the simulation results obtained from MD suffer from artifacts [50].

Periodic boundary condition (PBC), as the most popular choice in the MD simulations, is used to simulate a large system by only considering a representative volume element. Applying PBC achieves two goals: mimicking an infinite system with a

finite part and minimizing the surface effects.

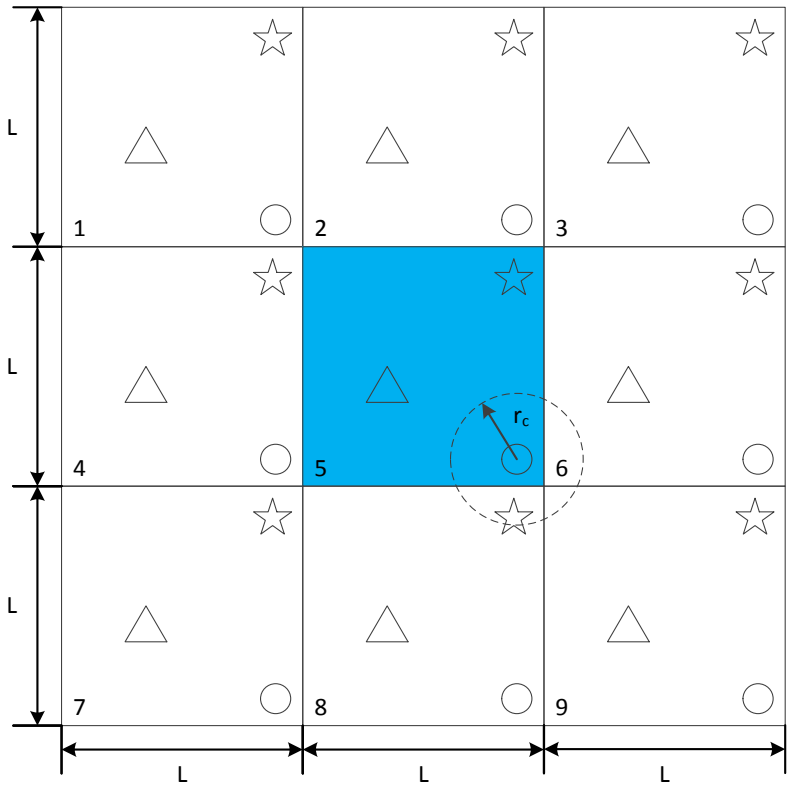

Figure 2.6: 2D schematic of periodic boundary condition.

Figure 2.6 shows 2D schematic of the periodic boundary condition. The blue box indicates the simulation region, which is surrounded by mirror images (note that only eight mirror images as shown in figure 2.6). It shows in figure 2.6 that the number and the positions of the atoms in nine boxes are the same during the whole simulations. Assume that the cutoff radius of the interaction potential is r_c shown in figure 2.6. The particle (circle, for example) in the blue box not only interacts with the other particles in the box but also with their images (star in box 8, for example). The atomic interactions occur when the distance between two particles is within the cutoff radius r_c. One limitation of the periodic boundary condition is that the box size L must be twice the length of the cutoff radius due to minimum image criterion.

2.3.2 Nanoscale contact using molecular dynamics

With the development over several decades, Molecular dynamics (MD) has become a comprehensive technique for various fields. A number of molecular dynamics software have been developed, such as Large-scale Atomic/Molecular Massively Parallel Simulator (LAMMPS) [51] and Orac [52] for simulation; Atomeye [53], VMD [54], and OVITO [55] for atomistic visualization. Due to the limitation of computational sources, the time and length scales of MD model are too small in most cases when compared to experiments. However, as a complement to conventional experiments, MD simulations can still produce some detailed observations which cannot be observed by experimental instruments, for example, the so-called buried interface in AFM experiments [7].

Apart from molecular dynamics, there are two other models that are widely used in numerical simulations of nanoscale contacts: ab initio technique and reduced-order model. The former can be used to calculate the atomic interaction with high accuracy [56], but it suffers from extremely high computational cost and only applies to a small system (less than 100 atoms). The latter one, which refers to the Prandtl-Tomlinson (PT) model [57], is limited to the elastic deformation, although it allows analyzing the atomic friction under almost all experimental conditions. In terms of lubricated contacts at the nanoscale, Monte-Carlo (MC) is also widely employed. Due to the neglect of dynamics and time notion, MC is only applicable when systems are only defined by an energy prescription [58].

Molecular dynamics (MD) can track the position of individual atoms, and systematic information, such as energy and temperature. More importantly, MD naturally represents the initiation and propagation of dislocations and these can be easily visualized for further analysis, making it a suitable tool for understanding the crystal deformation beyond the elastic limit. Meanwhile, computational expense of MD is much lower than ab initio technique for the cases with similar conditions. However, it

is still difficult to simulate a micro-size system (about a billion atoms) using MD simulations. It will be discussed in section 2.4 on how this limitation can be overcome by coupling MD and FEM, but before that, we briefly review the results of dry contact and lubricated surface contact obtained from molecular dynamics.

2.3.2.1 Single asperity contact without lubricant

Atomic force microscopy (AFM) is one of the most widely used instruments to perform surface measurements in tribology. Recently, molecular dynamics (MD) simulations of single asperity contact at the nanoscale are viewed as a part of AFM experiments. MD simulations can be used to model AFM experiments, reproduce experimental measurements, investigate the underlying mechanisms and even suggest new experiments [59, 60]. Besides, MD simulations can quantify some quantities (e.g. contact area) which cannot be directly observed by instruments [3].

During the last two decades, many MD simulations have been performed to clarify the stick-slip phenomenon observed in AFM experiments. Sorensen et al. [60] performed simulation studies of atomic-scale sliding friction for a number of tip-surface and surface-surface contacts consisting of copper atoms. The main finding in this work is that the kinetic friction could vanish if the crystal orientations of the tip and the substrate were different such that a mismatch existed at the interface. Shimizu et al [61] used a rigid diamond tip and a copper substrate. They found that the average coefficient of friction reduces with the increased spring constant of AFM cantilever, which is easily determined by MD simulations. Recently, Li et al [62] performed MD simulations with a Pt tip and a gold substrate, and claimed that slow MD speed ranging from 0.005m/s to 2m/s provides the high reliability of the results obtained from MD simulation used in analyzing AFM data.

MD simulations have also been used to test validity of continuum mechanics models at the nanoscale. Luan and Robbins [3, 15] performed MD simulations of single asperity contacts with different tip geometries. They showed that the atomic

roughness leads to the deviations of contact area, pressure distribution and friction from continuum mechanics.

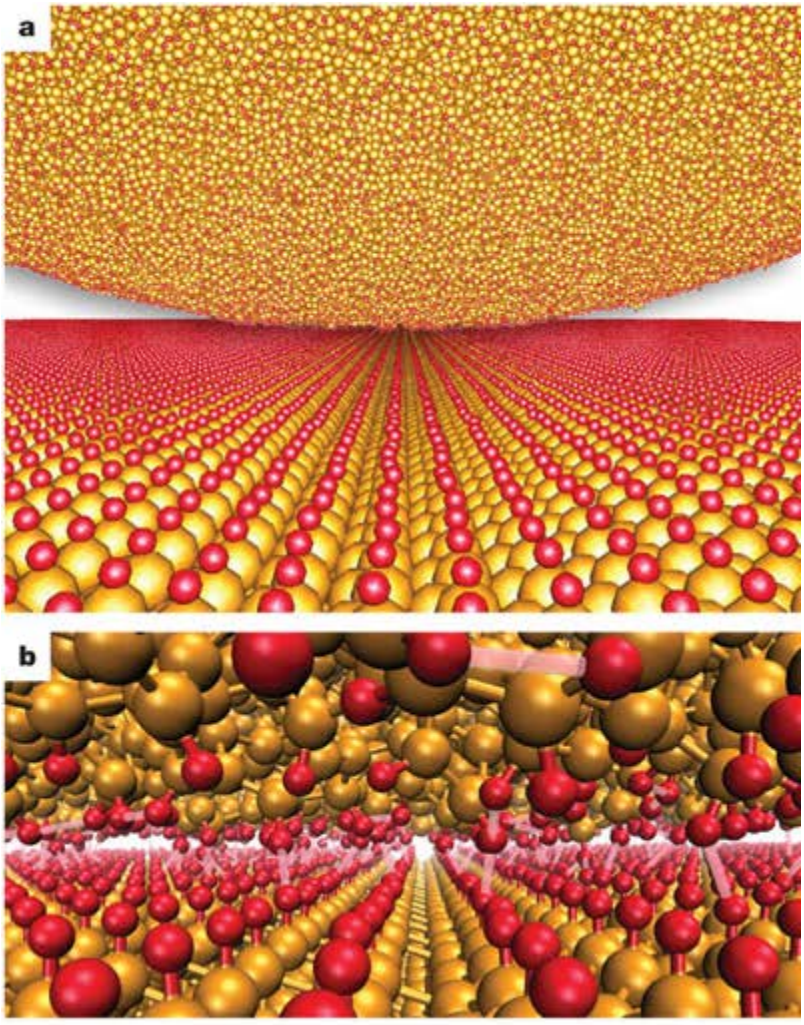

Figure 2.7: Contact between an amorphous carbon tip and a diamond substrate: (a) far view; (b) close view. Golden and red atoms indicate C and H (from [11]).

Mo et al. [11, 12] claimed in their work that if the contact area is calculated following continuum mechanics, macroscopic friction law known as the proportional relationship between friction force and normal force, still works for non-adhesive nanoscale contacts. In Mo's work [11], the model involves an H-terminated amorphous carbon tip and an H-terminated diamond substrate as shown in figure 2.7. To further elucidate the perceived breakdown of continuum in nanocontact, Solhjoo et al. [63] conducted molecular dynamics simulations of normal contact between a nominally flat substrate and different atomistic and non-atomistic spherical particles to

investigate the applicability of classical contact theories at the nanoscale. They suggested that the deviations between the atomistic systems and the continuum models could be related to energy loss and changes in the effective work of adhesion, as well as the anisotropic properties of the atomistic systems.

The definition of contact area is the key factor that influences the application of continuum mechanics to nanoscale contacts. Three existing methods for calculating contact area at the nanoscale are discussed in Ref. [64]. Besides, the effects of contact area on friction have also been investigated by MD simulations. It is found that friction is not related to the contact area when the contacting surfaces are incommensurate and mismatched (atomic spacing between the two surfaces not the same) [65, 66]. Conversely, when they are commensurate and matched, friction varies linearly with the contact area [11, 65].

With the exception of contact area, the effects of load on friction are also widely investigated in MD simulations. Investigation of the relation between load and friction can not only demonstrate accuracy of prediction on nanoscale contacts from macroscopic friction law mentioned above, but also shed light on rough surfaces contact, in which contact occurs between asperities. In some cases, friction increases linearly with load [2, 11]. However, due to the adhesive effect, sublinear dependences of friction on load have also been reported [3, 11, 14, 67].

2.3.2.2 Rough surfaces contact without lubricant

In tribology, the effects of surface roughness on compression and friction between two rough surfaces have been investigated for half a century. The early studies on this topic include experimental work [68-70] and analytical analysis [24, 25, 28]. In the last several years, molecular dynamics (MD) simulation was used to study contact between rough surfaces from a nanoscale point of view.

Due to its influence on friction in some cases of single asperity contact, the contact

area has also been studied in rough surface contact. Yang and Perrson [71, 72] performed MD simulations focusing on the contact between a rigid solid with a randomly rough surface and an elastic substrate with a flat surface. Their model is elastic and non-adhesive. They showed that the contact area increases linearly with the load under small loads. Spijker et al. [73] also found this linear relationship between contact area and load by using two deformable solids with self-affine surfaces as shown in figure 2.8. A similar observation was also reported by Akarapu et al [74]. Contact area is not just influenced by load, as it was observed that contact area decreases as surface roughness increases in atomistic simulations [73, 75, 76].

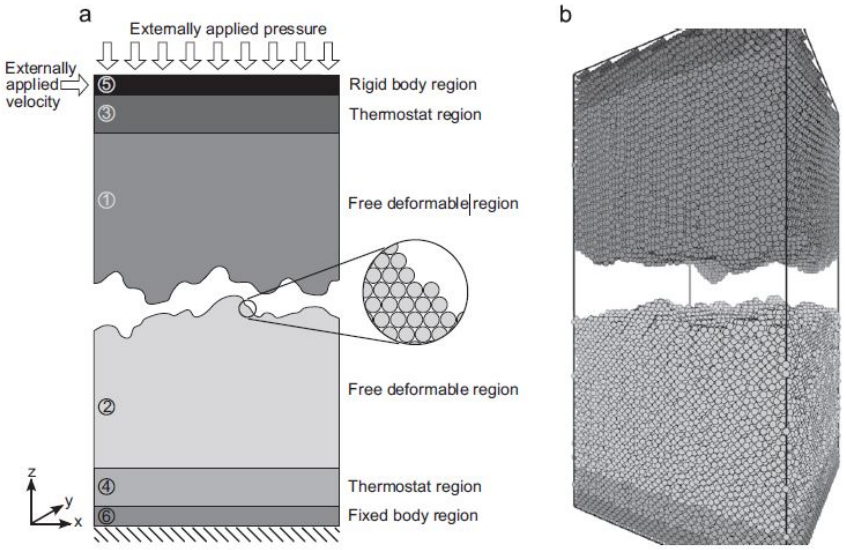

Figure 2.8: Schematic of the simulation system (a) Schematic is shown in 2D where the inset shows that the system has an atomic representation. (b) Snapshot of the system used in the MD simulations shows the 3D character of the set-up [77]

Adhesion plays an important role in rough surface contact at nanoscale. Spijker et al. [73] found that adhesion leads to a shift of the contact pressure distribution, compared to the non-adhesive contacts in other work [32, 78]. It is also found that friction forces go up with higher adhesive strength between two surfaces [75, 77]. In several studies, the relationship between adhesion and surface roughness was studied. Mulakaluri and Persson [79] added adhesion to elastic contact between self-affine rough surfaces and found that adhesion reduces with increased surface roughness. Similar observations

were found by Piotrowski et al. [80] and Jacobs et.al. [81]

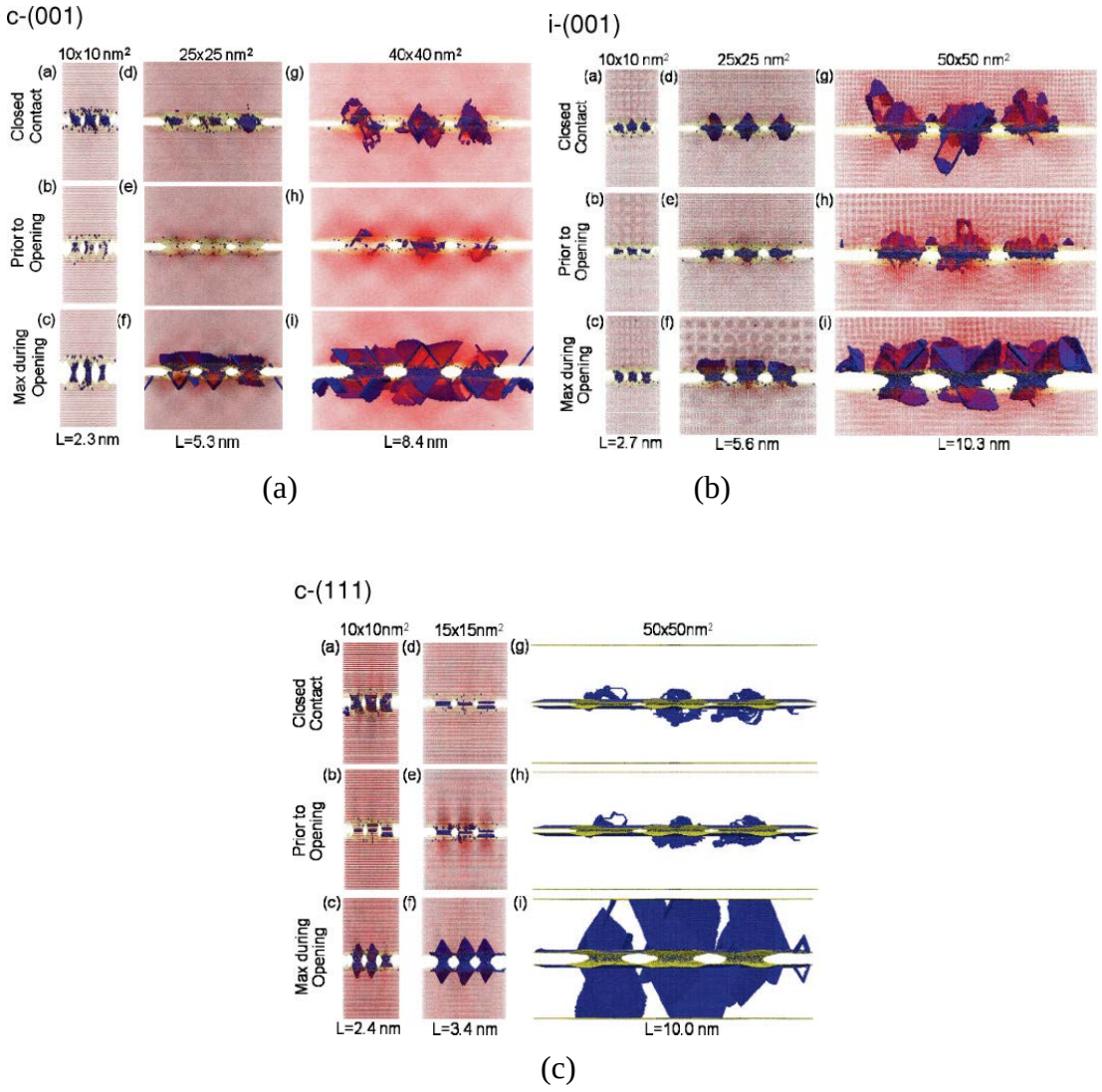

Figure 2.9: Snapshots of the first contact cycle with different sizes and at various times for (a) commensurate (001) contacts, (b) incommensurate (001) contacts and (c) commensurate (111) contacts (from [82]). The largest contact size is shown in the middle column. Yellow (light), red (light dark), and blue (dark) spheres denote surface, fcc, and hcp atoms, respectively. Top and bottom values indicate cross-sectional areas and contact lengths, respectively.

One of the most important tasks for studying rough surface contacts at the nanoscale is determining the factors that influence friction. Spijker et al. [83] and Xuan et al. [75] found that friction increases with the initial roughness of the surface and friction decreases due to the surface flattening after repetitive sliding. In a later study about the effects of temperature on friction, Spijker et al. [77] found that both the initial surface roughness and temperature had an effect on friction but the former is

dominant. There were two deformable bodies in both Spijker's [73, 77, 83] and Xuan's models [75, 76], in which plastic deformation was not considered. Meanwhile, Kim and Strachan [82, 84] observed the emission of dislocation in a study of mental-metal contact, but they have not performed surface sliding. Figure 2.9 shows the simulation results for three different cases.

2.3.2.3 Lubricated surface contact

For lubricated contact, molecular dynamics (MD) simulations are appropriate to the cases in which two surfaces are separated by a lubricant whose thickness is in the nanometer scale. This is because continuum fluid dynamics breaks down at this scale [85]. Many MD simulations of thin film lubrications have been carried out over the last two decades. In those simulations, different types of lubricant have been used. Linear chain molecules, such as hexadecane [76, 86], octane [87] and decane [88], consist of a long string of carbon-carbon bonds and have been commonly used. Nonlinear or branched molecules have also been studied [58, 89]. According to the density profile, the layering structure of linear decane decays slower at a close distance from surfaces compared to branched decane [58]. Recently, the effect of the additives to pure alkane has been widely investigated. Berro et al. [90] mixed hexadecane base oil and zinc dithiophosphate (ZDDP). They found that mechanical slip is considerably suppressed due to the interaction between ZDDP molecules and surface. Adding nanoparticles to lubricants can also improve lubrication [87]. In a recent study, Ta et al. [91] modeled a more complex 17R2 aqueous copolymer lubricant and investigated its tribological behavior.

For nano-asperities contact with lubricant, lubricant is squeezed between asperities. Some groups have used MD simulations to study this phenomenon. Sivebaek et al. [92] performed MD simulations of squeezing linear alkane molecules between two curved and smooth surfaces. A range of chain lengths from 3 to 14 carbon atoms were considered. They found that the performance of longer length alkanes is better than

shorter ones. In this work, Sivebaek et al. [92] investigated both pure squeezing and squeezing with sliding. Their results on the carbon atom number in the contact region indicated that there is no significant difference between the two cases as shown in figure 2.10. For lubricant squeezing between two flat surfaces, Savio et al. [93] found that the surface separation decreases in a step-like manner, which is in accordance with early observations by Gao et al. [94].

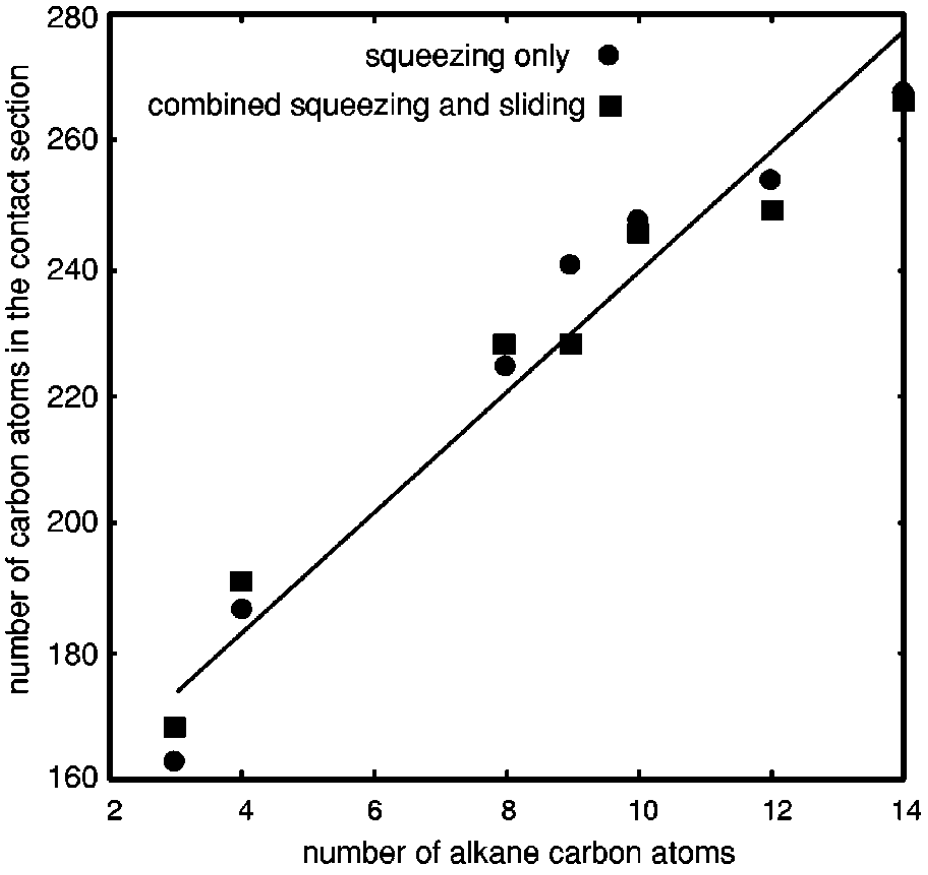

Figure 2.10: Number of alkane carbon atoms in the contact section as a function of the length of the alkane. Only one correlation line is drawn as the squeezing and the combined squeezing cases are not significant different (from [92]).

Squeezed lubricant simulations are used to explain the dynamic behavior before direct asperity contact. For a comprehensive investigation of the effects of lubricant on friction, it is important to carry out MD simulations of direct asperity interaction with a lubricant liquid. However, up to this point, only a few papers have been dedicated to this topic.

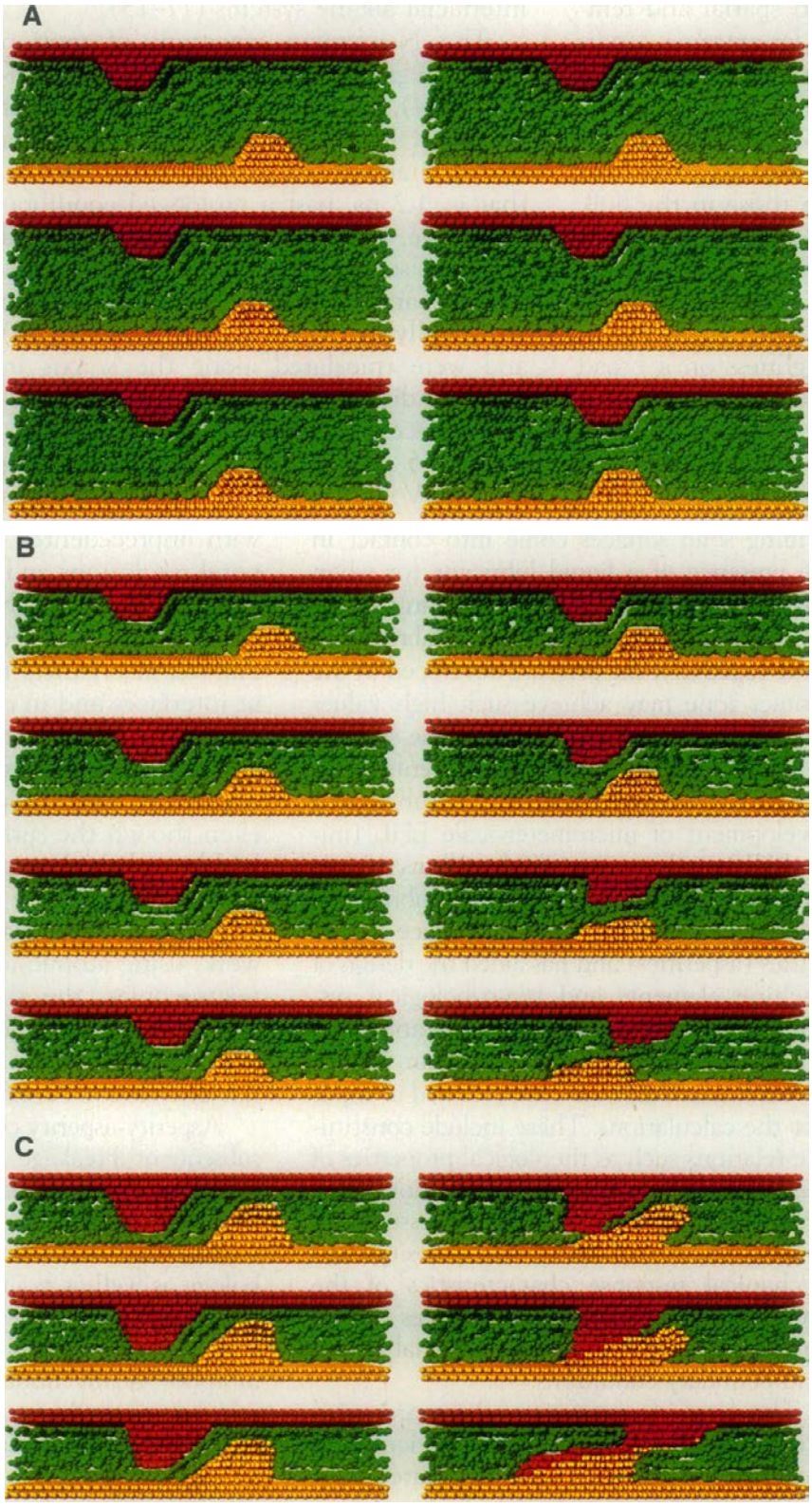

Figure 2.11: Side views of atomic configuration. (A) The system with a large separation. (B) The asperity near-overlap system. (C) The asperity-overlap system (from [95]).

Pioneering work was performed by Gao et al [95] who applied MD simulations to

model lubricated contact between two gold substrates with pyramidal asperities. In their work, the process of lubricated contact was divided into three stages: asperity fully separated, asperity near-overlap and asperity overlap as shown in figure 2.11. Gao et al [95] found that due to large densification and pressurization of lubricant being between asperities, there is a severe fluctuation in the shear and normal stress when asperities are near-overlap. Moreover, when the asperities passed over each other in the stage of asperity overlap, the magnitude of stress was larger as no lubricant molecules were in the inter-asperity region. At the end of third stage, some metal atoms were transferred between asperities.

Zhang and Tang [96] carried out MD simulations to study the effect of water and surface roughness on the friction. They found that water can change friction characteristics, but has little effect on the magnitude of the friction force. In this work, asperities on the top surface were rigid, so the coupling effect of deformation in both surfaces was not considered.

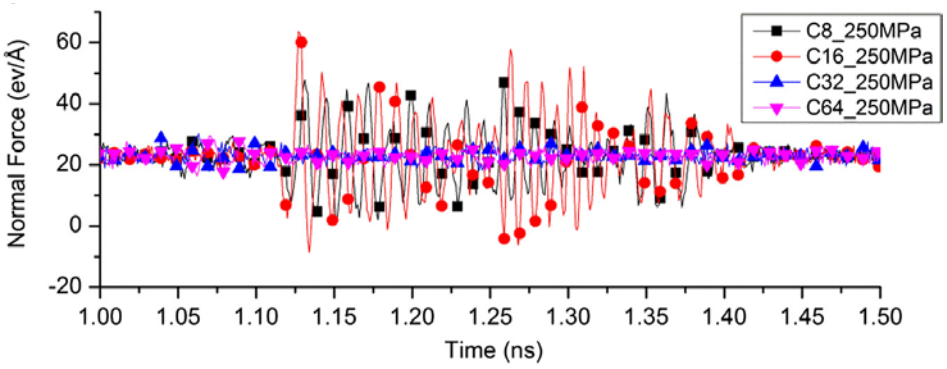

Figure 2.12: Time evolution of the friction force for different chain length under 0.25 GPa during contact [97].

Most recently, Xuan et al. [75] built a 3D model of two deformable bulks with self-affine surfaces to study surface contact in mixed lubrication. For comparisons, they performed simulations with both dry and lubricated conditions. In partially lubricated condition, the small amount of lubricants at small load could lead to higher friction force compared to dry contact, because the asperity contact still mainly supported the load. In another study, Xuan et al [76] showed that contact area in

lubricated contact with the amount of confined lubricant molecules is smaller than dry contact because lubricant molecules fill the cavities and support the load. Based on Sivebaek et al.'s work [92], Xuan et al [97] investigated the effect of chain length on friction. Under the same loads, the friction force using longer chains was smaller than those using short chains, as shown in figure 2.12. Xuan et al [97] explained that longer chains could provide a mono-layer of lubricant molecules in the inter-asperity region and separate the asperities.

2.4 Multiscale method

2.4.1 Introduction:

Molecular dynamics (MD) simulation is widely applied to study mechanics and materials at the nanoscale with a number of accurate potential functions. However, in spite of rapid development in computer techniques, MD still suffers from limitations in terms of spatial and temporal scales. On the other hand, Finite element method (FEM) is not capable of accurately describing physical phenomena at the nanoscale, despite of its efficiency. The core idea of the multiscale method is to overcome the shortcomings and couple the advantages of those existing simulation tools so that complex phenomena at small scale could be explored without sacrificing too much computational time. In the area of computational mechanics, multiscale simulation has been an active topic in the past two decades, with a number of favorable coupling schemes developed and applied to molecular scale mechanics and materials. In this section, some typical multiscale approaches will be reviewed. In the previous work, the multiscale methods were divided into two categories: force-based and energy-based [98], or more commonly: hierarchical and concurrent [50]. However, in this work, existing multiscale methods are grouped into two classes from the temperature point of view, which are zero-temperature coupling and finite-temperature coupling.

In terms of the atomistic/continuum coupling at zero Kelvin, there are three common issues in need of resolution. Firstly, in order to achieve the coupling, some information

(displacement, velocity or force) must be transferred from the atomistic region to the continuum region or vice versa. For most of the multiscale methods [98], information transfer occurs in the transition region, where the atomistic and the continuum regions overlap. In the transition region, the two models provide constraints to each other. Meanwhile, their boundary conditions are applied at this region. With the exception of passing information, the transition region is used to handle the spurious wave reflection at the atomistic/continuum interface. The spurious wave coming from the atomistic region is defined as the wave with the wavelength being smaller than the cutoff wavelength of the continuum model. The spurious waves cannot propagate into the continuum model across the interface and are unphysically reflected back into the atomistic region. The reflected waves raise the temperature of the atomistic region, which could result in numerical errors. This phenomena was first noted by Adelman and Doll [47] and also reported in transient FEM models with varying element sizes [99]. The elimination or reduction of the spurious reflection is an important issue of the multiscale coupling, and it will be described later. It must be noted that we focus on the dynamics coupling. For those static couplings, the spurious reflection is not involved, but other issues, such as ghost force [100], need to be addressed. The final issue for the multiscale coupling is that the constitutive equation of the continuum mode must be consistent with the mechanics of the atomistic model. To determine the constitutive equation, several options are available. One can obtain the relation between stress and strain using a separate atomistic simulation [101, 102]. Alternatively, the virtual atom cluster (VAC) [103] or the Cauchy-Born rule (CB) [13] can be used to construct the constitutive relation for the continuum model.

At finite temperature, the coupling between atomistic and continuum simulations is even more challenging since the mechanical and the thermal components of continuum models are governed by two different differential equations, momentum equation and heat equation. Conversely, the motion of the atoms in atomistic models describes fully the change in both mechanics and thermal energy of the system. Therefore, to successfully achieve the finite-temperature coupling, the components of atomistic

models must be clearly separated and to be compatible with the corresponding components of continuum models. In addition to those challenges, other issues with regards to temperature are thermal expansion/contraction and temperature-dependent elastic constants, which need to be appropriately handled. Moreover, similar to zero temperature coupling, the spurious reflections due to different dispersion relations of two models must be treated. In the following, some classic multiscale methods based on zero-temperature coupling will first be introduced. After that, recent developments in the finite-temperature multiscale coupling will be reviewed.

2.4.2 Zero temperature coupling

The quasicontinuum method. One pioneer work of the multiscale coupling is the quasicontinuum (QC) method, proposed by Tadmor et al.[13]. The QC method has a well-defined energy formulation for both atomistic region B^A and continuum region B^C as shown in figure 2.13(b). The basic idea of the QC method is that all atoms are divided into two categories: representative atoms (repatoms) and non-repatoms, indicated respectively by small filled circles and open circles in figure 2.13. Repatoms in this method are treated like the nodes in conventional FEM. The displacements of non-repatoms in B^C, for instance, atom A demonstrated in figure 2.13 (b), are linearly interpolated by those of the repatoms. In the regions with severe deformation or defects, the element size is refined down to the atomic level, establishing one-to-one correspondence between atoms and repatoms. In the region with small deformation, however, the elements are coarse. Therefore, the QC scheme reduces significantly the degrees of freedom.

It is worth pointing out that the QC method applies the Cauchy-Born (CB) rule to link atomistic with continuum. Based on the CB rule, the continuum energy density can be computed by using the atomistic potential. Although the use of the CB rule is limited to homogenous deformation, it has been widely used in later multiscale methods, and its details will be discussed in Chapter 3 for the coupling in our model. The QC method is

one of the most commonly used multiscale methods. A number of papers have been dedicated to its extension [98, 100] and its application [104, 105]. Despite its popularity, the QC method is often limited by the fact that refining the element size down to the atomic level complicates mesh generation and increases the computational time.

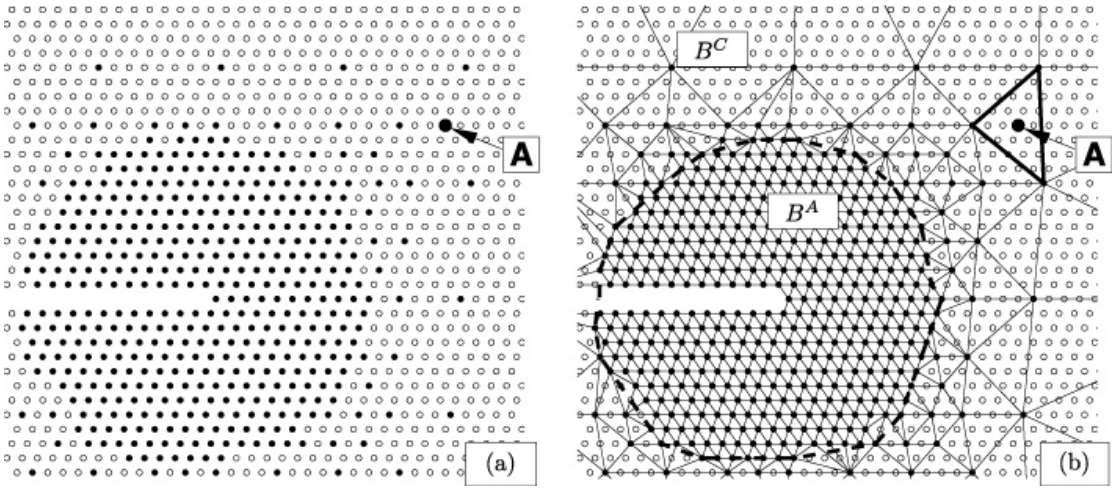

Figure 2.13: Repatoms are selected in crack tip using the QC method (a) and mesh generation (b) (from [98]).

The bridging scale method. Wagner and Liu [106] proposed a bridging scale method (BSM) in which the total displacement of the atoms is divided into fine and coarse scales by the means of a projection operator. The BSM starts by overlapping the MD and the FEM on the entire domain as shown in figure 2.14. The total displacements of the atoms are obtained by solving standard MD. The displacements of the nodes in FEM are represented as the coarse scales of the total displacements, which can be calculated through the projection. The fine and coarse scales are implicitly modeled on the entire domain so far. However, for most cases, critical phenomena only occur in a small domain. Therefore, The BSM reduced the atomistic calculations to a small domain with a description of the effects of the eliminated atoms via a time history kernel (THK) technique. As indicated in figure 2.14, the impedance force was added to the equation of the remaining MD in order to account for such effects. One advantage of the BSM is that the use of the THK results in a non-reflecting interface between the atomistic and continuum region. Besides, unlike the QC method, the element size in the

BSM is not refined down to the atomic separation, which simplifies mesh generation. The original BSM [106] was limited to one-dimensional problems, but Park et al. has extended it to 2D [107] and 3D [108]. The detailed application of the BSM on nanomechanics and nanomaterials can be found in Ref.[109-111].

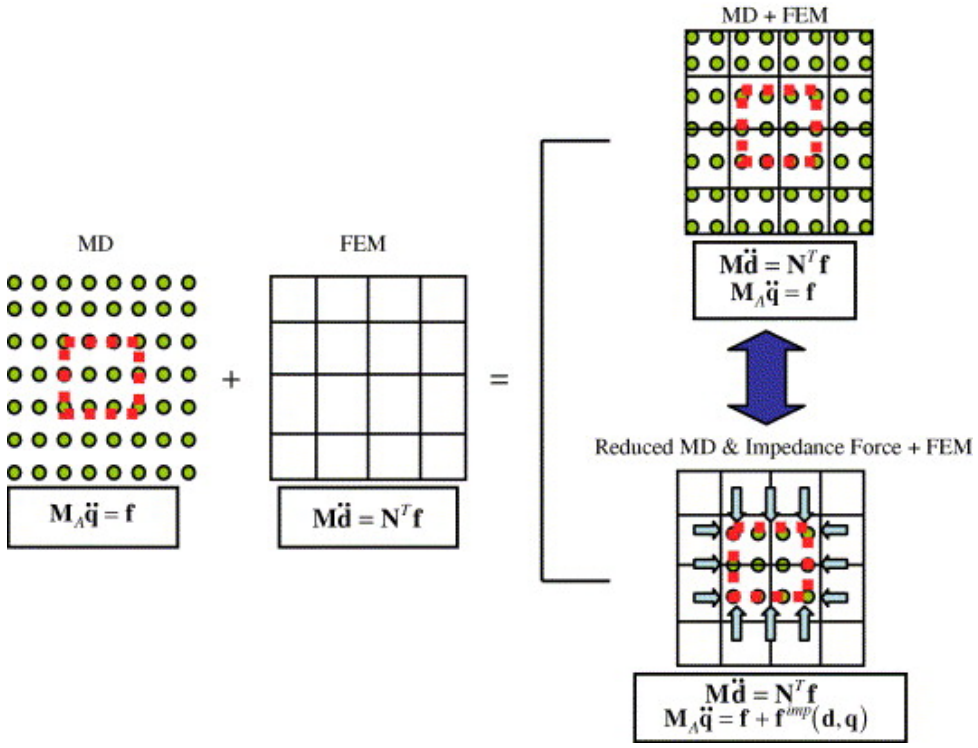

Figure 2.14: Coupling scheme of the bridging scale method(from [108]).

The bridging domain method. Xiao and Belytschko [112] developed a bridging domain method (BDM) for coupling the atomistic and continuum models. In this method, Lagrange multipliers are applied to impose displacement or velocity compatibility between the atomistic and continuum in a bridging domain. A well-defined Hamiltonian in the BDM is defined as a linear combination of Hamiltonians of the atomistic, continuum models as well as the Lagrange multipliers. There is a debate on the use of the Lagrange multipliers. Miller and Tadmor [98] claimed that the physical meaning of the Lagrange multipliers is not clear. Reduction of the spurious reflections at the interface in the BDM depends on the size of the bridging domain. An appropriate size could completely eliminate the reflections. Similar to the BSM, it is not necessary for the nodes to coincide with the atoms in the BDM. Much

work has been contributed to the analysis and extension of the BDM. Recently, the BDM have been applied to model composite lattice structures [113], cracks and dislocations [114, 115].

The hybrid simulation method. Luan et al [101] proposed a hybrid simulation method (HSM) that combines molecular dynamics with finite element method. The HSM consists of three parts, which include an atomistic region, a continuum region and a coupling region. The defects due to the atomic movement can occur in the atomistic region. The coupling between FEM and MD is achieved through the information exchange of the displacements. The displacements of the boundary nodes are determined by a simple weighted averaging method, which makes implementation of the HSM very simple. Moreover, the HSM is not based on a mathematical framework, but it provides highly accurate results [101]. Therefore, it is appropriate to study nanoscale contacts by using the HSM with consideration of simple implementation and accuracy.

The concurrent atomistic to continuum (AtC) coupling method proposed by Fish et al. [116] is a forced-based version of the BDM in essence [98, 113]. In the BDM, the energy or the Hamiltonian are combined in the bridging domain, where the atomistic and continuum regions overlap, while the continuum stress and the atomic force are blended in the AtC. As an extension of the AtC, Badia et al. [117] proposed four classes of the blending methods with a mathematical framework. The foundation of the original AtC is that the continuum stress is equivalent to the atomic stress [118]. Similar to the BDM, the AtC uses a linear weighting of the forces in the overlapping domain. Despite not having defined energy functional, the AtC performs favorably well according to the results of numerical simulations benchmarked by molecular dynamics.

Other multiscale methods based on zero-temperature coupling have been developed so far, including Coarse-grained MD method (CGMD) [119], macroscopic, atomistic-ab, initio dynamics (MAAD) [120], concurrent coupling of length scales (CLS) [121], coupled atomistic/discrete dislocation (CADD) [122]. The detailed introduction for

those multiscale methods or even others can be found in review papers [50, 123, 124].

2.4.3 Finite temperature coupling

Park et al. [125] derived a temperature equation for coupling MD and FEM simulations, from the projection matrix given in the conventional bridging scale method (BSM) [106]. In this work, the temperature of each atom was projected into the space of the FE shape functions. This projection corresponds to a linear approximation of the square velocity of each atom with the least squares error. With the temperature equation, the nodal temperature is obtained directly from the atoms. However, the temperature equation only works well when the change in the velocity gradient of the atoms is small. Besides, Park's work did not consider the energy equation in the continuum region. Later, Wagner et al. [126] proposed a coupling scheme at finite temperature that involves the continuum energy equation, featuring conservation of energy and seamless coupling. More importantly, this is the first coupling model in which thermal energy can pass from MD to FEM and vice versa. The temperature boundary condition applied to FEM is achieved by using Park's temperature equation [125]. Meanwhile, a drag force is used to describe the effects of FEM on the MD temperature. Wagner's model showed excellent performance based on the numerical simulations but it still requires the momentum equation to obtain a fully thermo-mechanical coupling. yet, the appropriate handling on elimination of the spurious refection from FEM to MD is needed for Wagner's model.

Dupuy et al. [127] presented a novel method to model the dynamics of crystalline solids at finite temperature. The method is a finite temperature version of the original Quasi-Continuum method (QC) [13], which is therefore called hot-QC.[128]. In hot-QC, the atoms in the whole system are divided into two groups: representative and constrained atoms. This is in agreement with the original QC. The representative atoms serve as the nodes of the traditional FEM and their momentum directly contribute to the Hamiltonians of the system. Meanwhile, the positons of the constrained atoms,

meanwhile, are obtained by interpolating the positions of the representative atoms. The most important part of Dupuy's hot-QC method was that the mean-force potential energy was defined to describe the contribution of the degrees of freedom of those constrained atoms to the system Hamiltonian. This method accurately captures thermodynamics properties of crystalline solids at different temperature. However, similar to the original QC [13], mesh generation in hot-QC is complicated due to the strong compatibility condition applied to severe deformation regions. Besides, Tadmor et al. [128] pointed out that hot-QC introduces an anomalous 'mesh entropy' and corrected this error. Kim et al. [129] presented another QC-based method, named 'hyper-QC', which overcame the limitation in terms of the small time step required for stability in hot-QC.

Qu et al. [102] developed a 'stadium' damping method to eliminate the spurious reflection at the atomistic/continuum interface and handle thermodynamics at finite temperature. Coupling the 'stadium' damping method and the coupled atomistic/discrete dislocation method (CADD) [122] creates a so-called finite-temperature CADD model. The basic idea of the 'stadium' damping method is that the motion equation of the atoms in the damping region is modified by adding a damping term. This method damps the waves inside the damping region in a ramping way. It reduces the dynamic incompatibility between damped and undamped atoms. In the finite-temperature CADD model, such a damping region shown in figure 2.15 is used to connect MD with FEM in order to absorb the unwanted waves and maintain the temperature of the MD region. The finite-temperature version of CADD has been successfully used to study nanoindentation [130] and material removal at the nanoscale [131]. It must be pointed out that the thermos-mechanical coupling for the continuum region was not considered in the finite-temperature CADD model. The continuum region only transfers mechanical deformation.

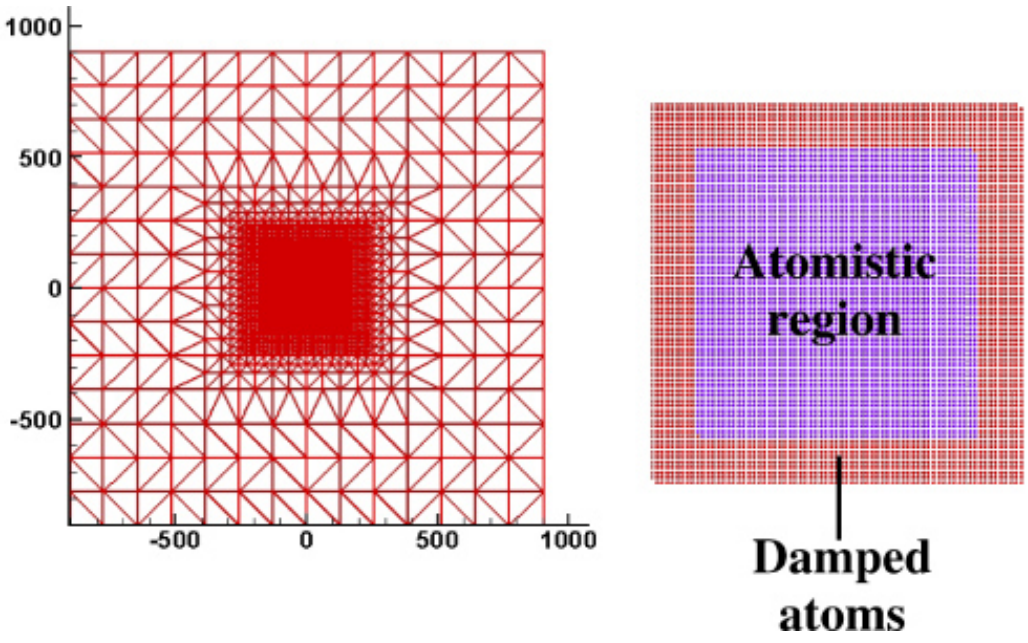

Figure 2.15: Schematic of the finite-temperature CADD model [102].

Mathew et al. [132] presented a finite-temperature multiscale method, based on the spectral decomposition of kinetic energy in the atomistic region. Energy that transfers from MD to FEM is divided into two parts. The high frequency components of energy in the atomist region are described by the heat transfer equation in the continuum region while the low frequency components are modelled by the momentum equation. A fully thermos-mechanical coupling in the continuum region is achieved by Mathew's model. However, the method does not provide a general criterion that discriminates high and low frequency. Furthermore, the use of Mathew's model is limited to 1-dimensional problems. Ramisetti et al. [133] introduced a digital filter technique into the area of the finite-temperature coupling between atomistic and continuum simulations. The digital filters were used to split the kinetic energy from the MD regions. More importantly, Ramisetti et al provided a criterion for selecting the cut-off frequency so that high frequency waves that cannot be resolved by FE are eliminated. Both Mathew's and Ramisetti's models used the generalized Langevin equation (GLE) [134] to perform a selective damping. However, the former was based on a time kernel while the latter one used spatial filters. Spatial filters perform better than the time kernel method since time kernel method damps some waves that should not be damped. Furthermore, spatial

filters have been coupled into a concurrent multiscale model [135] in order to damp the spurious reflections. Numerical simulations show the good performance of the concurrent model for coupling MD and FEM.

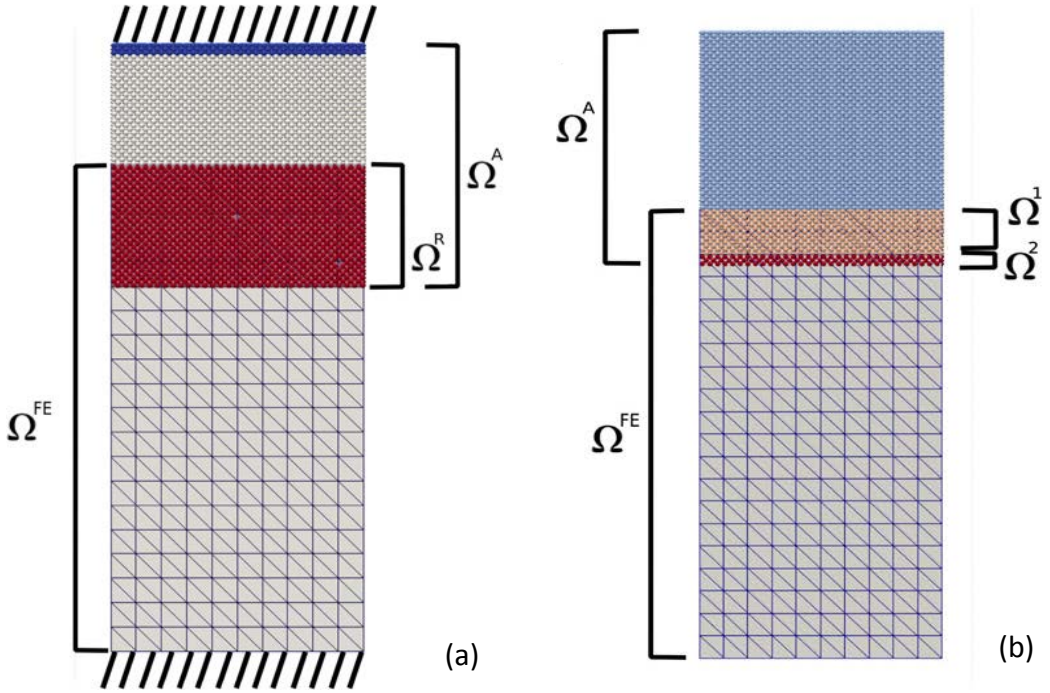

Figure 2.16: Schematic of (a) the original bridging domain method and (b) the new model (from [136]).

Anciaux et al. [136] revealed an artificial cooling effect by analyzing the original bridging domain method (BD) and claimed that the coupling scheme of the BD cannot handle finite temperature coupling. Therefore, Anciaux modified the original BD scheme by separating the coupling region from one part Ω^R to two parts Ω^1 and Ω^2 as shown in figure 2.16. In Ω^1, the movement of the atoms is not constrained by the mesh, unlike the atoms in the Ω^R. In Ω^2, the positions of the atoms are obtained by interpolating the nodal positions. The new model avoids the artificial cooling effect but the means of handling spurious reflection are missing.

Sadeghirad et al. [137] proposed a three-layer mesh scheme as an extension of the bridging domain method to couple atomistic and continuum simulations at finite temperature. In this method, they introduce a mesomesh in the bridging domain to

connect FE domain and MD domain, instead of standard FE mesh [112, 136]. The mesomesh serves as two roles. Firstly, the mesomesh is used to separate the mechanical and fine displacement of the atoms in the bridging domain via the projection operation. The mechanical displacement coupling between MD domain and FE domain is achieved by using the Lagrangian multiplier, following the original bridging domain method [112]. The fine scale of the atomistic displacement is removed by a damping boundary condition proposed by Sadeghirad et al. [138] in order to reduce spurious refection from FE to MD.

The second role of the mesomesh is providing temperature boundary conditions for both FE and MD domain shown in figure 2.17. The boundary atoms are thermally controlled to the temperature T^{target} with a thermostat of each element that contains those atoms. The temperature of each element is calculated by averaging its nodal temperatures. The temperature boundary condition for the FE domain is applied through MD ensembles associated with the ghost nodes inside the MD domain as seen in figure 2.17.

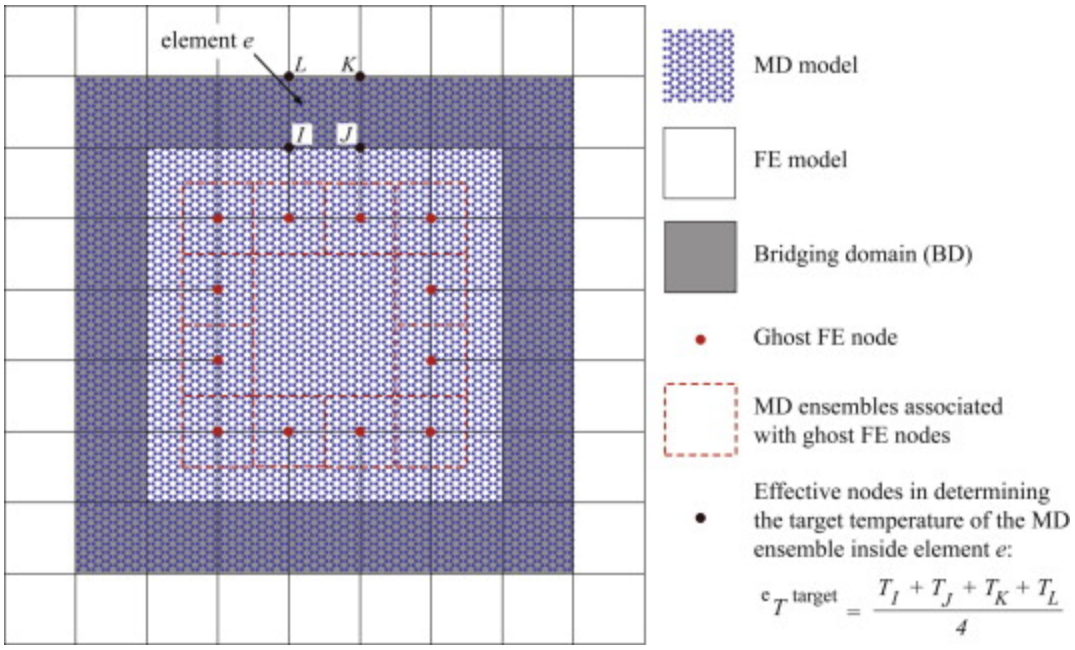

Figure 2.17: Temperature boundary conditions for both FE and MD domain(from [137]).

The three-layer mesh scheme successfully overcomes the cooling effect suffered by the original bridging domain method [112, 136]. Furthermore, according to heat transfer and mechanical deformation simulations, it presented a good performance in coupling MD and FE models. Besides, the three-layer mesh method has been used to study mechanical properties of graphene [139].

The appropriate mesomesh size of 1.069 nm for 300K was obtained by using a priori numerical test in Sadeghirad's work [137]. They also claim that the mesh with the size of 1.069 nm included all effective thermal vibrations. However, the change in the components of the thermal vibrations depends on the atom temperatures. Since the optimal size of the mesomesh varies with the temperature, an adaptive meso-mesh is required to optimally handle wide temperature changes. Furthermore, the effectiveness of the thermal vibrations requires a quantitative definition.

2.5 Summary

Some classical models of contact mechanic, finite element method (FEM) and molecular dynamics (MD) have been first briefly reviewed, with their applications to nanoscale contacts. Also, the advantages and limitations of FEM and MD on nanoscale contacts were discussed. Their individual limitations motivated the use of the multiscale method. The important issues of the multiscale coupling between FEM and MD were presented. Moreover, existing multiscale methods were categorized into zero temperature and finite temperature coupling techniques, and were reviewed with their advantages and limitations.

In terms of single asperity contact at the nanoscale, a large number of simulations have been performed, especially the cases with regarding to the contact between a rigid tip and a deformable substrate. However, the work of rough surface contacts (both unlubricated and lubricated) at this scale is limited. In the following chapters, we mainly focus on the breakdown of elastic continuum models, elasto-plastic deformation, effects of temperature and lubricant on the rough surface contact at the

atomic level. As mentioned in section 2.4.2, the hybrid simulation method [101] is well suited to perform simulations of rough surface contacts due to its simplicity and accuracy. However, for elastic rough surface contacts in 3D, the HSM is still computationally expense, as it has a relatively large atomistic region. Therefore, an extension of 2D model (DAMAS) developed by our group is carried out (chapter 3) in order to study elastic contacts. This model reduces maximally degrees of freedom. Then, the model is used to describe elastic contacts between rough surfaces (chapter 4). The DAMAS is limited to elastic deformation and low temperature due to in-phase motions of atoms in FEM element. To study effects of the temperature and the plastic deformation, the hybrid simulation method is more appropriate than DAMAS. The implementation and validation of the hybrid simulation method for zero Kelvin are first performed (chapter 5). Then, it is extended to finite temperature in order to study rough surface contacts at finite temperature. Finally, effects of the lubricant on rough surface contacts are investigated by using finite temperature HSM (chapter 6).

Chapter 3: Three dimensional single asperity contacts

Michal et al. [140] proposed a multiscale model which combines the simplicity of FEM model and the atomistic interactions between solids. The model has been integrated into the code named 'Development Algorithm for Multiscale Analysis and Simulations', DAMAS in short [141]. The accurate results in 2D verified the capacity of the model. Compared to fully molecular dynamic (MD) simulations, it saves significant computation time. However, the use of the current 2D model is limited. In this chapter, DAMAS is extended to 3D and a more comprehensive analysis for single asperity contacts at nanoscale is conducted. This chapter consists of two parts. In the first part, the basic theory of DAMAS is briefly introduced. Challenges and changes of software implementation are presented in the following subsection. The second part verifies the 3D model in static and kinetic aspects.

3.1 Extension of DAMAS to 3D

3.1.1 Multiscale model presentation

3.1.1.1 Brief review of bridging scale method

As the foundation of DAMAS is the bridging scale method (BSM) proposed by Wagner and Liu [106, 142], we start to briefly recall the basic of the BSM. In the BSM, the total displacement of an atom α which is written as $\mathbf{u}_\alpha$ can be separated into the coarse scale $\bar{\mathbf{u}}_\alpha$ and the fine scale $\mathbf{u}'_\alpha$ in equation (3.1).

$$\mathbf{u}_\alpha = \bar{\mathbf{u}}_\alpha + \mathbf{u}'_\alpha \tag{3.1}$$

The coarse scale $\bar{\mathbf{u}}_\alpha$ can be represented by the shape functions of finite element, as shown to be

$$\bar{\mathbf{u}}_\alpha = \sum_I \mathrm{N}_I \mathbf{d}_I \tag{3.2}$$

where N_I is the shape function of the initial position of the atom α at node I and $\mathbf{d}_I$ is the displacement of node I. The fine scale $\mathbf{u}'_\alpha$ describes the components of the total displacement that the coarse scale cannot represent. The fine scale is defined as the projection of the total scale subtracted from the total scale $\mathbf{u}_\alpha$. To minimize the difference between the coarse scale and the total scale, a projection is proposed to be

$$\mathbf{J} = \sum_{\alpha} m_\alpha (\boldsymbol{u}_\alpha - \sum_{I} N_I \boldsymbol{d}_I)^2 \tag{3.3}$$

Solving equation (3.3) with respect to the nodal displacement **d** yields

$$\mathbf{d} = \mathbf{M}^{-1}\mathbf{N}^{\mathbf{T}}\mathbf{M}_s\mathbf{u} \tag{3.4}$$

where $\mathbf{M} = \mathbf{N}^{\mathbf{T}}\mathbf{M}_s\mathbf{N}$ is the nodal mass matrix or the coarse scale mass matrix, $\mathbf{M}_s$ is the diagonal matrix with the atomic masses m_α and **u** is the displacement vector of all atoms. Similarly, the coarse scale vector and the fine scale vector can be defined as $\bar{\mathbf{u}}$ and $\mathbf{u}'$ respectively. Multiply **N** to both sides of equation (3.5) yields

$$\bar{\mathbf{u}} = \mathbf{N}\mathbf{d} = \mathbf{N}\mathbf{M}^{-1}\mathbf{N}^{\mathbf{T}}\mathbf{M}_s\mathbf{u} \tag{3.5}$$

The projection matrix is defined as $\mathbf{P} = \mathbf{N}\mathbf{M}^{-1}\mathbf{N}^{\mathbf{T}}\mathbf{M}_s$. The fine scale can be written to be

$$\mathbf{u}' = \mathbf{u} - \mathbf{P}\mathbf{u} \tag{3.6}$$

Finally, the total displacement can be given as

$$\mathbf{u} = \mathbf{N}\mathbf{d} + \mathbf{u} - \mathbf{P}\mathbf{u} \tag{3.7}$$

where $\mathbf{P}\mathbf{u}$ is called the bridging scale.

3.1.1.2 Presentation of DAMAS

The model has been presented to successfully handle interactions between two deformable bodies in 2D [141]. A simple case is used to clarify the basic idea of the model. When considering two interacting bodies in figure 3.1, a rigid tip and a deformable substrate, the equation of motion of an atom α in the substrate is given by equation (3.8).

$$m_\alpha \ddot{\mathbf{u}}_\alpha = \sum_{\beta_1 \neq \alpha} \mathbf{f}\left(\mathbf{u}_\alpha, \mathbf{u}_{\beta_1}\right) + \sum_{\beta_2} \mathbf{g}\left(\mathbf{u}_\alpha, \mathbf{u}_{\beta_2}\right) \tag{3.8}$$

where $\ddot{\mathbf{u}}_\alpha$ is the second derivative of the displacement $\mathbf{u}_\alpha$, $\mathbf{f}$ is the internal forces on the atom α while the external forces $\mathbf{g}$ on atom α are obtained from all other atoms β_2 in the tip.

Before coupling FEM with MD, two assumptions of small deformation and low temperature are made. Due to the small deformation, it is assumed the atoms in the substrate interact harmonically, and vibrate around their equilibrium positions. Therefore, $\mathbf{f}$ can be linearized about the equilibrium position of the atoms, which is written to be

$$\mathbf{f}_\alpha \approx \sum_{\beta_1 \neq \alpha} \mathbf{f}_{\alpha,\beta_1} + \sum_{\beta_1 \neq \alpha} \mathbf{f}'_{\alpha,\beta_1} \mathbf{u}_{\alpha,\beta_1} + \cdots + \frac{1}{n!} \mathbf{f}^{(n)}_{\alpha,\beta_1} \mathbf{u}^n_{\alpha,\beta_1} \tag{3.9}$$

where $\mathbf{u}_{\alpha,\beta_1} = \mathbf{u}_\alpha - \mathbf{u}_{\beta_1}$ and $\mathbf{f}^{(n)}_{\alpha,\beta_1} = \frac{\partial^n \mathbf{f}(\mathbf{u}_{\alpha,\beta_1})}{\partial \mathbf{u}^n_{\alpha,\beta_1}}$,. The first term on the right side of equation (3.9) is zero because the internal forces are zero when there is no deformation in the substrate. $\mathbf{u}^n_{\alpha,\beta_1}$ is equivalent to $\left(\bar{\mathbf{u}}_\alpha + \mathbf{u}'_{\beta_1}\right)^n$. Eliminate the first term and the terms of order $n > 1$ gives

$$\mathbf{f}_\alpha \approx \sum_{\beta_1 \neq \alpha} \mathbf{f}'_{\alpha,\beta_1} \bar{\mathbf{u}}_{\alpha,\beta_1} \tag{3.10}$$

The assumption of small displacement is not appropriate to the external force $\mathbf{g}$ because the distance between an atom α and any atoms on the tip could be large. However, based on the BSM, the displacement $\mathbf{u}_{\alpha,\beta_2} = \mathbf{u}_\alpha - \mathbf{u}_{\beta_2}$ can be separated into $\mathbf{u}_{\alpha,\beta_2} = \left(\bar{\mathbf{u}}_\alpha + \bar{\mathbf{u}}_{\beta_2}\right) - \left(\mathbf{u}'_\alpha + \mathbf{u}'_{\beta_2}\right)$, in which $\mathbf{u}'_{\alpha,\beta_2} = \mathbf{u}'_\alpha + \mathbf{u}'_{\beta_2}$ is an ideally small quantity. Therefore, the external force $\mathbf{g}$ can be linearized in terms of $\mathbf{u}'_{\alpha,\beta_2}$ at $\bar{\mathbf{u}}_{\alpha,\beta_2} = \bar{\mathbf{u}}_\alpha + \bar{\mathbf{u}}_{\beta_2}$ shown in equation (3.11).

$$\mathbf{g}_\alpha \approx \sum_{\beta_2} \mathrm{g}(\bar{\mathbf{u}}_{\alpha,\beta_2}) + \mathbf{g}'_{\alpha,\beta_2}\mathbf{u}'_{\alpha,\beta_2} \ldots + \frac{1}{\mathrm{n}!}\mathbf{g}'^{(n)}_{\alpha,\beta_2}\,\mathbf{u}'^{n}_{\alpha,\beta_2} \tag{3.11}$$

where $\mathbf{g}'^{(n)}_{\alpha,\beta_2} = \frac{\partial^{\mathrm{n}}\mathbf{g}(\mathbf{u}_{\alpha,\beta_2})}{\partial\bar{\mathbf{u}}^{\mathrm{n}}_{\alpha,\beta_2}}$. Since the atoms vibrate slightly at low temperature, the fine scales are neglected entirely. Therefore, equation (3.11) can be rewritten as

$$\mathbf{g}_\alpha \approx \sum_{\beta_2} \mathrm{g}(\bar{\mathbf{u}}_{\alpha,\beta_2}) \tag{3.12}$$

Substitute equation (3.10) and (3.12) into (3.8) gives

$$\mathrm{m}_\alpha\ddot{\mathbf{u}}_\alpha = \sum_{\beta_1\neq\alpha} \mathbf{k}_{\alpha,\beta_1}\bar{\mathbf{u}}_{\alpha,\beta_1} + \sum_{\beta_2} \mathrm{g}(\bar{\mathbf{u}}_{\alpha,\beta_2}) \tag{3.13}$$

where $\mathbf{k}_{\alpha,\beta_1} = \frac{\partial\mathbf{f}(\mathbf{u}_{\alpha,\beta_1})}{\partial\mathbf{u}_{\alpha,\beta_1}}$ is stiffness of the bond between atom α and atom β_1. Considering all atoms in the substrate derives the matrix system in equation (3.14).

$$\mathbf{M_s}\ddot{\mathbf{u}} = \bar{\mathbf{k}}_\mathbf{s}\bar{\mathbf{u}} + \bar{\mathbf{g}} \tag{3.14}$$

where $\mathbf{M_s}$ is the diagonal matrix with the atomic masses. $\bar{\mathbf{k}}_\mathbf{s}$ is internal stiffness matrices at atomic sites due to the coarse displacement $\bar{\boldsymbol{u}}$ taking place within the substrate. The external force vector $\bar{\mathbf{g}}$ is taken relative to the coarse displacement of individual atoms.

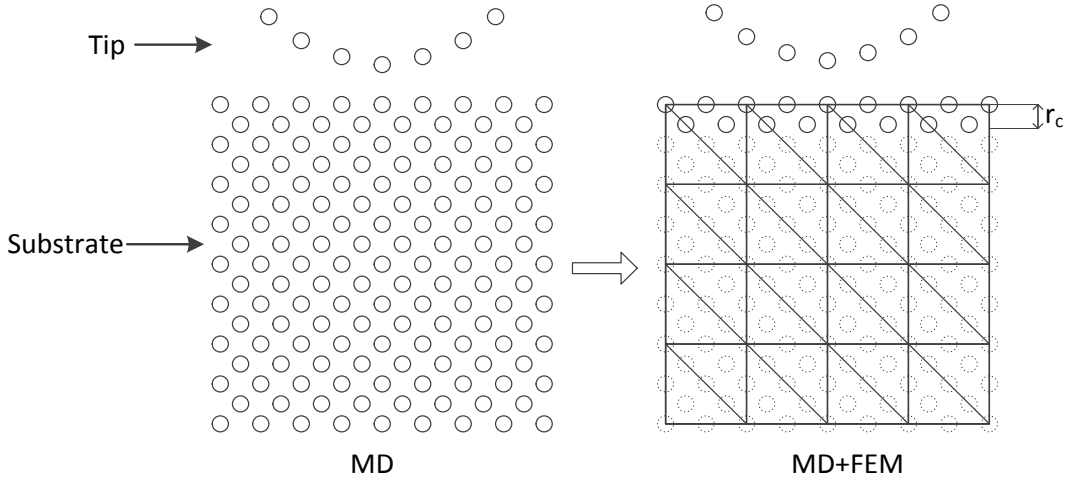

Figure 3.1: Schematic illustration of the multiscale model.

The FEM mesh is superimposed over the substrate in figure 3.1. Substituting equation (3.2) and (3.4) into equation (3.14), the final equation of the model in terms of nodal displacements is given in equation (3.15).

$$\mathbf{M}\ddot{\mathbf{d}}=\bar{\mathbf{K}}\mathbf{d}+\mathbf{N}^{\mathbf{T}}\bar{\mathbf{g}} \tag{3.15}$$

where $\bar{\mathbf{K}} = \mathbf{N}^{\mathbf{T}}\bar{\boldsymbol{k}}_{\mathbf{s}}\mathbf{N}$ is the coarse scale stiffness matrix. The last term $\mathbf{N}^{\mathbf{T}}\bar{\mathbf{g}}$ means that the external force on an FEM node is determined by extrapolating the forces of all atoms whose initial positions lie inside the elements that contain the node. In figure 3.1, the atoms in the substrate are only populated in the lattice sites within the cut-off distance r_c, while other lattice sites indicated by the dotted circles in figure 3.1 are empty. The equation (3.15) is the main result of this section. Several remarks are given below:

(1) The coarse scale stiffness matrix $\bar{\mathbf{K}}$ can be approximated by a linear elastic constitutive law commonly used in FEM. The elastic constants can be determined by molecular dynamics simulations [101].

Alternatively, we can use the Cauchy-Born rule (CBR) to approximate the internal forces following the quasicontinuum method [13]. The CBR assumes that the atomic-level lattice follows the homogenous deformation given by the

macroscopically imposed deformation gradient **F**. According to continuum mechanics, the deformation gradient **F** is a mapping that links the reference configuration with the deformed configuration shown in equation (3.16).

$$d\mathbf{x} = \mathbf{F}d\mathbf{X} \tag{3.16}$$

where d**X** and d**x** are infinitesimal vectors in the undeformed configuration and deformed configuration, respectively. In FEM scheme, the deformation gradient is calculated for every integration point at each loading step, based on the corresponding positions of the nodes. When there is no deformation, **F** equals identity tensor **I**. By using the CBR, a continuum stress tensor can be derived directly from the interatomic potential, which will be used to calculate the internal nodal forces in FEM. The first Piola-Kirchoff stress tensor can be obtained by the following equation (3.17).

$$\mathbf{P}^{\mathrm{K}} = \frac{\partial \mathrm{W}}{\partial \mathbf{F}^{\mathrm{T}}} \tag{3.17}$$

where W is the continuum energy density, which is a function of the continuum deform gradient F. Since it assumes in the CBR that the potential energy of the atoms equals the energy in the continuum system, W can be calculated by the summation of the potential energy. Moreover, the first Piola-Kirchoff stress tensor can easily be transformed to other stress measures [143], such as the Cauchy stress tensor. Based on the finite element formulation, the internal force $\mathbf{f}_{\mathrm{int}}$ is defined as

$$\mathbf{f}_{\mathrm{int}} = \int \mathbf{B}^{\mathrm{T}}\mathbf{P}^{\mathrm{K}}\, d\Omega \tag{3.17}$$

where **B** is the strain-displacement matrix. Compared with linear elasticity, the CBR is more accurate in terms of catching non-linear behavior but more time-consuming. Implementation of the CBR will be introduced in 3.1.2.2.

(2) The derivation of the system equation (3.15) is based on the conditions of low temperature (close to zero K) and small deformation. Compared to fully molecular

dynamics (MD), the external force $\bar{\mathbf{g}}$ is accurate at low temperatures since the fine scale of the atoms can be ignored. In our proposed model, $\bar{\mathbf{g}}$ is obtained by discrete summation. The external force $\bar{\mathbf{g}}$ between two contacting bodies can be evaluated by analytical integration proposed by Sauer and Li [144]. Unlike our model, the atoms in their model are represented in average sense and cannot be individually tracked. However, there are two factors that have effects on the accuracy of obtaining the atomic displacement in our model. One key to accurately describe the displacement of the atoms in the deformable substrate is the internal force $\mathbf{f}_{\text{int}}$, which depends on the accuracy of the constitutive relation. The other origin affecting the atomic displacements lies in the atomic movement in MU. The atoms in each element of the substrate move as a whole or in-phase while the atoms in MD move individually. Furthermore, the effects of the atomic structure on the contact are included due to explicit representation of the atom positions as it has been found that the atomic structure plays an important in nanoscale contacts [3, 15]. Compared to DAMAS presented here, analytical integration in Sauer's model [144], similar to those traditional FE models [38], smeared out those effects of the atomic structure.

(3) In order to dissipate thermal energy and eliminate the short-wavelength phonons due to mesh change in the substrate, the nodes in our model can be coupled to an implicit solvent, following the Langevin dynamics [45]. With two terms added to equation (3.15), the new governing equation can be written as

$$\mathbf{M}\ddot{\mathbf{d}}=\bar{\mathbf{K}}\mathbf{d}+\mathbf{N}^{\mathbf{T}}\bar{\mathbf{g}}+\mathbf{f}_{\text{damp}}+\mathbf{f}_{\text{rand}} \tag{3.18}$$

where the damping term $\mathbf{f}_{\text{damp}}=-(\mathbf{M}/c)\dot{\mathbf{d}}$ and the random force term $\mathbf{f}_{\text{rand}}$ is proportional to $\sqrt{\mathbf{M}\,k_B T/(c\Delta t)}$. Both terms here are the same as those in the Langevin equation for atoms in chapter 2.

Although acceptable results have been obtained by using the 2D model, extending

it to 3D means more realistic materials can be studied. For single asperity contacts, it is necessary to construct a 3D model to study adhesive effect at the nanoscale [15]. With such extension, it permits comparisons between nanoscale contacts and adhesive models, such as JKR [18] and DMT [19]. Compared to the derivation of the governing equation, more challenges happen to software implementation, which is discussed in next subsection.

3.1.2 Software implementation

DAMAS is a multiscale program developed by Guillaume Michal [141]. It was written in C language with high efficiency. The core of DAMAS is a FEM solver, within which other libraries are called. Software named 'Large-scale Atomic/Molecular Massively Parallel Simulator (LAMMPS)' [51] is used to handle the data of atoms. The atomic data is transferred between the FEM solver and LAMMPS. It is easy to call LAMMPS in C because of the interface functions provided by the code. To improve efficiency, LAMMPS was up dated to a new version in DAMAS with corresponding modifications of the interface functions, replacing old version 09Jan09. METIS [145] is a fast graph partitioning tool. In DAMAS, METIS is used to partition the finite element mesh before distributing the partitions to the processor. Running a 3D sample involving about 10^6 atoms, and associated multiscale mesh can be a time-consuming task, but parallel computation can mitigate this issue. Message Passing Interface (MPI) has been introduced into DAMAS, and full test and debug for 3D model are conducted in this work. Open MPI [146] continues to be used to handle the parallelism. More details about other libraries in DAMAS were given in previous work [141]. In the following of this section, changes in DAMAS, including the code structure, implementation of new constitutive law, are presented. Moreover, as mentioned in chapter 2, the Periodic boundary condition (PBC) is often used in Molecular Dynamics (MD), in order to mimic an infinite system with a finite part and minimize the surface effects. To achieve the same goals, the PBC is also implemented in DAMAS, which will be discussed in the

subsection 3.1.2.3. Finally, the parallelism of DAMAS is studied.

3.1.2.1 The code structure

As mentioned above, the main operations of the atoms data, including input, calculating, transferring and output are handled by LAMMPS so little changes happen in this part. Attention is paid more on the FEM solver. It is necessary to change the code structure of DAMAS when new features are brought in and the model is extended to 3D.

Handling matrices and vectors is a key task using the finite element method. DAMAS stores and manipulates matrices in a sparse form, which shows high efficiency and low memory storage. It is better to build a large sparse matrix at the initialization, and not rebuild it every time step. The stiffness matrix was constructed in a sparse form in Ref. [141]. The stiffness matrix for FEM in DAMAS is assembled to be a sparse matrix before solving the nodal equation. Their items are no longer changed during the subsequent simulation and each item will be used according to the nodal number at each time step when calculating the internal nodal forces. However, as mentioned in section 3.1.1, we use both linear elasticity and the Cauchy-Born rule as the constitutive law. Using the Cauchy-Born rule means the stiffness matrix is not constant anymore and assembling it at each step would be a time consuming task in DAMAS. Therefore, ‘elements loop’ is used instead in this work [147]. During the loop, strain or the deformation gradient, stress and the internal nodal forces of each element are calculated in order, and then the internal nodal forces are assembled to solve the governing equation..

3.1.2.2 Implementation of Cauchy-Born rule

In figure 3.2, the implementation of the CBR is illustrated. A ghost crystal composed of a central atom and its neighbors is constructed through the input data, including primitive lattice vectors and a cutoff radius. The number of neighbors of the central

atom is determined by the cutoff radius. For a FCC unit cell, the number of nearest neighbor for an atom is 12, second nearest neighbor 6, third nearest neighbor 24 and so on. Before simulation loop starts, all data about the CBR must be settled down. The potential and its parameters for calculation of the atomic interaction in ghost crystal have to be specified. Currently, DAMAS can work with Lennard-Jones potential, embedded atom method (EAM) potential and Morse potential.

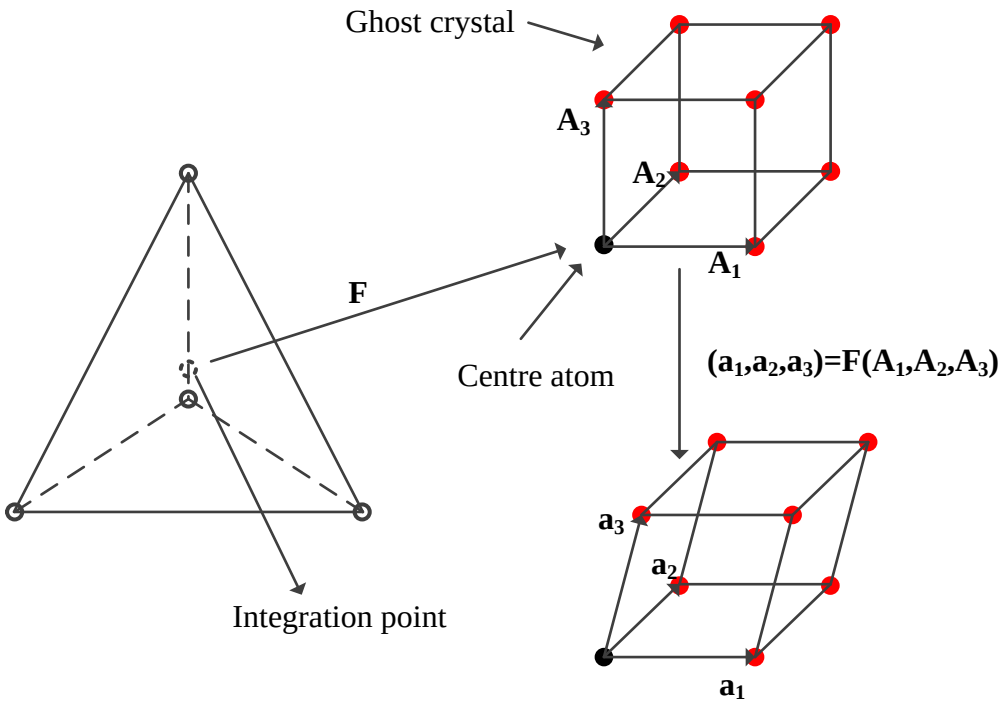

Figure 3.2: Illustration of the Cauchy-Born rule in DAMAS

New nodal positions are obtained by integration first after deformation. Then, the deformation gradient **F** of the integration point in a tetrahedron element is calculated according to equation (3.4). It shows in figure 3.2 that the lattice vectors $\mathbf{A_1}$, $\mathbf{A_2}$, $\mathbf{A_3}$ of the ghost crystal are mapped into new lattice vectors $\mathbf{a_1}$, $\mathbf{a_2}$ and $\mathbf{a_3}$ homogenously according to **F**. The potential energy related to the central atom in the deformed crystal contributes to W. Finally, the first Piola-Kirchoff stress tensor for the integration point is calculated according to equation (3.5).

It should be noted that the ghost crystal is not a part of the structure and it is just used

to calculate stress for each integration point. The role of the ghost crystal in DAMAS is similar to the virtual atomic cluster in VAC method [50]. There is no doubt that the implementation of the CBR is slower than that of a linear constitutive law. And computation time increases along with the increase in the cut-off radius. The performance of implementing the CBR is demonstrated in a later section.

3.1.2.3 Periodic boundary condition

In this section, implementation of the PBC in FEM is illustrated. One limitation of the PBC implementation in this work is that the meshes on opposite RVE boundaries must be identical. To relax such limitation, a polynomial interpolation method can be used [148].

An illustration of the PBC is shown in figure 3.3, taking two nodes as an example. Suppose that the PBC is just imposed along x direction on a cubic structure, so two

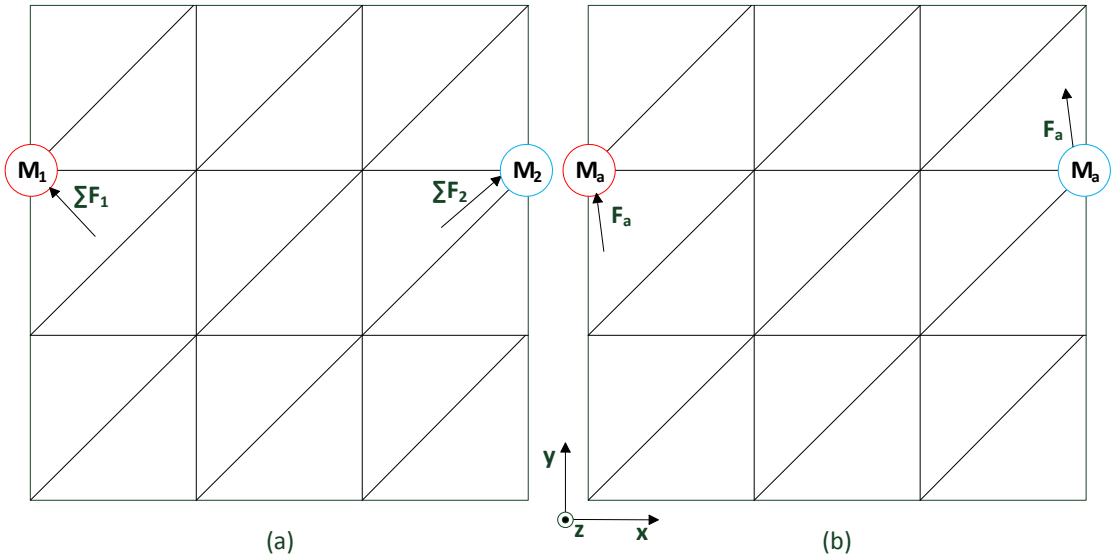

Figure 3.3: Illustration of imposing periodic boundary condition in FEM. (a) $\sum \mathbf{F}_1$ and $\sum \mathbf{F}_2$ are the nodal forces on node 1(red circle) and node 2(blue circle), respectively. $\mathbf{M}_1$ and $\mathbf{M}_2$ are their mass. (b) When imposing the periodic boundary condition, their nodal force and mass are averaged: $\mathbf{F_a} = \frac{\sum \mathbf{F_1} + \sum \mathbf{F_2}}{2}, \mathbf{M_a} = \frac{\mathbf{M_1} + \mathbf{M_2}}{2}$

opposite faces perpendicular to the x axis are considered. Firstly, the nodes on the one

face are paired to those on the opposite face. The nodes whose positions, $\mathbf{x}_i$ and $\mathbf{x}_j$, satisfy equation (3.19) are paired. Equation (3.6) is given

$$\left|\left\|(\mathbf{x}_i - \mathbf{x}_j)\right\| - L_x\right| \leq \varepsilon \tag{3.19}$$

where L_x is the length of the structure along x direction and ε is tolerance. Then, the mass matrix and the nodal forces in the whole structure are calculated. Before solving the nodal equation, the mass and the forces of each pair of nodes are averaged, for example, node 1 and node 2 in figure 3.3. If the PBC is imposed along both x and y directions, the procedure is similar.

3.1.2.4 Parallelism

For a fully MD contact model with a proper size in 3D, parallel computing is necessary, otherwise, it usually takes an unacceptably long time to compute using one processor. The proposed model in section 3.1.1 could significantly reduce degree of freedoms compared to pure MD. The FEM solver in DAMAS was written for parallel computation using Message Passing Interface (MPI). Since LAMMPS runs in parallel using message-passing techniques, most of the work was dedicated to the FEM solver. Open MPI [146] is chosen as the MPI library in DAMAS.

Another important tool on parallel computing is METIS [145], which is used to partition mesh for each process. It is seen in figure 3.4 that the mesh is partitioned into four parts for four processors in average. Every processor involved in the simulation is divided to occupy a part of mesh based on the METIS partition.

In Ref. [136], all processors were partitioned into two subgroups. Molecular dynamics occupied one subgroup of 32 processors, while the other subgroup of one processor calculated finite element elasticity. Ratio between the number of the atoms and the nodes in the current model is much less than the proposed one in Ref.[136]. Therefore, all processors in DAMAS work in the same group and are used to handle both the

atoms and the finite elements.

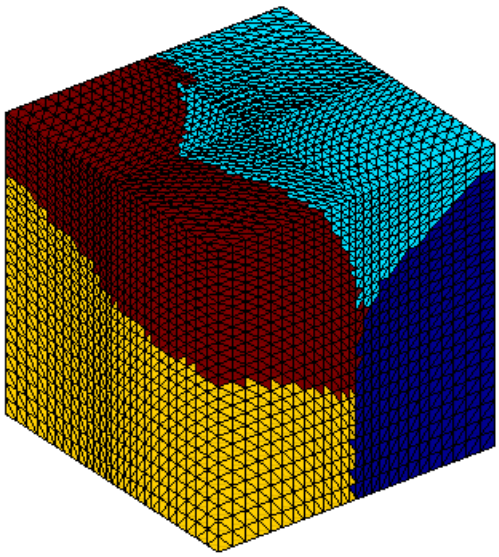

Figure 3.4: Mesh partitioned by Metis with four processors. Different colors stand for different processors.

The MPI implementation is evaluated on a parallel cluster. Speedup and efficiency are two key measures for evaluating the performance of a parallel program [149]. Speedup S_p is the ratio between sequential execution time T_1 on one processor and parallel execution time T_p on p processors given in equation (3.7).

$$S_p = \frac{T_1}{T_p} \tag{3.7}$$

The efficiency E_p of a parallel program is defined as a speedup divided by the number of processors shown in equation (3.8).

$$E_p = \frac{S_p}{p} \tag{3.8}$$

To evaluate the parallel performance of DAMAS, the contact between a rigid plane and a deformable substrate was used. The rigid plane is composed of one layer of the atoms, the number of which is 973. The substrate with a flat surface consisted of 20736 atoms, 198608 tetrahedron elements and 35937 nodes. A linear constitutive law

and the Cauchy-Born rule were used for comparison. The rigid plane was forced to press the substrate under a constant force. The simulation ran 50000 steps. The maximum number of the processors was 8 which equals the number of processors on each node of the cluster.

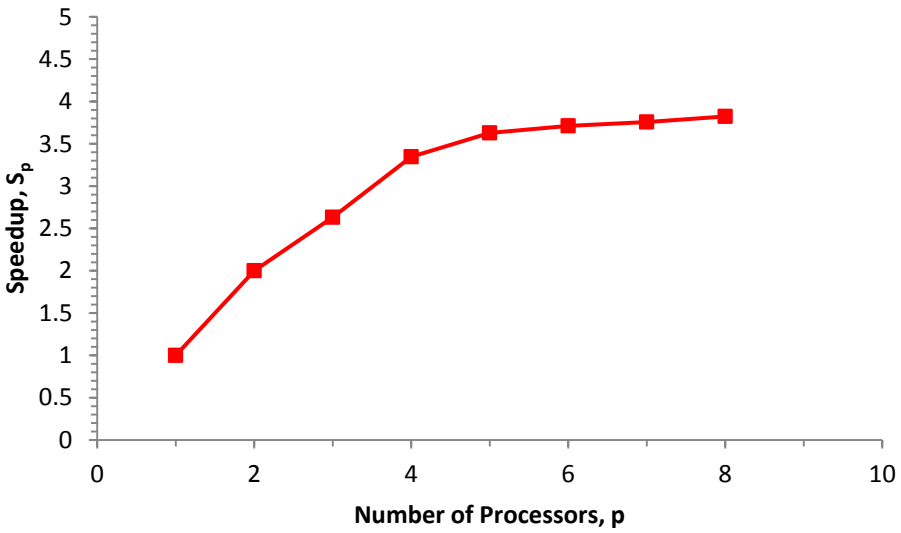

Figure 3.5: Speedup as a function of the number of processors. Linear constitutive law was used.

Figure 3.5 shows speedup as a function of the number of the processors. It is clearly seen that adding processors reduces the computation time. However, the slope is much decreasing after p reaches 5 because communication between processors increases significantly. The computation time of 8 processors is 3.82 times less than that of one processor. Although the speedup of 8 processors is a little larger than that of 4 processors, using 4 processors is a better choice in consideration of saving computation resources. Figure 3.6 demonstrates the relationship between efficiency and the number of processors. It is shown that efficiency drops as the number of processors increases. A loss of efficiency originates from communications. Therefore, the more processors, the better is not a case in terms of the MPI implementation. A compromise between speedup and efficiency is needed.

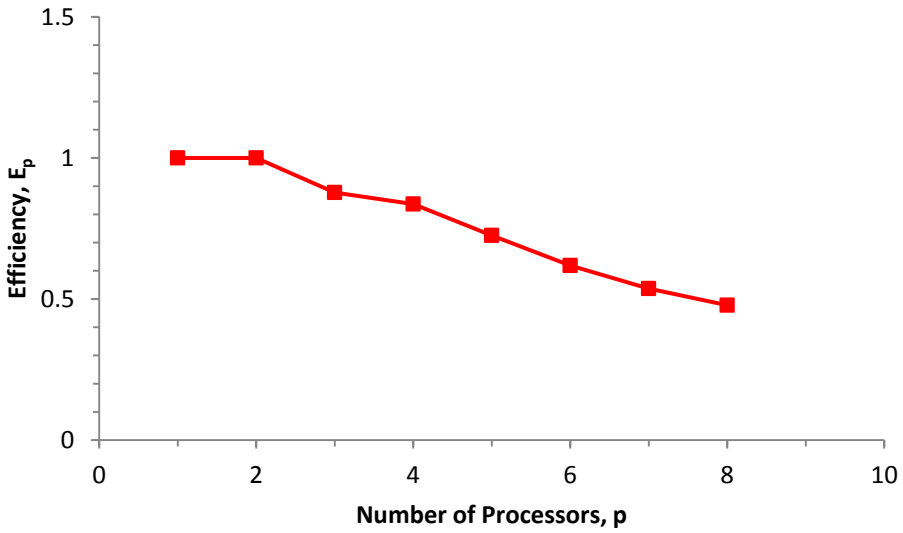

Figure 3.6: Efficiency as a function of the number of processors. Linear constitutive law was used.

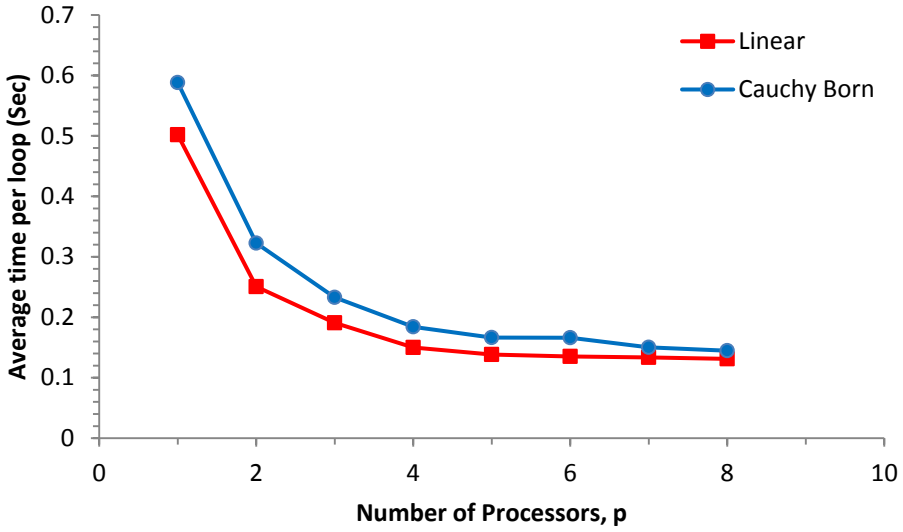

Figure 3.7: Average time per loop as a function of the number of processors. Linear constitutive law was used.

It has been tested that measures of parallel performance are not influenced by different constitutive laws. In spite of that, implementation of the Cauchy-Born rule raised the computation time in total. A FCC ghost crystal consisting of one center atoms and 12 neighbors was used. The atomic interaction was described by LJ potential. Figure 3.7 shows the relationship between average computation time of running a single step and the number of processors. The implementation of the linear constitutive law is faster

than the Cauchy-Born rule. Calculations of the atomic interactions in the ghost crystal are responsible for it. The speed of the Cauchy-Born rule is acceptable compared to the linear law. And the difference of the loop time drops as shown in figure 3.7.

The use of MPI for DAMAS aims to save computation time. In terms of speedup for a typical case, DAMAS ran at least 3 times faster when using more than 4 processors compared to one processor implementation, which proves its MPI performance. For a case of more degree of freedom, the speedup could be larger. To run a simulation, the appropriate number of processors must be chosen first. Again, more processors may not be better. Currently, parallel efficiency is not high due to the bottleneck of the server's memory bandwidth.

3.2 Validation of 3D multiscale scheme

3.2.1 Model set-up

In this section, non-adhesive contact between a rigid spherical tip on a deformable substrate is considered. Purely repulsive interactions of the atoms between the tip and the substrate are modelled using the Lennard-Jones potential with the characteristic binding energy ε and the characteristic length σ, the cutoff radius of $2^{1/6}\sigma$. All quantities in this work are expressed in terms of ε, σ with the atomic mass m. Two different tip forms, commensurate bent and stepped [15], were studied as shown in figure 3.8. The commensurate bent tip in figure 3.8(a) was created by bending a 2D crystal plane which is commensurate with the top surface of the substrate. Assume that the atoms on the crystal plane were projected on the x-y plane. Their heights along the z direction were determined from $x^2 + y^2 + z^2 = R^2$, where R is the given radius which equals 100σ and the center of the sphere is $(0, 0, 0)$. The stepped tip in figure 3.8(b) was formed by sectioning a FCC crystal. Atoms outside a given sphere with the radius 100σ were removed. The number of the atoms on the bottom layer can be changed by moving the center of the given sphere along the z direction.

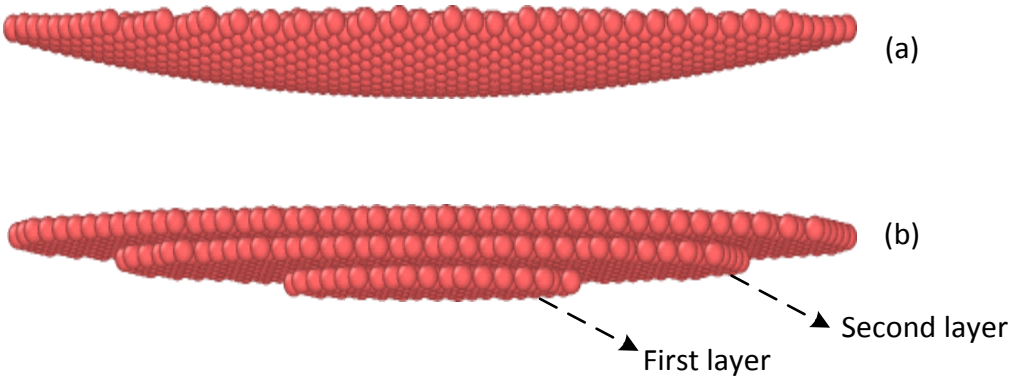

Figure 3.8: Tips of two different forms (a) Commensurate bent tip (b) Stepped tip. The radius R of two tips is 100σ. The stepped tip is in a terraced shape, and consists of several layers. The first and second layers, correspond to the two in figure 3.11 are indicated by arrows.

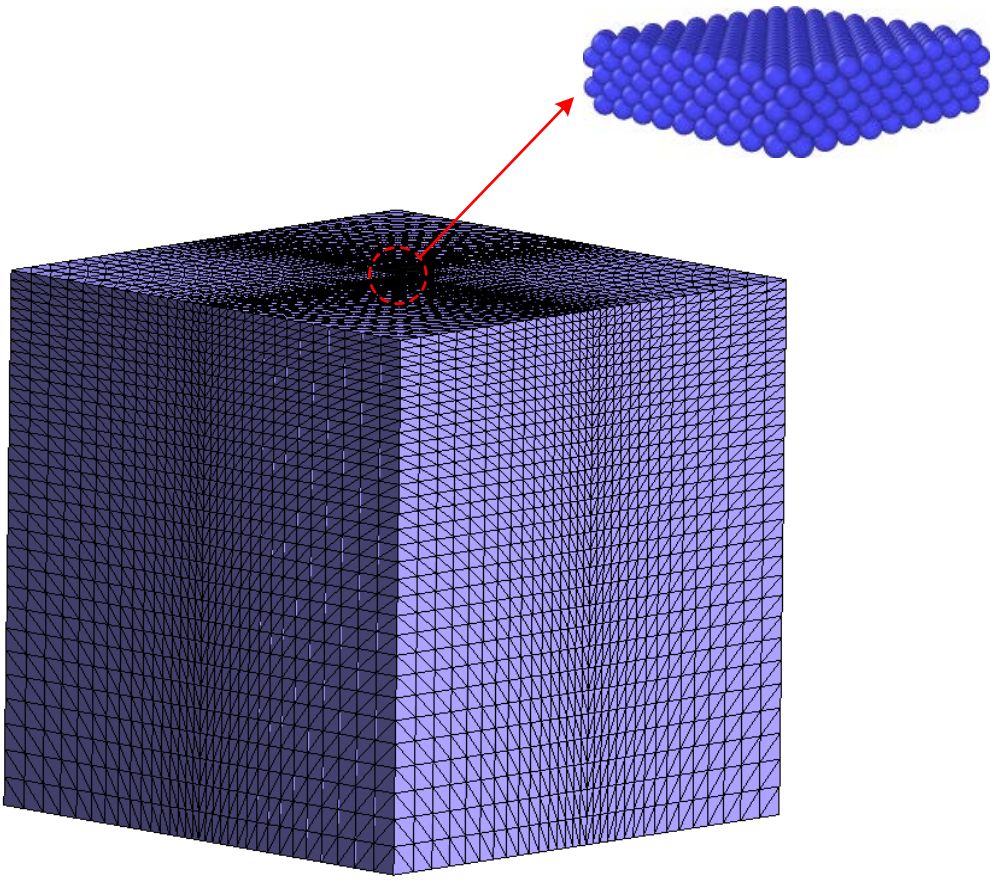

Figure 3.9: Mesh and atomic details of the substrate. The thickness of the atoms (blue sphere) depends on the cut-off radius of the potential.

The FEM mesh of the substrate was superimposed over a FCC crystal with a [001]

surface as shown in figure 3.9. Note the lattice constant equals to $2^{2/3}\sigma$ and the nearest-neighbor spacing of the atoms is $2^{1/6}\sigma$. The size of the substrate is $190.5\sigma \times 190.5\sigma \times 190.5\sigma$. Periodic boundary conditions were applied along the x and y directions. The bottom nodes in the substrate were fixed. Linear tetrahedral elements were used. The smallest edge size of elements in the contact region is 3σ as a compromise to both efficiency and accuracy. The mesh coarsens away from the contact region. The ratios of the computation time between the full MD simulation and the multiscale model with varying smallest edge size of the elements are shown in Table 3.1. In the fully MD simulation, the geometry of the substrate consisted of 691200 atoms. The atomic interactions in the substrate were described by the Lennard-Jones potential. The cut-off radius equals $2^{1/6}\sigma$ so that the interactions only include the nearest-neighbors. Other set-up of MD simulations was the same as the MU model. It shows in Table 3.1 that the proposed model can reduce a number of the degrees of freedom (DOFs). At the same time, it was capable of saving a large amount of time cost compared to the fully MD simulation.

Table 3.1: Ratio of the computational time between fully MD and the Multiscale model (MU) with varying smallest element edge size

Smallest element edge size	2σ	3σ	4σ	5σ
DOFs of the substrate in MU	177957	107811	75690	59049
Computational time ratio	5.86	9.74	14.29	17.92

The elastic tensor was determined by evaluating the relation between stress and strain for a small cubic crystal with Lennard-Jones potential. $C_{11}=72\varepsilon\sigma^{-3}$ and $C_{12}=36\varepsilon\sigma^{-3}$ were obtained for small displacements. For an approximation to an isotropic substrate [73], Poisson ratio and Young's modulus were calculated according to equation (3.9-3.10).

$$\nu = \frac{C_{11} - C_{12}}{2C_{11} - C_{12}} \tag{3.9}$$

$$E = C_{12}(1+\nu) \tag{3.10}$$

Poisson ratio equals 1/3 and Young's modulus equals $48\varepsilon\sigma^{-3}$ so the effective modulus $E^{*}= E/(1-\nu^{2}) = 54\varepsilon\sigma^{-3}$. Elastic constants has also been calculated by the Cauchy-Born rule presented in Ref.[73]. The results were almost identical.

The motion of the nodes was integrated using the Velocity Verlet algorithm [44] with the time step $\Delta t = 0.005t_{LJ}$, where $t_{LJ}=\sqrt{m\sigma^{2}/\varepsilon}$. The step loads were applied to the tips and after each load the system was allowed to equilibrate for $250t_{LJ}$. The Langevin thermostat [45] with the temperature $T=0.00001\varepsilon/k_{B}$ and the damping rate of $0.1t_{LJ}$ was used to remove the fraction of the kinetic energy of each node during the process of equilibration.

3.2.2 Non-adhesive contacts

3.2.2.1 Normal contact

Normal displacement, contact radius and normal pressure in non-adhesive elastic contact are expressed by Hertz theory [17]. In this section they were all expressed in dimensionless and power forms. The relationship between the contact radius a and load N follows equation (3.11).

$$\frac{a}{R} = \left(\frac{3}{4}\right)^{1/3}\left(\frac{N}{R^{2}E^{*}}\right)^{1/3} \tag{3.11}$$

The normal displacement δ is related to N by:

$$\left(\frac{\delta}{\sigma}\right)^{1/2} = \sqrt{\eta}\times\left(\frac{3}{4}\right)^{1/3}\left(\frac{N}{R^{2}E^{*}}\right)^{1/3} \tag{3.12}$$

where η is defined as R/σ. The dependence of the normal pressure p on the radial distance from the center r is given by:

$$\frac{p(r)}{E^*} = \frac{2}{\eta\pi}\sqrt{\left(\frac{a}{\sigma}\right)^2 - \left(\frac{r}{\sigma}\right)^2} \tag{3.13}$$

Figure 3.10 shows the variation of (a) normal displacement and (b) contact radius with the normal load for two tips. Both quantities are expressed by a power so that Hertz solution is indicated by straight lines. In figure 3.10, the results of pure MD simulation in Ref.[15] are also shown.

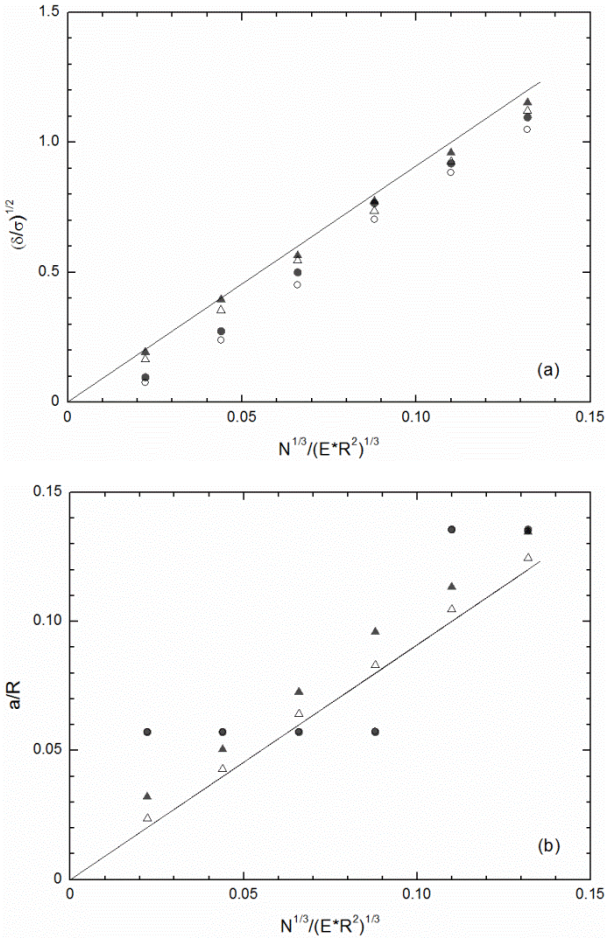

Figure 3.10 (a) Normal displacement δ, (b) contact radius a as a function of normal load. The Hertz prediction is indicated by a solid straight line. Open triangles and circles show the results of the commensurate bent tip and the stepped tip in the multiscale model. Filled triangles and circles show the corresponding results of full MD in Ref.[15].

The tip height where the tip suffers the first repulsive force from the substrate atoms is the initial position of normal displacement δ, or δ = 0. In figure 3.10(a), the normal displacement δ for both tips in figure 3.10(a) is close but below those from full MD

simulation. With the model, the tip is not pushing independent atoms of the substrate but the elements that contain the contacting atoms. Therefore, larger loads were required to push the tip into the substrate than MD. The normal displacement of the bent tip predicted by the proposed model shows a smaller deviation from the prediction of Hertz than the stepped tip at small loads. Since the bottom layer of the atom in the stepped tip contacts the substrate together, much lower δ is expected in figure 3.10(a). If a finite-size correction is applied to the Hertz prediction, the deviation of all simulation results can be reduced by about 2% [15].

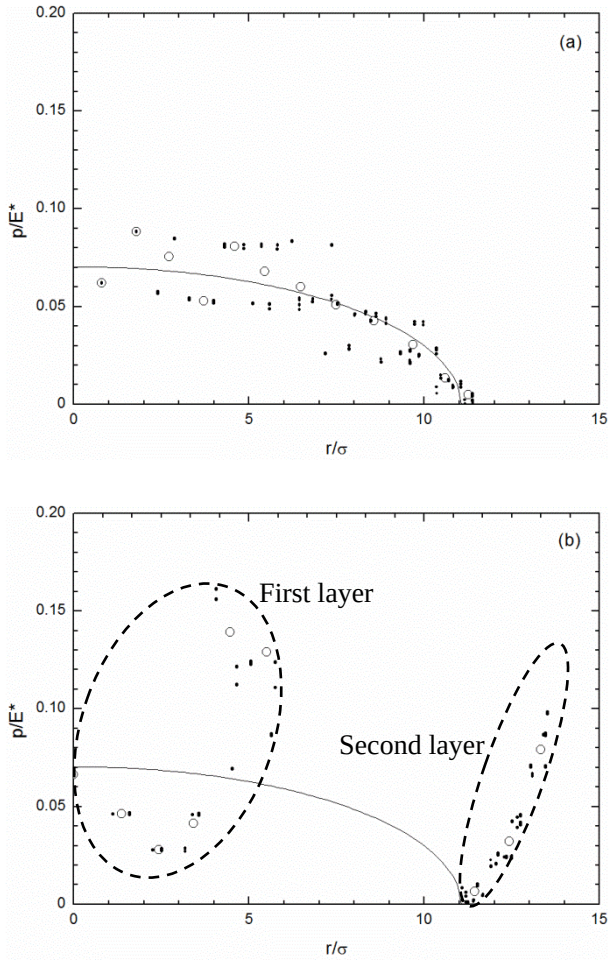

Figure 3.11: Dimensionless normal surface pressure vs. radius for two different tips: (a) commensurate bent, (b) stepped. Dots in the dashed lines in (b) indicate pressure on the surface atoms from the two different layers (see figure 3.8) of the stepped tip in contact with the substrate. The average pressure over all atoms within the indicated annulus of width σ is shown by circles. The solid straight lines show the Hertz prediction.

In figure 3.10(b), the contact radius of the commensurate bent tip obtained from the multiscale model is much closer to the Hertz prediction, compared with that of the full MD. Due to the finite range of the potential between the tip and the substrate, the radius of contact is still a little larger than the Hertz theory. Results from the 3D model demonstrate it could be a reliable tool for analyzing contact radii compared with adhesive continuum mechanics models in the future. The stepped tip shows a staggered evolution of the contact radius because of its terraced shape. The contact radius of the stepped tip obtained from the model shows little deviation from those from a full MD analysis. It must be noted that the number of atoms at each layer of the stepped tip have an important effect on the results.

Figure 3.11 demonstrates the distribution of normal pressure as a function of the radius r from the tip center when the dimensionless load is $N/R^2E^*=0.0018$. Solid lines show the pressure distribution of the Hertz prediction. The normal pressure on the surface atom indicated by the dots is taken as the atomic force divided by the atomic area. The circles represent the average pressure in a ring area with the width σ. In figure 3.11(a), the local pressure of the commensurate bent tip shows fluctuations along the Hertz prediction at the central contact area. In fully molecular dynamics simulations, the atoms on the substrate surface move freely to have the commensurate bent tip atoms entering into their interstitial position, which is called in registry [150]. When the atoms are in registry, fluctuations in force are minimal. Using our multiscale method, the substrate atoms in each element move in-phase so that being in registry cannot be ensured. After deformation, a few atoms on the tip are not located between substrate atoms, so a range of forces are exerted on the tip. The average pressure is, however, close to the Hertz solution, especially the region near the edge where deformation is small as seen in figure 3.11(a).

The presented model shows a qualitatively different pressure distribution of the stepped tip compared with the Hertz prediction in figure 3.11(b). The contact between the stepped tip and the substrate occurs layer by layer. As shown in the figure, the first

layer of the tip, or the bottom layer first contacts with the substrate. As load increases, the tip moves downwards, the second layer contacts with the substrate. At the same time, the distance between the first layer and the substrate is closer. Thus, the pressure on the atoms near centre are larger than on those on the edge of contact area. In continuum theory, the pressure in the center is smaller. Pure MD also shows qualitatively similar results [15]. However, the MU model shows some deviation from MD results due to the in-phase motions of the atoms within elements.

3.2.2.2 Friction

To study friction, the tips were forced to move along x direction after the step loading. The tips moved laterally at a constant velocity $0.01\sigma/t_{lj}$ with a constant load. The shear lasted 1000 t_{lj}, which means the tips were displaced a distance of 10σ. The friction force was recorded every t_{lj}. For easy comparisons, the loads $F_z/(E^*R^2)$ were taken as $(1\times0.132/6)^3$, $(2\times0.132/6)^3$, $(3\times0.132/6)^3$, $(4\times0.132/6)^3$, where 0.132 was chosen from Ref. [15].

Figure 3.12 illustrates the friction force along x direction for two forms of tips. The evolution of the friction force between two tips was similar in figure 3.12(a) and (b), as both tips have a similar commensurate relationship between the tip and the substrate. In details, the atoms of both tips climbed from interstitial positions of the substrate atoms to their top, and then dropped to their interstitial positions. Such a movement of the atoms on both tips determines the similar evolution in friction force between Figure 3.12(a) and (b). In addition, it determines the periodicity of the friction force found also in molecular dynamics simulations [7, 150] and in atomic force microscope(AFM) experiments [62, 151]. Peak values of the friction force depended on the loads shown in figure 3.12. To better show such dependence, static friction force were calculated by the average of the peak values.

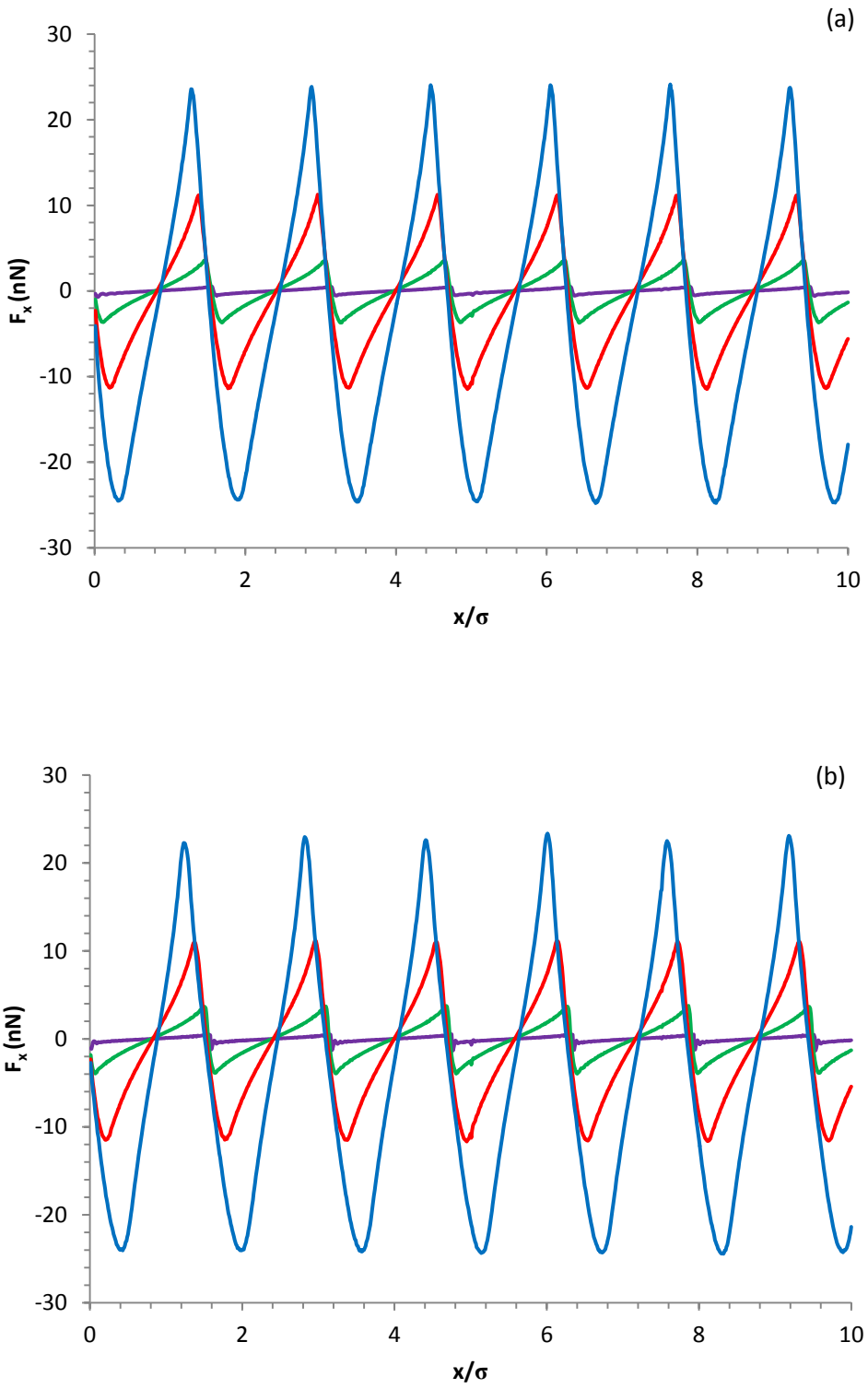

Figure 3.12: Friction force as a function of a lateral distance with different loads. Purple, green, red and blue lines indicated the loads of $(1\times0.132/6)^3$, $(2\times0.132/6)^3$, $(3\times0.132/6)^3$, $(4\times0.132/6)^3$. (a) Commensurate bent tip (b) stepped tip.

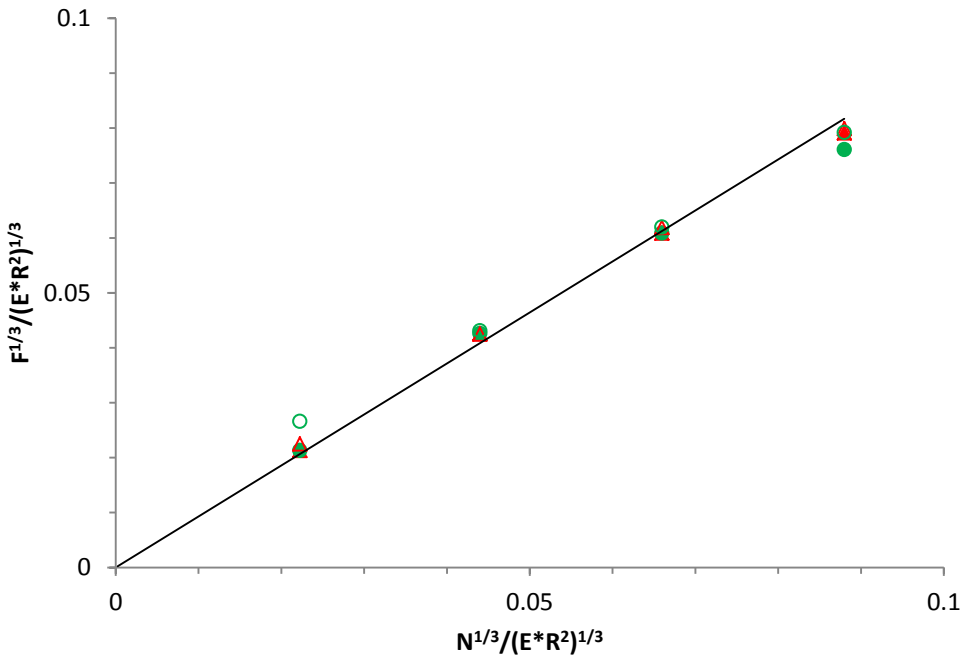

Figure 3.13: Static friction force as a function of the normal loads in dimensionless and power form. Open triangles and circles indicated commensurate bent and stepped tips in current work, respectively. Filled triangles and circles show the results in Ref. [15]. The solid line shows a linear trend for the bent tip in this work.

It shows in figure 3.13 that the static force obtained by using the multiscale method (MU) is close to that from pure MD simulations. As expected from the friction force curve in figure 3.12, the static force of the bent and stepped tips in MU shows little difference. The coefficient of friction of the bent tip equals 0.80 in MU while 0.77 was obtained in the literature [15]. The deviation originates from the in-phase movement of the atoms in MU, which causes higher barrier energy relative to pure MD [101].

The flat substrate was used for studying non-adhesive contacts. From the results of the friction, it clearly shows that flat or smooth here is different from continuum mechanics. From the atomic point of view, there is on flat surface, as the discrete positions of the atoms constitute natural roughness. Figure 3.14 demonstrates the instantaneous position of the tips along z direction as a function of a sliding distance. The tips moved over the substrate surface in the form of ‘up and down’.

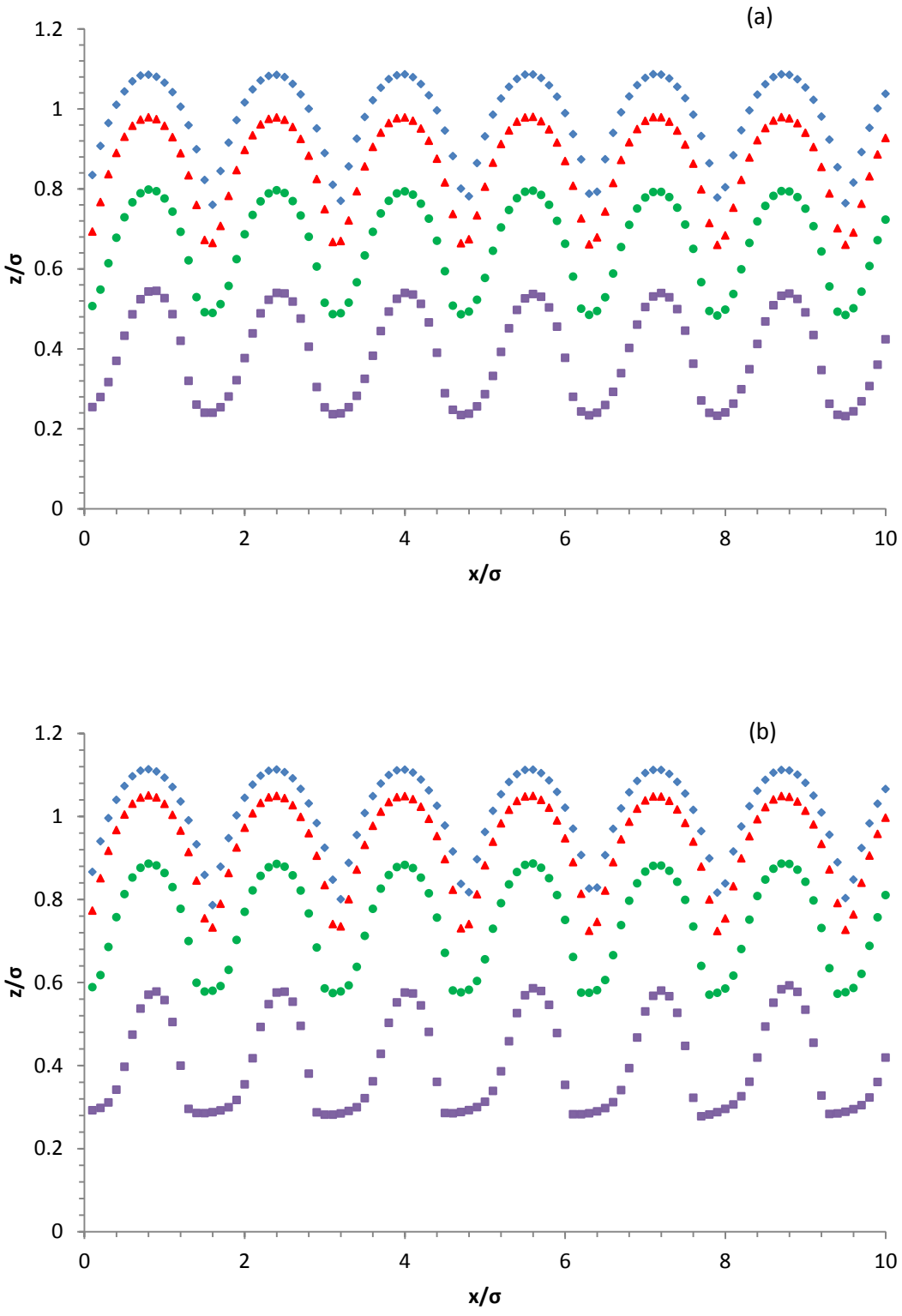

Figure 3.14: Position of the tip along z direction as a function of a sliding distance with different loads. Purple, green, red and blue lines indicated the loads of $(1\times0.132/6)^3$, $(2\times0.132/6)^3$, $(3\times0.132/6)^3$, $(4\times0.132/6)^3$. (a) Commensurate bent tip (b) stepped tip.

The periodicity of the instantaneous position in figure 3.14 and the friction force in figure 3.12 is identical for both tips. The waviness shown in figure 3.14 proves that the roughness of the surface is not zero. The height change (difference between highest position and lowest position in each periodicity) deviates little under different loads, about 0.3σ for both tips and about 0.33σ in MD [15]. Peak values of the instantaneous positions increase with load, similar to the relationship between the friction force and load.

3.2.3 Summary

A 3D multiscale model has been used to analyze the results of non-adhesive contacts at the nanoscale. The results were compared with those obtained from molecular dynamics simulations. The proposed model can reduce the atomistic region to the very small domain with one or several layers atoms (depends on the cutoff radius) at the surface, saving a large amount of computational time. In addition, some important features of nanoscale contacts can be captured by the scheme. However, it has been found in our model that the in-phase motions of the atoms inside the elements affect the results of nanoscale contacts.

The interactions between the tip atoms and the substrate elements in the multiscale model decrease the magnitude of the normal displacement. The normal displacement of two different tips shows smallest deviation, although their pressure distribution is qualitatively different. In terms of the contact radius, the proposed model is between pure MD and the Hertz theory when using the commensurate bent tip. The proposed model successfully shows the contact radius of discrete steps with increasing loads and reproduces the MD results. The mean pressure of the commensurate bent tip is close to the Hertz prediction. Despite of deviation, the stepped tip in the proposed model can shows a similar behavior of a flat punch in continuum mechanics.

In addition to normal contact, the model has also been used to study friction. The periodicity of the friction force in MD is accurately achieved by MU. The static force

and the coefficient of friction by using MU are close to the benchmark for both bent and stepped tips.

Chapter 4: Rough surface contacts using DAMAS

4.1 Introduction

In chapter 3, DAMAS was used to perform simulations of single asperity contacts at nanoscale. The results benchmarked by the molecular dynamics simulations demonstrate the adequate performance of DAMAS. In addition, it was shown with acceptable accuracy that nanoscale contacts deviate from continuum theory. It indicates that DAMAS has the potential to handle more complicated problems. Therefore, in this chapter, the use of DAMAS on rough surface contacts is further investigated.

The real surfaces consist of a multitude of asperities whose lengths cover a wide range [28]. Self-affine fractals are widely used to describe those surfaces [152]. Self-affine fractal surface is characterized by the non-uniform scaling, where any parts of the surface are statistical invariant under the transformation that scales in different directions by different amounts. Continuum contact between the rough surfaces is generally based on the Hertz theory of elastic deformation of asperities.[24]. It has been found that the contact area varies linearly with loads when loaded lightly [26, 153]. Due to the breakdown of continuum mechanics [3], the nanoscale contacts between rough surfaces may deviate from continuum counterparts.

The effects of roughness on contact between rough surfaces have been studied by Luan et al [154]. Purely elastic deformation was modelled by connecting the atoms with ideal harmonic springs. Although the largest size used in Luan et al' work reached the micrometers, the system was only 2-dimensional. As a result, it is difficult to make a direct comparison between their results and continuum theory. Besides, the accuracy of the results could be lower at 2D, as mentioned in Luan's work. Other work in the literature [74] suffered from the limitation of the system size (<169a, where a is lattice constant), despite being 3-dimensional.

In this chapter, we performed the simulations of elastic contacts between rough surfaces using DAMAS. The interactions between the upper and lower surfaces are achieved through the few layers of atoms near the surface, thus, reducing the scale of computation. The system of all cases is 3D, and the maximum size of simulation is 200 nm. The influence of different roughness is considered. As mentioned in chapter 3, only elastic deformation is allowed. Small loads are applied to avoid serious distortion of the elements

4.2 Simulation description

4.2.1 Geometry

In this work, two different types of contacts were considered: flat-on-rough and rough-on-rough [154]. In the former, the flat surface, formed by a layer of atoms, is rigid and the substrate with the rough surfaces is deformable. In the latter, the upper solid with the rough surface is rigid and the lower substrates are elastic. The initial substrate in each case was cubic with edges of length L, before it was roughened. We denote the nominal contact area as A, where $A = L \times L$. The normal contact area depends on the geometry size. The real contact area A_C, formed due to asperity contact, has a profound effect on friction [155].

As the continuum theory is limited to a specific crystal structure, a simple FCC crystal with the lattice constant $a = 4.76\text{Å}$ is used. Contact occurs on the (100) surfaces of two solids. The cubic length L ranges from 64a to 512a, which approximately covers the range from 30 nm to 200 nm.

The initial substrate is cubic with six flat faces. To model contact between rough surfaces, one of its faces needs to be roughened, which means the height h(x, y) on the face changes, according to a generated self-affine rough surface. The self-affine rough surface with a rms roughness Δ, is generated by applying Voss's algorithm [156]. There are two input parameters for the algorithm: the grid spacing δ and the Hurst exponent H.

The uniform grids with spacing δ are placed on the x-y plane. At the initial step, the height of the central grid point on the x-y plane is displaced by a height, extracted from a Gaussian random variable with variance $l^H\Delta$, where l=L/2 denotes half of the diagonal distance. Then, the central point with any two neighboring corners forms four new squares. The central heights of the new squares are obtained by averaging three corner heights plus a random number with width $l^H\Delta$. Now the initial surface has been divided into four small squares with an edge length L_S=L/2. The procedure is iterated until the spacing δ reaches the input value. The self-affine surfaces generated by virtue of Voss's algorithm have the same self-affine scaling properties as well as uncorrelated roughness [153].

The Hurst exponent H is related to the fractal dimension D of the surface by D=3-H. The fractal dimension is a measure of geometry complexity, which ranges from 2 to 3. For most self-affine surfaces, H ranges from 0 to 1 [157]. The surface is rougher with a smaller H. The rough surface is in this work are generated with a Hurst exponent from 0.5 to 0.9. Different random seeds for the Gaussian random number can generate different surface topographies, so three random seeds were tested. The spacing δ for all surfaces is 2a so the number of the grids for the surface with an edge length L is $(L/2a)^2$. For the surfaces size considered in this work, the number of the grids were 32 ×32, 64×64 and 128×128.

Continuum studies show that the rms slope ∇h_0 of the rough surface has a major effect on the change of the contact area [153, 158]. As only elastic deformation is considered, values of ∇h_0 were chosen below 0.23 [154] in this thesis.

4.2.2 Mesh

Mesh generation for the deformable solid was proceeded in two steps. First, the initial cubic solid without roughness was constructed in the commercial FEM software Abaqus. Then the four-node tetrahedral elements were used to discretize it. To correspond to the generated rough surface, the top face of the solid for contact was

divided by the structured triangular elements with the length of two right-angle sides being 2a, as shown in figure 4.1(a). As the depth increases, the mesh gets coarser.

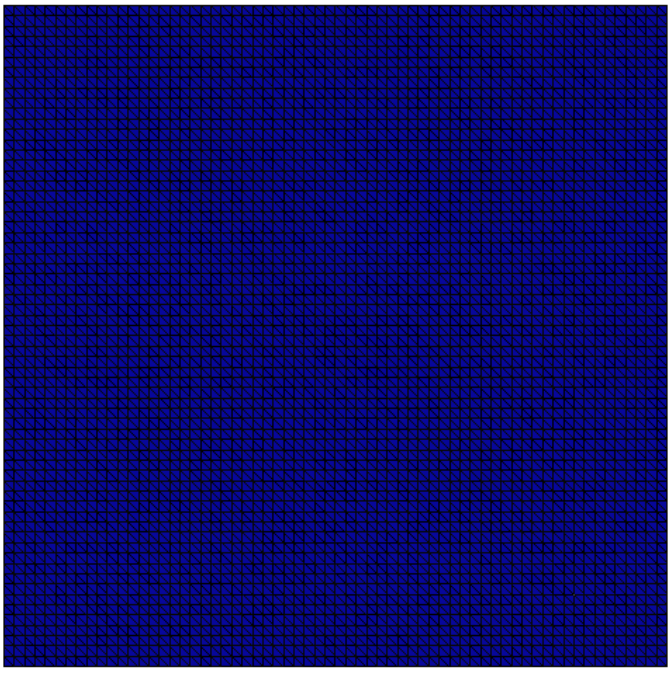

(a)

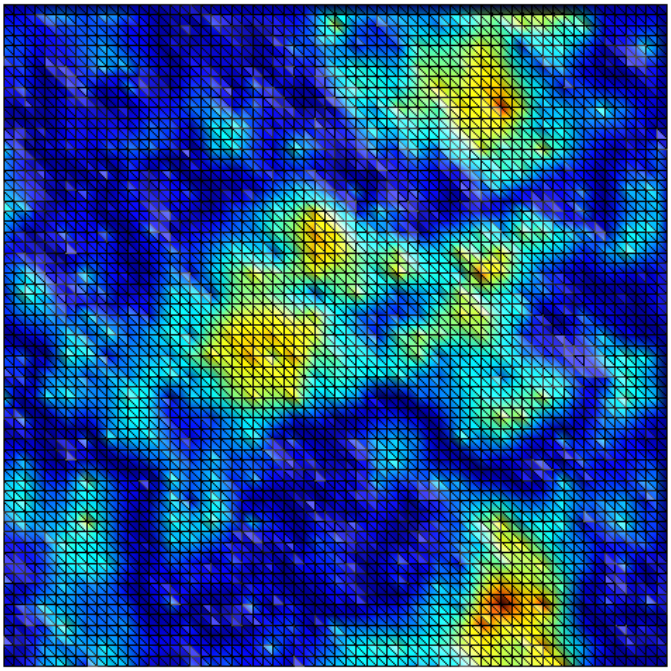

(b)

Figure 4.1: Mesh of the top surface. (a) Initial mesh; (b) After displacing the nodes (Blue indicates the valley and red indicates the high asperity).

After the initial mesh was created, the generated heights h(x, y) were imposed onto the

nodes on the top surface. As discussed in Hyun's work [153], displacing only the nodes on the top surface produced badly distorted elements. Thus, all nodes except those on the fixed surface were adjusted along the z direction. In Hyun's work, a power law was proposed in order to roughen a flat surface, as shown by equation (4.1).

$$\Delta z(x, y, z_0) = h(x, y) * (L - z_0)^6 \tag{4.1}$$

where Δz is the change in nodal height and z_0 is the initial height of the node. This power law is not applicable in this work, because our model consists of the atoms and cannot be scaled too much.

Table 4.1: Number of the nodes (N_{node}), the elements (N_{ele}) and the atoms inside the mesh (N_{atom}) for different substrate size L. The rms slope of three surfaces is 0.13.

L	N_{node}	N_{ele}	N_{atom}
64a	2773	10957	17428
128a	6945	25597	69295
256a	45210	197025	276452
512a	176182	775954	1103756

We proposed a simple interpolation method to displace the nodes below the top surface. First, each node below the top surface was projected onto a corresponding triangular element on the top surface, based on their x and y coordinates. Take one triangular element T_1 formed by nodes 1-3 and node n in figure 4.2 for an example. The projection of node n (x_n, y_n, z_n) onto the x-y plane lies in the element T_1. Then, the shape functions $N_1(x_n, y_n)$, $N_2(x_n, y_n)$ and $N_3(x_n, y_n)$, of node n were calculated. The changes in height for the three nodes, denoted as Δz_1, Δz_2 and Δz_3, were known from a generated rough surface. Thus, the height change Δz_n of node n below the element T_1 is

$$\Delta z_n = N_1(x_n, y_n)\,\Delta z_1 + N_2(x_n, y_n)\,\Delta z_2 + N_3(x_n, y_n)\,\Delta z_3 \tag{4.2}$$

After displacing the nodes, the new elements were verified in Abaqus, ensuring that

shape and size metrics of those elements were below the recommended values of element failure criteria given in table 4.2. The mesh of the top surface after displacing the nodes is shown in figure 4.1(b). Note that the bottom nodes were fixed.

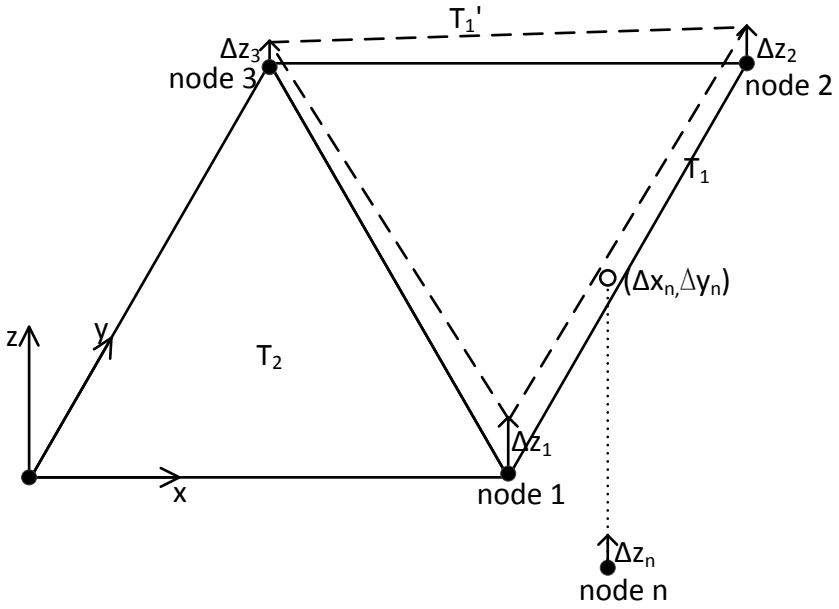

Figure 4.2: Interpolation method of displacing the nodes below the top surface.

Table 4.2: Recommended values of element failure criteria in Abaqus (> and < mean greater than and less than, respectively)

shape metrics		size metrics	
Shape factor	< 0.0001	Geometric deviation factor	> 0.2
Face corner angle	> 5	Edge length	< 0.01
Face corner angle	> 170	Edge length	> 1
Aspect ratio	> 10		

Next, the atoms on a face-centered cubic (FCC) lattice were placed into the mesh and their z-coordinates were lower than the top surface of the substrate. The mesh of a typical case used in this work is shown in figure 4.3 while the corresponding atomic structure is illustrated in figure 4.4. The length of the bottom edge is 128a in figure 4.3. The Hurst exponent for generating the rough surface with the rms slope 0.23 is 0.7. In

table 4.1, statistics of the deformation substrate with different sizes are given. For the case of 256a, the mesh and the inside atoms replace more than 50 million atoms in a fully molecular simulation, which means a significant reduction in the degrees of freedom.

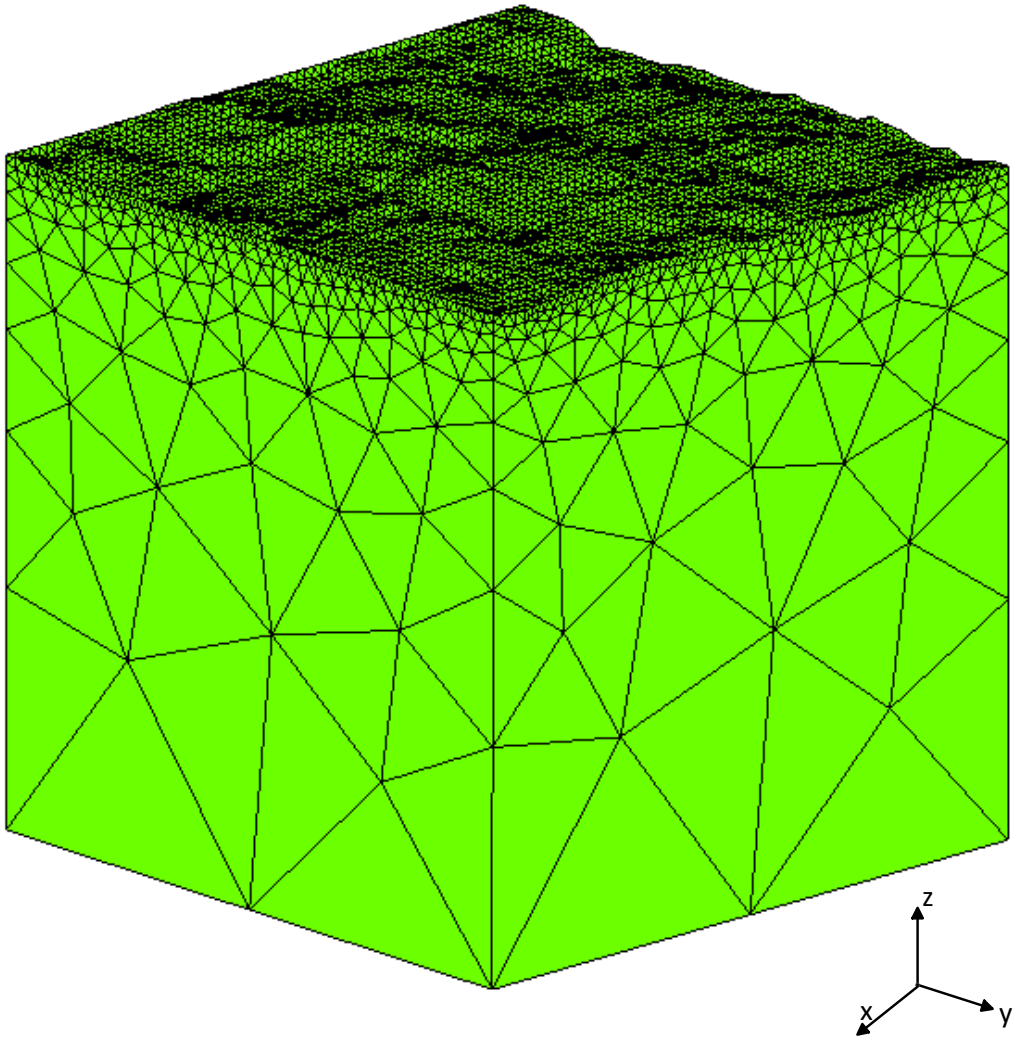

Figure 4.3: Geometry of the mesh for a deformable solid with self-affine surfaces.

4.2.3 Model set-up

As mentioned in chapter 3, the external forces that deform the solids, are obtained from the interactions of the atoms belonging to the upper and the lower solids, respectively. Those atomistic interactions between two bodies were modelled using the Lennard-Jones (LJ) potential with the characteristic binding energy ε and the

characteristic length σ. For comparisons with the previous work, the adhesion was not considered. We used $2^{1/6}\sigma$ as the cutoff radius of the LJ potential to remove the attractive force. The characteristic length σ is related to the lattice constant by $\sigma = a/2^{2/3}$. All quantities in this chapter are expressed in terms of ε, σ and the atomic mass m.

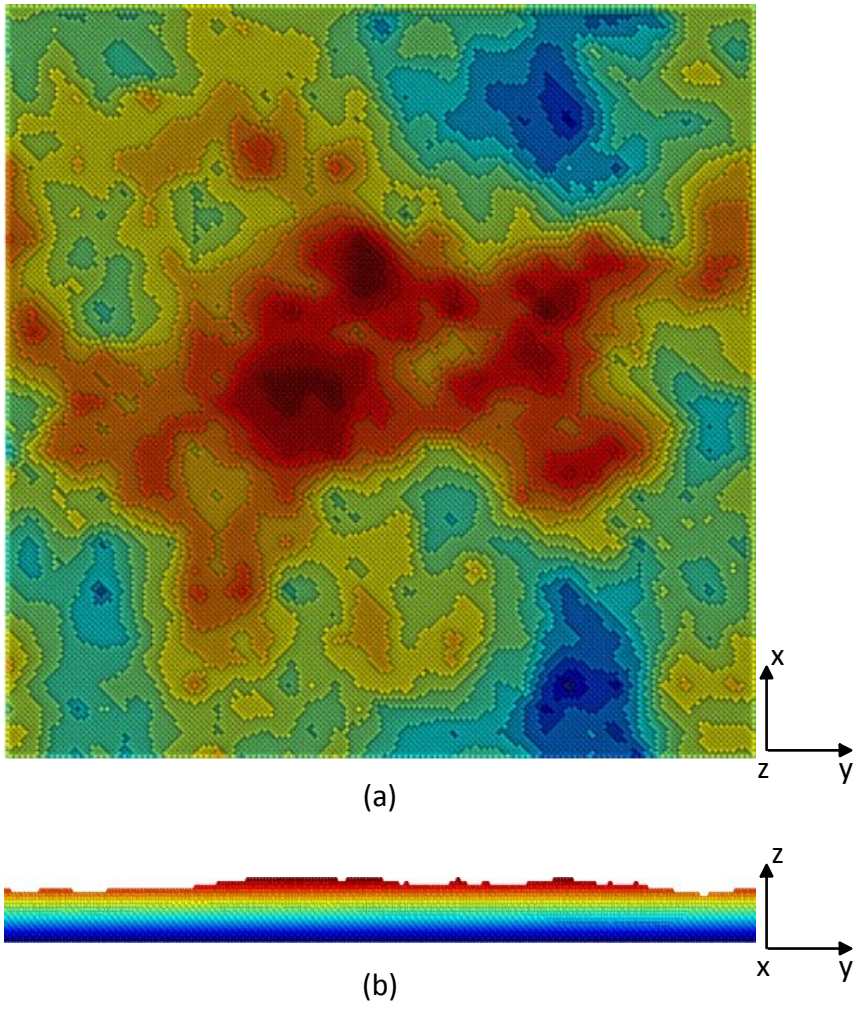

Figure 4.4: Atomic structures inside the mesh in figure 4.2. (a) Top view (b) Front view plotted with the use of Ovito [55]. The height decreases from red to blue.

Two constitutive laws (linear elasticity and Cauchy-Born rule [13]) were used to describe the relationship between stress and strain for Gaussian integration points inside each element. The elastic constants, $C_{11}=72\varepsilon\sigma^{-3}$ and $C_{12}=36\varepsilon\sigma^{-3}$, were determined by evaluating the relation between stress and strain for a small FCC crystal with the LJ potential. The characteristic binding energy ε and the characteristic length σ

were the same as the ones used to describe the interactions between the two bodies. As the cut-off radius was 1.5σ, the atoms of the crystal can only interact with their nearest-neighbors. According to equation (3.9-3.10), the Poisson ratio is 0.33 and Young's modulus $48\varepsilon\sigma^{-3}$ so the effective modulus $E^{*}= E/(1-\nu^{2}) = 54\varepsilon\sigma^{-3}$. Linear elastic constitutive law is similar to the harmonic potential that was used to model a purely elastic material in the molecular dynamics simulation [154]. To include more nonlinearly elastic deformation, the Cauchy-Born rule was also used. The atomistic interactions in the ghost crystal were described by the LJ potential with the same parameters for the small FCC crystal. Therefore, the ghost crystal consisted of a central atom and its 12 nearest-neighbors. Details about the theory and implementation of Cauchy-born rule have been discussed in section 3.1.

The Velocity Verlet algorithm [159] was used to integrate the motion of the nodes with the time step $\Delta t = 0.005t_{LJ}$, where $t_{LJ} = \sqrt{m\sigma^{2}/\varepsilon}$. The top plane was forced to compress the substrate along the z direction. The loads on the top plane were stepped. The system was allowed to equilibrate for $250t_{LJ}$ after each load. The Langevin thermostat [45] with a temperature $T=0.00001\varepsilon/k_{B}$ and the damping rate of $0.1t_{LJ}$ was used to remove a fraction of the kinetic energy of each node during the process of equilibration. All cases were run on a parallel cluster using up to 6 processors.

4.3 Normal contact

4.3.1 Flat-on-rough

The definition of an outer surface of the substrate in this thesis is similar to Luan's 2D work [154]. The atoms that formed the outer surface satisfied two conditions. First, all atoms inside the mesh are grouped based on the same (x, y) coordinates. The heights of the atoms belonging to the outer surface were the highest in each group, e.g. seven atoms as shown in figure 4.5. Second, those outer atoms do not have four near-neighbors in the adjacent and upper layer. In figure 4.5, the green atom and the

five red atoms are a part of the outer surface. However, the blue one has four neighbors above so it is not an outer atom.

The rms slope of the outer surface deviated a little from the generated surface using Voss' algorithm. For $\nabla h_0 = 0.13$ and 0.23, the rms slope ∇h_{rms} of the atomic surface is 0.11 and 0.17. For different surface length or input parameters such as the Hurst exponent, such deviation may be a little different but the difference is below 5%.

The real contact area A_c was obtained by counting atoms on the outer surface that suffered the repulsive forces from the rigid plane. Then, these atoms were projected into identical square grids with a spacing of the lattice constant on the x-y plane. The contact area was calculated by summing of the area of the grids that contain more than one atom [136].

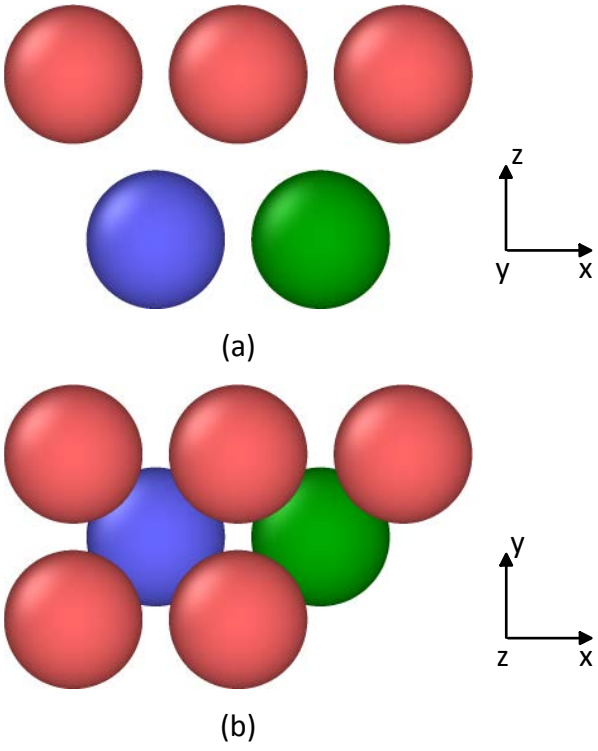

Figure 4.5: Schematic of atoms on the outer surface (a) front view; (b) top view.

Different random seeds construct different surface topographies when Voss's algorithm is used to generate the self-affine surface. Especially, the positions of the high asperities

depend on the choice of random seed [153]. It first needs to verify that the relationship between the contact area ratio and the loads are independent of the surface topography. Three random seeds named S_1, S_2 and S_3, were used to construct three surfaces with the length $L = 128a$, the rms slope $\nabla h_{rms} = 0.17$, the Hurst exponent $H = 0.7$. The linear elastic constitutive law was used in FEM. Figure 4.6 shows the relationship between the contact area ratio and the loads for three seeds. It indicates that the general trends for the three seeds are consistent with increasing loads, which is in agreement with the results of the finite element simulation [153]. The small discrepancy between the three seeds in figure 4.6 occurs due to different asperity distributions. In particular, at the first few loads, the contact area A_c depends on the heights of the highest asperity peaks. The stepped change, where A_c/A is about 0.02 in the figure, of the relationship between contact area ratio and load is due to stepped atomic structure of the substrate. As mentioned in chapter 3, the contact between the stepped tip and the substrate occurs layer by layer, leading to a discontinuous or jump increase for contact area as shown in figure 3.10(b). As the rough surface consists of many single asperities, the stepped change is observed in figure 4.6. Without further mention, all cases in this work used S_1.

It is expected that the loading and unloading curves are similar for purely elastic deformation. Our model incorporating the elastic constitutive law should be similar to the MD model using harmonic potential [150], which approximated a perfectly elastic material. A simple loading and unloading were performed to verify our model. Stepped loads were applied to the rigid plane and the system was allowed to be relaxed under each load. After that, the rigid plane was forced to move upwards at a constant speed of $0.01\sigma/t_{LJ}$. During the unloading, the positions of all atoms and the force between two bodies were recorded every $2.5t_{LJ}$.

As shown in figure 4.7, the loading and unloading curves are almost identical. This indicates that our model can simulate purely elastic materials. It seems that this method for generating mesh works well as elements were not distorted during the loading.

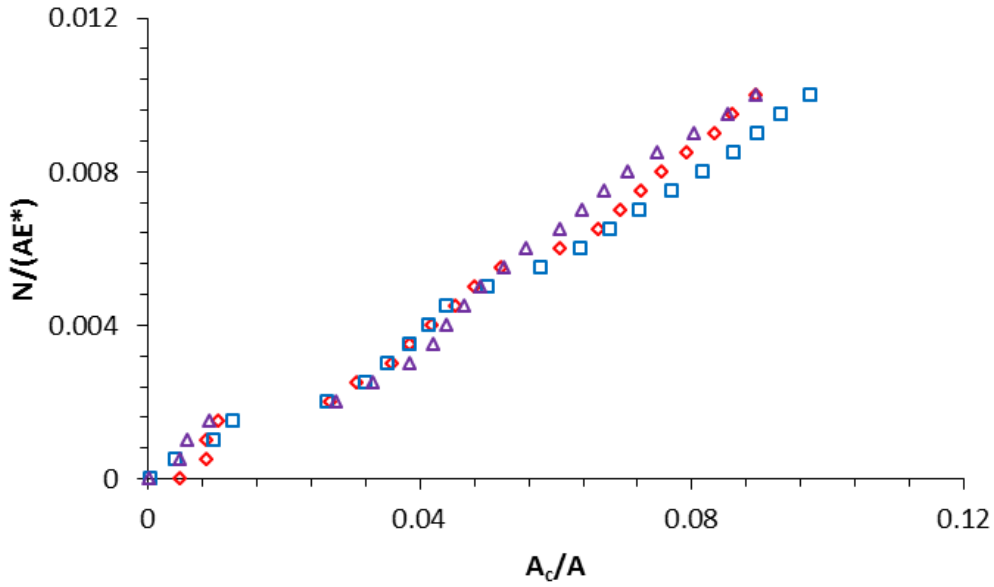

Figure 4.6: Relationship between contact area ratio A_c/A and dimensionless load $N/(AE^*)$ for three random seeds, S_1 (blue square), S_2 (red diamond) and S_3 (purple triangle).

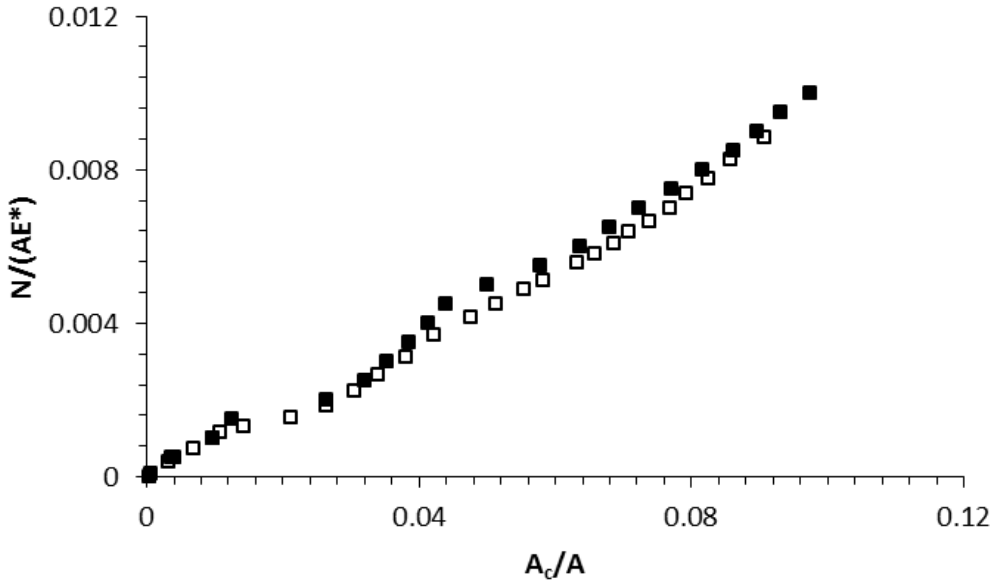

Figure 4.7: Relationship between contact area ratio A_c/A and dimensionless load $N/(AE^*)$ for loading (filled square) and unloading (open square).The length $L = 128a$ and $\nabla h_{rms} = 0.17$ for this case.

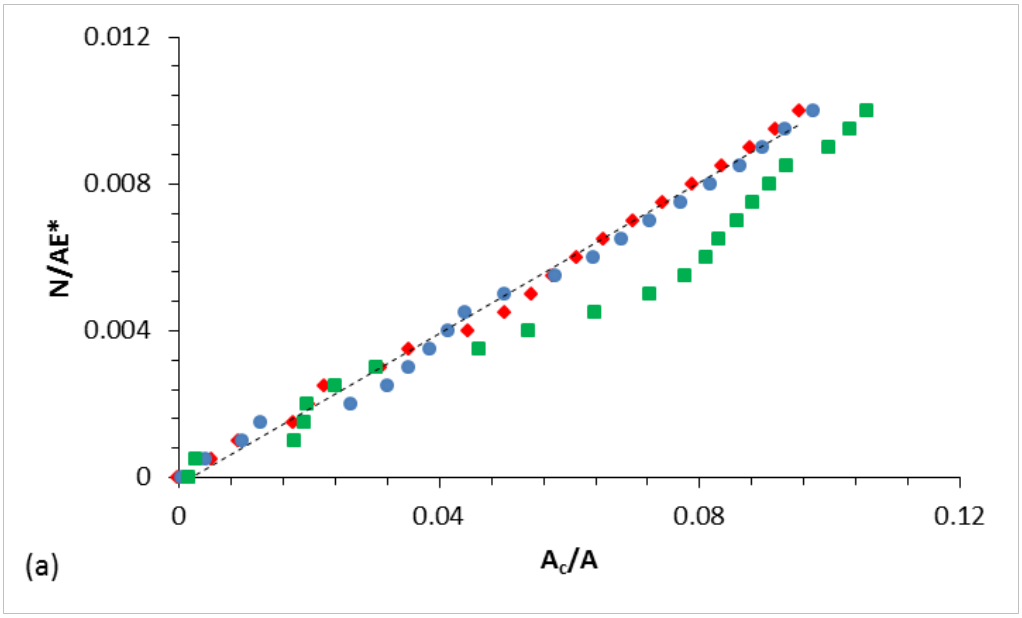

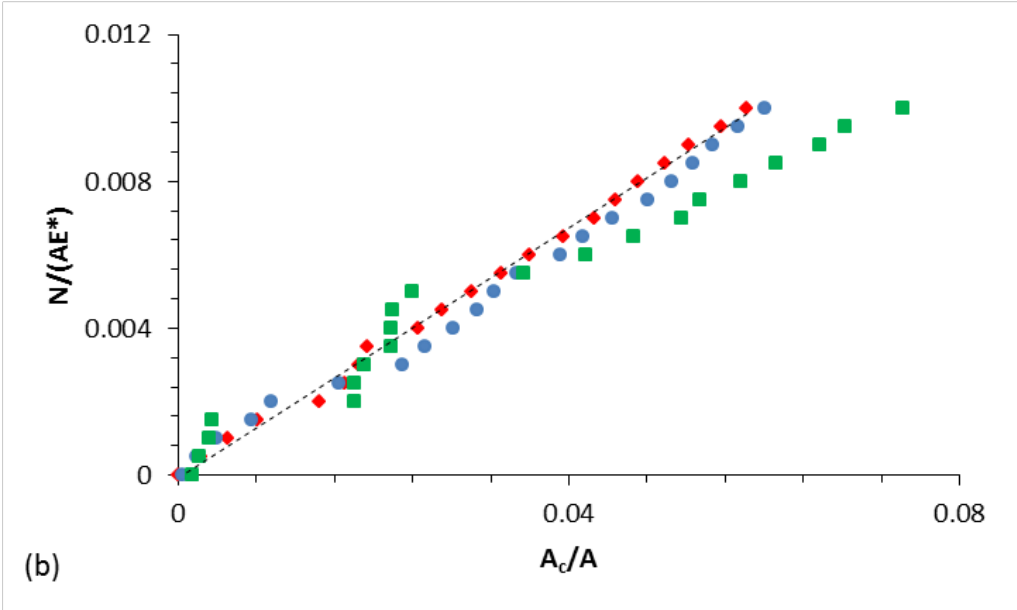

Figure 4.8: Relationship between contact area ratio A_c/A and dimensionless load $N/(AE^*)$ for different L, 64a (green square), 128a (blue circle) and 256a (red diamond). Two constitutive laws are used (a) Linear elastic (b) Cauchy-Born rule. The rms slope ∇h_{rms} is 0.17 for all cases.

The relationship between the contact area ratio A_c/A and the loads $N/(AE^*)$ for different system sizes and different constitutive laws is depicted in figure 4.8. It generally indicates that the contact area A_c varies linearly with the loads, which is consistent with the continuum prediction [17, 25]. The dashed lines in figure 4.8 (a) and (b) show best fits of the results where $L = 256a$. As the size increases, the deviations

of the results from the lines of best fit decrease and thus the linear relation between the contact area ration and the loads is more obvious. It is seen in figure 4.8 (a) that the results for L = 64a deviate significantly from the dashed line while clear deviations for L = 128 occur at small A_c/A (below 0.04). Statistical variation resulted in the deviation in figure 4.8, since too few peaks on the rough surface were in contact. In Hyun's FEM simulation [153], before the contact area ratio A_c/A reached 0.2, the results for L = 64a and L = 128a fluctuated dramatically. Such deviation were also found when the system size reached 1024a in Luan's 2D simulation [154].

Figure 4.8 (b) shows the relationship between the contact area ratio and the loads when the Cauchy-Born (CB) rule [13] is used as the constitutive law for each element in the mesh. Compared to the results in figure 4.8 (a), the real contact area with the CB rule is reduced. The material stiffness of the substrate based on linear elasticity was constant under any loads. Meanwhile, when using the CB rule, the material become stiffer in compression as the load increased. Therefore, the deformation of the substrate was less than that using linear elasticity. The linear relationship between the contact area ratio and the loads was obtained using the two constitutive laws in this work. This is consistent with the results obtained from the harmonic potential and the Lennard-Jones potential in the MD simulation for low ∇h_{rms} [154]. For high ∇h_{rms}, such as 0.46 or higher, plastic deformation which cannot be described currently by our model occurs at most loads.

In continuum studies [25, 160], it was found that the real contact area is inversely proportional to the rms slope of the surface. In this work, the effects of the rms slope ∇h_{rms} were also studied. Figure 4.9 shows the relation between the contact area ratio A_c/A and dimensionless loads $N/(AE^*)$ for ∇h_{rms}= 0.11 and 0.17. The dashed lines are linear fits for the results. When the system size L = 256a, the slope of the curve for ∇h_{rms} = 0.17 (open diamond) is larger than that of ∇h_{rms} = 0.11 (filled square). Asperities on the surface with high ∇h_{rms} are prominent and sharp. Conversely, asperities on the surface with low ∇h_{rms} are low and blunt. Therefore, few asperities on the flatter surface have sufficient atoms to support the top plane. Meanwhile, due to

their bluntness, the area in contact was relatively large.

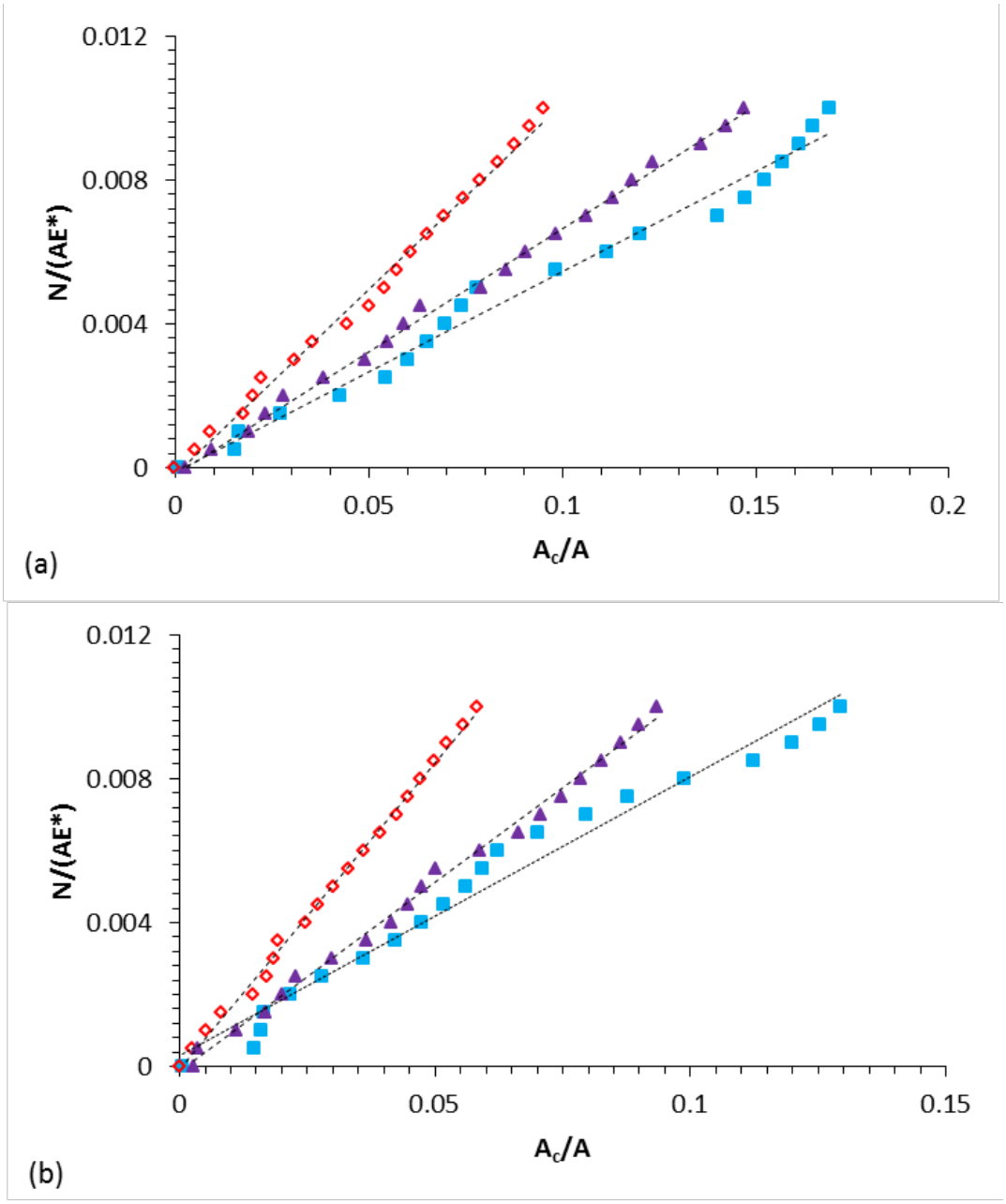

Figure 4.9: Relationship between contact area ratio A_c/A and dimensionless load $N/(AE^*)$ for different ∇h_{rms}, 0.11 (filled symbols) and 0.17 (open symbols). Two constitutive laws are used (a) Linear elastic (b) Cauchy-Born rule. Red diamond indicates the length $L = 256a$. Purple triangle and blue square show 512a and 256a, respectively.

Moreover, figure 4.9 (a) shows significant deviation from the fitting line for the flatter surface of L = 256a, which indicates that the number of the asperities in contact was too small based on the discussion in figure 4.8. The deviations were considerably reduced

when the system size reached 512a (filled triangle). Seemingly, it requires larger system sizes to converge the relation between the contact area and the loads for different roughness. A comparison between figure 4.9 (a) and figure 4.9 (b) indicates that the real contact area with the Cauchy-Born rule is reduced for the flatter surface as well.

The average pressure is defined as $\bar{p}= N/A_c$ [17]. The linear relationship between the contact area and the loads shown in figure 4.7 indicates that $\bar{p}$ is not dependent on the load. Based on the continuum analysis [25, 160, 161], the average pressure $\bar{p}$ is proportional to the rms slope ∇h_{rms}. The relationship between $\bar{p}$ and ∇h_{rms} is given in equation (4.3).

$$\frac{\bar{p}}{E^*} = \frac{\nabla h_{rms}}{\kappa} \tag{4.3}$$

where E^* is the effective young's modulus and κ is a constant [161].

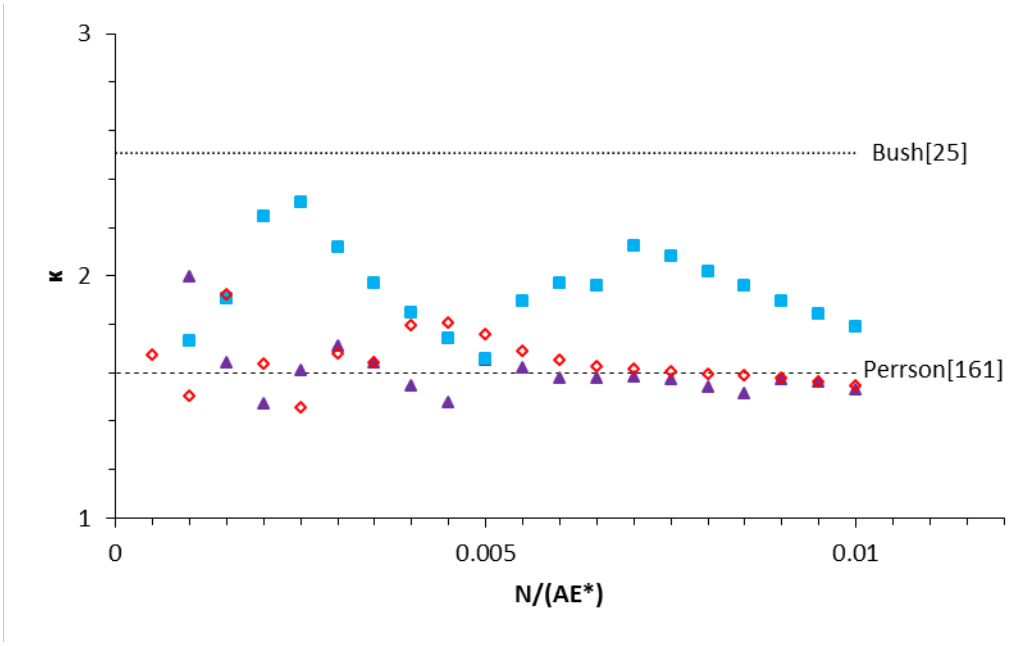

Figure 4.10: Ratio κ as a function of dimensionless loads $N/(AE^*)$ for the same cases shown in figure 4.8 (a). Dashed line and dotted line indicate the constants 1.6 and 2.51 predicted by Perrson [161] and Bush et al [25] in continuum mechanics studies.

The constant $\kappa = E^*\nabla h_{rms}A_c/N$, predicted by the continuum work ranged

approximately from 1.6 [161] to 2.51 [25]. Due to the lack of dimensionality in Luan's MD simulation [154], the value of κ was relatively large, exceeding 10. In our work, when the load N was larger than 0.007 AE*, the results (red diamond and purple triangle) are close to but a little below Perrson's prediction [161] as shown in figure 4.10. Due to the in-phase movement of the atoms inside the FEM element as mentioned in Chapter 3, the real contact area A_c obtained by our model was relatively small. Therefore, if the condition of atom movement within FEM elements can be relaxed and resulting in a larger A_c, the constant κ at the nanoscale could be larger than the value predicted by our model.

4.3.2 Rough-on-rough

Continuum mechanics [17] predicts that the contact between two surfaces, where the root-mean-square(rms) slopes ∇h_1 and ∇h_2 are equivalent to the contact between a flat surface and a rough surface with the effective slope $\nabla h^* = \left(\nabla h_1{}^2 + \nabla h_2{}^2\right)^{1/2}$. It is not clear if this prediction is applicable to the nanoscale contacts in 3D. With the results of the flat-on-rough contacts in the last section, we carry out the simulations of the rough-on-rough contacts and make comparisons of the two in this section.

Figure 4.11 shows that the relationship between the contact area ratio A_c/A and the loads $N/(AE^*)$ for rough-on-rough (filled symbols) contacts is linear for different roughnesses at large loads. Peter et al [73] performed MD simulations to study the contacts between two bulk bodies with the rough surfaces. However, as they only applied five loads, the relation between A_c/A and $N/(AE^*)$ was not clear. Furthermore, their system size was only 32a. The real contact area A_c decreases with increased rms slope ∇h_{rms} in flat-on-rough contacts. This relationship still works in the rough-on-rough contacts. Moreover, the real contact area A_c of two rough surfaces with ∇h_{rms}= 0.17 (blue filled squares) in figure 4.11 (b) is smaller than that of the two with ∇h_{rms}= 0.11 (red filled squares) in figure 4.11 (a). In figure 4.11, contact area is constant at small loads (below $0.0012N/(AE^*)$). The shape of the rough surface is

terraced. The top plane is first in contact with several highest surface atoms on the substrate surface. As these atoms can support the top plane at the aforementioned small loads, the contact area is not changed. It is expected that more of these atoms can support larger loads.

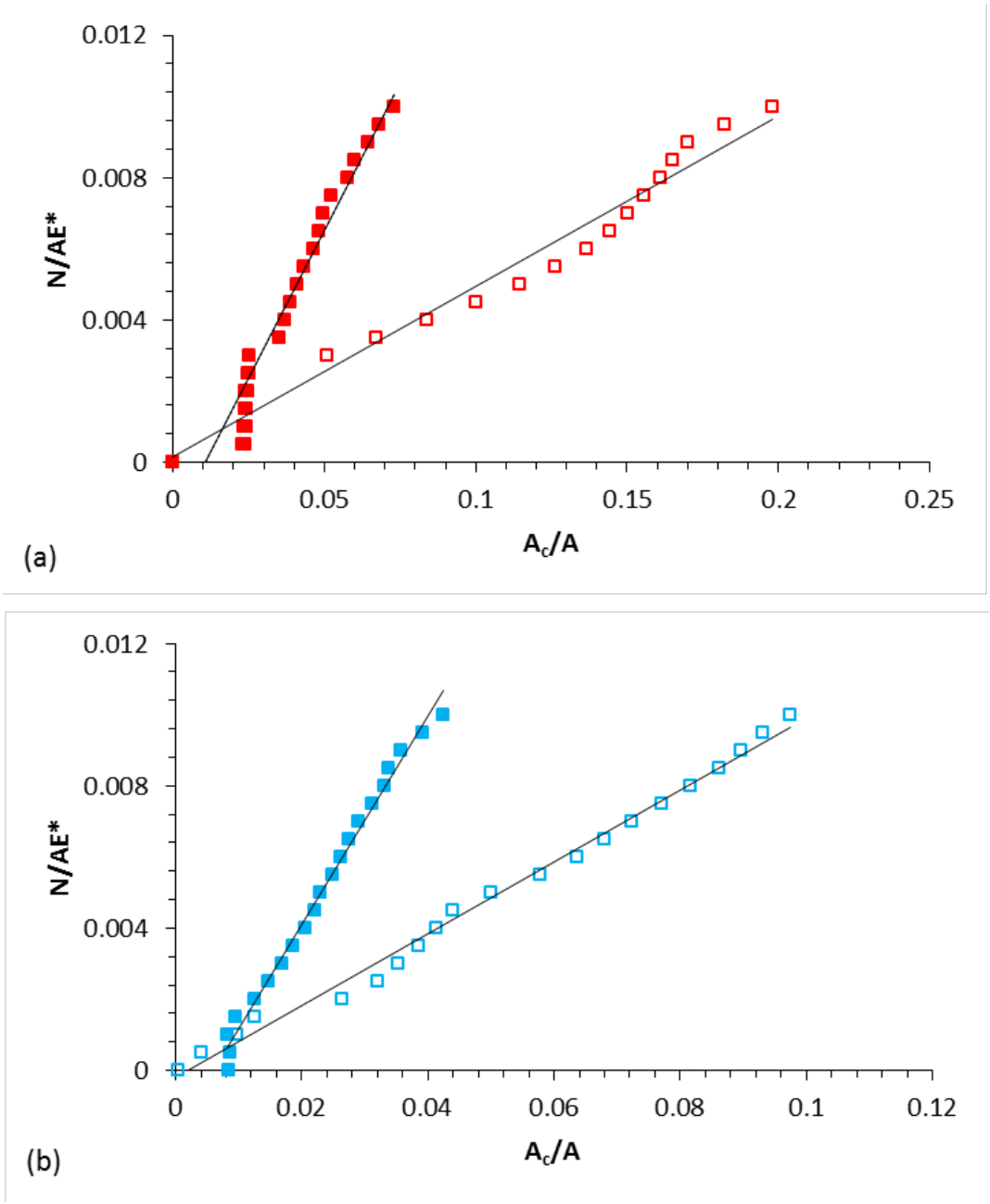

Figure 4.11: Relationship between contact area ratio and load for flat-on-rough (open squares) and rough-on-rough (filled squares). The rms slope of the rough surface is (a) ∇h_{rms}= 0.11; (b) ∇h_{rms}= 0.17. The system size L is 128a for all cases. Solid lines are the linear fits.

Compared to the flat-on-rough contacts (open symbols) in figure 4.11, the real contact area of the rough-on-rough contacts (filled symbols) dropped. The slope ratio of the fit between rough-on-rough and flat-on-rough for ∇h_{rms}= 0.11 is 3.4 while for ∇h_{rms}= 0.17 it is about 3.0. However, according to the continuum prediction, the ratio is approximately 1.414. One possible factor for the discrepancy between our results and the continuum prediction is the system size. In figure 4.12, it shows the relation between A_c/A and $N/(AE^*)$ for the system size L = 256a. In figure 4.12, the slope ratio of the fit for ∇h_{rms}= 0.11 is 2.4 while for ∇h_{rms}= 0.17 it is about 2.2. We also tested the system size L = 512a and ∇h_{rms}= 0.11, where the ratio is close to 2.3. It seems that the slope ratio for different roughnesses converged to a scaling value, like 1.414 that was predicted by the continuum theory. A comparison between the ratio obtained here and 1.7 from Luan et al [154] indicated that the deviation from the continuum prediction is related to the system size and not to the dimension. Compared to 128a, the results for 256a are closer to but still deviate from 1.414.

In the continuum theory, frictionless contact during the compression required as a prior condition for equivalence between rough-on-rough and flat-on-rough contacts. However, finite friction forces were observed when using our model in rough-on-rough contacts, which may be a reason for the deviations.

Another factor for the discrepancy between the results in this thesis and the continuum prediction originated from the change in the commensurability of two surfaces after deformation. For the commensurate surfaces considered in this work, at small loads, the atoms on the top rigid plane sit in interstitial positions between any two atoms where the interaction forces are smallest. However, the spacing between the two nearest-neighbor atoms on the rigid plane was not changed while it varied with the loads on the substrate. Consequently, some atoms on the rigid plane sit directly above the atoms on the substrate and usually were subjected to the large forces. Those atomic forces played a major role in supporting the top plane. Meanwhile, the number of the atoms in contact, or the real contact area, was reduced.

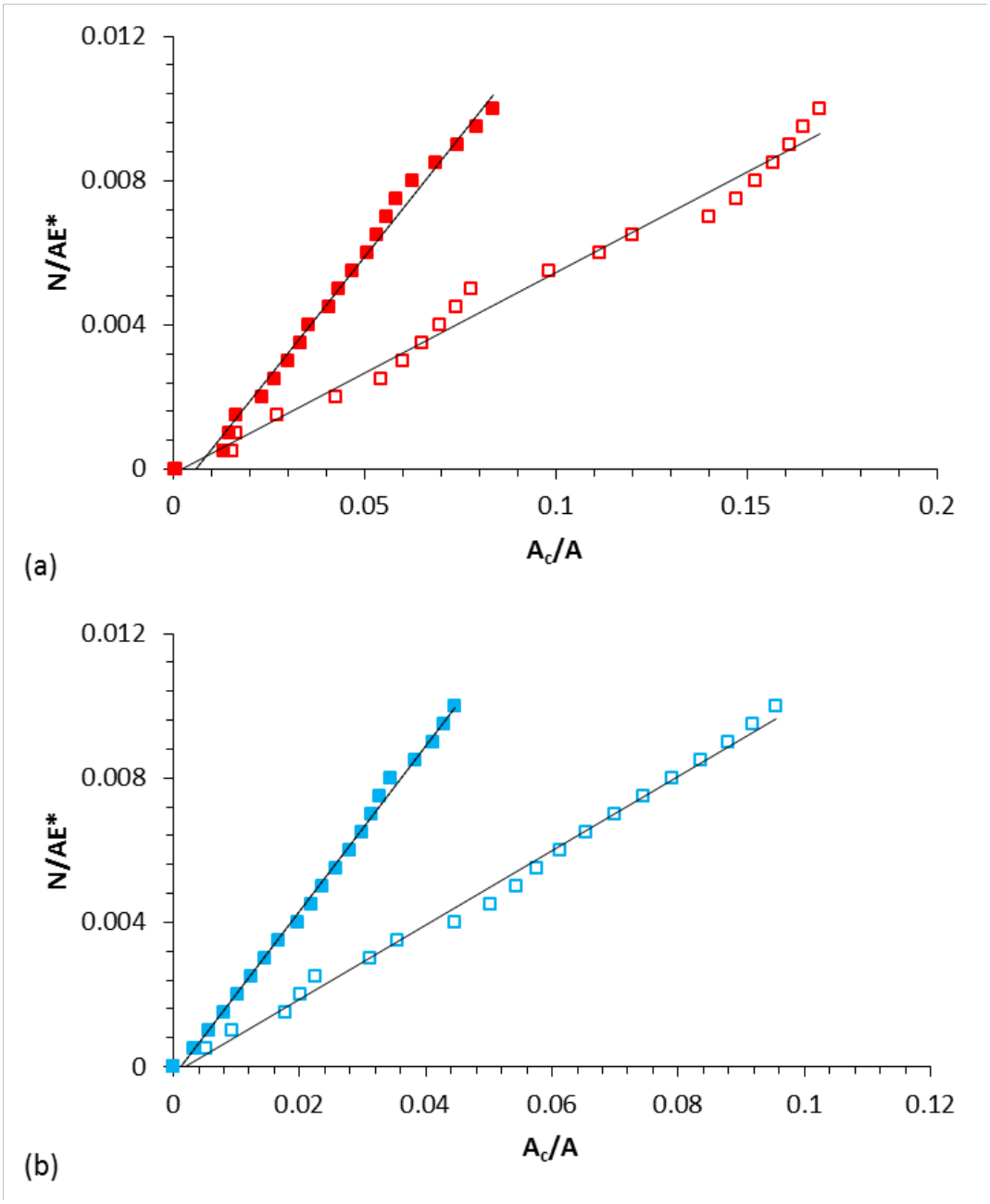

Figure 4.12: Relation between contact area ratio and load for flat-on-rough (open squares) and rough-on-rough (filled squares). The rms slope of the rough surface is (a) $\nabla h_{rms} = 0.11$; (b) $\nabla h_{rms} = 0.17$. The system size L is 256a for all cases. Solid lines are the linear fits.

Furthermore, the friction force mentioned above mainly originated from those atomic forces. Based on the larger friction forces in rough-on-rough contacts, it seems that the change in the commensurability had a more significant influence on rough-on-rough contacts than flat-on-rough contacts. It must be noted the commensurability change cannot be avoided in the MD simulation. Yet, the atoms in MD move freely on the

surface and can find positions with relatively low potential energy to reduce the local forces to some extent. However, it was difficult for the atoms in our model to find the appropriate positions because their positions were determined by the positions of the elements, especially when there are several contacting atoms in one element.

4.4 Summary

The multiscale model proposed in Chapter 3 has been used to perform 3D simulations of the flat-on-rough contacts and the rough-on-rough contacts. The effects of the system size on the relationship between the contact area and load were studied. By virtue of the multiscale model, the largest system size reached approximately 243nm. For a direct comparison with the continuum theory, the root-mean-square (rms) slope was used to describe the surface roughness. Roles of the rms slope in normal contact between the rough surfaces were presented. The main findings in this chapter are listed below.

The real contact area is proportional to the loads in the system of different sizes considered. The slope of the linear relation varies with the system size. However, when the system sizes are larger than a threshold, the linear relation converges to one line and the threshold changes with different surface roughness. For ∇h_{rms} = 0.11 and 0.17, the corresponding thresholds are 256a and 512a, respectively. In the previous 2D work [154], this value was 1024a.

The constant $\kappa = E^{*}\nabla h_{rms}A_c/N$ calculated from the converged results is close to Perrson's prediction κ = 1.6 [161]. If the constraint of in phase movements of the atoms within the FEM elements is relaxed and produced a higher contact area, the constant κ at nanoscale would lie between κ = 1.6 and 2.51 [25].

The variation in the rms slope has a significant effect on the real contact area in both flat-on-rough and rough-on-rough contacts. The decrease of the rms slope increases the real contact area, which is in agreement with the continuum prediction. Besides, for

rough-on-rough contacts, a clearly linear relationship between contact area and load was obtained. However, in our work, the slope of the fitting line for the relations between the contact area and load in rough-on-rough contact is about 2.2~2.3 times larger than in the flat-on-rough contact, which deviates from 1.414 predicted by the continuum theory. The possible factors for such discrepancy were discussed above.

Although the acceptable results were obtained by using our model, there are still some limitations. The simple interpolation method mentioned in section 4.2.2 for roughening mesh is not appropriate for all generated rough surfaces from Voss's algorithm [156]. Therefore, we only considered the rough surfaces with $\nabla h_0 \leq 0.23$ in this work. For creating the rougher mesh, a new mesh generation method is required. In addition, the plastic deformation of the rougher surfaces is beyond the scope of this chapter, and is not considered in this model.

Chapter 5: A finite temperature hybrid simulation method

Based on the results in the previous chapters, DAMAS has demonstrated the advantages of computational efficiency and acceptable accuracy. However, DAMAS is limited to study nanoscale contacts with small deformation and at low temperature (close to zero Kelvin).

DAMAS has been used to study elastic nanocontacts in Chapter 3. The constitutive law of FEM is fitted for purely elastic deformation with small strain, so the defects, such as dislocation nucleation, are not generated. Moreover, in the scheme of DAMAS, the atoms in the region near the free surface are positioned inside the elements. The atoms in each element move in phase because their displacements are interpolated from the nodal displacements. Such in-phase movement prevents dislocation and the reshuffling of the atoms at the free surface.

The in-phase movement of the atoms in each element has another side effect at finite temperatures. Those constrained atoms have the same vibrational frequency as the element. The frequency of the element, however, is lower than that of single atom in molecular dynamics (MD) at finite temperatures. The frequency deviation between them rises with an increased element size. Such deviation has been shown in 1D case [133] by plotting the dispersion curve which gives the dependence of the frequency on the wave number [162]. Therefore, DAMAS is appropriate for low temperature problems where the atoms hardly vibrate.

Because of the limitations of DAMAS, a hybrid simulation method (HSM) proposed by Luan et al [101] is used to study nanoscale contacts with consideration of plasticity and the effect of the temperature in this section. HSM was limited to study the problems at zero Kelvin in original work but it will be given an analysis at a higher finite temperature in this chapter. This chapter consists of three parts. In the first part, basic coupling principle and software implementation of HSM are presented. The HSM is validated at zero Kelvin in the second section. Finally, the HSM is studied at

the temperatures of hundreds of Kelvins in the third section.

5.1 Introduction

Luan et al [101] proposed a hybrid simulation method (HSM), which combines molecular dynamics with finite element method. It is one of the force-based multiscale methods due to the lack of well-defined total energy [98]. The HSM has proved to be effective and reliable for contact problems, such as 2D contact between rough surfaces [101, 154], 2D sliding contacts of textured surfaces [163], 3D nanoindentation and nanoscratch [164]. It must be pointed out that the nodal movement was integrated by static Newton-Raphson method [98, 163] while an explicit second-order Newmark method was employed in original HSM and others' work.

The HSM consists of three parts, which include an atomistic region, a continuum region and a coupling region. The defects due to the atomic movement can occur in the atomistic region. Although the number of the atoms increases considerably compared to DAMAS, the computational speed of the HSM is high. For a relatively small system, the cost of computation time of the HSM was only 1/20 of the full MD simulation [101] and 1/7 [164]. In the following, the atomistic and continuum regions as well as strategy of coupling the two regions will be briefly described.

5.1.1 Atomistic region

The atomistic region plays an important role in the HSM. For nanocontacts, external interactions always occur on the atomistic region first. It is also a container within which dislocations or other defects are generated and propagated. In the HSM, the atomistic region consists of two types of atoms, which play different roles. One is the free atom, and the other is the padding atoms [98]. Their differences are discussed in a later section about the coupling. This section focuses on the free atoms.

The interactions between the free atoms are calculated by the embedded atom method (EAM) potential [43]. In Luan's work, the Lennard-Jones (LJ) potential is used to drive the free atoms in the atomistic region. The LJ potential is a typical two-body potential, which has an advantage of low cost. However, the EAM potential is more appropriate for mental than two body potential. The non-adhesive interactions between two surfaces are still described by the LJ potential with different parameters because it is easy to remove adhesive effect and change the binding energy.

The equations of atomistic motion are integrated with the Velocity-Verlet algorithm. The temperature is controlled by a Langevin thermostat [45] with a damping rate (50 time units in this chapter) determined from trial and error.

5.1.2 Continuum region

The size of the mesh in the FEM is not refined to the atomic separation, which is one of the most significant advantages compared to the quasicontinuum (QC) method [13] and the coupled atomist/discrete dislocation (CADD) model [122]. Triangular elements in 2D and tetrahedron elements in 3D are used to divide the continuum region, respectively. All elements are linear. The FE region is usually set up far away from the region of large deformation but its position depends on the constitutive law and the continuous displacement field. A linear constitutive law is adequate if the FEM is located in a small strain region. However, the computational time will increase considerably due to the additional atoms included. In the original work [101], a non-linear constitutive law for FEM was used in an independent MD simulation at low temperature (close to 0K). In this work, the Cauchy-Born rule presented in section 3.1.2 is used and linear elastic constitutive law is employed as well.

As in the MD simulations, the periodic boundaries conditions are applied. The nodal motion is integrated by the explicit Velocity-Verlet algorithm [44] in this work. To remove the fraction of the kinetic energy of each node, the Langevin thermostat [45] is added to the nodal equations. The damping rate is identical to that applied in the MD

region.

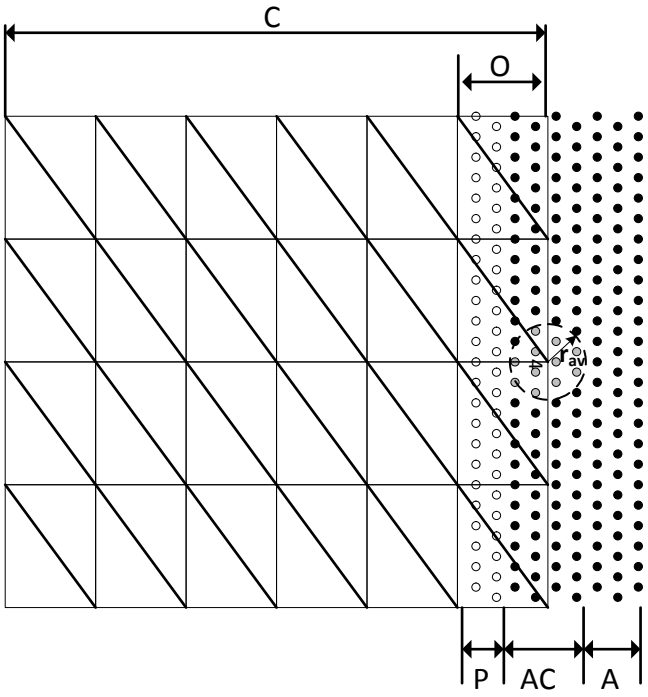

Figure 5.1: Coupling scheme of the HSM in 2D. C denotes the FEM region while A is the atomistic region. The coupling region O overlaps with the padding region P and the averaging region AC.

5.1.3 Coupling region

The coupling between FEM and MD is achieved through the information exchange of the displacements. In figure 5.1, the boundary atoms or the pad atoms in *P* indicated by open circle provide the physical boundary for *AC* and *A* shown by filled circle. Each boundary atom is adhered to the element which contains it. In other words, the displacement **u** of the boundary atom is interpolated from the nodal displacements **d** of the corresponding elements.

$$\mathbf{u}_\beta = \sum_{j=1}^{m_{\mathbf{nodes}}} \mathbf{N}_j \mathbf{d}_j \tag{5.1}$$

where **N** is the shape function of atom β corresponding to the nodes in each element.

m_{nodes} is the number of the nodes in each element. The displacements of the boundary nodes are determined by a weighted averaging method, which relaxes the condition of the strong compatibility [98]. In figure 5.1, one of the boundary nodes in *AC* within big dashed circle is taken as an example. Its displacement is determined by weighted averaging the displacements of the free atoms (grep solid circles) within a circle of radius r_{av} (called the averaging circle in the following).

$$\mathbf{d_i} = \sum_{\alpha=1}^{n_{atoms}} \omega_\alpha \mathbf{u}_\alpha \tag{5.2}$$

where n_{atoms} is the number of the atoms in the average circle for node i. The weight ω of each atom within the averaging circle can be calculated by a weighting function [98]. The weighting function used in this work is

$$\omega(\mathrm{d}) = \begin{cases} 1 - 3d^2 + 2d^3, & d < 1 \\ 0, & d \geq 1 \end{cases} \tag{5.3}$$

where $\mathrm{d} = \mathrm{r}/\mathrm{r}_{av}$ and r is the distance between the atom within the average circle and the node. Other weighting function has also been tried, but they showed little difference to the final results. Note the averaging circle will be a sphere in 3D case.

5.1.4 Software implementation

Before the implementation of the Hybrid simulation method (HSM), DAMAS in the third chapter is reviewed. Since the architecture of DAMAS is efficient, the HSM could be implemented based on DAMAS.

In DAMAS, a parallel FEM solver calls other libraries and calculates all the continuum data. LAMMPS [51] handles atomistic information. The coupling between molecular dynamics (MD) and FEM is achieved through extrapolating forces and interpolating displacements of atoms which overlap with the mesh. In the HSM, only displacement data transfers between MD and FEM, which results in a different

implementation from DAMAS. Moreover, for any typical cases, the number of the atoms of the HSM is much more than that in DAMAS, which means MPI is also needed for the HSM. At the same time, the number of the elements is vastly different. For the HSM, it is seemingly sufficient for one processor to handle the continuum information while other processors perform the detailed calculation of the atoms. One example of such parallel strategy is in the implementation of the bridging domain method (BD), where one processor was used to calculate finite element while 32 processors were dedicated to MD [136]. METIS [145] is used to partition the continuum domain. DAMAS distributes the data to the processors using MPI based on the partitioning setup by METIS.

Despite of the differences, many parts of DAMAS could be transplanted to the program of the HSM. For instance, the main change in the FEM solver is the methodology to impose the boundary condition on the nodes in the circular domain *O* in figure 5.1. Other parts, such as the constitutive law, nodal integration and output, still work for the HSM. In the next sections, attention is paid more to the coupling implementation and parallel implementation.

5.1.4.1 Coupling implementation

The coupling of the HSM includes two-way information exchange. From FEM to MD, the displacement of the pad atom in coupling area is interpolated from the nodal displacements. From MD to FEM, the displacement of the boundary nodes is obtained by averaging the displacement of the atoms within the specified distance.

From FEM to MD, it is most important to determine the shape functions of the pad atoms based on their initial positions. It is easy to handle the shape functions when only one processor is used, because the number of the atoms is constant on that processor. A complication is that the atoms will dynamically move between processors via LAMMPS when more than one processor is used. The approach of DAMAS is used here. Instead of counting local atoms, the elements-atoms mapping

and shape functions are copied to all processors [141].

From MD to FEM, it takes three steps before implementation. Firstly, the boundary nodes are found inside the circular domain O in figure 5.1. It usually happens that the boundary nodes are located in different processors. However, different from the atoms transfer, the IDs and the number of the nodes are not changed on each processor. Secondly, for each boundary node, the atoms within its average circle are searched based on the given radius. After the node-atom groups are established, finally, the distance weight for each atom is calculated and stored in a weighting matrix. The ID of each row of the weight matrix corresponds to the ID of a boundary node while the ID of each column corresponds to a neighbor atom. Each item of the weighting matrix is the weight of the corresponding atom. After calculation, the weighting matrix is decomposed in rows and distributed to the processors according to the IDs of the boundary nodes.

With the key components of the coupling, the whole loop can be briefly described like:

(1) run LAMMPS to obtain the atomistic displacement;

(2) calculate the displacements of the boundary nodes according to equation (5.3);

(3) solve the nodal equation with the displacement boundary condition from (2);

(4) interpolate the displacement of the pad atoms according to equation (5.2);

(5) go to step (1);

5.1.4.2 Parallel implementation

To increase calculation speed, the code of the HSM was written in parallel C using MPI. In terms of degrees of freedom, the HSM features less finite elements and more atoms compared to DAMAS. With such differences, it is worth considering the role of the processor distribution. In DAMAS, all processors are dedicated to both finite elements and atoms. For the HSM, three different implementations are performed for comparisons, named Imp 1, Imp 2 and Imp 3, respectively.

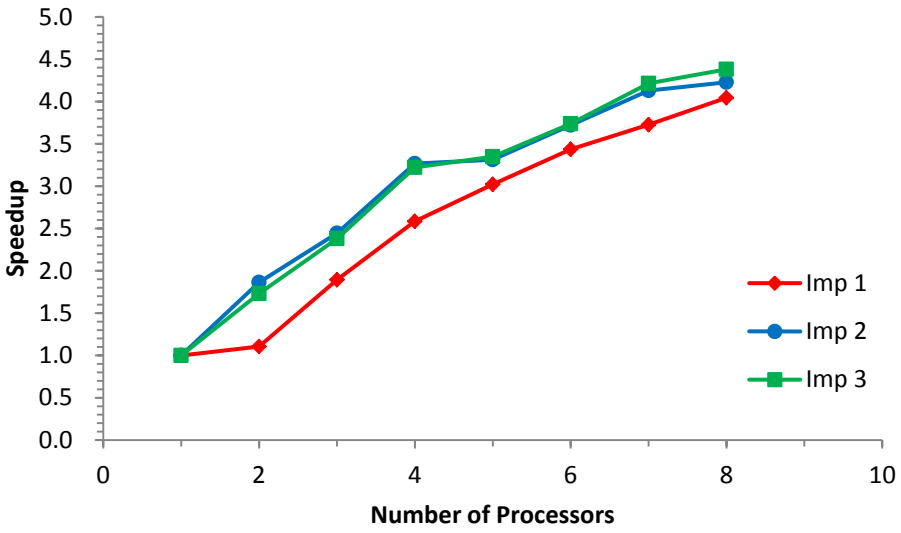

Figure 5.2: Speedup as a function of the number of processors for three implementations.

Imp 1: The master processor only handles the FEM while other processors run LAMMPS to obtain atomistic information. No partition of the FEM domain is used.

Imp 2: All processors run LAMMPS to obtain atomistic information while one of them handles the FEM. No partition of the FEM domain is used.

Imp 3: All processors perform both the FEM and LAMMPS. The FEM domain is partitioned. This implementation is used by DAMAS.

To compare the parallel performance of all three implementations, a simple case, of the contact between a rigid plane and a deformable substrate was used. The size of the substrate is $32a \times 32a \times 96a$ (a is the lattice constant). The number of total atoms is 85711 while the number of elements and nodes is 6912 and 1539, respectively. A linear constitutive law was used to describe the relationship between stress and strain in FEM. An EAM potential was applied to calculate the interactions between the atoms in the substrate while LJ potential was used for the interactions between the top rigid plane and the substrate. The width of the coupling region was 4a along the z direction. The average radius for the boundary nodes in the coupling region was 4a. The rigid plane applied a constant force on the substrate. The simulation ran 5000 steps. The maximum number of the processors on each node of the cluster was 8.

Table 5.1: Computation time (wall time) ratio with respect to Imp 1 for the different number of the processors

Processors	Imp 1/ Imp 1	Imp 2/Imp 1	Imp 3/Imp 1
1	1.000	1.000	0.909
2	1.000	0.593	0.580
3	1.000	0.775	0.723
4	1.000	0.791	0.729
5	1.000	0.912	0.820
6	1.000	0.923	0.835
7	1.000	0.902	0.803
8	1.000	0.957	0.839

Figure 5.2 shows the relationship between the speedup and the number of processors for different implementations. Firstly, the speedup increases with the number of the processors for all. The speedup of Imp 2 and Imp 3 are much closer. The decomposition of the elements and the nodes via METIS has little effect on the speedup because the communication time between processors is comparable to the saved calculation time when the continuum region is relatively small. In terms of Imp 1, when the number of the processors increases from one to two, a little calculation time was saved because two processors are dedicated to respective jobs. However, at the same time, the communication time between them increased. After that, the speedup of Imp 1 continuously rises with the number of the processors to 4.04 at 8 processors. The maximum speedups of Imp 2 and Imp 3 are 4.227 and 4.381, respectively. From the point of view of parallel efficiency, Imp 2 and Imp 3 are better than Imp 1 since their speedups are all higher than that of Imp 1.

The computation time ratio of Imp 2/Imp 1 and Imp 3/Imp 1 is given in table 5.1. Both Imp 2 and Imp 3 require less computational time than Imp 1 when using more than one processor. As clearly shown in the table, Imp 3 is superior to Imp 2. Imp 3 is the best implementation compared to other two implementations. Without further

mention, Imp 3 is used to perform the HSM simulations in this thesis. Note that other cases have also been tested in order to compare the three implementations. Although there was a little difference, the conclusion is not changed.

5.2 Validation at zero Kelvin

In the previous sections, the coupling scheme and software implementation of the hybrid simulation method (HSM) in 3D were introduced. To validate the coupling method in 3D and the code, static simulations were performed in this section. Results from the multiscale scheme are benchmarked against molecular dynamics simulation. In order to validate the static properties of the model, Hertz contact with adhesion is performed and compared against other multiscale methods [101, 165].

5.2.1 Simulation presentation

The aim of this section is to validate the multiscale model through single asperity contact with adhesion considering of two aspects, namely contact parameters at the surface and stress continuity in the coupling area. The self-developed code proposed in section 5.1.4 was used to perform the simulations. Each simulation was run by 8 processors on a parallel cluster.

Prior to the validation, the multiscale (MU) simulation and pure MD simulation are briefly discussed. The geometry of the MU simulation follows Anciaux and Molinali's work [165]. In figure 5.3, the filled atoms and the open atoms are free and padded, respectively. The tip is rigid and stepped, which was obtained by cutting a FCC crystal according to a sphere whose radius equals 50a. The size of the substrate is $90a \times 90a \times 110a$, which corresponds to 3564000 atoms in MD simulation while the substrate in figure 5.3 is composed of 567000 atoms, 32674 nodes and 178200 elements. Thus, the multiscale model considerably reduces the degree of freedom. In this work, four-node tetrahedral elements were used. The top surface of the substrate was free and the bottom of the continuum region was fixed. Along both x and y

directions, periodic boundary conditions were applied.

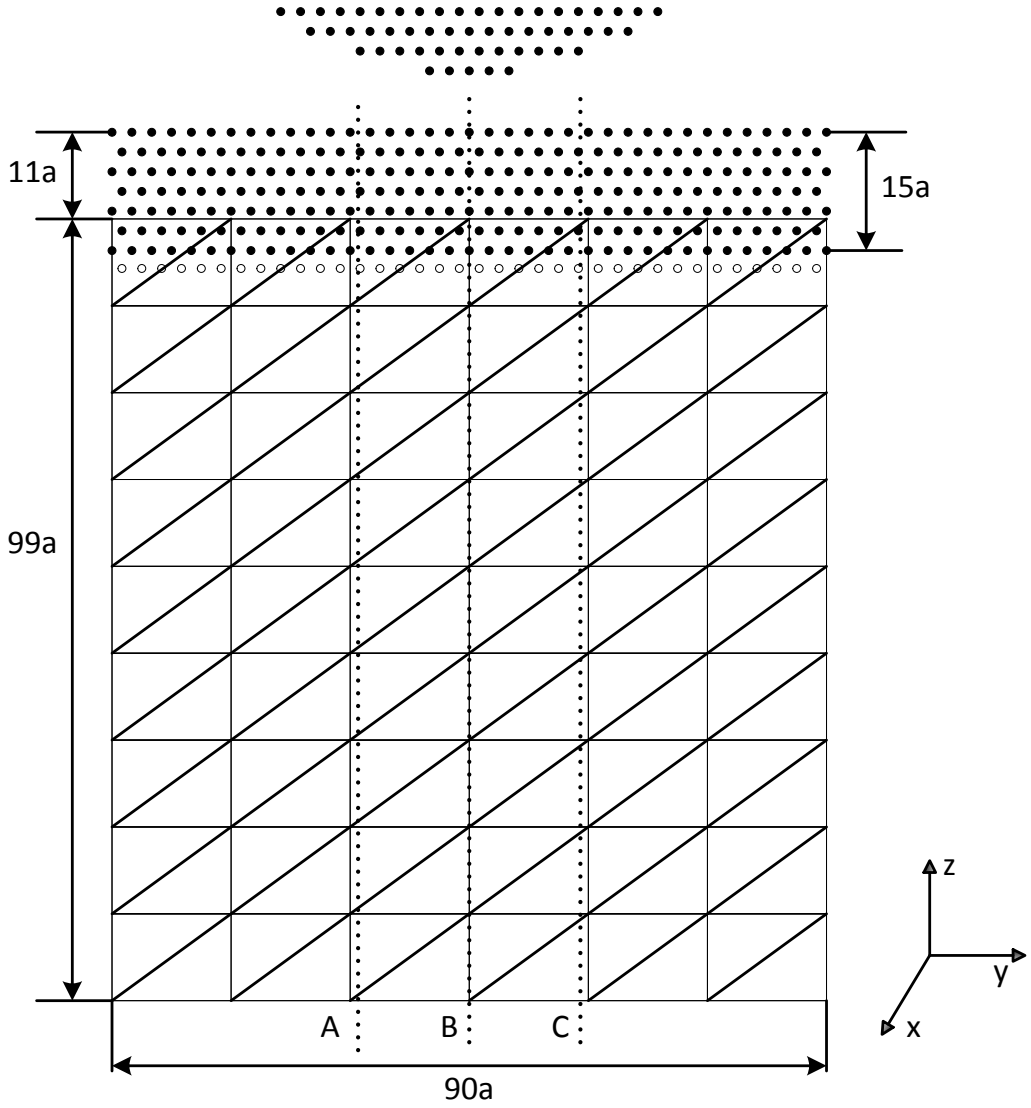

Figure 5.3: Geometry of the multiscale simulation. The lattice constant a of single crystal copper is 3.615 Å.

The atomistic interactions between the tip and the substrate, as well as within the substrate were calculated by the EAM potential [43] while the EAM-based Cauchy-Born rule was applied as a constitutive law for FEM. In the coupling region, the radius of the average sphere is 3a, which equals the smallest edge of the element. Therefore, the width of the coupling region is larger than the cutoff radius of the EAM potential, which is consistent with the rule in the original work [101].

The tip was initially positioned above the substrate surface with a distance 5 Å (beyond the cut off radius of the EAM potential). After the whole system was relaxed for the equilibrium, the tip was moved downwards in a constant speed of 10 m/s. During loading, the temperature was controlled by the Langevin thermostat every 50 steps. The Langevin thermostat [45] was used to reduce the kinetic energy of the nodes in the continuum region.

To characterize crystal defects, central symmetry parameter (CSP) [166] were calculated to characterize whether the atom belonging to a local defect (such as dislocation), a perfect crystal, or a surface. The CSP for an atom is defined as

$$\mathrm{CSP} = \sum_{i=1}^{N/2} \left| \mathbf{r}_i + \mathbf{r}_{i+N/2} \right|^2 \tag{5.4}$$

where $\mathbf{r}_i$ and $\mathbf{r}_{i+N/2}$ are vectors from the central atom to a particular pair of nearest neighbors. N is the number of nearest neighbors for the central atom, depending on the crystal lattice, e.g. N = 12 for FCC and N = 8 for BCC. The CSP will be 0 for a perfect lattice and larger than 0 for defect atoms or atoms on the free surface. Common neighbor analysis (CNA) [167] was also performed to analyze crystal structure. The CNA distinguishes different crystal structures, like FCC (CNA =1) and HCP (CNA = 2), via the specified cutoff radius. The CNA ranges from 1 to 5, which is 1 for FCC, 2 for HCP, 3 for BCC, 4 for icosahedral and 5 for unknown patterns.

Both the CSP and the CNA were recorded every 200 steps. At an interval of 200 time steps, a stress component σ_{zz} was recorded along three lines A, B and C as shown in figure 5.3.

The pure MD model plays a role of the benchmark for the MU model. The FEM region of the MU was replaced by the atoms in the pure MD model. All Other settings were identical between them.

5.2.2 Contact parameters

At the nanoscale, contact happens when there is a force interaction between the tip and the substrate or the distance of two atoms is within a specified value [76]. The formal definition is used to define the contact here. And the zero value of the normal displacement δ of the tip is defined as the tip height where the first contact occurs.

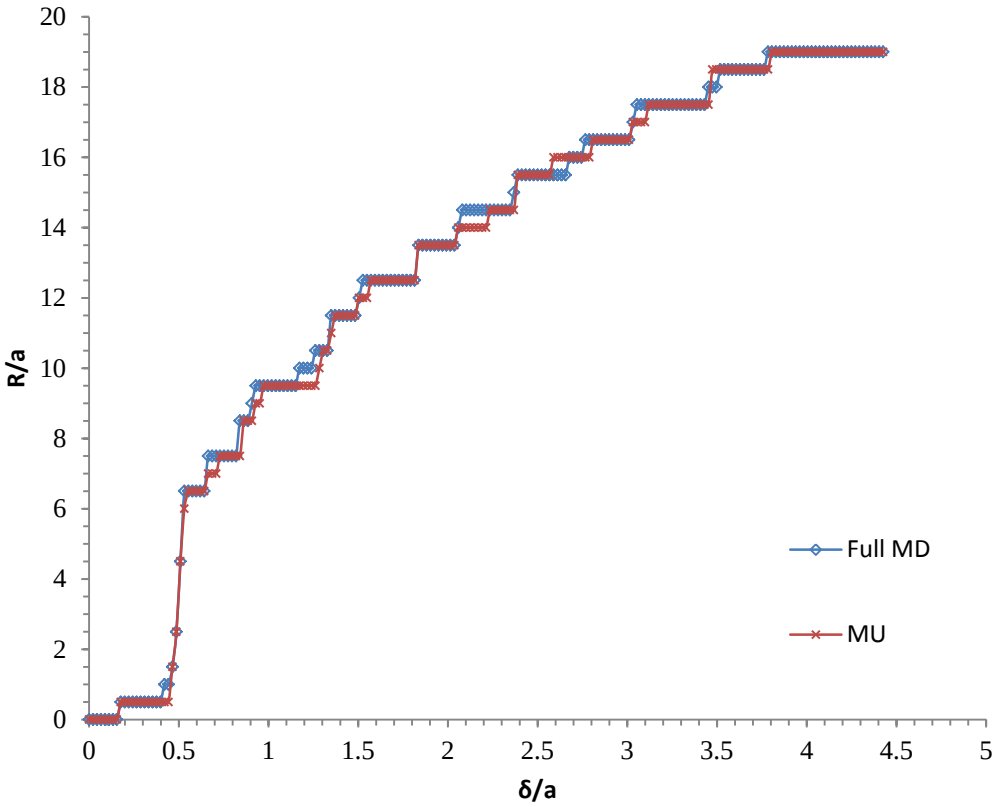

Figure 5.4: Contact radius R as a function of the normal displacement δ

Figure 5.4 shows the relationship between the contact radius R and the normal displacement δ. The contact region consists of the atoms on the stepped tip and is close to the area of a circle. R was determined by averaging the distances between the center of the circle and the atoms outermost. In terms of the contact radius, the MU predicts the MD well. It is found from Figure 5.4 that the results between two models are very close.

When the tip moved downwards, it suffered from the force exerted by the substrate in x-, y- and z- directions. Figure 5.5 shows the normal force F_z as a function of the normal displacement δ. Due to adhesion, F_z is negative from *A* to *C*. With a decreasing distance between the tip and the substrate, the repulsive component of F_z increased. Therefore, the net F_z reached zero and became positive from *C*. It is seen in figure 5.5 that MU and MD are close before *D*. From the point D where $\delta = 3.05a$, however, two models diverge.

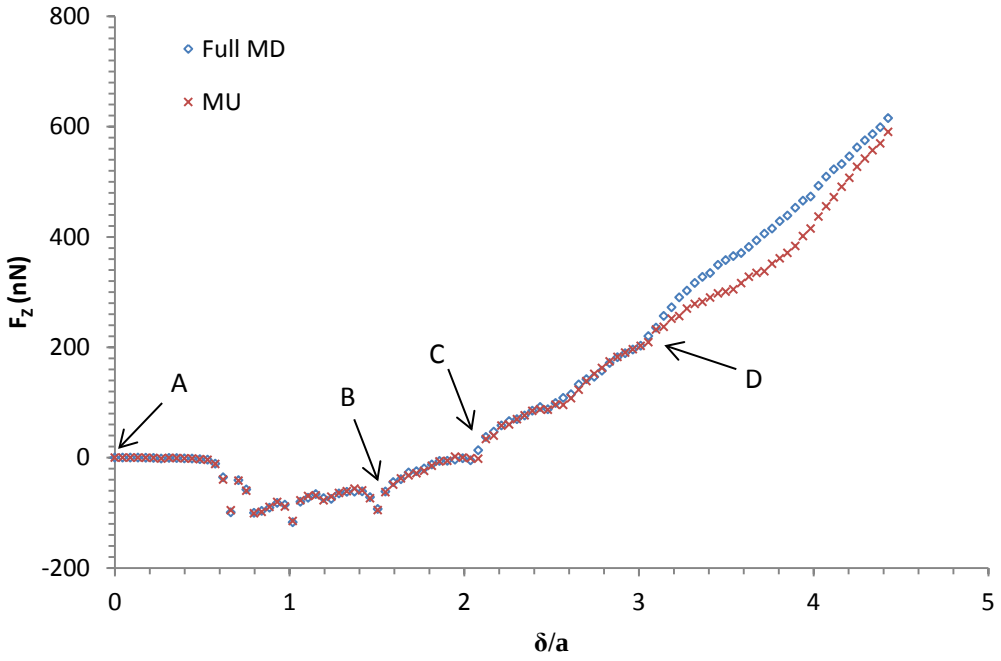

Figure 5.5: Normal force F_z as a function of the normal displacement δ

Before discuss the divergence point, the critical point B, where $\delta = 1.75a$, will be introduced. Figure 5.6 shows atomic configurations during contact at two stages. In order to visualize the atom configuration in the planar defect, the atoms in a perfect FCC lattice were removed. The CNA method [167] gives a classification of all the atoms by their local crystallinity. For metals of the FCC structure type, two adjacent HCP atom layers indicate an intrinsic stacking fault, and two HCP atom layers with an intermediate FCC atom layer represent an extrinsic stacking fault.

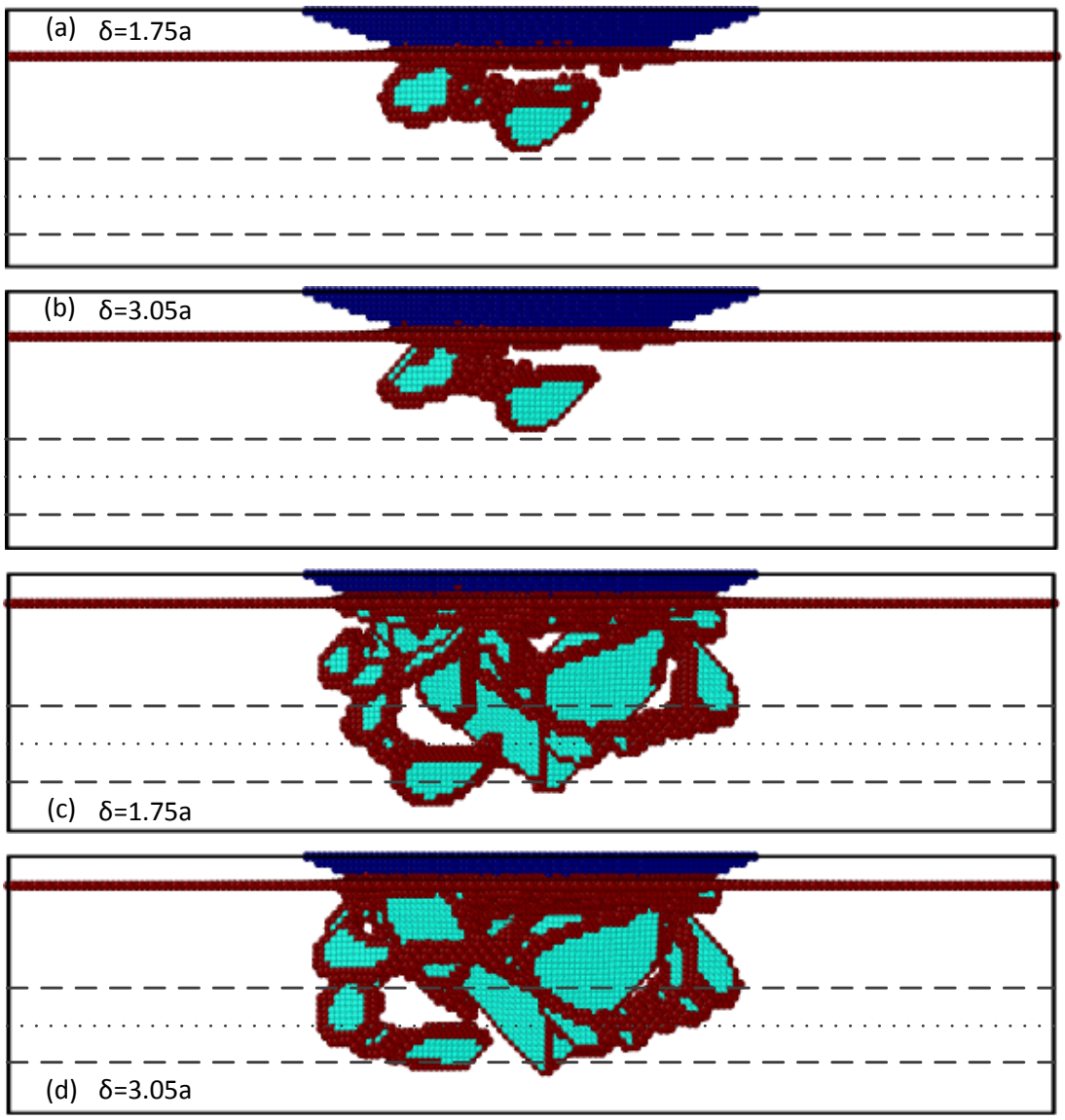

Figure 5.6: Atoms with perfect FCC structures were removed to facilitate viewing the defect structures. The blue atoms represent the rigid tip, the red atoms indicate the surface and the dislocation core, and the light blue atoms represent the stacking fault. The dotted line is the FEM boundary in the coupling region. The average region is located between the two dashed lines. (a) and (c) show the results of full MD when $\delta = 1.75a$ and $\delta = 3.05a$, respectively. (b) and (d) show the corresponding results of MU.

When δ=1.75a, plastic deformation took place at the subsurface of the substrate due to the high local stress at the subsurface. The onset of plastic deformation was evidenced by the initial dislocation nucleation from the subsurface, as shown in figure 5.6 (a) and (b). The dislocation loops were composed of two pairs of parallel dislocations. In the crystal, dislocations were nucleated and propagated along the slip system of the crystal, which corresponded to the slip plane and direction of the maximum resolved

shear stress. With the further movement of the tip, $\delta = 3.05a$, the first set of dislocations propagated in the crystal. Also, the contacting area between the tip and the surface were becoming wider, resulting in the nucleation of many new dislocations from the subsurface, as shown in figure 5.6 (c) and (d).

Figure 5.6 (b) shows that when $\delta = 1.75a$, dislocations fronts reached the average region in MU. It claimed that the HSM is not accurate if the distance between dislocations and the continuum region is close [154]. However, the MU predicted the normal force well before $\delta = 3.05a$. Unlike the situations when $\delta = 1.75a$, in figure 5.6, the dislocations in MU were different from those in MD when $\delta = 3.05a$. Due to dislocation interactions near the contact surface, the stiffness of the material in MD after the point D is larger compared to those from MU as shown in figure 5.5.

In addition, the deformation was too large in the FEM region when $\delta = 3.05a$ such that the Cauchy-Born rule cannot accurately describe the relationship between stress and strain. To ensure accuracy at this indent displacement, the FEM region could be moved to a lower place. The validity range of the CB rule has been discussed by Steinmann et al. in Ref. [168], which is beyond the scope of this work. It is interesting that in figure 5.5 the normal forces of two models deviate significantly after $\delta = 3.05a$, but their contact radius are close in figure 5.4. A similar result has also been obtained by using the Bridging Domain method [165]. Contact radius is less sensitive to the normal displacement than the normal force because the stepped tip was used and the range of the atomistic interactions was finite. Detailed discussion about this was given in Chapter 3.

From the energy point of view, MU works well based on the results in figure 5.7. Although there are a few deviating points, the kinetic energies of MU and MD are close to each other. Unlike the complex thermostat condition in the Bridging Scale method [106], the Langevin thermostat in the HSM eliminates excess kinetic energy due to contact and stabilizes the whole system at low temperature.

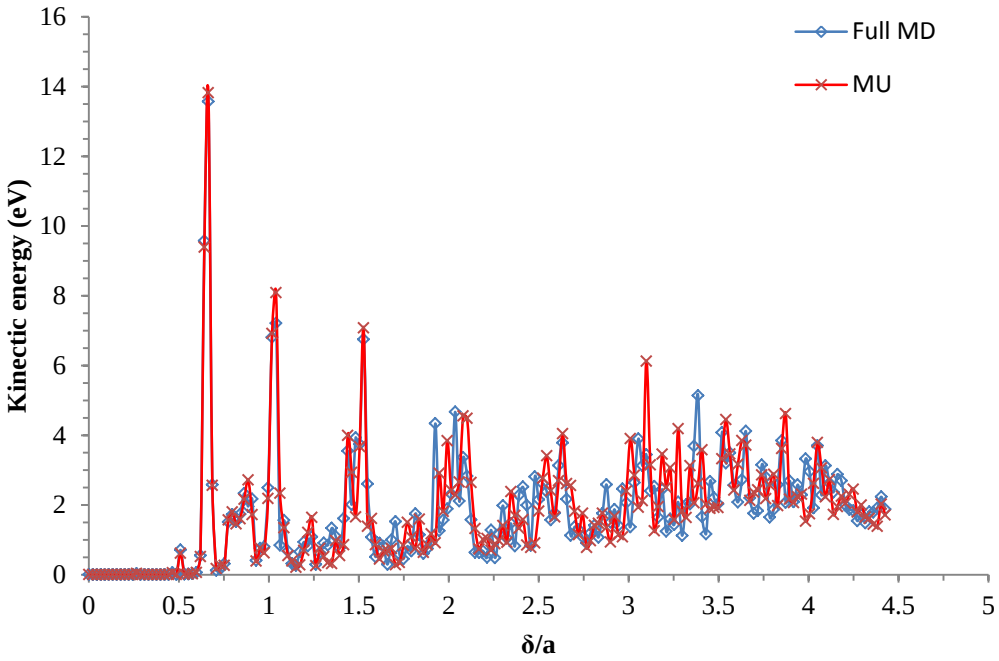

Figure 5.7: Kinetic energy near the substrate surface as a function the normal displacement δ

5.2.3 Stress continuity

To validate whether the coupling method can accurately transmit the mechanical force between the atomic region and the FEM region, the stress continuity is analyzed in this section.

In the MU model, the atomic, or the virial stress was calculated for the MD region while the Cauchy stress for the FEM region. There are many definitions of atomic stress such as Hardy's stress [169], but the virial stress we used in this study is the most widely used one in MD simulations, multiscale simulations and in the MD software such as LAMMPS. A detailed discussion of the atomic stress can be found in Zimmerman's work [170]. Moreover, the virial stress is equivalent to the Cauchy stress. The velocity term of the virial stress is ignored at the temperature of 0 K. In the MD model, only the atomic stress was determined. Stresses along three lines A, B and C in figure 5.3 were obtained through interpolating the values of nearby atoms or nearby nodes.

The stress component σ_{zz} of both the MU model and the MD model when $\delta = 1.31a$ was shown in figure 5.8. First and foremost, the HSM can ensure stress continuity after comparing σ_{zz} of both the FEM region and the MD region. Another important result shown in figure 5.8 is that the MU model can predict the full MD model well.

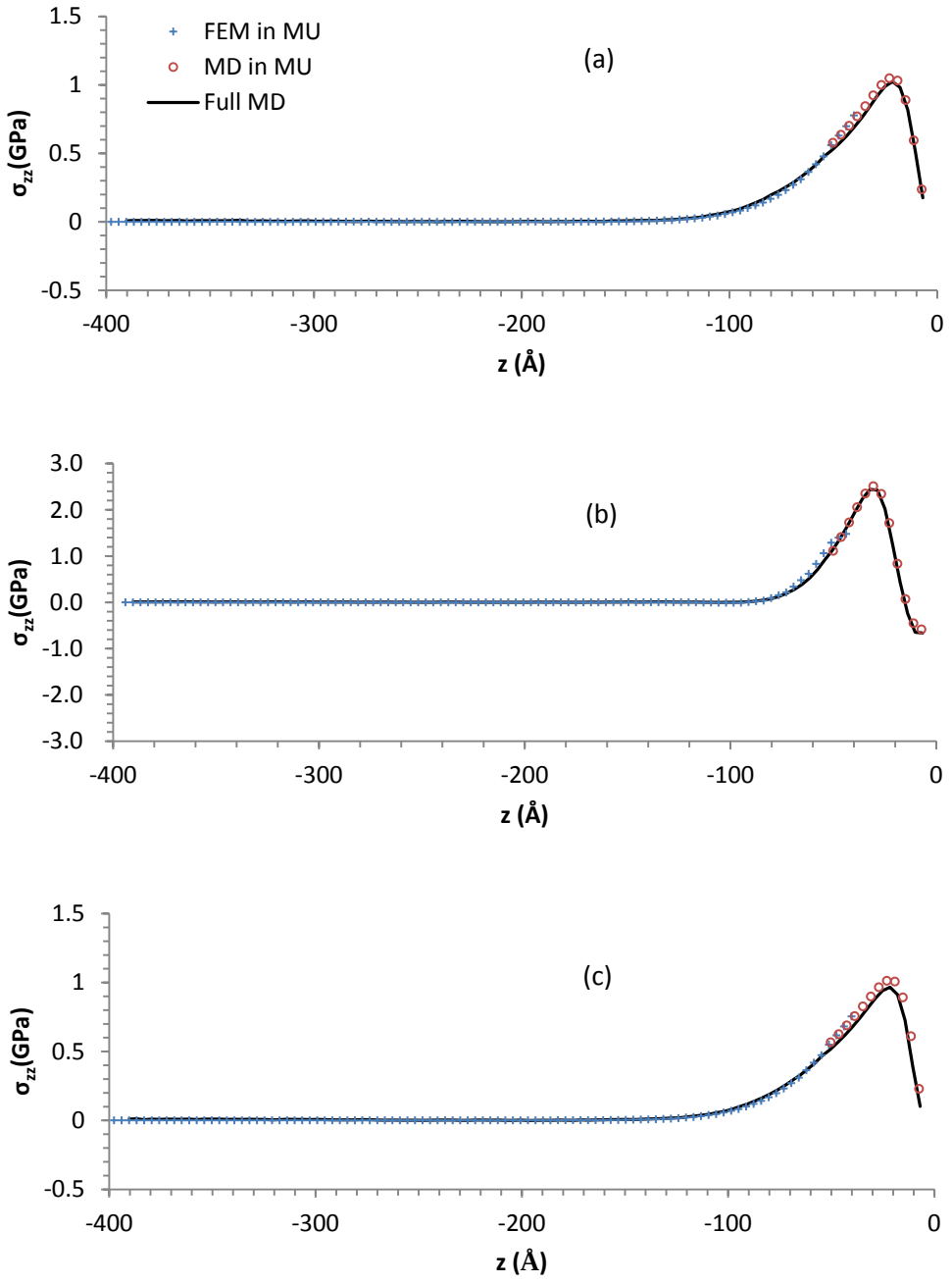

Figure 5.8: Stress component σ_{zz} along three lines (a) A, (b) B and (c) C. Solid line denotes full MD while cross and circle denote the FEM region and the MD region in MU, respectively.

5.2.4 Summary

To validate the HSM method in 3D and in the code, a classic Hertz contact has been used. All results obtained from the multiscale method (MU) have been compared to those from the pure MD. The MU can accurately predict the plastic deformation below the contact surface. Stresses are continuously transmitted from the atomic region to the FEM region through the coupling scheme. For the contact parameters at the surface, the MU performed even better. Both the contact radius and the kinetic energy calculated from the MU have little deviation. The normal force obtained from the MU followed the benchmark well before the normal displacement was too large. More importantly, the HSM method can save at least 5 times computational time compared with fully MD simulations for the same domain.

The HSM showed a good performance in some cases when the distance between the dislocations and the continuum region was close. However, in general it is better to avoid such the close distance because it can be difficult to ensure the accuracy of the results. In contact problems, the generation and the propagation of dislocation are directly related to the compressive loads. Therefore, in most situations, the direct method is to apply smaller loads [154]. At higher loads, the FEM domain could be moved further from the atomistic region. Or, by virtue of the coupled atomistic and discrete dislocation (CADD) technique, dislocations could be detected by detection elements and accommodated in the continuum region [171]. However, the CADD method only works in 2D as a fully 3D version is still being developed [172].

5.3 Validation and application at finite temperature

In the previous section, the HSM model has been validated by using static simulations. More importantly, it has shown that the developed code for the HSM model performs quite well. Although the HSM has been proved to be effective and reliable when studying contact problems at low temperatures, the finite temperature analysis of the HSM has not been considered in previous research. Moreover, an increasing number of

the groups have devoted to developing finite temperature coupling schemes [135, 137] recently. In this section, the capability of the HSM at finite temperatures is investigated.

5.3.1 Finite-temperature validation

Anciaux et al. modified the Bridge Domain method to overcome the cooling effect, and defined a patch test [136]. The goal of the test was to evaluate the capacity of maintaining temperature by a multiscale method in a thermal equilibrium process under condition of zero pressure. The details of the patch test coupling with the HSM at finite temperature up to 500K are presented in the following.. In figure 5.9, the size of the 3D structure for the test is $32a \times 32a \times 96a$, where a is the lattice constant of single crystal copper. Due to the effect of thermal expansion, the lattice constants increase with temperature. An anisotropic constitutive law $\sigma_i = C_{ij}\varepsilon_j$ with temperature –dependent elastic constants C_{ij} at different temperatures, shown in table 5.2, characterizes the relation between stress σ_i and strain ε_j. The data shown in table 5.2 was obtained from the literature [136, 173] and used in this work. Temperature-related density was calculated from a lattice constant in table 5.2 and atomic mass (63.55g/mol). Note that we constructed the bulk from FCC copper crystal considering the temperature effect.

Table 5.2: Lattice constant a taken from [136], density σ and elastic constants (C11, C12, C44) taken from [173] at temperature T

T[K]	a[Å]	σ[g/cm^3]	C11[eV/Å^3]	C12[eV/Å^3]	C44[eV/Å^3]
100	3.620	8.901	1.110	0.780	0.510
200	3.625	8.865	1.019	0.717	0.471
300	3.631	8.821	1.000	0.701	0.451
400	3.637	8.777	0.949	0.682	0.436
500	3.643	8.734	0.894	0.638	0.414

The FEM part is made of structured linear tetrahedron elements with edge size of 4a. The FEM part in the presented method only transfers mechanical information, which

has been successfully used in finite-temperature CADD [102] and Bridge Domain Method [136].

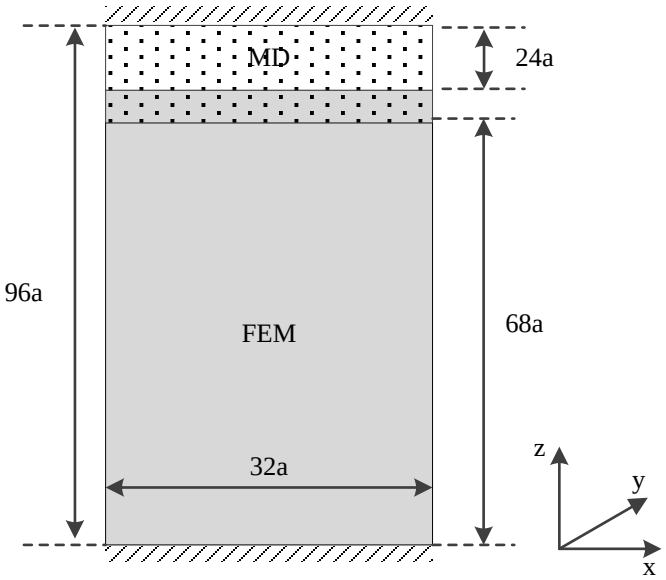

Figure 5.9: Geometry of the patch test

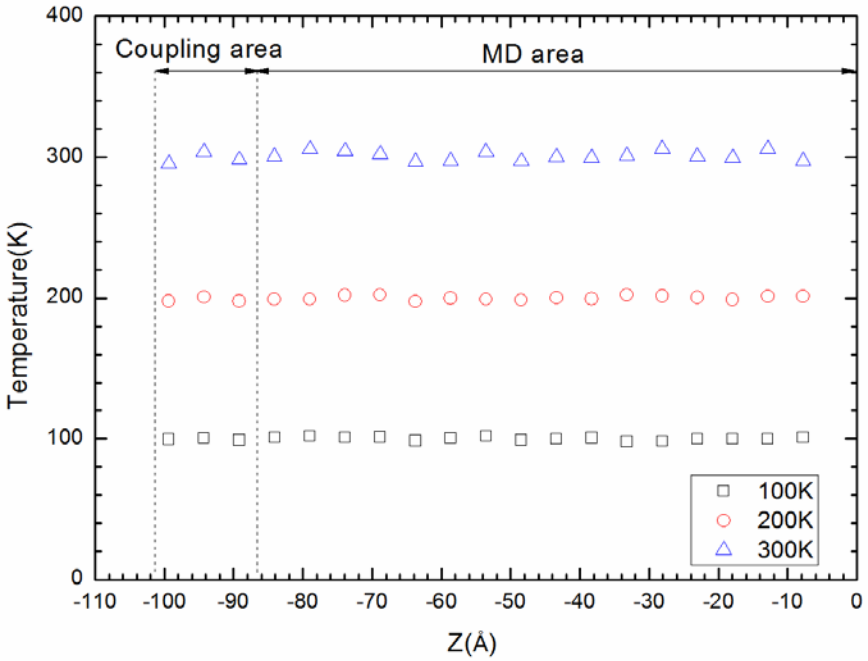

Figure 5.10: Temperature profile along z direction at the MD region and at the coupling region

The top layer of the atoms in the MD and the bottom nodes in the FEM are fixed. The interactions of the atoms below the top layer were calculated by the EAM potential

[174]. The periodic boundary conditions are applied along x and y directions. No external load is applied to the system. Both a Langevin thermostat [45] and a Berendsen thermostat [48] were tested to maintain temperatures. There was no obvious difference of the results obtained by them. Therefore, for comparisons with the previous work, all the following results were obtained by using a Berendsen thermostat.

The temperatures are recorded after the system evolved for 10 ps. Figure 5.10 shows that the temperature profile is nearly constant with a statistical variance of 1.31K, 2.42K, and 10.93K at 100K, 200K, and 300K, respectively. There is an acceptable stability of temperature. A similar test was also performed by Qu et al. in Ref. [102], the variance at 100K and 300K is 1.409K and 9.394K. The atoms within the average circle of the HSM in figure 5.1, serve as the atoms which constrain the nodes in the finite temperature Bridging Domain (BD) method [136]. However, the atoms in both methods constrain the nodes in the coupling region in different ways. In the BD method, the constraints enforced by using the Lagrange are added to the nodal equation, while the motions of the nodes in the HSM are governed by the displacements of the atoms in the average circle. On the other hand, the kinetic energy of those atoms in both methods is not modified by the elements so constant temperatures can be achieved.

5.3.2 Rough surface contacts

In section 5.3.1, the HSM has been analyzed at finite temperatures, and it has been demonstrate that the HSM is capable of handling finite-temperature simulations. Therefore, the normal loading of a rigid flat plane on a deformable rough surface at different temperatures is considered and compared with the work in Ref. [136].

5.3.2.1 Simulation presentation

A self-affine rough surface was generated based on a Voss algorithm [156] with the

Hurst exponent H = 0.7 and the root mean square of heights RMS_0 = 10 Å. The geometry of the substrate is similar to that in figure 5.9 except that the top layer of the atoms is free to move and all atoms in MD part whose heights lay above the generated self-affine rough surface were removed, as shown in figure 5.11. The flat plane has the same FCC lattice as the substrate.

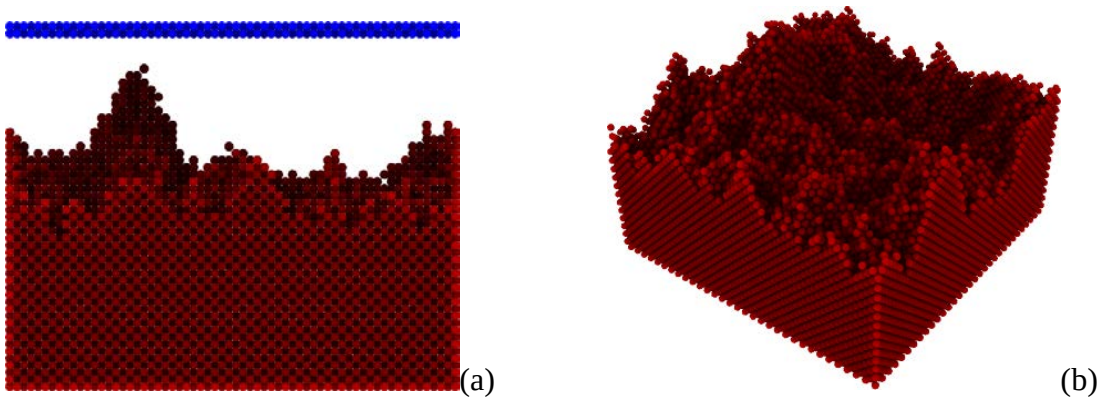

(a) (b)

Figure 5.11: (a) Front view (with the top plane) and (b) perspective view (without the top plane) of the MD part with the use of Ovito [55].

Before loading, the rough surface was allowed to fully relax. The flat plane was forced to press on the rough surfaces with an increment of 0.1GPa to 4GPa. After each loading, the system was allowed to equilibrate for 10 ps. The repulsive interaction between the flat plane and the rough surface was described by the LJ potential. The temperature of the MD part was controlled by a Berendsen thermostat [48], during the process of equilibration. All cases were run on a parallel cluster using 8 processors.

5.3.2.2 Relaxed surface statistics

Table 5.3 shows the surface statistics of the rough surface after relaxation. The temperature has little effect on the surface roughness. The RMS of the relaxed surface is less than RMS_0 after relaxation. Lattice discreteness is responsible for this. The generated self-affine surface consists of atomic spacing [73]. Some peaks of asperity composed of few atoms during relaxation are unstable due to lack of enough neighboring atoms and thermal fluctuations. Those atoms tend to join other atoms

nearby to construct a relatively flatter surface, which is more stable. Lattice discreteness is the main factor for the reduced RMS in this paper. The skewness indicates that the surfaces have no preference for valleys or peaks. The height distribution of the rough surface is close to the Gaussian distribution indicated by the Kurtosis.

Table 5.3: Surface statistics for the lower surface at temperature T

T[K]	RMS_0[Å]	RMS[Å]	Ra[Å]	Skewness	Kurtosis
100	10	9.110	6.989	0.0826	3.454
300	10	9.114	6.991	0.115	3.462
500	10	9.098	6.968	0.105	3.453

The first column shows the input temperatures. The second column gives the roughness (RMS_0) used as an input. All other columns present the output values.

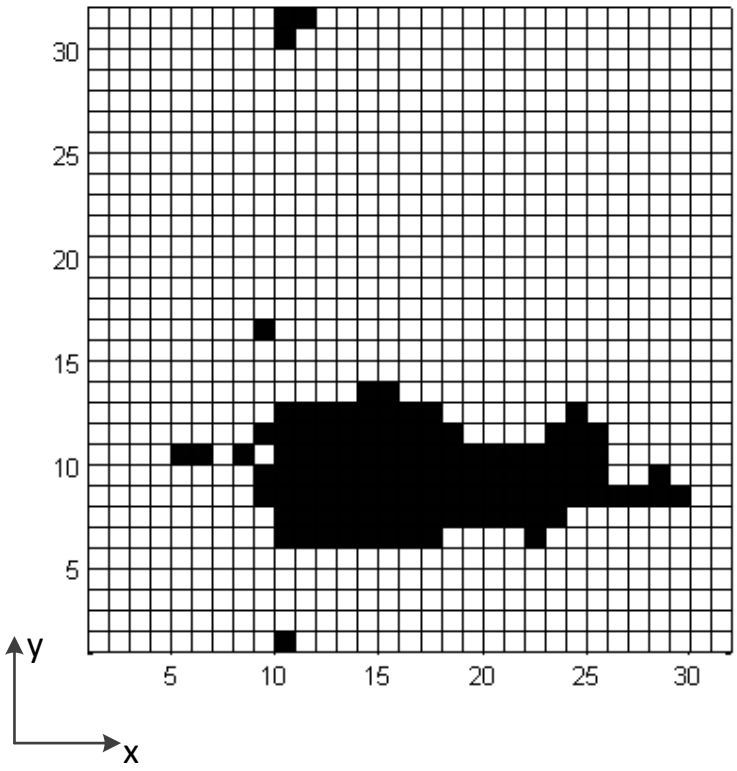

Figure 5.12: Contact area of the substrate under a load of 1.0 GPa at 300K. The black squares indicate the contact area.

5.3.2.3 Contact area

In terms of the contact area, contacting atoms are defined by two atoms within a specified distance. Then, the contacting atoms are projected on the x-y plane with square grids to obtain the contact area. Figure 5.12 shows an example of the contact area for the substrate under a pressure of 1.0 GPa at 300K.

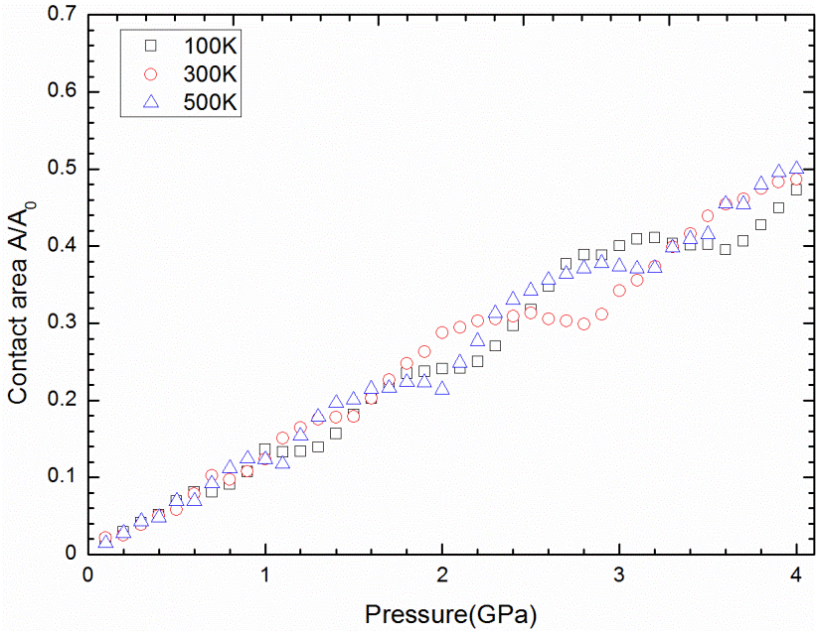

Figure 5.13: Contact area as a function of the pressure.

In figure 5.13, the contact area was plotted as a function of the pressure. The linear trend is shown for the loads smaller than 1.6GPa, and the corresponding contact area is about 20% of the nominal area. The results are comparable with those found by the Bridging Domain method in Ref.[136]. In MD simulations [75], the linear relationship between the contact area ratio and load has also been observed for the cases of dry contact with RMS = 5Å and RMS = 8Å. After 1.6GPa, dislocation generation and propagation result in a variation of the relationship between contact area and pressure as shown in figure 5.13.

However, it is strange that the relationship between contact area and load is temperature independent while materials normally become softer at higher temperatures. The dominant effect of plasticity at the nanoscale and the system size being too small could

explain it [136]. Beyond the linear region, dislocation emissions and atoms reshuffling dominate the change of the contact area with pressure [154]. Therefore, the contact area evolves in discrete steps, due to the hardening caused by atoms reshuffling and further loading.

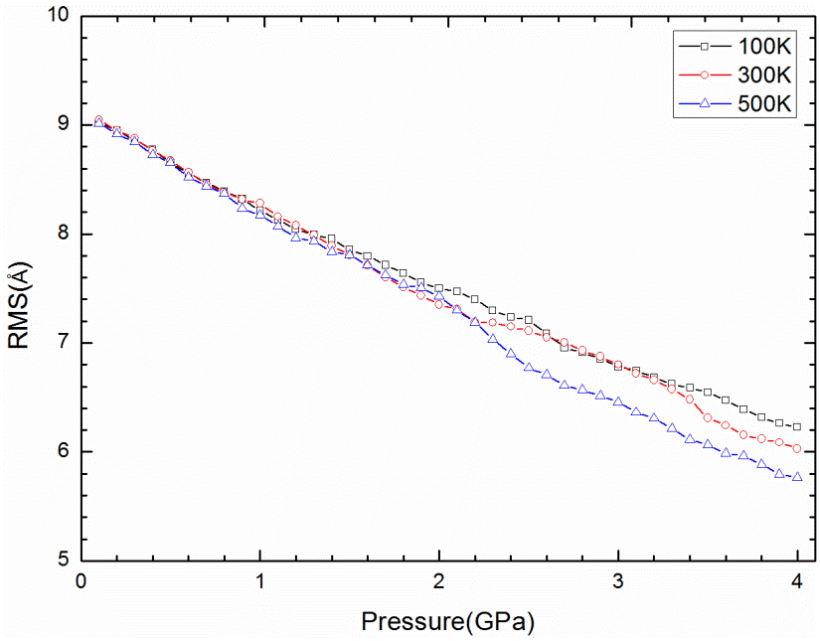

Figure 5.14: Root mean square (RMS) of the substrate surface as a function of the pressure

Figure 5.14 shows the root mean square (RMS) of heights as a function of the applied pressure at different temperature. Before the loads reach 2GPa, the change in RMS with the temperatures is almost the same as shown in figure 5.14. In addition, the linear trend is clearly observed at small loads. The effect of the temperature is small at this range. However, temperature plays an important role in the evolution of the RMS after the loads exceed 2GPa, especially at 3.5GPa. The surface roughness decreases faster with the high temperature 500Kcompared with lower temperatures of 100 and 300K. This indicates that temperature may have an effect on friction force, which will be studied in later work.

5.3.3 Summary

The hybrid simulation method [101] has been explored further at different temperatures.

The constant temperature profile in the coupling region and the MD region has been achieved during a patch test. It is found, from normal loading of the self-affine rough surface, that the surface statistics, due to relaxation, is independent of temperature except for a skewness factor. Moreover, at small loads, the evolution of both contact area ratio and RMS with the applied pressure is linear and temperature independent. From continuum theory, the contact area ratio should be larger due to smaller elastic constants at higher temperature. It seems that it is not a case at nanoscale. One possible explanation is that thermal collisions of the atoms between the substrate surface and the top plane affected extraction of the contact area because a few contacting atoms could provide the normal load due to a large instantaneous force. Thermal collisions became more severe at higher temperatures. The results obtained by the HSM are close to those obtained by the finite temperature Bridging Domain Method [136], which confirms the capability of the HSM at finite temperatures. However, compared with the Bridging Domain Method, the coupling scheme of the HSM is much simpler. The HSM provides an opportunity for studying 3D micro scale contacts with atomic details.

Chapter 6: 3D rough surface contacts with lubricant using the hybrid simulation method

In chapter 5, the hybrid simulation method (HSM) has been introduced and fully implemented through a self-developed parallel code. To validate accuracy and reliability of both the coupling scheme and software implementation, a test of single asperity contact at zero Kelvin was used. The results of the HSM show a good agreement with those obtained pure molecular dynamics. More importantly, the HSM has been studied at temperatures up to several hundred Kelvin in chapter 5. Therefore, we can apply the HSM to investigate the role of lubricant that usually works at room temperature or higher, rather than zero Kelvin in the rough surface contact.

In this chapter, the HSM is used to carry out the simulations of 3D rough surface contact with and without lubricant. Such problems are usually modeled using molecular dynamics (MD) simulation [58, 90, 93]. To the best of our knowledge, the multiscale methods have not been used to perform the simulations of lubricated surface contact. Due to expensive computation cost for calculation of the interactions of lubricant, the size of the deformable bulk is usually very small in MD simulations [76, 97]. Compared with MD simulation, the multiscale simulation can handle a domain of a larger size with acceptable computational time. The results obtained from the multiscale simulation are expected to be closer to the experiment results. We can generate the larger number of asperities in a domain of a larger size. Xuan [175] argued that more asperities can capture a general trend of rough surface contact with higher accuracy. In addition, Kim and Strachan [82, 84] used MD to observe the emission of dislocation in a study of dry contact for metals. The larger bulk in multiscale simulation provides a chance to observe the generation and the emission of dislocation when contact occurs under loads.

This chapter consists of four parts. The first part refers to simulation description, including lubricant, rough surface generation, and model set-up. The second and third

sections show the results of compression and sliding, respectively. A conclusion is made in the final section.

6.1 Simulation description

6.1.1 Surface roughness

Many surfaces have a roughness ranging from atomic dimension to macroscopic distances. They are close to self-affine fractals [176]. Self-affine fractals have an important input parameter called the Hurst exponent which plays an essential role in roughness determination of a self-affine surface. There are several numerical methods that can be used to generate a self-affine surface, such as the random midpoint displacement (RMD) [156], a Fourier based filtering algorithm [177] and the Weierstrass-Mandelbrot function [178].

According to the original algorithm, the random midpoint displacement (RMD) starts to displace the central point by interpolating the heights of the corner points in a square. Then the central point serves as a new corner point to generate a new central point until the original square is divided to the smaller squares with the required size [156]. Figure 6.1 shows an example of the original RMD algorithm, where the surface points increase from 4 to 25 after five iterations and the squares increase from 1 to 16.

The original RMD can ensure that the predefined resolution is reached and that the boundary of the generated surface is periodic. However, the original algorithm of the RMD creates the rough surface with few large asperities, whereas more asperities are needed in a study multi-asperity contact [75]. Therefore, the modified algorithm proposed in Spijker's work [73] is used here. Based on the new algorithm, the original square is firstly divided to equally small squares ($2^n \times 2^n$, where n is integer). Then the original RMD is applied to each small square. Some examples of rough surfaces generated based on the original and modified algorithms are shown in figure 6.2. It clearly indicates that the number of the asperities increases with the number of the

small squares. Without a further mention, 4×4 is used in this chapter.

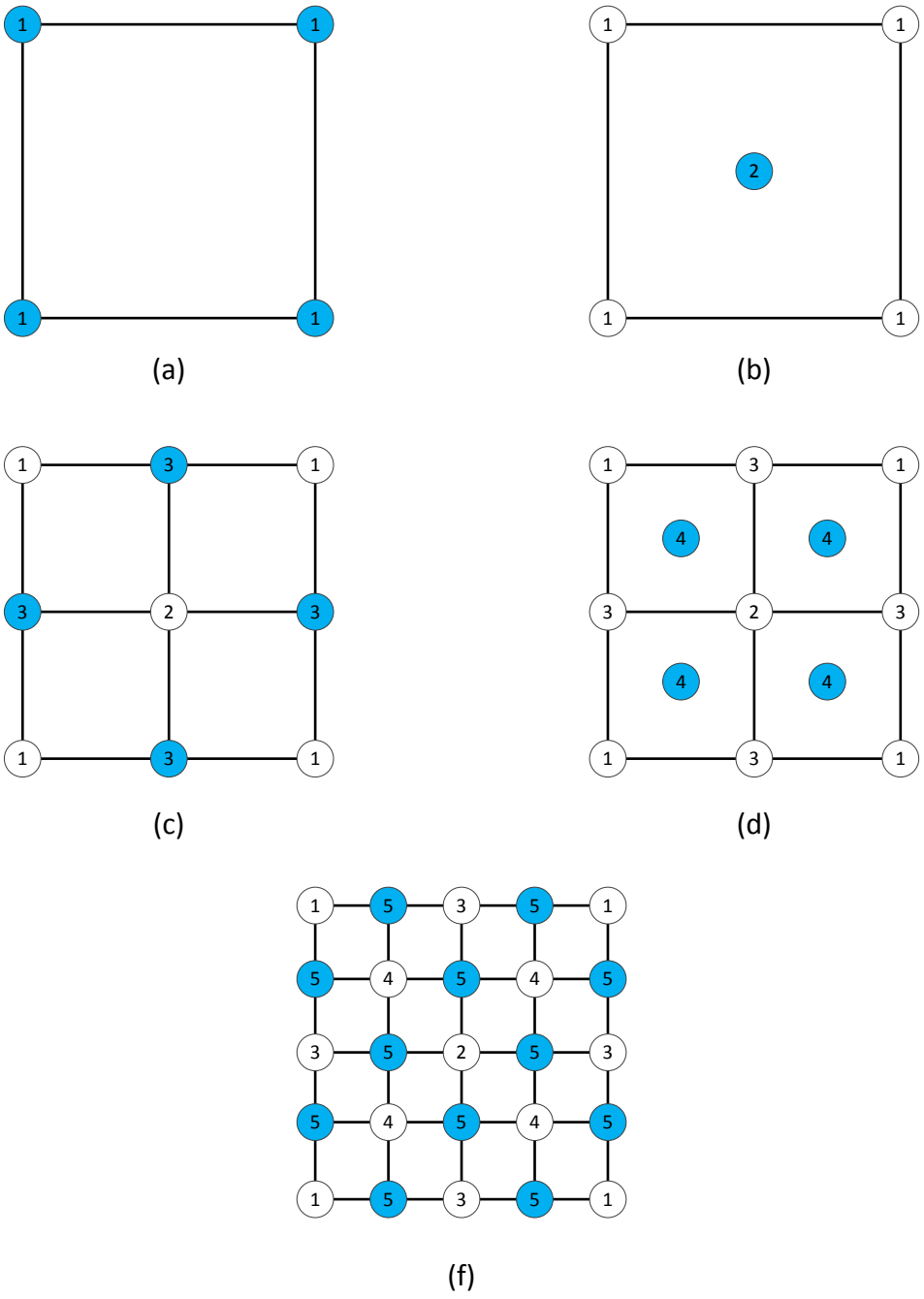

Figure 6.1: A schematic view of the original RMS algorithm within first five iterations (a-f). The surface points are indicated by circles, within which numbers give the iteration number. The open circles indicate the points in the current iteration while the blue circles indicate those from the previous iteration.

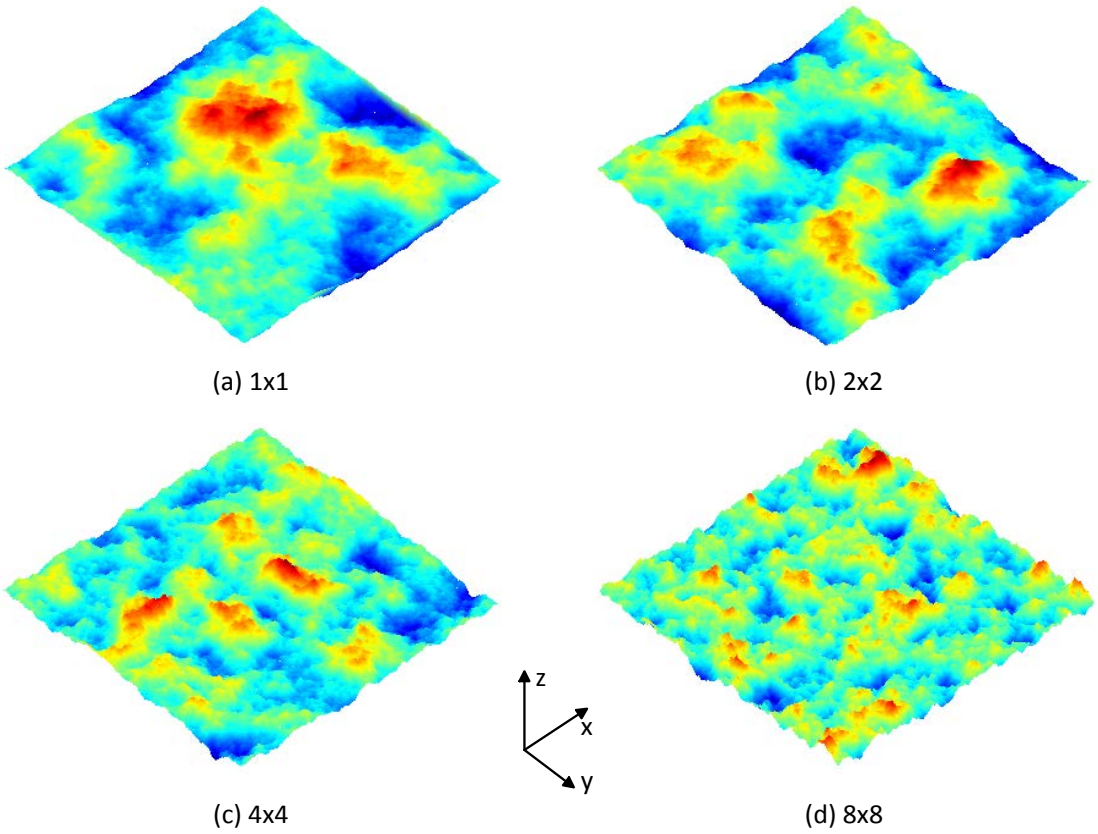

Figure 6.2: Examples of a generated rough surface for different number of small squares using a modified RMD algorithm [73]. The color varies from blue to red with increasing height.

Table 6.1: Number of molecules, CH3 and CH2 for different cases

Case	Contact	Molecules	CH_3	CH_2
1	non-lubricated	0	0	0
2	lubricated	16000	2000	14000
3	lubricated	32000	4000	28000
4	lubricated	48000	6000	42000
5	lubricated	64000	8000	56000

The root mean square (RMS) roughness is one of the most important quantities that characterize the rough surface. To create a surface with a required RMS, the heights of the points on the surface need to be scaled. In figure 6.2, the RMS of four surfaces is 8 Å. In this work, the rough surfaces with the RMS roughness of 2 Å, 5 Å and 8 Å were generated, similar to Xuan's work [75].

6.1.2 Lubricant

Linear chain molecules of hexadecane with the chemical formula $C_{16}H_{34}$ or $CH_3(CH_2)_{14}CH_3$, is chosen as the lubricant liquid. A chain of hexadecane is made of connected CH_3 and CH_2 .groups. The interactions between CH_3 and CH_2 in each molecule is governed by a 'united atom' (UA) model, which will be discussed in section 6.1.4.

Since the bulk size or the wall size goes up significantly in the multiscale method, the number of the lubricant molecules is much higher than that in pure MD. Case 1 indicates dry contact, while other cases are lubricated contact.

6.1.3 Model set-up

The contact between a rigid flat plane and a deformable substrate with a self-affine surface is considered in figure 6.3. The substrate was built from FCC crystal aluminum with a (001) top surface. The lattice constant a of the crystal at 300K is 4.045 Å. The dimension of the substrate is $80a \times 80a \times 80a$, which approximately corresponds to $323.6Å \times 323.6Å \times 323.6Å$, which is at least 8 times larger than MD simulation in the literature [73, 75-77, 83, 97]. Except the lubricant molecules, the total number of the atoms ranges from 670000 to 700000 for different surface roughness, see table 6.2. The atomic region of the substrate consists of three layers: (2) deformable layer, (4) thermostat layer and (3) pad layer. Contact occurs among the rigid plane, the lubricant and the deformable layer. The thermostat layer is used to maintain the temperature of the deformable layer. The 'pad' layer as a part of the FEM region provides a physical boundary for the atomic region. The displacements of the atoms in the pad layer are interpolated from the nodal displacements.

Along x and y direction, periodic boundary condition was applied to both the atomic region and the FEM region. The bottom boundary of the FEM region was fixed while the top surface of the deformable layer was free.

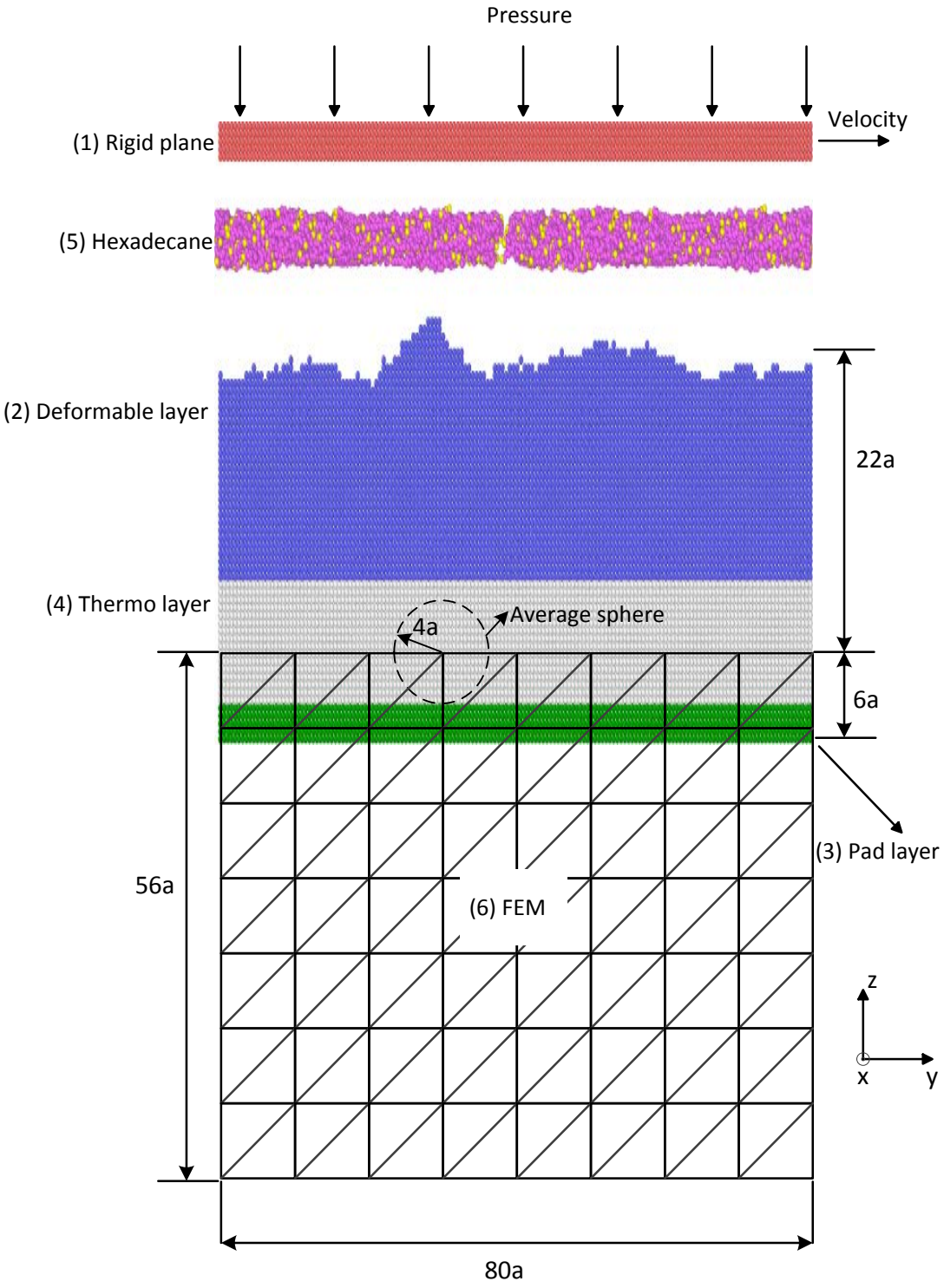

Figure 6.3: Schematic of the model set-up where $a = 4.045\text{Å}$ is the lattice constant of single crystal aluminum.

As can be seen in figure 6.3, the top boundary of the FEM region lies in the thermostat layer. The displacements of the nodes on this boundary are obtained by

averaging the displacements of the atoms within the average spheres. The radius of each sphere is 4a, which corresponds to the smallest size of the element edge. The four-node tetrahedron elements were used to divide the continuum region. The FEM region consists of 33600 elements and 6615 nodes, which corresponds to 1433600 atoms. A constitutive anisotropic law describes the relation between stress and strain for each integration point. The elastic constants $C_{11} = 0.7116, C_{12} = 0.3845, C_{44} = 0.1973$ (unit: eV/Å^3) were taken from Mishin's work [179]. Before loading, the substrate is allowed to relax for equilibrium. The system has 400 ps to equilibrate after applying a load. With a system in equilibrium, the rigid plane is set free along the x direction and forced to shear at a velocity of 40 m/s. To study the effects of different pressure on the lubricated contact, 50, 150 and 250MPa were applied on the rigid plane.

Table 6.2: Parameters of the multiscale simulations

Dimension	$323.6Å \times 323.6Å \times 323.6Å$
Element number	33600
Node number	6615
Aluminum atom number	670000~700000
Calculation time	74~98 hours

The multiscale program mentioned in chapter 5 was used to carry out the simulations while the Larger-scale Atomic/Molecular Massively Parallel Simulator (LAMMPS) MD code handled the atomic calculations [51]. The calculation time of the multiscale simulations ranges from 74 hours to 98 hours due to the different number of the atoms. For different simulations, the number of the FEM elements and nodes are not changed.

6.1.4 Force field

The plastic deformation on the rough surface with atoms reshuffling or dislocations will be involved during compression and shearing between the rough surfaces, so the EAM potential [179] was used to model the interactions between the aluminum atoms

in the substrate. The atomic interactions between the rigid plane and the substrate, however, were calculated by the LJ potential which is characterized by a distance parameter σ and an energy parameter ε. The LJ potential has been used to simulate the aluminum oxide surface by reducing the adhesion force [83]. A United-Atom (UA) model [180] was used to model the hexadecane molecules. The UA model simplified all CH_X groups with pseudo carbon atoms. One typical linear chain hexadecane is shown in figure 6.4. The deformation of the hexadecane molecule in figure 6.4(b) is due to the intra-molecular interactions which include bond stretching, angle bending and dihedral angle torsion given in equation (6.1-6.3).

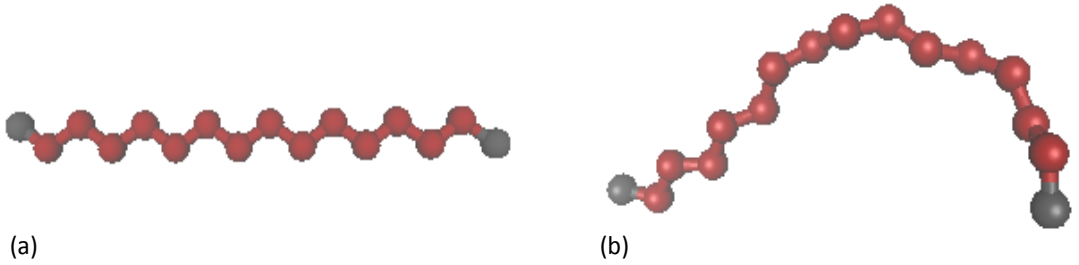

Figure 6.4: Schematic of one hexadecane molecule (a) before deformation (b) after deformation. The red and grey atoms indicate the united-atom of CH_2 and CH_3.

$$E_{bond} = k_b(r - r_0)^2 \tag{6.1}$$

$$E_{bend} = k_\theta(\theta - \theta_0)^2 \tag{6.2}$$

$$E_{torsion}=c_0+c_1[1+\cos\phi]+c_2[1-\cos(2\phi)]+c_3[1+\cos(3\phi)] \tag{6.3}$$

The corresponding parameters in equation (6.1-6.3) are shown in table 6.3. The inter-molecular interactions and the liquid-solid interactions are described by the LJ potential with cutoff distance of 14 Å. The parameters of the LJ potential for the liquid-solid interactions were estimated via the Lorentz-Berthelot mixing rules given in equation (6.4-6.5). All parameters for the LJ potential are given in table 6.4.

$$\sigma_{ls} = (\sigma_l + \sigma_s)/2 \tag{6.4}$$

$$\varepsilon_{ls} = \sqrt{\varepsilon_l \varepsilon_s} \tag{6.5}$$

where σ_l and ε_l are the parameters of the LJ potential for liquid, while σ_s and ε_s are for solid. σ_{ls} and ε_{ls} obtained from the arithmetic mean in equation (6.4) and the geometric mean in equation (6.5) are the LJ parameters for describing he liquid-solid interactions.

Table 6.3: Parameters of the potentials for the intra-molecular interactions taken from [180]

Potential	Parameters	
Bond	$k_b = 39.0279\ \text{eV/Å}^2$	$r_0 = 1.545\text{Å}$
Bend	$k_\theta = 5.3858\ \text{eV/rad}^2$	$\theta_0 = 114^\circ$
Torsion	$C_0 = 0.0\ \text{eV}$	$C_1 = 0.0306\ \text{eV}$
	$C_2 = -0.0059\ \text{eV}$	$C_3 = 0.0682\ \text{eV}$

Table 6.4: Parameters for the LJ potentials the non-bonded interactions

Neighbors	σ(Å)	ε(eV)
$Al - Al$[a]	2.596	0.010677
$Al - CH_2$[c]	3.273	0.006506
$Al - CH_3$[c]	3.173	0.009496
$CH_2 - CH_2$[b]	3.950	0.003964
$CH_3 - CH_3$[b]	3.750	0.008445
$CH_3 - CH_2$[c]	3.850	0.005786

a taken from Ref.[73]
b taken from Ref.[180]
c calculated from the Lorentz-Berthelot rules

6.1.5 Contact area

Calculation of the real contact area is of importance at the atomic scale, especially when the dimension of the devices is reduced down to nanometer. The real contact area has an important effect on heat conduction, friction and adhesion and so on.

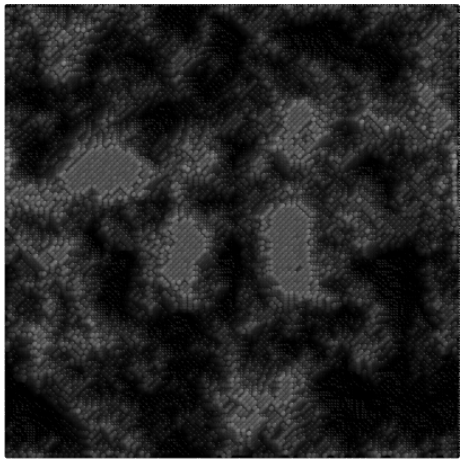

(a) dry

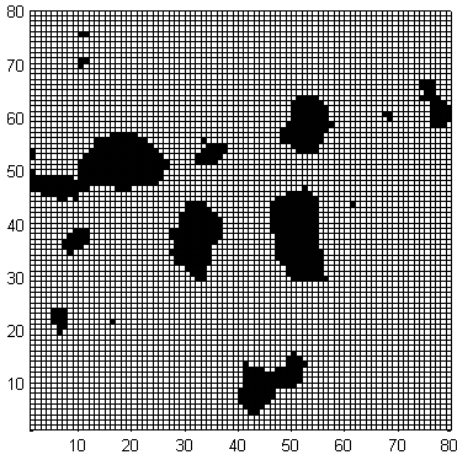

(d) dry

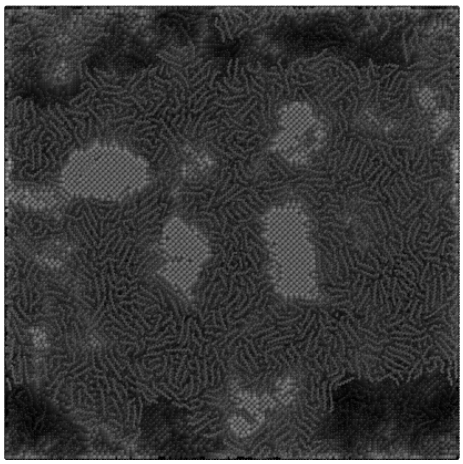

(b) 2000 $C_{16}H_{34}$

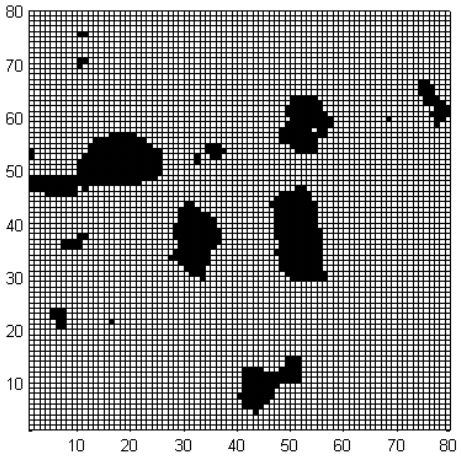

(e) 2000 $C_{16}H_{34}$

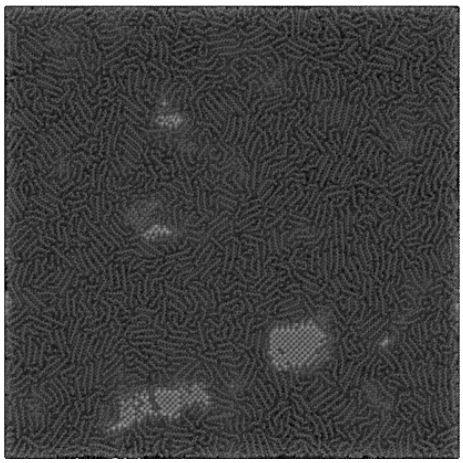

(c) 4000 $C_{16}H_{34}$

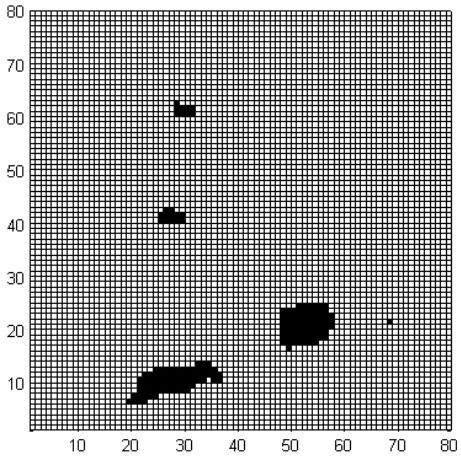

(f) 4000 $C_{16}H_{34}$

Figure 6.5: Contact area of dry and lubricated substrate with RMS = 8Å under 250MPa. Images on the right show the grid representation, in which black cells indicate the contact area. The left ones show the atomic representation.

In continuum mechanics, contact area can be obtained based on the edge of the contact zone. It is difficult to accurately define the atomic area and even the atomic contact [12]. The atomic contact is determined by either force [11, 15, 154] or distance [77, 136]. Contact is considered established when the distance of two atoms is less than or equals 5Å [76]. The real contact area is estimated from a projected rectangular cuboid method [73]. In this method, the $n \times n$ grids as a bottom face of the rectangular cuboids are plotted on the x-y plane, on which all the atoms of the deformable layer are projected. Those atoms are divided into the corresponding grids according to their x and y coordinates. The length of each cuboid is the maximum z coordinate values of the atoms within it. Similar cuboids can be plotted for the rigid plane. The top faces of the deformable layer cuboids and the bottom faces of the rigid plane cuboids can determine approximately the atomic contact.

In this work, the edge of each grid is equal to the lattice constant, which means there are 80×80 grids on the x-y plane in figure 6.5 (d-f). Black cells indicate atomic contact between the top plane and the substrate. It clearly shows in figure 6.5 that the lubricant has an important effect on the contact area. With 2000 and 4000 molecules, the contact area reduces by 11.8% and 75.2%, respectively. As hexadecane molecules covered some asperities and separated the substrate from the top plane, the contact area decreases from Figure 6.5 (d) to Figure 6.5 (e-f). The detailed discussion about this will be presented in section 6.2.

6.2 Normal contact

6.2.1 RMS roughness

Before compression, the rigid plane was above the substrate with a distance larger than the cut off radius of the interaction potential. The root mean square (RMS) roughness of the generated surface was 2Å, 5Å, and 8Å while the RMS roughness of the atomic surface was 2.04Å, 4.92Å, and 7.71Å. The system was then allowed to equilibrate by relaxing hexadecane molecules and maintaining a temperature of 300K.

The relaxation allowed stabilization of the thermal vibrations of the atoms on the free surface of the substrate. To some extent the stabilization process modifies the surface roughness. After the relaxation, the atomic surface became smoother with RMS = 1.98Å, 4.84Å and 7.60Å. Although the RMS roughness of the surfaces changes, it is still close to the required values. Figure 6.6 shows the deformation of the FEM region in the multiscale model before and after compression. As the FEM region is far from the surface, the deformation is small in this region as shown in figure 6.6 (b). More deformation occurred in the FEM region since asperities were flattened in the corresponding area on the surface.

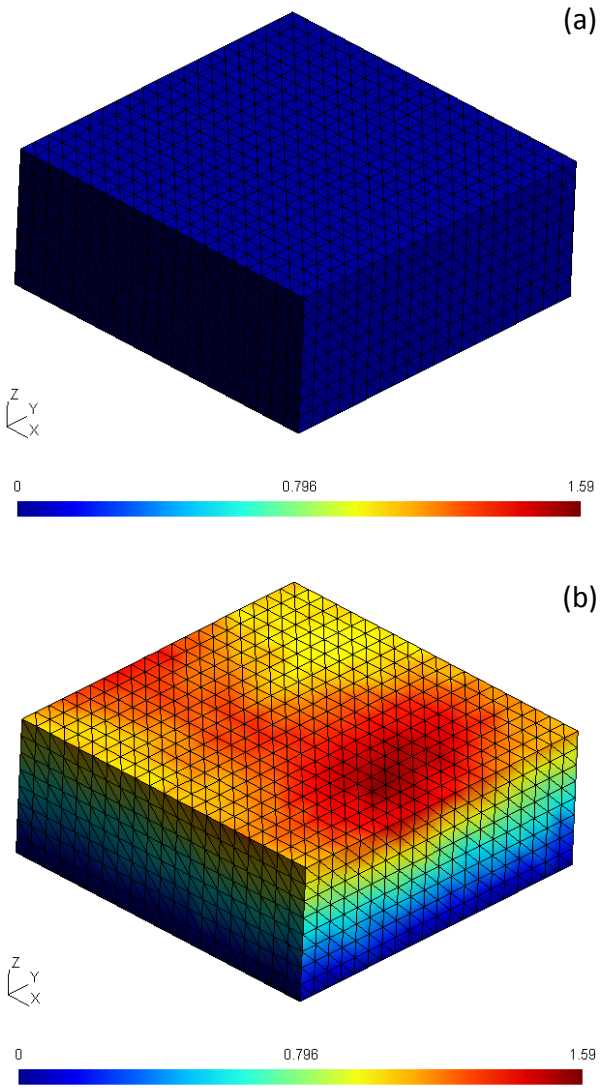

Figure 6.6: Deformation of the FEM region (a) before compression and (b) after compression for dry contact. The unit of the color bar is angstrom.

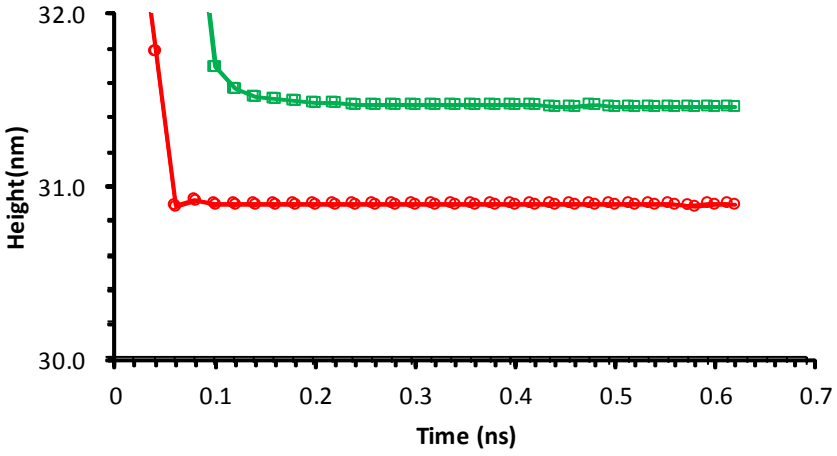

(a)

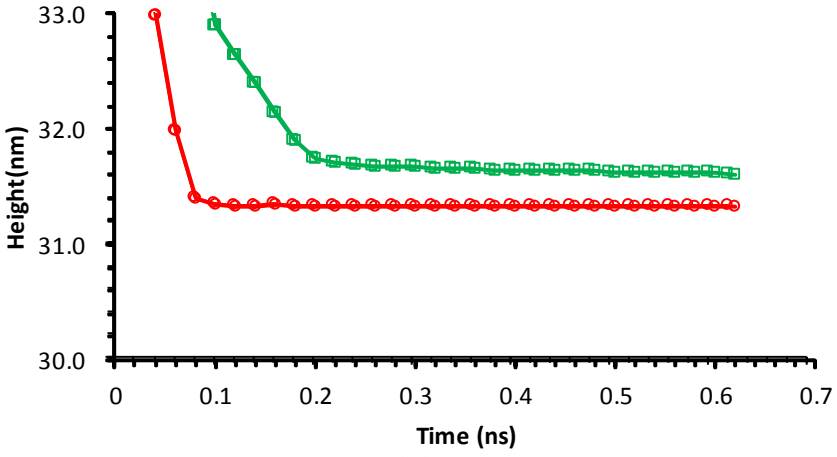

(b)

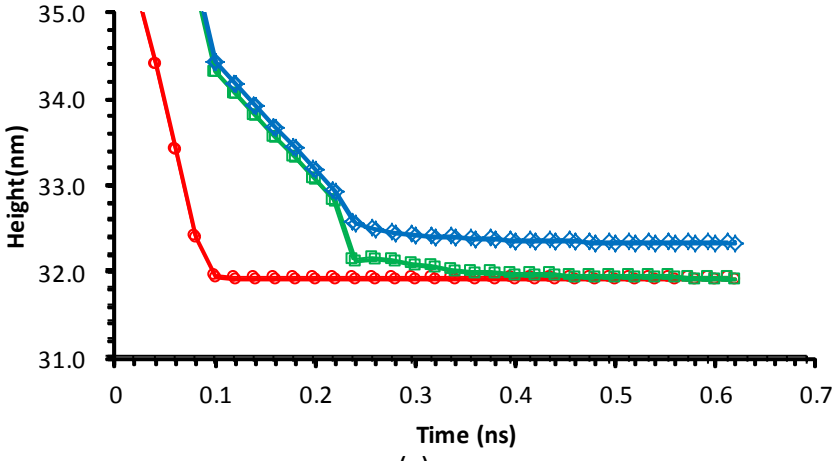

(c)

Figure 6.7: Variation of system heights with time for RMS = (a) 2Å, (b) 5Å, (c) 8Å under 250MPa. Red lines indicate dry contact while green and blue lines indicate lubricated contact with 2000 and 4000 hexadecane molecules, respectively.

After relaxation, the top plane was forced to move downwards under constant pressure. Without any resisting force, the top plane will impact on the substrate with a high speed. This is not acceptable, since it will cause significantly plastic deformation on the substrate [76].

Moreover, the initial distance between two surfaces will dominate the substrate deformation. The further away the initial distance is, the larger the deformation is. This is because the top surface reaches a higher velocity upon impact. To eliminate the effects of the distance and ensure a quasi-static contact, a nve/limit command provided by LAMMPS [51] was applied on the top plane to limit its movement. With this command, the top plane can only move the maximum distance of 0.001Å every time step. The limitation wasn't removed until the top plane moved a preset distance determined by trial and error.

The system heights were calculated during the whole compression. In figure 6.7, the relationship between the system height and simulation time for dry and lubricated contact is shown. It indicates that all simulation reached equilibrium after 0.4 ns were in equilibrium. The simulations with the lubricated show higher heights of the lubricant contact compared with the dry contact seen in figure 6.7(a-b). The thickness of the thin film formed by the hexadecane molecules contributed to the system height.

In figure 6.7 (c), two thousand hexadecane molecules had no effect on the system height when the surface roughness is 8Å, as there is not enough quantity to fill the cavity between two contacting surfaces. Meanwhile, four thousand hexadecane molecules lifted the top plane by a distance about 0.4 nm. The film thickness of the lubricants play an important role in friction force, which will be discussed more in section 6.3.2.

When contact occurs, the top plane will flatten the asperities of the substrate. The RMS roughness of the flattened surface changes as the load increases. The RMS of the flattened surface is denoted as RMS_f while that of the initial surface is RMS_u.

The change of RMS therefore is defined as $\Delta RMS = RMS_f - RMS_u$. Figure 6.8 shows the variations of ΔRMS with load for different surface roughness. Firstly, it indicates that RMS_f.decreases with the increase of the loads for three surfaces, and this relationship is independent of RMS_u. However, the percentage of change in RMS roughness is related to RMS_u. There was a much smaller change for the rougher surfaces (blue and green line in figure 6.8), because the contact for those rougher surfaces occurred on a few high asperities which support the load. It is the rest of the surface that dominated the roughness. However, the RMS of the surface changed more for $RMS\ 2Å$, because much more asperities of the substrate contacted with the top plane were simultaneously flattened. The peak to valley distances (PV) [73] indicates roughly the number of the contacting asperities. The PV of the atomic surfaces for RMS 2Å, 5Å and 8Å are 17.2Å, 32.85Å and 51.4Å. The height of the highest asperity for RMS 2Å is approximately 8.6 Å. Therefore, many asperities support the top plane simultaneously.

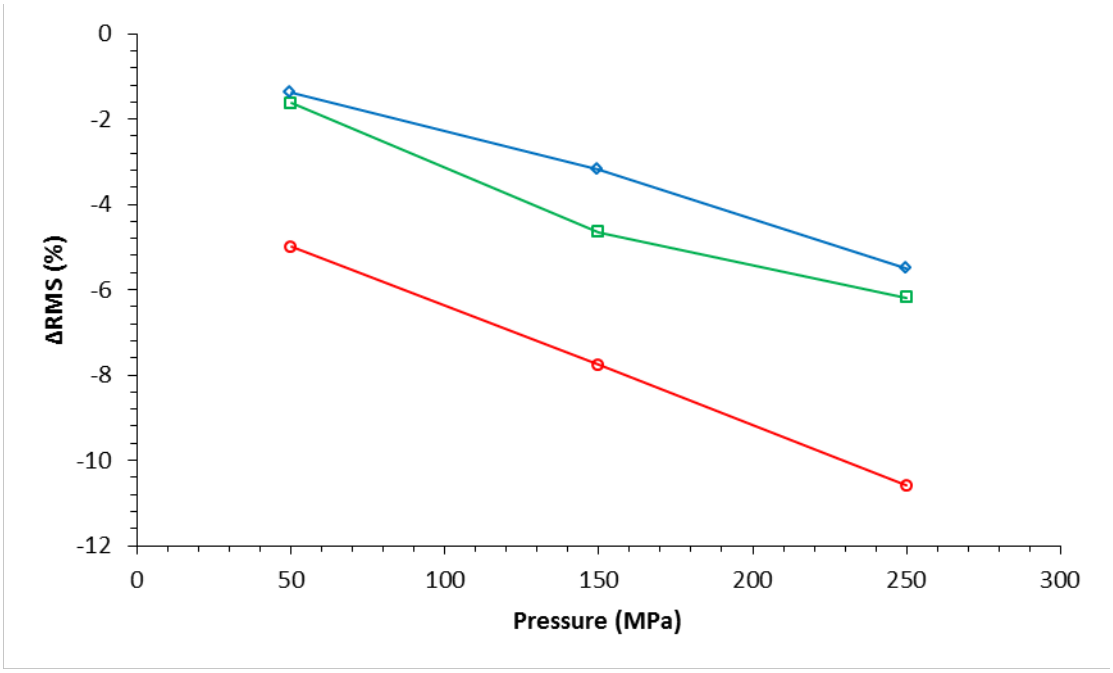

Figure 6.8: RMS change ΔRMS of dry contact as a function of pressure. Red, green and blue lines indicate $RMS = 2Å,\ 5Å$ and 8Å, respectively.

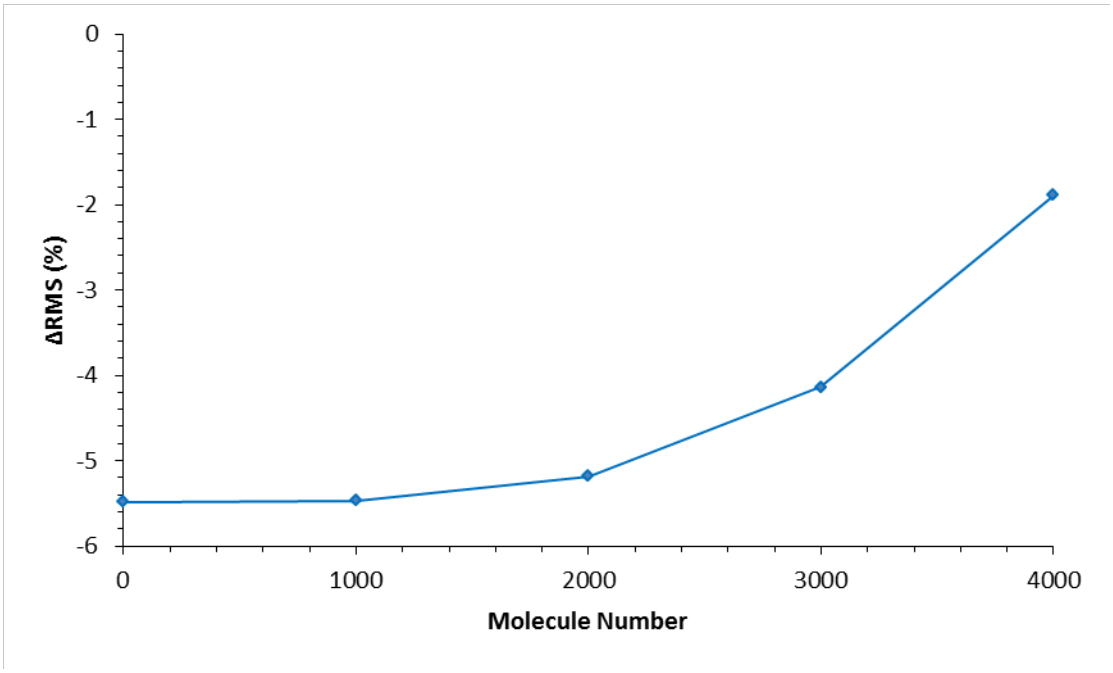

Figure 6.9: Variations of RMS change ΔRMS with molecule number under 250MPa. The RMS roughness of the surface is 8Å.

Figure 6.9 shows the effects of the molecule number on the RMS change. Results for 2Å and 5Å are not shown as the results for 8Å can show the clearest trend. Zheng et al. [97] demonstrated that the appropriate amount of lubricant is dependent on the RMS roughness. The increase in the molecule number reduces the change in RMS roughness or reduces asperity flattening. After compression, the lubricant molecules tend to fill the valleys and covered the surface. With 4000 molecules, the surface could be almost entirely covered. Most of the asperities were covered by the lubricant and were not contacted by the top plane. Consequently, the RMS changed little, about 1.8%. In addition to the effect of the lubricant amount, Wu et al. [181] indicated that the lubricant viscosity has an important effect on the changes of the surface roughness. In their work, the smaller reduction of the surface roughness was obtained for the lubricant with a high viscosity. The viscosity in Wu's work plays a similar role as the lubricant amount here. A well-formed lubricant film due to the higher viscosity reduced the direct metal-metal contact, and protected the surfaces.

For lubricated contact, the new surface was formed by the lubricant molecules and the substrate atoms. The RMS roughness of the new surface is 3.3Å and 0.6Å for 3000

and 4000 molecules, respectively. They are much lower than the original roughness of 8Å.

6.2.2 Contact area

In this section the effects of roughness and lubricant on the contact area will be studied. The projection method which is used to calculate the contact area has been presented in section 6.1.5.

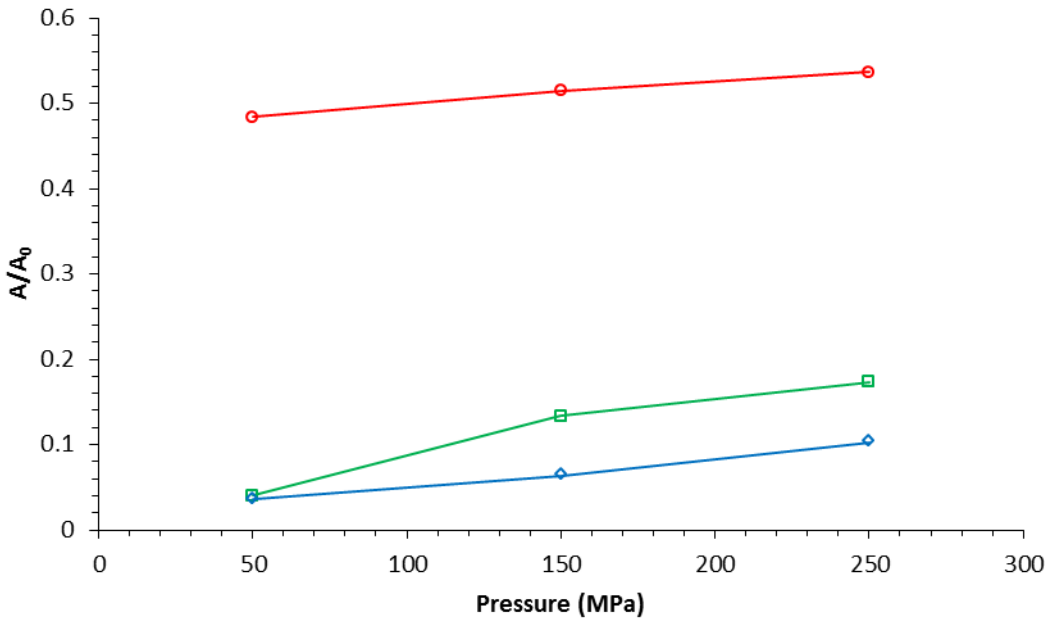

Figure 6.10: Contact area as a function of pressure for dry contact with the surface roughness RMS = 2Å (red line), 5Å (green line), 8Å (blue line).

In figure 6.10, the variations of contact area with the loads for dry contacts are shown. It indicates that the contact area goes up with an increase of the loads for three different RMS. The results are qualitatively consistent with the previous work [71, 182]. Under the load of 50MPa, the contact area of RMS 2Å is close to 50%, which is much higher than 4% and 3.5% of RMS 5Å and 8Å. As mentioned in the previous section, the heights of the asperities on the surface of RMS 2Å are relatively low, so a number of them were in contact simultaneously. For the rougher surface, however, only few asperities supported the load applied from the top plane, which could clearly

be seen in figure 6.5. With the increase of the loads, the previous asperity contacts deformed and their heights decreased while the lower non-contacting asperities were joined to support the top plane. Therefore, the contact area of three surfaces increases in figure 6.10. Considering the different topography due to the different random seed when generating the self-affine surfaces [77] and adhesive strength [73], the results could deviate a little. The relationship between the contact area and the loads obtained in this work show a general behavior that agrees qualitatively with published literature [182].

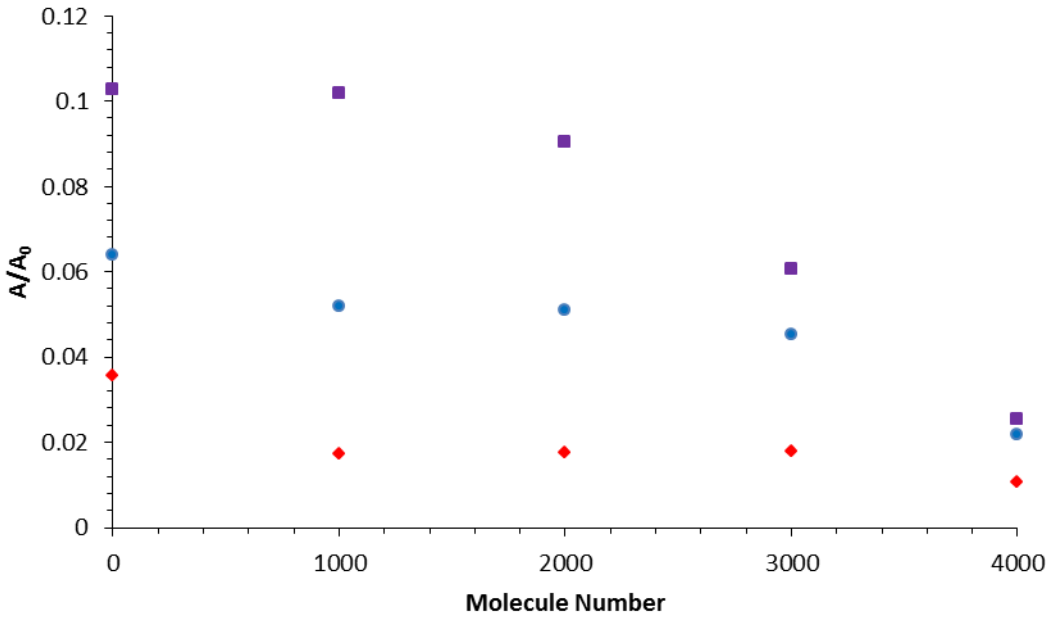

Figure 6.11: Contact area as a function of lubricant molecule number for surface with roughness RMS = 8Å under different loads, 50MPa (red diamond), 150MPa (blue circle), 250MPa (purple square).

For lubricated contacts, the contact area still increased with the loads at the range of 50MPa (red diamond) to 250MPa (purple square) as shown in figure 6.11. However, the contact area reduced with the increasing number of molecules.

The lubricants could separate the substrate from contacting the top plane. The separating gap depends on the lubricant amount. It indicates that under 250MPa the contact area of 0 molecules and 1000 molecules is almost identical while the contact area of 4000 molecules reduced by 75%. The 4000 molecules were able to cover most

of asperities except several peaks as shown in figure 6.5 (f). However, it was not enough for the 2000 molecules to fill the valleys on the rough surface. From the point of view of the normal force, it could also provide some clues. The normal force on the top plane of lubricated contact was divided into two parts: normal force F_S from the substrate and normal force F_L from the lubricant. The sum of F_S and F_L is equal to the normal force F_0 on the top plane of dry contact (0 lubricant molecules).

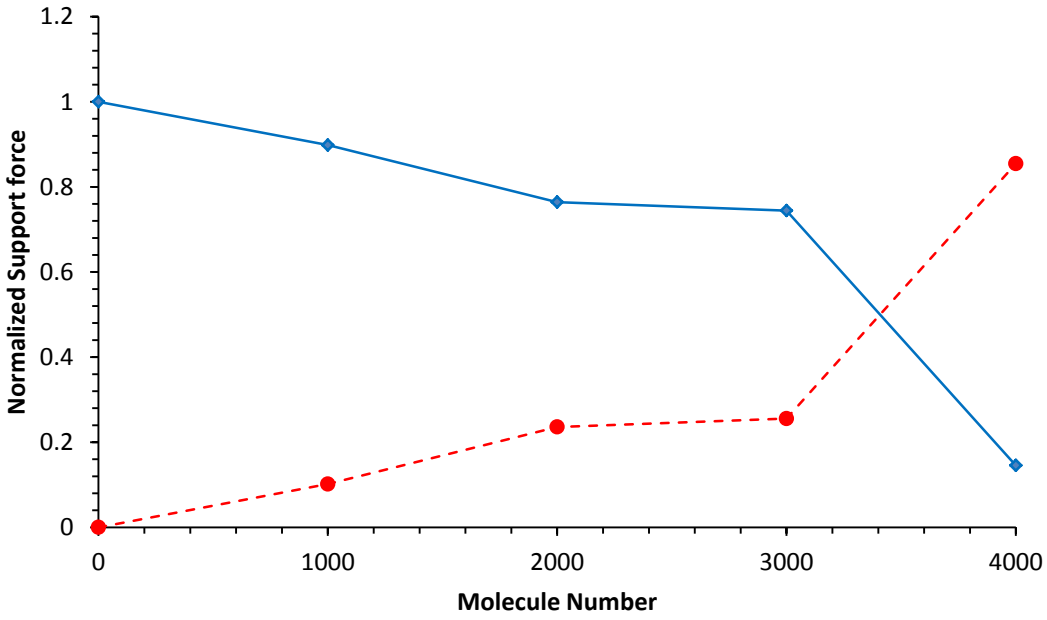

Figure 6.12: Normalized normal force (unit: nN) on the top plane supported from dry and lubricated substrate under 250MPa. The surface roughness is 8Å. The molecule number of zero indicates dry contact. Red, blue lines indicates F_L/F_0 and F_S/F_0, respectively.

Figure 6.12 shows the normal force on the top plane supported from dry and lubricated contacts as a function of molecule number. In the figure, the support force F_S/F_0 from the asperities roughly decreased with the larger number of the molecules, which is consistent with the trend in contact area. Meanwhile, the normal force F_L/F_0 from the lubricant increased with a higher number of the molecules. The decrease of the normal force F_S/F_0 under each load means the number of the contacting asperities dropped. At 250MPa, more lubricant endured the larger force. When 4000 hexadecane molecules were used, F_L reached 87.17nN under 250MPa, which corresponds to 85.45% of F_S in dry contact. Therefore, only a few asperities were in lubricated contact and

the contact area was small.

6.2.3 Cavity

The cavity is defined as a space between the top plane and the substrate. It is important to calculate it to determine the amount of the filled lubricant in the space [76].

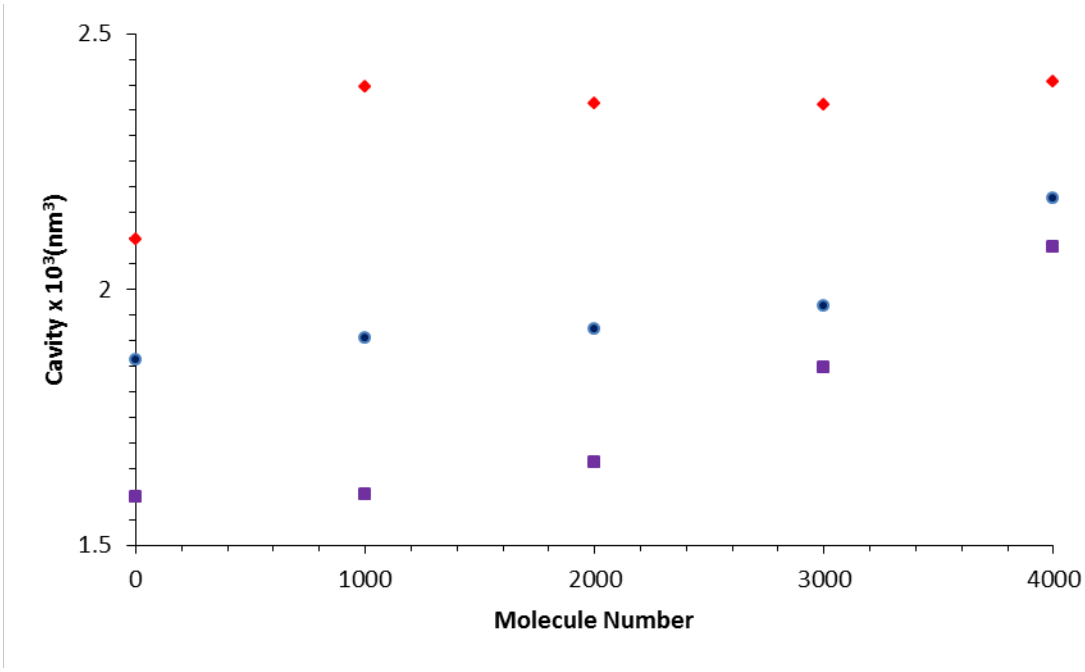

Figure 6.13: Cavity between two surfaces as a function of molecule number for the rough surface RMS = 8Å under different loads, 50MPa (red diamond), 150MPa (blue circle), 250MPa (purple square).

The method of calculating the cavity is based on the projection method proposed in section 6.1.5, which assumes that the whole cavity consists of small cavities. After dividing two contacting bodies into small cuboids, any two cuboids from different bodies are paired if they can be projected into the same grid on the x-y plane. The distance between the bottom face of the cuboid on the top plane and the top face of its paired cuboid on the substrate is the height of small cavity. Geometry of small cavity is a cuboid, so its volume is calculated based on the height and the grid area. The whole cavity is a sum of the volume of all those small cavities. Note this approach is just an approximation for obtaining a general trend. For more accurate calculation,

Voronoi tessellation could be used [183].

Figure 6.13 shows the cavity formed by the upper and the lower surfaces as a function of the molecule number. As expected, the cavity increased with the molecule number because of the supporting effect of the lubricants. The cavity difference between the dry contact and the lubricated contact is related to the deformation of the asperities. The large difference indicates a large distance between the top plane and the substrate for a typical load or the small deformation of the asperities. Therefore, it seems the sufficient amount of the lubricants can protect the surface topography, which plays important role in friction of mixed lubrication [76]. The appropriate lubricant amount for such protection depends on the loads and the surface roughness. In this work, for RMS = 2Å and 5Å under 250MPa, it required 2000 molecules and 3000 molecules, respectively.

Table 6.5: Total cavity (unit: 10^3 nm^3) for different molecule number under different loads. The surface RMS roughness is 8Å.

Molecule Number	50MPa	150MPa	250MPa
1000	1.0171	0.7723	0.5949
2000	0.404	0.3087	0.2167
3000	0.1552	0.0739	0.0549
4000	0.0332	0.0096	0.0095

The small cavities that formed the whole cavity for the lubricated condition could be further divided along the z direction. Some of the smaller cavities contained the hexadecane molecules while others were empty. Adding the volume of the empty cavities can roughly determine the absolute cavity defined in this work.

It shows in table 6.5 that the absolute cavity dropped with an increase of both loads and the molecule number. It indicates that although 4000 molecules have the favorably supporting effects for the surface of RMS 8Å under 250MPa, there was still about the space of 9.5 nm^3 which can be filled with more molecules. The volume occupied by the lubricants, could be used to estimate the density of the hexadecane.

For RMS 8Å with 4000 molecules under 150MPa and 250MPa, the hexadecane has the density of 6.9 and 7.2 g/cm^3, respectively. The estimations are lower than 7.7 g/cm^3 in Tanaka et al's experimental data [184]. The discrepancy could be due to the approximation of the volume obtained here. A higher number of molecules will produce a closer value. Quantitative study on this will be conducted in the future.

6.2.4 Surface pressure

Surface pressure was calculated based on the projection method in section 6.1.5. There are other approaches for calculating surface pressure [12, 51], but for comparisons the projection method was used. The virial stress of each atom was calculated at all time. After the cuboids were obtained, the surface pressure was estimated by averaging the virial stress along the z direction of all atoms within each cuboid.

In figure 6.14, the surface pressure for unlubricated and lubricated contact is shown. In this figure, positive values correspond to compressive stresses. The light color indicates compression area, where the asperity contacts occur. Compression region in figure 6.14 corresponds well to the contact area in figure 6.5. Conversely, the dark color describes tension area, in which the atoms bear the attractive forces from the top plane. The pressure at the range from -1.27 GPa to 2.83 GPa in figure 6.13(a) is comparable to -1.0 GPa to 3.0GPa from Xuan et al's work [76]. The deviations could originate from the larger dimensions that we used here, compared with those in the reference. And the flatter top surface in this work compared with Xuan's MD simulations [76] may be responsible for such deviations.

It shows pressure distribution for unlubricated and lubricated contacts in figure 6.15. To obtain the distribution histogram, the surface pressure in each cuboid was binned with an interval of 0.05 GPa. In figure 6.15(a), the sum of the distribution of the negative pressure is 88.1%, 80.0% and 66.79% for 50MPa, 150MPa and 250MPa, respectively while it is 89.2%, 72.8% and 63.4% in figure 6.15(b).

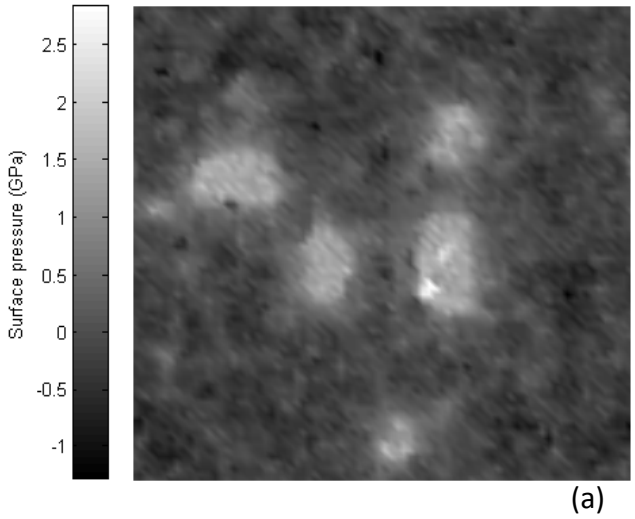

(a)

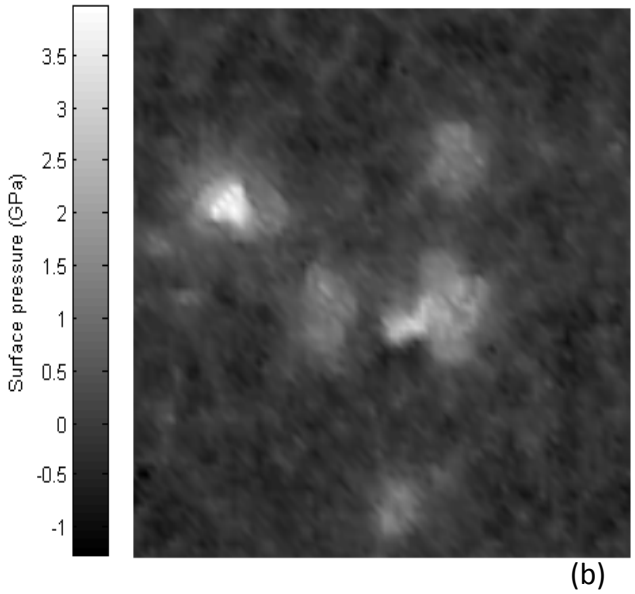

(b)

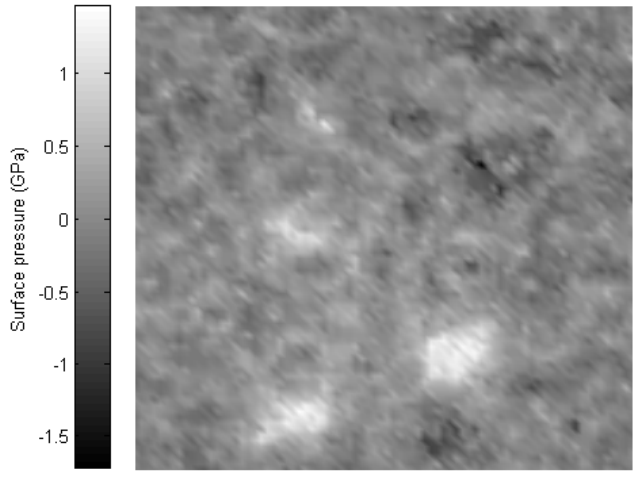

(c)

Figure 6.14: Surface pressure of the surface with RMS = 8Å under 250MPa. (a) Dry contact (b) 2000 molecules (c) 4000 molecules.

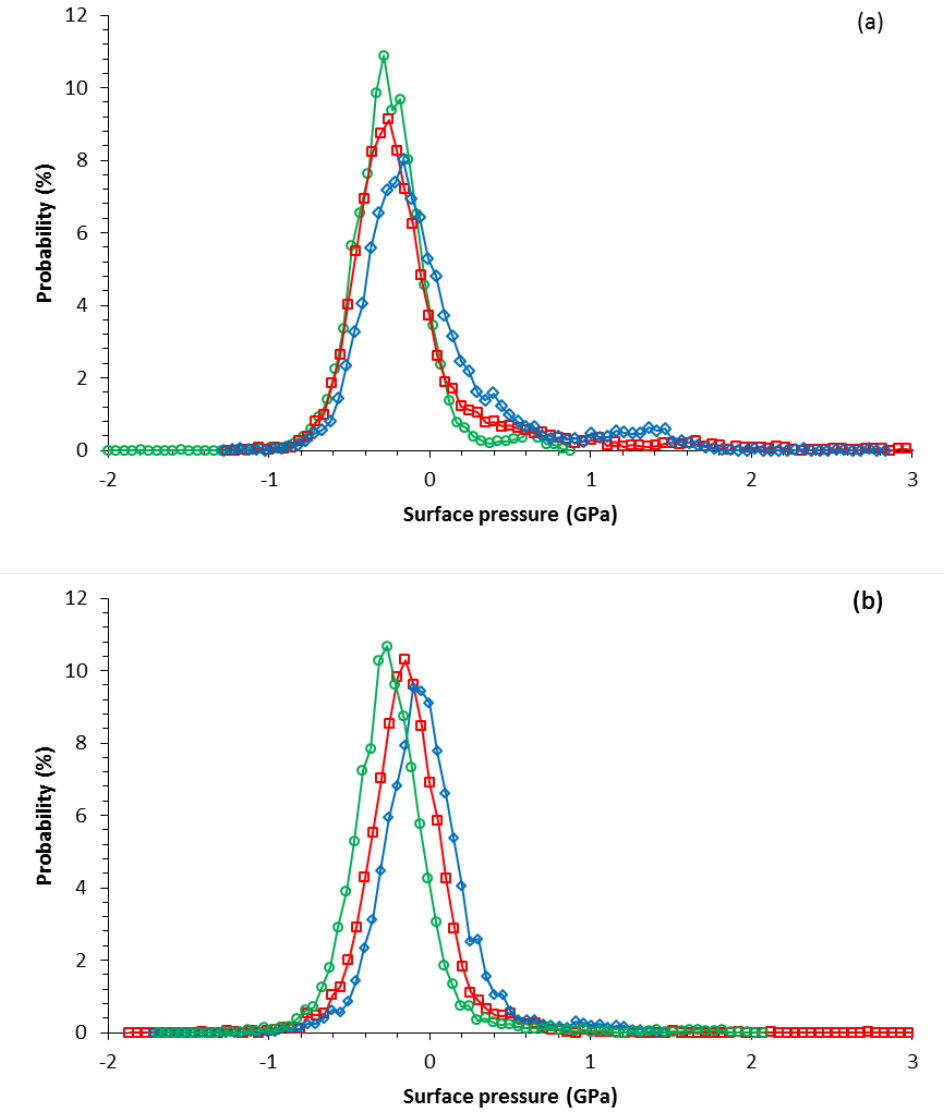

Figure 6.15: Pressure distribution in the dry contact (a) and lubricated contact (b) under 50MPa (green line), 150MPa (red line) and 250MPa (blue line).

As also reported in the molecular dynamics (MD) simulations [73, 76], more than half of the surface area mainly suffered the attractive forces. The shape of the probability distribution in this work is also in agreement with the results obtained from the MD [73, 76]. It seems that the size of the system and the roughness of the top surface have little effect on the shape of the probability distribution. The relationship between pressure distribution and load, and the shape of pressure distribution could be referred to the literature [12, 26]. In addition, for both dry and lubricated surfaces, the probability sum of the positive pressure goes up as

the loads increase as shown in figure 6.15. It is expected because further compression caused the increase of the repulsive forces between the top plane, the lubricants and the substrate.

6.3 Kinetic friction

6.3.1 Effect of load

Although there are many deviations between macroscopic and nanoscale contacts [3, 11], one agreement that the friction force is related to the normal load is reached [2]. In this section, the effects of the loads on dry and lubricated contacts are studied.

After compression pressure were stable between the upper and lower surfaces, the top plane was forced to move along x direction with a relatively high speed of 40 m/s under a constant load. The sliding distance is 32 nm in total, which corresponds to the lateral size or one cycle of the top plane. Since the top plane is flat, there is flattening of one rough surface during the sliding as opposed to that of two rough surfaces in the Spijker's work [83]. Therefore, it is not necessary to slide several cycles to obtain equilibrium in this work [75].

In figure 6.16, the relationship between the friction force and the sliding distance at various loading is shown. Because the friction forces are periodic and they are stable after 6 nm for all cases, the sliding distance shown in the figure is only 10 nm. Without the flatness of the asperities due to wear, the friction forces in figure 6.16(a) had a periodicity close to the lattice contact.

The average friction force in figure 6.16(b) was obtained by averaging the instantaneous friction force every 0.4 nm. It clearly indicates that the friction force increased with the loads. According to the results in section 6.2.2, the contact area became larger with the increase of the loads so more atomic interactions occurred. It can be said that the contact area was a dominant effect for the increase of the friction

force in this situation. In addition, the surface became smoother under larger loads, shown in figure 6.8. This means that the friction force could increase with a decrease of the RMS roughness due to a larger contact area. The friction coefficients are 0.639, 0.381 and 0.317 for 50MPa, 150MPa and 250MPa, respectively. The dependence of the friction coefficient on the loads was also found in MD simulations of Ref.[83].This dependence disobeys the continuum friction law, where the friction coefficient is independent of load.

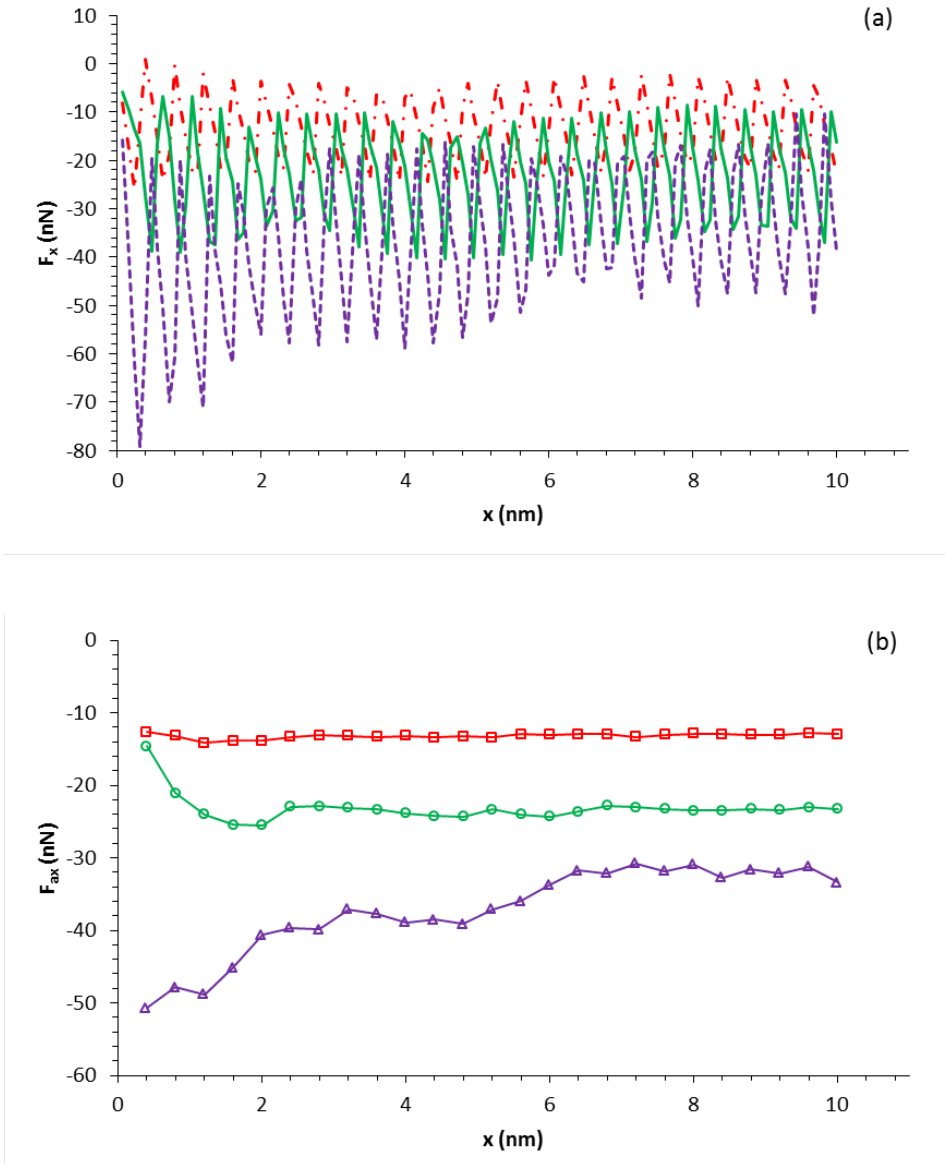

Figure 6.16: Variations of (a) instantaneous friction force and (b) average friction force with the sliding distance for dry contacts of RMS = 8Å under different loads. Red lines indicate 50MPa while blue and purple lines indicate 150MPa and 250MPa, respectively.

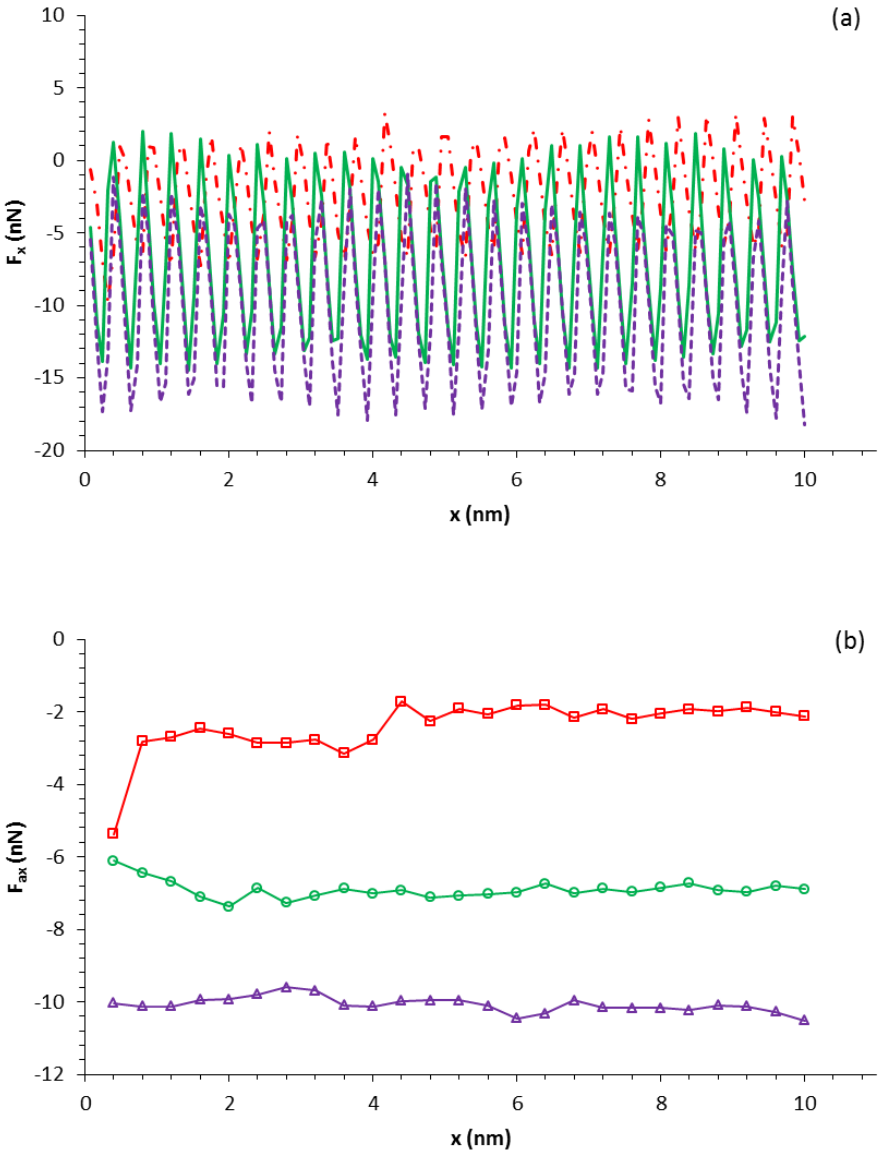

Figure 6.17: (a) Instantaneous friction force and (b) average friction force from asperity contact as a function of the sliding distance under different loads. 4000 molecules are used. Red lines indicate 50MPa while blue and purple lines indicate 150MPa and 250MPa, respectively.

For the wet contacts, the net friction force on the top plane consists of the contributions of the asperity contact and that of the lubricant. This is similar to lubricated and loaded contact discussed in figure 6.12. Those two components for a case of 4000 molecules are shown in figures 6.17 and 6.18. Firstly, the friction forces from the asperity contact and the lubricant depend on the loads, similar to the dry contact. The friction coefficients of the lubricated contacts decreased with the load

increase, corresponding to 0.176, 0.153 and 0.126 at 50MPa, 150MPa and 250MPa of loading, respectively.

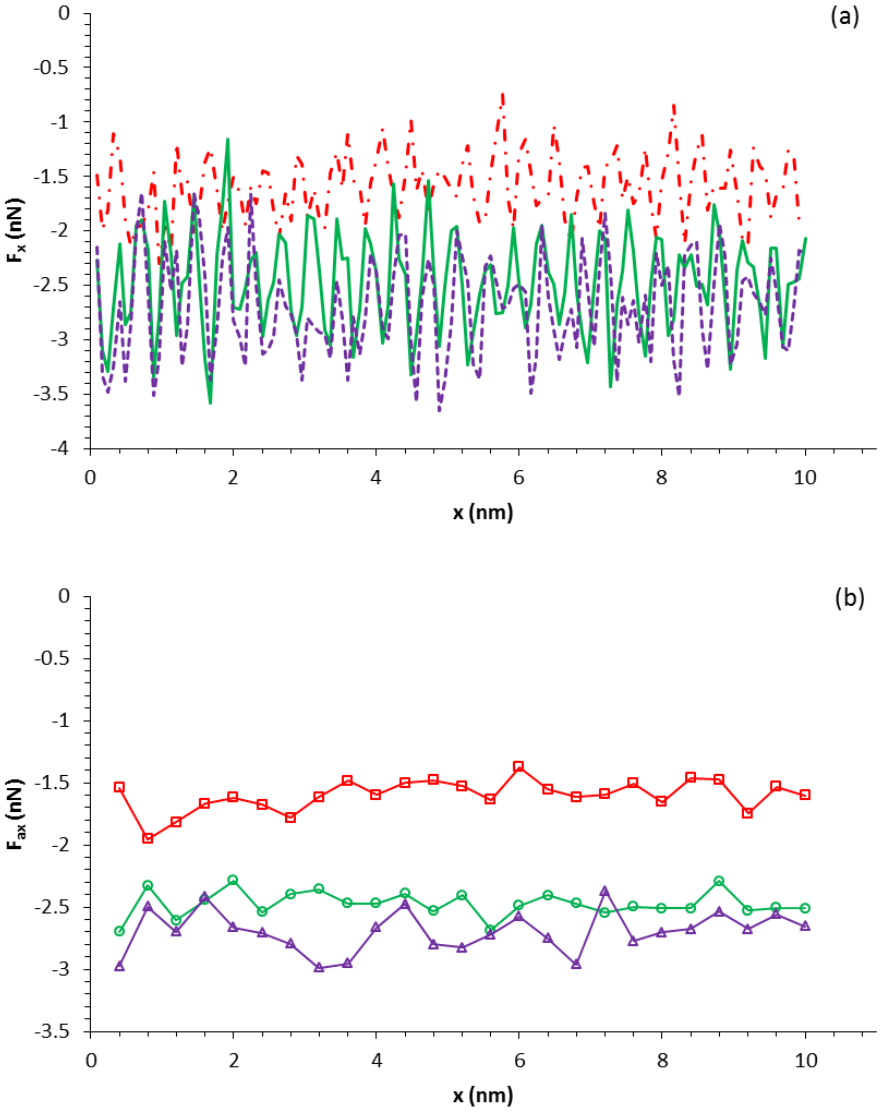

Figure 6.18: (a) Instantaneous friction force and (b) average friction force from the lubricant as a function of the sliding distance under different loads. 4000 molecules are used. Red lines indicate 50MPa while blue and purple lines indicate 150MPa and 250MPa, respectively.

In figures 6.17 and 6.18, the friction force of asperity contact is -2.0, -6.9 and -10.2 nN while the lubricant contributed to -1.57, -2.47 and -2.67 nN for 50MPa, 150MPa and 250MPa. The larger loads lead to a higher ratio between the friction force from asperity contact and that from the lubricant. Therefore, the contact area has main

effect on the friction force in partial lubrication.

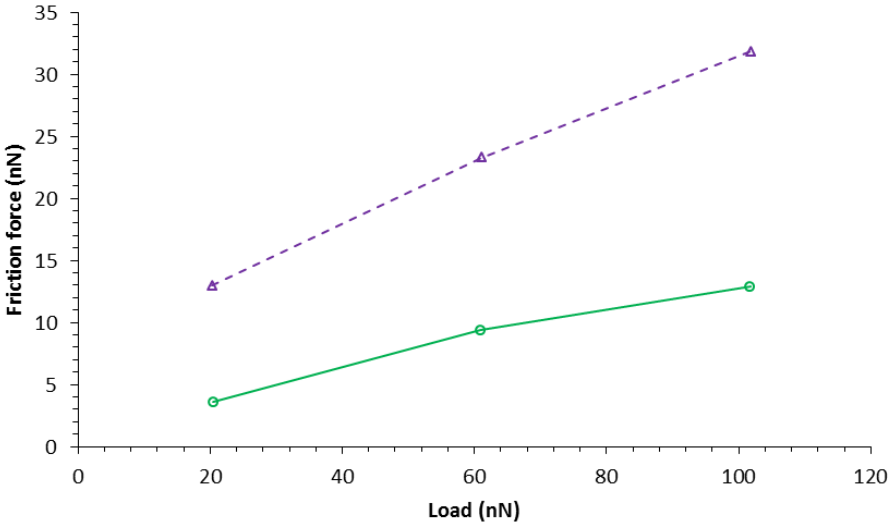

Figure 6.19: Friction force as a function load under dry (purple dashed line) and lubricated (4000 molecules, green line) conditions during sliding.

Figure 6.19 shows the relationship between the friction force and the loads. For the dry contact, the slightly sublinear relationship between the friction force and the loads was obtained in the load range of this study, which is consistent with the work in the literature [2, 73]. The applied loads in Ref. [75] were larger than 250MPa, but the relationship was qualitatively same. With 4000 molecules, however, the non-linearity was more pronounced as the load increased.

6.3.2 Effect of lubricant

The amount of lubricant plays important role on the kinetic friction. The appropriate amount depends on the RMS roughness of the surface, the loads and the chain length of the molecule [97]. The amount of the molecules is appropriate when lubricant can provide most of supporting force on the top plane, and lead to a significant reduction of friction force. Three surfaces of different RMS roughness are individually lubricated by 2000 molecules, with the results shown in figure 6.20. The rougher surfaces lead to the larger friction force with 2000 hexadecane molecules. For RMS 2Å, those molecules almost eliminated all friction force seen in the close-up part of

figure 6.20. For RMS 8Å, the friction force was larger than -40 nN. This is five order of magnitude higher than that of RMS 2Å.

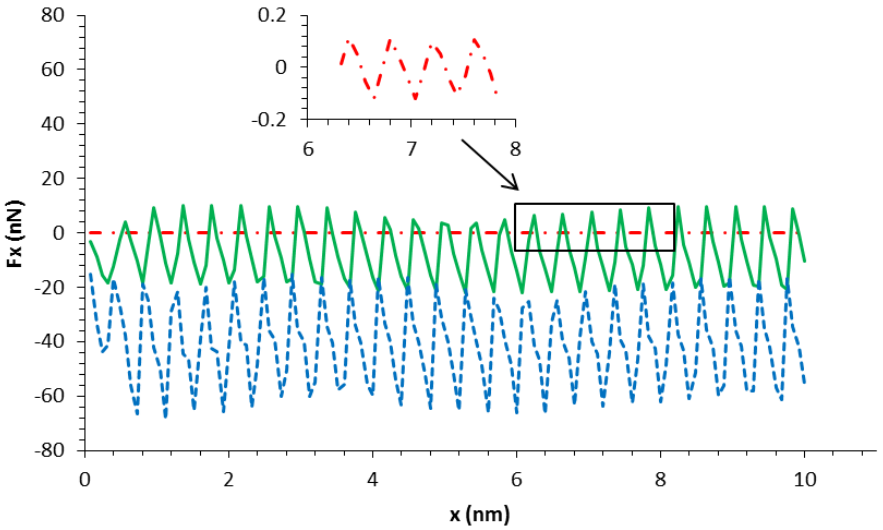

Figure 6.20: Instantaneous friction force as a function of a sliding distance for RMS = 2Å (Red line), 5Å (dash dot line) and 8Å (Dash line) under 250MPa with 2000 hexadecane molecules.

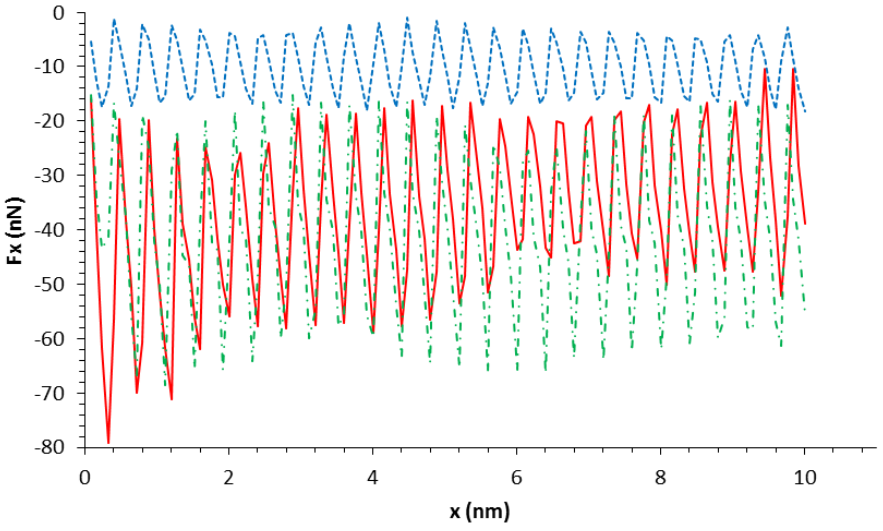

Figure 6.21: Instantaneous friction force as a function of a sliding distance for a surface of RMS = 8Å under dry and lubricated conditions. Red line indicates dry contact while green and blue dash lines describe 2000 and 4000 hexadecane molecules, respectively. The load is 250MPa.

For any surface roughness, it is possible to find the appropriate amount of lubricant. For a surface of RMS 8Å, three contacting conditions are considered. Compared to

2000 molecules, 4000 molecules reduced about 75% friction force in figure 6.21. It is expected that the friction force will be lower with more molecules. More interestingly, 2000 molecules had hardly any effect on the reduction of the friction force compared to dry contact. This was also reported in the molecular dynamics simulations [75].

The difference of the contact area between dry contact and 2000 molecules is only 1%. As the contact area dominates the friction force, 2000 molecules have little effect on the reduction in the friction force.

6.4 Summary

In this chapter, the multiscale simulations based on the hybrid simulation method (HSM) have been carried out for unlubricated and lubricated contact. The number of atoms in the multiscale model in this chapter is equivalent to about 2 million atoms in a pure MD model, which are far more than the atomic number used in previous molecular dynamics simulations [73, 75-77, 83, 97]. More importantly, the surface area formed the atoms in this work covered 1024 nm^2, whereas the surface area of molecular dynamics simulations [73, 75-77, 83, 97] ranges from 169nm^2 to 256nm^2. As mentioned by Anciaux et al.[136], more statistics data provide more accurate information.

As the load increases, the surface becomes smoother and the RMS roughness decreases. The changes in the RMS roughness are smaller with a rougher surface. The relationship between the contact area and the load is linear. It is independent of the surface roughness. The cavities between the smoother surfaces are smaller. Fewer molecules fill the cavities due to the reduced volume. The probability distribution of the surface pressure is related to the loads.

It is also found that the friction force is sublinear to the loads for dry sliding while the friction force increases nonlinearly with the loads for lubricated sliding. In addition, the friction coefficients decreased with the loads for both dry and lubricated

conditions in the load range of this study. In partial lubrication, where both asperities and lubricant molecules contributed to the supporting force, the contact area determined the friction force.

The lubricant performs several functions during the compression and the sliding. It can protect the surface topography and reduce the contact between the upper and lower surfaces. In addition, the lubricant is able to support force from the upper surface, which is really important in the reduction of the friction force. However, the big challenge is to determine the threshold of the amount of lubricant molecules for different roughness and different loads, which could be the future work.

Chapter 7: Conclusions and future work

7.1 Conclusions

In this work we have developed two multiscale models to investigate fundamental mechanisms of nanoscale contacts in several aspects. The main findings drawn from this thesis are summarized in the following paragraphs.

In chapter 3, derivation and parallel implementation of a 3D multiscale model coupling finite element method (FEM) and molecular dynamics (MD) are presented. In the model, atoms are just used to describe interactions between two contacting bodies. Their displacements follow the movement of the elements covering the whole domain of the two bodies. The scheme of the model minimizes degrees of freedom for computation in comparison to other multiscale methods. However, the scheme disables the free movement of the atoms inside the elements, and forces their in-phase movements.

The 3D multiscale model is applied to study single asperity contacts between a deformable substrate and two rigid tips (a commensurate bent tip and a stepped tip) at the nanoscale. The proposed model successfully captures some important features of nanoscale contacts such as the increasing contact radius in discrete steps and the periodicity of the kinetic friction force. The structures of the two tips have an important effect on pressure distribution and contact radius. They showed qualitatively different pressure distribution and contact radius. However, normal displacement obtained from the two tips was close. There were little influences of the structures on static friction force, kinetic friction force and friction coefficient.

In chapter 4, multiscale simulations of elastic rough surface contact were performed. The rough surfaces described by self-affine fractals consist of a number of asperities. Statistic errors were considered by using different random seeds to generate rough surfaces. One key issue of generating rough surface is mesh generation. The proposed

interpolation method was used, and performs well for generating the surfaces of the root-mean-square (rms) slope less than 0.23. Two different rms slopes have been considered in the simulations of flat-on-rough and rough-on-rough contacts. In addition, the effects of the system size on the relationship between contact area and load have also been studied.

A linear dependence of real contact area on load is observed in flat-on-rough contacts of different system sizes. The slope of this linear relation varies with the system size. Nevertheless, as the system size reaches or exceeds a threshold, the linear relationship between the load vs contact area converges to one curve. The values of constant $\kappa = E^{*}\nabla h_{rms}A_c/N$ obtained in this work are close to Perrson's prediction $\kappa = 1.6$, indicating the validation of our model. In flat-on-rough and rough-on-rough contacts, the real contact area increases with the decreasing rms slope. This observation is in agreement with the continuum prediction. In rough-on-rough contacts, a linear relationship between contact area and load is also observed. According to the continuum prediction, the slope of this relation is 1.414 times larger than that obtained from equivalent flat-on-rough contacts. However, due to finite friction force and the commensurability change of two surfaces after deformation, the obtained values here are 2.3~2.4.

In chapter 5, the effects of temperature on rough surface contact and plastic deformation of contacting bodies are studied by using a hybrid simulation method (HSM), instead of using the proposed model limited to small deformation and low temperature in the previous chapter. The coupling techniques and parallel implementation of the HSM were presented. The mechanical deformation transmitted from the atoms to the nodes is achieved by a weighted average method. The ghost atoms follow the movement of the elements, providing a physical boundary for the atomic region. We preformed multiscale simulations of single asperity contact with adhesion at low temperature to validate the method and the developed code. Parameters such as contact radius, kinetic energy extracted from the multiscale simulations were

consistent with those from molecular dynamics simulations. Their normal force and dislocation match well when the loads do not exceed 220nN. Moreover, appropriate transmission of mechanical deformation from the atomic region to the continuum region was observed in the coupling region.

The constant temperature profile in the coupling region and the MD region in a patch test has demonstrated the capability of the HSM at finite temperatures. The changes in the RMS roughness are smaller with the rougher surface. The linear relationship between contact area and load at different temperatures is observed. However, in contrast to continuum theory, the effects of temperature on this relation at the nanoscale are small as also found by other methods[136]. One possible explanation is that thermal collisions of the atoms between the substrate surface and the top plane affect the determination of the contact area because a few contacting atoms can provide the normal load due to a large instantaneous force.

In chapter 6, we study the role of lubricant in rough surface contact at temperature of 300K by performing multiscale simulations based on the hybrid simulation method (HSM). The results obtained from non-lubricated and lubricated contacts are compared. The changes of the RMS roughness indicated that rough surfaces become smoother with the larger loads. The changes in the RMS roughness are smaller for the rougher surface, and for more lubricant amount. The contact area decreases with the larger number of the lubricant molecules. This trend of the contact area is consistent with the change of the supporting force provided by the asperities in contact.

The friction force is slightly sublinear to the loads for dry sliding while the relationship between the friction force and the loads for lubricated sliding shows a more pronounced non-linearity. In addition, the friction coefficients decrease with the loads for both dry and lubricated conditions in the load range 50MPa-250MPa. In partial lubrication, where both asperities and lubricant molecules contribute to the supporting force, the contact area determines the friction force. It is also observed that the friction force reduces considerably when lubricant molecules provide a large portion of the

supporting force.

7.2 Future work

In this section, some possible extensions for an improvement of the multiscale modeling and a better understanding of nanoscale contacts are proposed.

The finite temperature hybrid simulation method is capable of studying isothermal process (constant temperature). Only mechanical deformation can be transmitted from the atomic region into the FEM region. Hence, the thermal coupling is needed to develop a fully thermomechanical multiscale model, where there is a two-way transmission of both mechanical and thermal information. This is challenging, because the mechanical and the thermal components of continuum models are governed by two different differential equations, while they are fully described by the motion of the atoms in atomistic models. Separating atomic energy into mechanical and thermal information could be the first step for thermal coupling[137].

The loads by applying the hybrid simulation method to contact problems are limited to small values, avoiding that defect such as dislocation and the FEM region are too close. The close distance can affect accuracy of results. Moving the FEM domain further from the interface will allow larger loads, but more computational time requires. A better approach is to detect dislocations by detection elements and accommodate them as elastic defects in the continuum region, following the coupled atomistic and discrete dislocation (CADD) method [171]. Unfortunately, the CADD can only work in plane strain. Development of 3D detection and accommodation techniques for dislocation is challenging but enables a significant improvement of the hybrid simulation method.

For elastic rough surface contact in chapter 4, the acceptable results were obtained by using our model. However, we only considered the rough surfaces with $\nabla h_0 \leq 0.23$ due to the limitations of the interpolation method mentioned in section 4.2.2. One direction for future work is to develop a new mesh generation method for roughening

mesh. For lubricated contacts, a more realistic potential is required to describe more realistic systems [91, 185, 186], instead of the Lennard-Jones potential using in chapter 6.

Bibliography

[1] D. Dowson, History of Tribology, Longman, 1979.
[2] J. Gao, W.D. Luedtke, D. Gourdon, M. Ruths, J.N. Israelachvili, U. Landman, Frictional Forces and Amontons' Law: From the Molecular to the Macroscopic Scale, The Journal of Physical Chemistry B, 108 (2004) 3410-3425.
[3] B. Luan, M.O. Robbins, The breakdown of continuum models for mechanical contacts, Nature, 435 (2005) 929-932.
[4] J. Israelachvili, P. McGuiggan, M. Gee, A. Homola, M. Robbins, P. Thompson, Liquid dynamics in molecularly thin films, Journal of Physics: Condensed Matter, 2 (1990) SA89.
[5] B. Bhushan, Nanotribology and nanomechanics, Wear, 259 (2005) 1507-1531.
[6] B. Bhushan, Handbook of Micro/Nano Tribology, Second Edition, Taylor & Francis, 1998.
[7] Y. Dong, Q. Li, A. Martini, Molecular dynamics simulation of atomic friction: A review and guide, Journal of Vacuum Science & Technology A: Vacuum, Surfaces, and Films, 31 (2013) 030801.
[8] R. Carpick, N. Agrait, D. Ogletree, M. Salmeron, Variation of the interfacial shear strength and adhesion of a nanometer-sized contact, Langmuir, 12 (1996) 3334-3340.
[9] U. Landman, Materials by numbers: Computations as tools of discovery, Proc. Natl. Acad. Sci., 102 (2005) 6671-6678.
[10] J. Li, K.J. Van Vliet, T. Zhu, S. Yip, S. Suresh, Atomistic mechanisms governing elastic limit and incipient plasticity in crystals, Nature, 418 (2002) 307-310.
[11] Y. Mo, K.T. Turner, I. Szlufarska, Friction laws at the nanoscale, Nature, 457 (2009) 1116-1119.
[12] Y. Mo, I. Szlufarska, Roughness picture of friction in dry nanoscale contacts, Phys. Rev. B, 81 (2010).
[13] E.B. Tadmor, M. Ortiz, R. Phillips, Quasicontinuum analysis of defects in solids, Philos. Mag. A, 73 (1996) 1529-1563.
[14] L. Wenning, M.H. Müser, Friction laws for elastic nanoscale contacts, EPL (Europhysics Letters), 54 (2001) 693.
[15] B. Luan, M.O. Robbins, Contact of single asperities with varying adhesion: Comparing continuum mechanics to atomistic simulations, Phys. Rev. E, 74 (2006) 026111.
[16] S. Cheng, M. Robbins, Defining Contact at the Atomic Scale, Tribol. Lett., 39 (2010) 329-348.
[17] K.L.Johnson, Contact Mechanics, Cambridge University Press, New York, 1985.
[18] K.L. Johnson, K. Kendall, A.D. Roberts, Surface energy and the contact of elastic solids, Proc.R.Soc.Lond.A, 324 (1971) 301-313.
[19] B.V. Derjaguin, V.M. Muller, Y.P. Toporov, Effect of contact deformations on the adhesion of particles, J. Colloid Interface Sci., 53 (1975) 314-326.
[20] D. Maugis, Adhesion of spheres: The JKR-DMT transition using a dugdale model, J. Colloid Interface Sci., 150 (1992) 243-269.
[21] D. Tabor, Surface forces and surface interactions, J. Colloid Interface Sci., 58 (1977) 2-13.
[22] F.P. Bowden, D. Tabor, The Area of Contact between Stationary and between Moving Surfaces, Proceedings of the Royal Society of London A: Mathematical, Physical and Engineering Sciences, 169 (1939) 391-413.
[23] J.F. Archard, Elastic Deformation and the Laws of Friction, Proceedings of the Royal Society of London A: Mathematical, Physical and Engineering Sciences, 243 (1957) 190-205.

[24] J.A. Greenwood, J.B.P. Williamson, Contact of Nominally Flat Surfaces, Proc. Roy. Soc. Lond. A Mat, 295 (1966) 300-319.
[25] A.W. Bush, R.D. Gibson, T.R. Thomas, The elastic contact of a rough surface, Wear, 35 (1975) 87-111.
[26] B.N.J. Persson, F. Bucher, B. Chiaia, Elastic contact between randomly rough surfaces: Comparison of theory with numerical results, Phys. Rev. B, 65 (2002) 184106.
[27] J.A. Greenwood, J.J. Wu, Surface Roughness and Contact: An Apology, Meccanica, 36 (2001) 617-630.
[28] J.A. Greenwood, A Unified Theory of Surface Roughness, Proc. Roy. Soc. Lond. A Mat, 393 (1984) 133-157.
[29] M. Ciavarella, V. Delfine, G. Demelio, A "re-vitalized" Greenwood and Williamson model of elastic contact between fractal surfaces, J. Mech. Phys. Solids, 54 (2006) 2569-2591.
[30] B.N.J. Persson, Theory of rubber friction and contact mechanics, J. Chem. Phys., 115 (2001) 3840-3861.
[31] B.N.J. Persson, Contact mechanics for randomly rough surfaces, Surf. Sci. Rep., 61 (2006) 201-227.
[32] W. Manners, J. Greenwood, Some observations on Persson's diffusion theory of elastic contact, Wear, 261 (2006) 600-610.
[33] L.W. Belytschko T, Moran B, Nonlinear finite elements for continua and structures, Wiley, New York, 1994.
[34] T.J. Hughes, The finite element method: linear static and dynamic finite element analysis, Courier Corporation, 2012.
[35] N. Yu, A.A. Polycarpou, Adhesive contact based on the Lennard–Jones potential: a correction to the value of the equilibrium distance as used in the potential, J. Colloid Interface Sci., 278 (2004) 428-435.
[36] Y. Du, L. Chen, N.E. McGruer, G.G. Adams, I. Etsion, A finite element model of loading and unloading of an asperity contact with adhesion and plasticity, J. Colloid Interface Sci., 312 (2007) 522-528.
[37] Y. Du, G.G. Adams, N.E. McGruer, I. Etsion, A parameter study of separation modes of adhering microcontacts, J. Appl. Phys., 103 (2008) 064902.
[38] S.-S. Cho, S. Park, Finite element modeling of adhesive contact using molecular potential, Tribol. Int., 37 (2004) 763-769.
[39] J. Li, T. Zhu, S. Yip, K.J. Van Vliet, S. Suresh, Elastic criterion for dislocation nucleation, Materials Science and Engineering: A, 365 (2004) 25-30.
[40] Y. Choi, K.J. Van Vliet, J. Li, S. Suresh, Size effects on the onset of plastic deformation during nanoindentation of thin films and patterned lines, J. Appl. Phys., 94 (2003) 6050-6058.
[41] X. Liu, J. Gu, Y. Shen, J. Li, C. Chen, Lattice dynamical finite-element method, Acta Mater., 58 (2010) 510-523.
[42] H. Eid, G.G. Adams, N.E. McGruer, A. Fortini, S. Buldyrev, D. Srolovitz, A Combined Molecular Dynamics and Finite Element Analysis of Contact and Adhesion of a Rough Sphere and a Flat Surface, Tribol. T., 54 (2011) 920-928.
[43] M.S. Daw, M.I. Baskes, Embedded-atom method: Derivation and application to impurities, surfaces, and other defects in metals, Phys. Rev. B, 29 (1984) 6443-6453.
[44] D.C. Rapaport, The art of molecular dynamics simulation, Cambridge university press, New York, 1995.
[45] M.P. Allen, D.J. Tildesley, Computer simulation of liquids, Oxford university press, 1989.

[46] W. Greiner, D. Rischke, L. Neise, H. Stöcker, Thermodynamics and Statistical Mechanics, Springer New York, 2000.
[47] S.A. Adelman, J.D. Doll, Generalized Langevin equation approach for atom/solid-surface scattering: General formulation for classical scattering off harmonic solids, The Journal of Chemical Physics, 64 (1976) 2375-2388.
[48] H.J.C. Berendsen, J.P.M. Postma, W.F. van Gunsteren, A. DiNola, J.R. Haak, Molecular dynamics with coupling to an external bath, The Journal of Chemical Physics, 81 (1984) 3684-3690.
[49] S. Nosé, A unified formulation of the constant temperature molecular dynamics methods, The Journal of Chemical Physics, 81 (1984) 511-519.
[50] W.K. Liu, E.G. Karpov, S. Zhang, H.S. Park, An introduction to computational nanomechanics and materials, Comput. Method. Appl. M, 193 (2004) 1529-1578.
[51] S. Plimpton, Fast Parallel Algorithms for Short-Range Molecular Dynamics, J. Comput. Phys., 117 (1995) 1-19.
[52] P. Procacci, T.A. Darden, E. Paci, M. Marchi, ORAC: A molecular dynamics program to simulate complex molecular systems with realistic electrostatic interactions, J. Comput. Chem., 18 (1997) 1848-1862.
[53] J. Li, AtomEye: an efficient atomistic configuration viewer, Model. Simul. Mater. Sc, 11 (2003) 173.
[54] W. Humphrey, A. Dalke, K. Schulten, VMD: visual molecular dynamics, Journal of molecular graphics, 14 (1996) 33-38.
[55] A. Stukowski, Visualization and analysis of atomistic simulation data with OVITO–the Open Visualization Tool, Model. Simul. Mater. Sc, 18 (2010) 015012.
[56] W. Zhong, D. Tomanek, First-principles theory of atomic-scale friction, Phys. Rev. Lett., 64 (1990) 3054.
[57] G.A. Tomlinson, CVI. A molecular theory of friction, The London, Edinburgh, and Dublin Philosophical Magazine and Journal of Science, 7 (1929) 905-939.
[58] H. Berro, A molecular dynamics approach to nano-scale lubrication. Ph. D. thesis, MEGA, INSA de Lyon, 2010ISAL0084, http://theses. insa-lyon. fr/publication/2010ISAL0084/these. pdf, 2010.
[59] J. Pascual, J. Mendez, J. Gomez-Herrero, A. Baro, N. Garcia, U. Landman, W. Luedtke, E. Bogachek, H.-P. Cheng, Properties of metallic nanowires: from conductance quantization to localization, Science, 267 (1995) 1793-1795.
[60] M.R. Sørensen, K.W. Jacobsen, P. Stoltze, Simulations of atomic-scale sliding friction, Physical Review B - Condensed Matter and Materials Physics, 53 (1996) 2101-2113.
[61] J. Shimizu, H. Eda, M. Yoritsune, E. Ohmura, Molecular dynamics simulation of friction on the atomic scale, Nanotechnology, 9 (1998) 118.
[62] Q. Li, Y. Dong, D. Perez, A. Martini, R.W. Carpick, Speed Dependence of Atomic Stick-Slip Friction in Optimally Matched Experiments and Molecular Dynamics Simulations, Phys. Rev. Lett., 106 (2011) 126101.
[63] S. Solhjoo, A.I. Vakis, Single asperity nanocontacts: Comparison between molecular dynamics simulations and continuum mechanics models, Comp. Mater. Sci., 99 (2015) 209-220.
[64] S. Solhjoo, A.I. Vakis, Definition and detection of contact in atomistic simulations, Comp. Mater. Sci., 109 (2015) 172-182.
[65] D. Dietzel, C. Ritter, T. Mönninghoff, H. Fuchs, A. Schirmeisen, U.D. Schwarz, Frictional Duality Observed during Nanoparticle Sliding, Phys. Rev. Lett., 101 (2008) 125505.
[66] Z. Liu, J. Yang, F. Grey, J.Z. Liu, Y. Liu, Y. Wang, Y. Yang, Y. Cheng, Q. Zheng, Observation of

microscale superlubricity in graphite, Phys. Rev. Lett., 108 (2012) 205503.
[67] R.W. Carpick, D.F. Ogletree, M. Salmeron, A General Equation for Fitting Contact Area and Friction vs Load Measurements, J. Colloid Interface Sci., 211 (1999) 395-400.
[68] J.H. Dieterich, B.D. Kilgore, Direct observation of frictional contacts: New insights for state-dependent properties, Pure Appl. Geophys., 143 (1994) 283-302.
[69] P. Berthoud, T. Baumberger, Shear stiffness of a solid–solid multicontact interface, Proceedings of the Royal Society of London A: Mathematical, Physical and Engineering Sciences, 454 (1998) 1615-1634.
[70] J. Krim, G. Palasantzas, Experimental observations of self-affine scaling and kinetic roughening at sub-micron lengthscales, Int. J. Mod. Phys. B, 9 (1995) 599-632.
[71] C. Yang, B.N.J. Persson, Contact mechanics: contact area and interfacial separation from small contact to full contact, Journal of Physics: Condensed Matter, 20 (2008) 215214.
[72] C. Yang, B.N.J. Persson, Molecular Dynamics Study of Contact Mechanics: Contact Area and Interfacial Separation from Small to Full Contact, Phys. Rev. Lett., 100 (2008).
[73] P. Spijker, G. Anciaux, J.-F. Molinari, The effect of loading on surface roughness at the atomistic level, Comput. Mech., 50 (2012) 273-283.
[74] S. Akarapu, T. Sharp, M.O. Robbins, Stiffness of Contacts between Rough Surfaces, Phys. Rev. Lett., 106 (2011) 204301.
[75] X. Zheng, H. Zhu, A.K. Tieu, B. Kosasih, Roughness and Lubricant Effect on 3D Atomic Asperity Contact, Tribol. Lett., 53 (2013) 215-223.
[76] X. Zheng, H. Zhu, A. Kiet Tieu, B. Kosasih, A molecular dynamics simulation of 3D rough lubricated contact, Tribol. Int., 67 (2013) 217-221.
[77] P. Spijker, G. Anciaux, J.-F. Molinari, Relations between roughness, temperature and dry sliding friction at the atomic scale, Tribol. Int., 59 (2013) 222-229.
[78] C. Campañá, M.H. Müser, M.O. Robbins, Elastic contact between self-affine surfaces: comparison of numerical stress and contact correlation functions with analytic predictions, Journal of Physics: Condensed Matter, 20 (2008) 354013.
[79] N. Mulakaluri, B. Persson, Adhesion between elastic solids with randomly rough surfaces: Comparison of analytical theory with molecular-dynamics simulations, EPL (Europhysics Letters), 96 (2011) 66003.
[80] P.L. Piotrowski, R.J. Cannara, G. Gao, J.J. Urban, R.W. Carpick, J.A. Harrison, Atomistic factors governing adhesion between diamond, amorphous carbon and model diamond nanocomposite surfaces, J. Adhes. Sci. Technol., 24 (2010) 2471-2498.
[81] T.D. Jacobs, K.E. Ryan, P.L. Keating, D.S. Grierson, J.A. Lefever, K.T. Turner, J.A. Harrison, R.W. Carpick, The effect of atomic-scale roughness on the adhesion of nanoscale asperities: A combined simulation and experimental investigation, Tribol. Lett., 50 (2013) 81-93.
[82] H. Kim, A. Strachan, Molecular dynamics characterization of the contact between clean metallic surfaces with nanoscale asperities, Phys. Rev. B, 83 (2011).
[83] P. Spijker, G. Anciaux, J.-F. Molinari, Dry Sliding Contact Between Rough Surfaces at the Atomistic Scale, Tribol. Lett., 44 (2011) 279-285.
[84] H. Kim, A. Strachan, Nanoscale metal-metal contact physics from molecular dynamics: The strongest contact size, Phys. Rev. Lett., 104 (2010).
[85] J. Tu, G.-H. Yeoh, C. Liu, Chapter 8 - Some Advanced Topics in CFD, in: Computational Fluid Dynamics (Second Edition), Butterworth-Heinemann, 2013, pp. 349-394.

[86] A. Jabbarzadeh, J.D. Atkinson, R.I. Tanner, Wall slip in the molecular dynamics simulation of thin films of hexadecane, The Journal of Chemical Physics, 110 (1999) 2612.
[87] C. Hu, M. Bai, J. Lv, X. Li, Molecular dynamics simulation of mechanism of nanoparticle in improving load-carrying capacity of lubricant film, Comp. Mater. Sci., 109 (2015) 97-103.
[88] V. Kalyanasundaram, D.E. Spearot, A.P. Malshe, Molecular dynamics simulation of nanoconfinement induced organization of n-decane, Langmuir, 25 (2009) 7553-7560.
[89] A. Jabbarzadeh, J. Atkinson, R. Tanner, The effect of branching on slip and rheological properties of lubricants in molecular dynamics simulation of Couette shear flow, Tribol. Int., 35 (2002) 35-46.
[90] H. Berro, N. Fillot, P. Vergne, Molecular dynamics simulation of surface energy and ZDDP effects on friction in nano-scale lubricated contacts, Tribol. Int., 43 (2010) 1811-1822.
[91] T.D. Ta, A.K. Tieu, H. Zhu, Q. Zhu, P.B. Kosasih, J. Zhang, G. Deng, Tribological Behavior of Aqueous Copolymer Lubricant in Mixed Lubrication Regime, Acs Appl. Mater. Interfaces, 8 (2016) 5641-5652.
[92] I.M. Sivebæk, V.N. Samoilov, B.N.J. Persson, Squeezing molecular thin alkane lubrication films between curved solid surfaces with long-range elasticity: Layering transitions and wear, J. Chem. Phys., 119 (2003) 2314-2321.
[93] D. Savio, N. Fillot, P. Vergne, A molecular dynamics study of the transition from ultra-thin film lubrication toward local film breakdown, Tribol. Lett., 50 (2013) 207-220.
[94] J. Gao, W. Luedtke, U. Landman, Structures, solvation forces and shear of molecular films in a rough nano-confinement, Tribol. Lett., 9 (2000) 3-13.
[95] J. Gao, W. Luedtke, U. Landman, Nano-elastohydrodynamics: Structrue, dynamics, and flow in nonuniform lubricated junctions, Science, 270 (1995) 605.
[96] L. Zhang, C. Tang, Friction and wear of diamond–silicon nano-systems: Effect of moisture and surface roughness, Wear, 302 (2013) 929-936.
[97] X. Zheng, H. Zhu, B. Kosasih, A. Kiet Tieu, A molecular dynamics simulation of boundary lubrication: The effect of n-alkanes chain length and normal load, Wear, 301 (2013) 62-69.
[98] R.E. Miller, E.B. Tadmor, A unified framework and performance benchmark of fourteen multiscale atomistic/continuum coupling methods, Model. Simul. Mater. Sc, 17 (2009) 053001.
[99] N. Holmes, T. Belytschko, Postprocessing of finite element transient response calculations by digital filters, Computers & Structures, 6 (1976) 211-216.
[100] V. Shenoy, R. Miller, E. Tadmor, D. Rodney, R. Phillips, M. Ortiz, An adaptive finite element approach to atomic-scale mechanics—the quasicontinuum method, J. Mech. Phys. Solids, 47 (1999) 611-642.
[101] B. Luan, S. Hyun, J.F. Molinari, N. Bernstein, M.O. Robbins, Multiscale modeling of two-dimensional contacts, Phys. Rev. E, 74 (2006) 046710.
[102] S. Qu, V. Shastry, W.A. Curtin, R.E. Miller, A finite-temperature dynamic coupled atomistic/discrete dislocation method, Model. Simul. Mater. Sc, 13 (2005) 1101-1118.
[103] R.H.G. Dong Qian, A Virtual Atom Cluster Approach to the Mechanics of Nanostructures, International Journal for Multiscale Computational Engineering, 2 (2004) 277-289.
[104] J. Jin, S.A. Shevlin, Z.X. Guo, Multiscale simulation of onset plasticity during nanoindentation of Al (0 0 1) surface, Acta Mater., 56 (2008) 4358-4368.
[105] C. Fang, X. Yang, Study of nanocontact and incipient nanoscratch process using the quasicontinuum method, Materials Science and Engineering: A, 600 (2014) 221-230.
[106] G.J. Wagner, W.K. Liu, Coupling of atomistic and continuum simulations using a bridging scale

decomposition, J. Comput. Phys., 190 (2003) 249-274.
[107] H.S. Park, E.G. Karpov, W.K. Liu, P.A. Klein, The bridging scale for two-dimensional atomistic/continuum coupling, Philosophical Magazine, 85 (2005) 79-113.
[108] H.S. Park, E.G. Karpov, P.A. Klein, W.K. Liu, Three-dimensional bridging scale analysis of dynamic fracture, J. Comput. Phys., 207 (2005) 588-609.
[109] W.K. Liu, H.S. Park, D. Qian, E.G. Karpov, H. Kadowaki, G.J. Wagner, Bridging scale methods for nanomechanics and materials, Comput. Method. Appl. M, 195 (2006) 1407-1421.
[110] H. Kadowaki, W.K. Liu, Bridging multi-scale method for localization problems, Comput. Method. Appl. M, 193 (2004) 3267-3302.
[111] D. Qian, G.J. Wagner, W.K. Liu, A multiscale projection method for the analysis of carbon nanotubes, Comput. Method. Appl. M, 193 (2004) 1603-1632.
[112] S. Xiao, T. Belytschko, A bridging domain method for coupling continua with molecular dynamics, Comput. Method. Appl. M, 193 (2004) 1645-1669.
[113] M. Xu, R. Gracie, T. Belytschko, A continuum-to-atomistic bridging domain method for composite lattices, Int. J. Numer. Meth. Eng., 81 (2010) 1635-1658.
[114] R. Gracie, T. Belytschko, Concurrently coupled atomistic and XFEM models for dislocations and cracks, Int. J. Numer. Meth. Eng., 78 (2009) 354-378.
[115] R. Gracie, T. Belytschko, An adaptive concurrent multiscale method for the dynamic simulation of dislocations, Int. J. Numer. Meth. Eng., 86 (2011) 575-597.
[116] J. Fish, M.A. Nuggehally, M.S. Shephard, C.R. Picu, S. Badia, M.L. Parks, M. Gunzburger, Concurrent AtC coupling based on a blend of the continuum stress and the atomistic force, Comput. Method. Appl. M, 196 (2007) 4548-4560.
[117] S. Badia, M. Parks, P. Bochev, M. Gunzburger, R. Lehoucq, On Atomistic-to-Continuum Coupling by Blending, Multiscale Modeling & Simulation, 7 (2008) 381-326.
[118] M. Zhou, A new look at the atomic level virial stress: on continuum-molecular system equivalence, Proceedings of the Royal Society of London A: Mathematical, Physical and Engineering Sciences, 459 (2003) 2347-2392.
[119] R.E. Rudd, J.Q. Broughton, Coarse-grained molecular dynamics and the atomic limit of finite elements, Phys. Rev. B, 58 (1998) R5893-R5896.
[120] F.F. Abraham, J.Q. Broughton, N. Bernstein, E. Kaxiras, Spanning the continuum to quantum length scales in a dynamic simulation of brittle fracture, EPL (Europhysics Letters), 44 (1998) 783.
[121] J.Q. Broughton, F.F. Abraham, N. Bernstein, E. Kaxiras, Concurrent coupling of length scales: Methodology and application, Phys. Rev. B, 60 (1999) 2391-2403.
[122] L.E. Shilkrot, W.A. Curtin, R.E. Miller, A coupled atomistic/continuum model of defects in solids, J. Mech. Phys. Solids, 50 (2002) 2085-2106.
[123] W.K. Liu, D. Qian, S. Gonella, S. Li, W. Chen, S. Chirputkar, Multiscale methods for mechanical science of complex materials: Bridging from quantum to stochastic multiresolution continuum, Int. J. Numer. Meth. Eng., 83 (2010) 1039-1080.
[124] W.A. Curtin, R.E. Miller, Atomistic/continuum coupling in computational materials science, Model. Simul. Mater. Sc, 11 (2003) R33.
[125] H.S. Park, E.G. Karpov, W.K. Liu, A temperature equation for coupled atomistic/continuum simulations, Comput. Method. Appl. M, 193 (2004) 1713-1732.
[126] G.J. Wagner, R.E. Jones, J.A. Templeton, M.L. Parks, An atomistic-to-continuum coupling method for heat transfer in solids, Comput. Method. Appl. M, 197 (2008) 3351-3365.

[127] L.M. Dupuy, E.B. Tadmor, R.E. Miller, R. Phillips, Finite-temperature quasicontinuum: Molecular dynamics without all the atoms, Phys. Rev. Lett., 95 (2005).
[128] E.B. Tadmor, F. Legoll, W.K. Kim, L.M. Dupuy, R.E. Miller, Finite-Temperature Quasi-Continuum, Applied Mechanics Reviews, 65 (2013) 010803-010803.
[129] W.K. Kim, M. Luskin, D. Perez, A.F. Voter, E.B. Tadmor, Hyper-QC: An accelerated finite-temperature quasicontinuum method using hyperdynamics, J. Mech. Phys. Solids, 63 (2014) 94-112.
[130] B. Shiari, R.E. Miller, D.D. Klug, Multiscale modeling of solids at the nanoscale: dynamic approach, Can. J. Phys., 86 (2008) 391-400.
[131] B. Shiari, R.E. Miller, D.D. Klug, Multiscale simulation of material removal processes at the nanoscale, J. Mech. Phys. Solids, 55 (2007) 2384-2405.
[132] N. Mathew, R.C. Picu, M. Bloomfield, Concurrent coupling of atomistic and continuum models at finite temperature, Comput. Method. Appl. M, 200 (2011) 765-773.
[133] S.B. Ramisetti, G. Anciaux, J.F. Molinari, Spatial filters for bridging molecular dynamics with finite elements at finite temperatures, Comput. Method. Appl. M, 253 (2013) 28-38.
[134] S.A. Adelman, J.D. Doll, Generalized Langevin equation approach for atom/solid-surface scattering: Collinear atom/harmonic chain model, The Journal of Chemical Physics, 61 (1974) 4246-4250.
[135] S.B. Ramisetti, G. Anciaux, J.F. Molinari, A concurrent atomistic and continuum coupling method with applications to thermo-mechanical problems, Int. J. Numer. Meth. Eng., 97 (2014) 707-738.
[136] G. Anciaux, S.B. Ramisetti, J.F. Molinari, A finite temperature bridging domain method for MD-FE coupling and application to a contact problem, Comput. Method. Appl. M, 205-208 (2012) 204-212.
[137] A. Sadeghirad, F. Liu, A three-layer-mesh bridging domain for coupled atomistic–continuum simulations at finite temperature: Formulation and testing, Comput. Method. Appl. M, 268 (2014) 299-317.
[138] A. Sadeghirad, A. Tabarraei, A damping boundary condition for coupled atomistic–continuum simulations, Comput. Mech., 52 (2013) 535-551.
[139] A. Sadeghirad, N. Su, F. Liu, Mechanical modeling of graphene using the three-layer-mesh bridging domain method, Comput. Method. Appl. M, 294 (2015) 278-298.
[140] G. Michal, C. Lu, A. Kiet Tieu, Multiscale model of elastic nanocontacts, Comp. Mater. Sci., 81 (2014) 98-103.
[141] G. Michal, Multiscale modelling of an Atomic Force Microscope for the study of nanoscale contacts. Ph.D. thesis, University of Wollongong, University of Wollongong. School of Mechanical, Materials and Mechatronic Engineering, 2011.
[142] H.S. Park, W.K. Liu, An introduction and tutorial on multiple-scale analysis in solids, Comput. Method. Appl. M, 193 (2004) 1733-1772.
[143] R.W. Ogden, Non-linear elastic deformations, Courier Corporation, New York, 1997.
[144] R.A. Sauer, S. Li, A contact mechanics model for quasi-continua, Int. J. Numer. Meth. Eng., 71 (2007) 931-962.
[145] G. Karypis, V. Kumar, A fast and high quality multilevel scheme for partitioning irregular graphs, Siam. J. Sci. Comput., 20 (1998) 359-392.
[146] Openmpi website. URL http://www.open-mpi.org/.
[147] A. Curnier, Computational methods in solid mechanics, Springer Science & Business Media, 2012.

[148] V.-D. Nguyen, E. Béchet, C. Geuzaine, L. Noels, Imposing periodic boundary condition on arbitrary meshes by polynomial interpolation, Comp. Mater. Sci., 55 (2012) 390-406.
[149] M.J. Quinn, Parallel Programming in C with MPI and OpenMP, McGraw-Hill, New York, 2004.
[150] S. Cheng, B. Luan, M.O. Robbins, Contact and friction of nanoasperities: Effects of adsorbed monolayers, Phys. Rev. E, 81 (2010).
[151] R.W. Carpick, M. Salmeron, Scratching the Surface: Fundamental Investigations of Tribology with Atomic Force Microscopy, Chem. Rev., 97 (1997) 1163-1194.
[152] P. Meakin, Fractals, Scaling and Growth Far from Equilibrium, Cambridge University Press, 1998.
[153] S. Hyun, L. Pei, J.F. Molinari, M.O. Robbins, Finite-element analysis of contact between elastic self-affine surfaces, Phys. Rev. E, 70 (2004).
[154] B. Luan, M.O. Robbins, Hybrid Atomistic/Continuum Study of Contact and Friction Between Rough Solids, Tribol. Lett., 36 (2009) 1-16.
[155] G.G. Adams, M. Nosonovsky, Contact modeling — forces, Tribol. Int., 33 (2000) 431-442.
[156] R.F. Voss, Fundamental Algorithms in Computer Graphics, Springr-Verlag, Berlin, 1985.
[157] R. Pohrt, V.L. Popov, Contact stiffness of randomly rough surfaces, Sci Rep, 3 (2013) 3293.
[158] L. Pei, S. Hyun, J.F. Molinari, M.O. Robbins, Finite element modeling of elasto-plastic contact between rough surfaces, J. Mech. Phys. Solids, 53 (2005) 2385-2409.
[159] L. Verlet, Computer "Experiments" on Classical Fluids. I. Thermodynamical Properties of Lennard-Jones Molecules, Phys. Rev., 159 (1967) 98-103.
[160] S. Hyun, M.O. Robbins, Elastic contact between rough surfaces: Effect of roughness at large and small wavelengths, Tribol. Int., 40 (2007) 1413-1422.
[161] B.N.J. Persson, Elastoplastic Contact between Randomly Rough Surfaces, Phys. Rev. Lett., 87 (2001) 116101.
[162] C. Kittel, Introduction to solid state physics, 8th ed., J. Wiley, New York, 2005.
[163] R. Tong, G. Liu, T. Liu, Multiscale Analysis on Two Dimensional Nanoscale Sliding Contacts of Textured Surfaces, Journal of Tribology, 133 (2011) 041401.
[164] P. Zhu, Y. Hu, F. Fang, H. Wang, Multiscale simulations of nanoindentation and nanoscratch of single crystal copper, Appl. Surf. Sci., 258 (2012) 4624-4631.
[165] G. Anciaux, J.-F. Molinari, Contact mechanics at the nanoscale, a 3D multiscale approach, Int. J. Numer. Meth. Eng., 79 (2009) 1041-1067.
[166] C.L. Kelchner, S.J. Plimpton, J.C. Hamilton, Dislocation nucleation and defect structure during surface indentation, Phys. Rev. B, 58 (1998) 11085-11088.
[167] J.D. Honeycutt, H.C. Andersen, Molecular dynamics study of melting and freezing of small Lennard-Jones clusters, J. Phys. Chem., 91 (1987) 4950-4963.
[168] P. Steinmann, A. Elizondo, R. Sunyk, Studies of validity of the Cauchy–Born rule by direct comparison of continuum and atomistic modelling, Model. Simul. Mater. Sc, 15 (2007) S271-S281.
[169] R.J. Hardy, Formulas for determining local properties in molecular‐dynamics simulations: Shock waves, The Journal of Chemical Physics, 76 (1982) 622-628.
[170] J.A. Zimmerman, E.B. WebbIII, J. Hoyt, R.E. Jones, P. Klein, D.J. Bammann, Calculation of stress in atomistic simulation, Model. Simul. Mater. Sc, 12 (2004) S319.
[171] L.E. Shilkrot, R.E. Miller, W.A. Curtin, Multiscale plasticity modeling: coupled atomistics and discrete dislocation mechanics, J. Mech. Phys. Solids, 52 (2004) 755-787.
[172] J. Cho, T. Junge, J.-F. Molinari, G. Anciaux, Toward a 3D coupled atomistic and discrete dislocation dynamics simulation: dislocation core structures and Peierls stresses with several character

angles in FCC aluminum, Advanced Modeling and Simulation in Engineering Sciences, 2 (2015).
[173] S. Kazanc, Y.Ö. Çiftci, K. Çolakoğlu, S. Ozgen, Temperature and pressure dependence of the some elastic and lattice dynamical properties of copper: a molecular dynamics study, Physica B: Condensed Matter, 381 (2006) 96-102.
[174] Y. Mishin, M.J. Mehl, D.A. Papaconstantopoulos, A.F. Voter, J.D. Kress, Structural stability and lattice defects in copper:Ab initio, tight-binding, and embedded-atom calculations, Phys. Rev. B, 63 (2001).
[175] X. Zheng, Molecular dynamics simulation of boundary lubricated contacts. Doctor of Philosophy thesis, University of Wollongong, 2014. http://ro.uow.edu.au/theses/4170.
[176] B.N. Persson, O. Albohr, U. Tartaglino, A.I. Volokitin, E. Tosatti, On the nature of surface roughness with application to contact mechanics, sealing, rubber friction and adhesion, J Phys Condens Matter, 17 (2005) R1-R62.
[177] Y.Z. Hu, K. Tonder, Proceedings of the 5th International Conference on Metrology and Properties of Engineering Surfaces Simulation of 3-D random rough surface by 2-D digital filter and fourier analysis, Int. J. Mach. Tools Manuf, 32 (1992) 83-90.
[178] M. Ausloos, D.H. Berman, A Multivariate Weierstrass-Mandelbrot Function, Proc. R. Soc. Lond. A, 400 (1985) 331-350.
[179] Y. Mishin, D. Farkas, M.J. Mehl, D.A. Papaconstantopoulos, Interatomic potentials for monoatomic metals from experimental data and \textit{ab initio} calculations, Phys. Rev. B, 59 (1999) 3393-3407.
[180] M.G. Martin, J.I. Siepmann, Transferable Potentials for Phase Equilibria. 1. United-Atom Description of n-Alkanes, The Journal of Physical Chemistry B, 102 (1998) 2569-2577.
[181] C. Wu, L. Zhang, S. Li, Z. Jiang, P. Qu, A unified method for characterizing multiple lubrication regimes involving plastic deformation of surface asperities, Tribol. Int., 100 (2016) 70-83.
[182] C. Campañá, M.H. Müser, Contact mechanics of real vs. randomly rough surfaces: A Green's function molecular dynamics study, EPL (Europhysics Letters), 77 (2007) 38005.
[183] M. Tanemura, T. Ogawa, N. Ogita, A new algorithm for three-dimensional voronoi tessellation, J. Comput. Phys., 51 (1983) 191-207.
[184] H. Tanaka, Y. Yamaki, M. Kato, Solubility of carbon dioxide in pentadecane, hexadecane, and pentadecane + hexadecane, Journal of Chemical & Engineering Data, 38 (1993) 386-388.
[185] T.D. Ta, A.K. Tieu, H. Zhu, B. Kosasih, Adsorption of Normal-Alkanes on Fe(110), FeO(110), and Fe2O3(0001): Influence of Iron Oxide Surfaces, The Journal of Physical Chemistry C, 119 (2015) 12999-13010.
[186] D.T. Ta, A.K. Tieu, H.T. Zhu, B. Kosasih, Thin film lubrication of hexadecane confined by iron and iron oxide surfaces: A crucial role of surface structure, The Journal of Chemical Physics, 143 (2015) 164702.